Universidad Autónoma de Madrid
Facultad de Ciencias

Transport Property Measurements of Nanostructured Materials

Miguel Muñoz Rojo

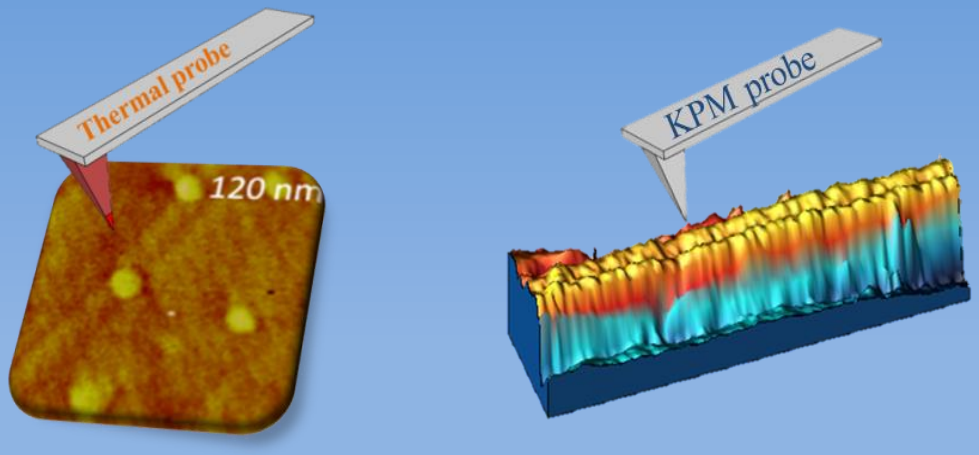

Supervisor:
Dr. Marisol Martín Gonzalez

Instituto de Microelectrónica de Madrid (IMM)

Centro Superior de Investigaciones Científicas (CSIC)

Transport Property Measurements of Nanostructured Materials

Ph. D. Thesis

A dissertation submitted in satisfaction of the requirements for the degree of Doctor in Matter Physics and Nanotechnology of the

Universidad Autónoma de Madrid

at the

Department of Condensed Matter Physics

9th June 2015

by

Miguel Muñoz Rojo

under the direction of

Dra. Mª Soledad Martín Gonzalez

and the academic tutorship of

Dr. Rodolfo Miranda Soriano

INSTITUTO DE MICROELECTRÓNICA DE MADRID

CONSEJO SUPERIOR DE INVESTIGACIONES CIENTÍFICAS (IMM-CSIC)

La realización de esta tesis doctoral ha sido posible gracias a la financiación del proyecto Europeo ERC StG NanoTEC 240497 y a la concesión de una beca JAE Pre-Doc del CSIC.

Este trabajo doctoral ha sido realizado en el Instituto de Microelectrónica de Madrid (IMM), perteneciente a la Agencia Estatal Consejo Superior de Investigaciones Científicas (CSIC), y dirigido por la Dra. Mº Soledad Martín Gonzalez.

A mis padres, hermano y Silvia.

‘‘Te digo que no vale

guardar la sed de estrellas bajo llave’’

Agustín Millares Sall

(1917-1989)

Agradecimientos

Durante estos cuatro años que ha durado esta tesis doctoral han sido numerosas las personas que han contribuido directa o indirectamente a engrandecerla. En primer lugar, me gustaría agradecer a mi directora de tesis, la Dra. Dña. Marisol Martín González todo el apoyo que me ha brindado durante estos cuatro años. Su pasión, su entusiasmo y su dedicación a la ciencia han sido, sin duda, inspiradores para mí. Sus ideas, su esfuerzo y su exigencia para sacar lo mejor de mí mismo han motivado enormemente mi trabajo, siendo ella un fantástico ejemplo de éxito profesional y un excelente modelo a seguir en mi carrera científica. Por todo ello, ha sido un honor ser su estudiante de doctorado durante todo este tiempo.

Quiero destacar también la inmensa contribución, tanto humana como científica, de los miembros del grupo: Olga Caballero, Pablo Díaz, Jaime Martín, Juan José Romero, Jon Maiz, David Solís, Cristina Vicente, Begoña Abad, Marina Casas, Liliana Vera, Marta Rull y Jaime Andrés Pérez. Su colaboración y su amistad han sido indispensables para llevar a cabo varios de los proyectos descritos en esta tesis. En especial, me gustaría destacar la amistad con Marta Rull y Jaime Andrés Pérez, puesto que sin su apoyo, sin sus risas y sin las experiencias que hemos compartido, nada hubiera sido igual. También me gustaría agradecer a Olga Caballero su ayuda, sus contribuciones y su cariño durante todo este tiempo.

Durante las estancias científicas que he realizado, he tenido la oportunidad de conocer a muchas personas, cuya contribución científica y personal ha sido de gran valor. En primer lugar, me gustaría dar un agradecimiento profundo y sincero al Profesor Dr. Theodorian Borca-Tasciuc de la Rensselaer Polytechnic Institute (RPI), por quien siento una gran admiración. Sin su ayuda, varios apartados de esta tesis doctoral no hubieran sido posibles. Su gran capacidad de raciocinio, su inteligencia y su perfeccionismo han constituido una importante enseñanza para mí. En la misma línea, me gustaría destacar a la brillante profesora, la Dra. Diana Borca-Tasciuc de esta misma Universidad, puesto que su ayuda fue crucial en varios trabajos.

Gracias a los intercambios estudiantiles entre el Instituto de Microelectrónica de Madrid (IMM-CSIC) y la Rensselaer Polytechnic Institute (RPI) pude conocer a personas cuyas conversaciones sólo pueden traerme buenos recuerdos: Jon, Adriana, Michelle, Michael y Adam. Durante mi estancia en la Universidad de Bourdeaux, la experiencia y profesionalidad de los excelentes científicos Dr. Stéphane Grauby y el profesor Dr. Stefan Dilhaire han constituido una fuente de aprendizaje para mí, sintiéndome muy agradecido por ello. Por lo que respecta a mi última estancia en el Lawrence Berkeley National Laboratory, agradezco al profesor Dr. Miquel Salmeron sus consejos y su sabiduría, que fueron altamente formativos para mí. Entre sus estudiantes, querría agradecer en especial a Yingjie Zhang por su ayuda y apoyo. Finalmente, me gustaría hacer una mención especial a mi tutor académico, el catedrático Dr. Rodolfo Miranda Soriano, por sus consejos y su ayuda personal durante todo este tiempo.

En el Instituto de Microelectrónica de Madrid (IMM-CSIC) he tenido el placer de conocer a excelentes personas que posibilitan el buen funcionamiento del centro tanto a nivel científico como administrativo. Aprecio enormemente el trabajo del área de administración, llevado a cabo por Margarita, Natividad, Carmen, M^{ra} Carmen, Toña y Mercedes. Si bien, destaco la especial relación que he tenido con Margarita Sousa, de la cual agradezco sus gestiones, su genio y su cariño. Agradezco a Manuel su sonrisa eterna y su calidez, haciendo nuestros días en el IMM más agradables. Para el sector de técnicos, Lorena, Mercedes Antón, Antonio, Mercedes del Rey, Raquel y Carmen, solo puedo dedicarles buenas palabras por su apoyo y ayuda. En especial, quiero agradecer a Raquel Álvaro su enorme dedicación y buen hacer, ya que sin su contribución, más de un proyecto no hubiera sido posible. Quisiera agradecer también a los directores y vicedirectores del IMM su gestión, y al resto de científicos titulares su implicación para que el instituto sea un centro referente de calidad científica. Por último, quisiera acordarme del resto de compañeros por su compañía y por los buenos momentos que hemos pasado juntos. Con José, Andrés, Iván y Guille he disfrutado jugando al *Pádel Mesa*, una invención que algún día patentaremos. Asimismo, me gustaría agradecer también las buenas relaciones con varios estudiantes que he

conocido en congresos o durante el máster, con especial mención a Carla de Tomás, cuyas aportaciones y conversaciones fueron de gran interés.

No puedo olvidarme de todos los amigos que provienen de diferentes lugares: el Instituto Floridablanca, la Universidad Autónoma de Madrid, el Colegio Mayor Chaminade, el club Natación Fuensanta, así como los que he conocido en el extranjero, como Berlín y Londres. Quiero acordarme de ellos, porque son personas que siempre han estado a mi lado, independientemente de la distancia o del tiempo que hemos permanecido separados; cuando nos hemos reencontrado, la amistad permanecía intacta. Entre ellos, me gustaría hacer una mención especial a Pablo, Carlos, Toni y Dani, con quienes he vivido momentos inolvidables y, dentro de este grupo, a Pablo Gambín, mi eterno amigo.

A mi abuela Maruja, por enseñarme, con su ternura, la belleza de lo pequeño; a mi abuelo Pepe, por su rectitud y su formalidad elegantes; a mi abuela Guadalupe, por cuidar de nosotros con generosidad; y a mi abuelo Mateo, por ser una buenísima persona. A mis tíos Pedro y Ángela, mis segundos padres, que me enseñaron que la cultura es infinita y que la vida, aun en las condiciones más adversas, tiene un sentido irrenunciable. A mi hermano Andrés, mi compañero de juegos y de peleas, mi amigo, por su carácter fresco y cercano, y siempre atento a todo lo que ocurre para extraer las mejores conclusiones. A mis Padres, quienes despertaron mi interés por la ciencia cuando me llevaron de niño al laboratorio, y me enseñaron que el mundo se ve mejor cuando se sale del lugar donde nacemos. Mi Padre, por sus ganas insaciables de mejorar, su preocupación por las personas y por una actuación vinculada a una dignidad que le define, y a unos valores humanos a los que no renuncia; mi Madre, por su nobleza, su honestidad y su transparencia, aquellas que un día me ayudaron cuando yo, siendo un niño, más lo necesité. Mi Madre, quien me enseñó que la única verdad es la que sale del corazón. Por último, a mi Silvia, por ser mi compañera de viaje y recorrer juntos el camino de la vida.

Acknowledgements

During the four years that my PhD has lasted, several people have contributed directly or indirectly to enrich it. First and foremost, I would like to thank my thesis director, Dr. Marisol Martín Gonzalez, for all her support during these four years. Her passion, enthusiasm and dedication to science have been, without doubt, inspirational to me. Her ideas, efforts and demands for me to make the most of my abilities have motivated my work enormously, being a perfect example of professional success and an excellent model to follow in my scientific career. For all of these reasons, being her PhD student has been an honour.

I would like to highlight the great contribution, both human and scientific, of the members of the group: Olga Caballero, Pablo Díaz, Jaime Martín, Juan José Romero, Jon Maiz, David Solís, Cristina Vicente, Begoña Abad, Marina Casas, Liliana Vera, Marta Rull and Jaime Andrés Pérez. Their collaboration and friendship have been essential to perform several projects described in this thesis. I would like to make a particular mention of the friendship with Marta Rull and Jaime Andrés Pérez, since without their support, their laughter and the common experiences we have shared, nothing would have been the same. Moreover, I would like to thank Olga Caballero for her help, contributions and affection during all this time.

During my scientific stays overseas, I have had the opportunity to meet many people whose scientific and human contribution has been very valuable to me. First of all, I would like to express my deepest and most sincere appreciation of Professor Dr. Theodorian Borca-Tasciuc from Rensselaer Polytechnic Institute (RPI), for whom I feel great admiration. Without his help, several parts of this doctoral thesis would have been incomplete. His great capacity for reasoning, his intelligence and his perfectionism have constituted a very important lesson for me. Likewise, I would like to thank the brilliant teacher Dr. Diana Borca-Tasciuc from the same university, whose help was crucial in several works. Thanks to the student program exchange between the Instituto de Microelectrónica de Madrid (IMM-CSIC) and the Rensselaer

Polytechnic Institute (RPI), I was able to meet really nice people, Jon, Adriana, Michelle, Michael and Adam, who bring to mind great memories. In my stay at the University of Bourdeaux, the experience and professionalism of the excellent scientists: Dr. Stéphane Grauby and Dr. Stefan Dilhaire constituted a source of knowledge to me, for which I am very grateful. As for my last stay, at Lawrence Berkeley National Laboratory, I would like to express my appreciation to Professor Dr. Miquel Salmeron for his remarkable advice and wisdom, which were highly educational to me. Among his students, I would like to especially thank Yingjie Zhang for his support and help. Finally, I want to make a special mention of my academic tutor, Professor Dr. Rodolfo Miranda, for his advice and support during this time.

At the Instituto de Microelectrónica de Madrid (IMM-CSIC) I have had the pleasure to meet a number of excellent people who make possible the efficient functioning of the centre both at a scientific and at an administrative level. I greatly appreciate the work of the administrative area, carried out by Margarita, Natividad, Carmen, M^{ra} Carmen, Toña and Mercedes. I would especially like to express my appreciation of the special relation that I have had with Margarita Sousa, to whom I am grateful for her management ability, her ingenuity and her affection. I thank Manuel for his eternal smile and his warmth, which made our days at IMM so much more pleasant. As for the technicians sector, Lorena, Mercedes Antón, Antonio, Mercedes del Rey, Raquel and Carmen, I only have words of praise for their support and help. I would particularly like to thank Raquel Alvaro for her complete dedication and know-how, since without her contribution, several projects would never have seen the light of day. I would also like to express my gratitude to the directors and vice-directors of IMM for their good management, and to the other senior scientists for their commitment to making the institute a reference point for high quality science. Last but not least, I would like to mention the rest of my colleagues for their company and all the good times we had together. With José, Andrés, Iván and Guille, I enjoyed playing “Paddle Table Tennis”, an invention which one day we will patent. Likewise, I would also like to express my gratitude for fruitful relationships with several students whom I met at congresses or while I was doing my Master´s

Degree, with a special mention for Carla de Tomás, whose contributions and conversations were of such great interest.

I must not forget all my friends from different places such as the Instituto Floridablanca, la Universidad Autónoma de Madrid, el Colegio Mayor Chaminade, el club Natación Fuensanta, together with those friends I met abroad, in Berlin and London. I wish to mention them because they have always been right by my side, regardless of however far we were away in time and distance, whenever we found ourselves together again the friendship was as strong as ever. Among these companions I would like to make special mention of Pablo, Carlos, Toni, and Dani, with whom I've shared unforgettable moments and, above all Pablo Gambín, my lifelong friend.

To my grandmother Maruja, for tenderly teaching me the beauty of small things; to my grandfather, Pepe, for the elegance of his rectitude and formality; to my grandmother, Guadalupe, for the generous care she took of us; to my grandfather, Mateo, for being such a wonderful person. To my aunt and uncles, Angela and Pedro, my second parents, who taught me that culture is infinite and that life even in the most adverse circumstances, never loses meaning. To my brother Andrés, my playmate and occasional sparring partner, my friend too, for always so close and always full of fresh ideas, always fully aware of what is going on in order to come to the best conclusions. To my parents, who awoke my interest in science since when as a child they took me to the laboratory, they showed me that we get a better view of the world when we venture away from the place where we were born. My father, for his insatiable desire to always improve, his concern for other people and for a way of being in perfect harmony with the dignity that defines him, and the set of values he holds and which he will never renounce; my mother, for her nobility, her honesty and her clarity, the values that helped me as a child when I most needed them. To my mother, who taught me that the only truth is the one that resides in your heart. And last but not least, my beloved Silvia, my travelling companion as we walk together along the path of life.

Contents

Abstract

The aim of this doctoral thesis is the measurement of the transport properties of nano-structures and its correlation with the physical phenomenon that give rise to those results. This thesis can be divided in two fundamental sections: a) Measurements of thermal properties and b) measurements of electrical properties.

Regarding the samples that have been analyzed, a wide variety of materials that correspond to either inorganic samples, like silicon germanium or bismuth telluride, or organic ones, like several types of polymers, are found. However, all of them present a common thread, they are thermoelectric materials. These kinds of materials are able to transform a difference of temperature into electrical energy, and vice-versa, by means of the Seebeck and Peltier effects, respectively. These materials are considered as energy harvesting devices because of their capability to transform waste heat from power plants or car exhaustion, among others, into electricity in a renewable way. In a world with an increasingly demand of energy, thermoelectric devices are very promising. However, as a counterpoint, they present a relatively low efficiency for bulk materials. It has been predicted theoretically and observed experimentally, that these materials enhance its efficiency when they reduce its dimensionality, as for instance thin films (2D structures) or nanowires (1D structures). However, in order to determine the efficiency of these structures, the transport properties must be measured and it becomes extremely difficult as its dimension is reduced. Therefore, thermoelectric materials are excellent candidates to measure transport properties and they have been chosen in this thesis because of their highly interest as energy harvesting devices.

The thesis is divided in five different chapters. In the first chapter, an introduction to thermoelectricity and a review of the characterization of transport properties of films and nanowires is presented. In the second chapter, the experimental methods used to characterize the nano-structures under study are explained. In the third chapter, the thermal transport properties of films and nanowires made

of inorganic or organic materials are studied with scanning probe techniques. Once these properties are obtained, a physical explanation of the phenomenon involved in each case that give rise to that result is presented. In the fourth chapter, the electrical transport properties of films and nanowires are studied by scanning probe microscopy and other techniques, like a four probe station. It is worth mentioning, that in several sections of either the third or fourth chapter the experimental work was combined with simulations to perform the analysis of the transport properties and to elucidate the physical process involved behind. Finally, the fifth chapter summarizes the most important conclusions reached in this doctoral work.

Resumen

El principal objetivo de esta tesis es la medida de transporte de nano-estructuras y su relación con los fenómenos físicos que dan lugar a dichos resultados. Podemos dividir esta tesis en dos apartados fundamentales: a) medidas de propiedades térmicas y b) medidas de propiedades eléctricas.

Respecto a las muestras que han sido analizadas, encontramos una gran variedad de materiales correspondiente tanto a muestras inorgánicas, como el silicio germanio o el teluro de bismuto, como orgánicas, donde se encuentran varios tipos de polímero. Sin embargo, todos ellos presentan un denominador común, tienen propiedades termoeléctricas. Un dispositivo basado en estos materiales es capaz de transformar una diferencia de temperatura en energía eléctrica, o vice-versa, mediante el efecto Seebeck y el efecto Peltier, respectivamente. Estos materiales se consideran como recuperadores de energía debido a su capacidad para transformar perdidas de calor de plantas industriales o del tubo de escape de un coche, entre otros, en electricidad de una forma sostenible. En un mundo cuya demanda de energía aumenta, los dispositivos termoeléctricos son muy prometedores. Sin embargo, como contrapunto, la eficiencia de los materiales en volumen es relativamente baja. Se ha predicho teóricamente y observado experimentalmente, que la eficiencia de dichos materiales aumenta al reducirse su dimensionalidad, como por ejemplo en forma de películas delgadas (estructuras 2D) y nanohilos (estructuras 1D). Para poder determinar la eficiencia de dichas estructuras se requiere medir sus propiedades de transporte, lo que se vuelve extremadamente difícil conforme disminuye la dimensionalidad de la estructura. Por estos motivos, los materiales termoeléctricos son excelentes candidatos para llevar a cabo medidas de transporte y se han seleccionado debido a su alto interés.

Esta tesis está dividida en cinco capítulos. En el primer capítulo, se realiza una introducción a la termoelectricidad y una revisión de las técnicas de caracterización de películas y nanohilos. En el segundo capítulo, se introducen las técnicas experimentales que se han utilizado

para llevar a cabo la caracterización de las nano-estructuras estudiadas. En el tercer capítulo, se estudian las propiedades térmicas de transporte, tanto de películas como de nanohilos, tanto orgánicos como inorgánicos, mediante técnicas de sonda local. Una vez se obtienen dichas propiedades, se aporta una explicación física de los motivos que implican dichos resultados. En el cuarto capítulo, se estudian las propiedades eléctricas, tanto de películas como de nanohilos, por técnicas de sonda local o por otras técnicas, como la estación de cuatro puntas. Es importante mencionar que en varias secciones del capítulo tres como el cuatro, el trabajo experimental llevado a cabo fue combinado con simulaciones para realizar el análisis o para esclarecer los procesos físicos que causan dichos resultados. Posteriormente, se explican desde un punto de vista físico los resultados obtenidos. Finalmente, el quinto capítulo resume las conclusiones más importantes alcanzadas en este trabajo doctoral.

Chapter 1

Introduction

For time immemorial, materials have been a foundation of all civilizations. The understanding of how materials behave and the control and malleability of them have given rise to the birth of different ages from the Stone or Bronze Age to the current age of "Nanotechnology". It was not until 1930s that was possible to give an explanation to the different properties of the materials and why they differ from each other. This was possible thanks to the atomistic understanding of the materials allowed by quantum mechanics. "Material Science" can be defined as an interdisciplinary field that is in charge of studying the structure of materials and relating them with their properties. Centered on this understanding, it is possible to design materials and provide a knowledge base for engineering applications, which is known as "Materials Engineering".

Focusing on the properties of a material, one can define it as the response of the material to the environment. As an example, the mechanical, electrical and magnetic properties are the material response to mechanical, electrical and magnetic forces, respectively. Others, like the thermal or optical properties are the ability of a material to transmit the heat and the capability to absorb, transmit or scatter the light, respectively. The processing of the materials through physical or chemical processes affect the microstructure of the material and therefore their properties. As a consequence, materials with different properties can be fabricated in order to use them in a wide variety of

applications whose latest advances form part of our recent technology that has contributed enormously to enhance our comfort.

Among the different applications that go from basic electronics to even medical applications, thermoelectricity has attracted much attention due to its potential as energy harvesting devices[1]. The world's demand of energy is causing a dramatic escalation of social and political unrest. Likewise the environmental impact of global climate change owing to the combustion of fossil fuels is becoming increasingly alarming. One way to improve the sustainability of our electricity system is through the scavenging of waste heat with thermoelectric generators. Thermoelectric materials are capable to transform heat into electricity, and vice-versa, by means of the Seebeck and Peltier effects, which make them excellent candidates as a renewable energy sources. Home heating, automotive exhaust pipe, and industrial processes all generate an enormous amount of unused waste heat that could be converted to electricity by using thermoelectrics. As an example, about 90% of the world's power (approximately 10 TW) is generated by heat engines that convert heat to mechanical motion, which can then be converted to electricity when necessary. Energy harvesting (or energy scavenging) thermoelectric devices could potentially convert part of this low-grade heat to electricity without any pollution using semiconductors, so increasing the total energy efficiency of those heat engines. Those thermoelectric devices are solid-state, so they have no moving parts and are therefore silent, reliable, lightweight and durable. Moreover, they are also scalable and hence ideal for miniature to power and cooling laptops, among others. However, the major drawback of these kind of material is their low efficiency. The efficiency of a thermoelectric material depends on its figure-of-merit (zT)[1] of their components, which is defined as $zT = \frac{S^2\sigma}{k}T$ where S, σ, κ, and T are the Seebeck coefficient, electrical conductivity, thermal conductivity and absolute temperature, respectively. A good thermoelectric material should have high electrical conductivity, low thermal conductivity, and a high Seebeck coefficient for maximum conversion of heat to electrical power or electrical power to cooling. Hence, to make the figure-of-merit larger, a high S and σ, but low κ are required. Semiconductors, such as bismuth telluride, are the best candidates for these applications at temperatures around the enviroment, especially on account of the balance required between electrical and thermal conductivity. In section 1.1.6. the different strategies that can be used to increase the efficiency of

thermoelectric materials will be explored. These are nowadays mainly focused on the reduction of the dimensionality of the material (nanostructuration). Thin films or nanowires are examples of nanostructures that are predicted theoretically and confirmed experimentally to improve the thermoelectric performance of the materials.

It can be concluded that it is mandatory to measure experimentally the physical transport properties, i.e. S, σ and κ, of thermoelectric materials to evaluate its efficiency at the nanoscale. One must take into account that as the dimension of the material is reduced, the measurement of their properties becomes more complex.

In this chapter, it is firstly given a brief introduction about thermoelectricity and its constitutive equations, the most used materials in this field and their applications. Finally, an up to date review of the most usual techniques to measure the electrical and thermal conductivity and the Seebeck coefficient of nanostructures, like thin films and nanowires, are described and discussed.

1.1. Thermoelectricity.

Thermoelectricity is defined as the ability of a material to transform heat into electrical energy, and *vice-versa*. In this section, the constitutive equations that govern thermoelectric effects, which explain how a thermoelectric material generates a current flow from a temperature difference, are presented. Then, a brief description of some of the best thermoelectric materials and their properties is given.

1.1.1. Elastic resistor. Current driven by an electrical potential.

The macroscopic equation used for a conductor, obtained from Maxwell equations, is [2],

$$\varepsilon = \rho J \tag{1.1}$$

where ε is the electrical field in the conductor, J current density and ρ is the resistivity of the material. The resistivity is an intrinsic property that quantifies how strongly a given material opposes the flow of an electrical current. The inverse of the resistivity is the electrical conductivity. The standard expression for the resistivity comes from the Boltzmann equation[3] and it is described mathematically by

$$\frac{1}{\rho} = \sigma = q^2 \int dE \left(-\frac{\partial f_0}{\partial E}\right) \Sigma(E) \qquad (1.2)$$

where q is the charge, σ electrical conductivity, E is energy and f is the Fermi function of the material, which is explained in detail later.

However, when it refers to thermoelectric materials, Equation 1.1 is expanded to

$$\varepsilon = \rho J + S\frac{dT}{dx} \qquad (1.3)$$

where S is called the Seebeck coefficient and $\frac{dT}{dx}$ is the gradient of temperature generated across the material [3].

In order to understand where this term comes from and its meaning, an analysis of what happens in a thermoelectric material from the point of view of the electronic band structure is going to be shown. For that purpose, it is considered a material with a simple band structure, with just one level with energy E, and contacts at their sides. Solid state physics shows that at the equilibrium the system has a common electrochemical potential or Fermi level, μ, whose states below are full. Figure 1.1 shows the density of states, D(E) or DOS, of a material with empty states above the Fermi level and occupied states below it.

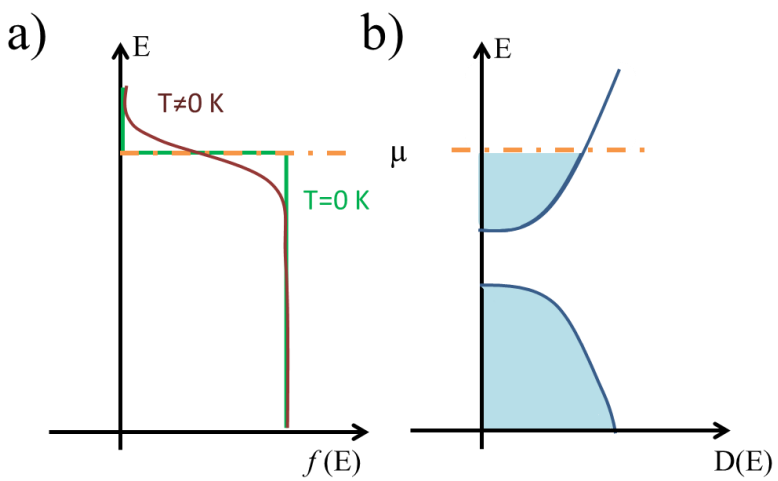

Figure 1.1. a) Fermi functions of the density of states at zero and non-zero Kelvin degrees. b) Density of states (DOS) for a simple conductor.

The Fermi function is usually defined as the probability that a given available electron energy state will be occupied at a given temperature. The transition of the Fermi function happens abruptly when the material is at zero degrees Kelvin, but it becomes smoother when it is at higher temperature [4].

The way the current flows across the material can be understood using a simple solid state scheme with just one energy *E* level. Figure 1.2 shows this representation out of equilibrium when an electric field is applied to the material. The Fermi level of the positive contact of the sample goes down while the negative one goes up. Electrons from the filled band of the material put out electrons into the lower electrochemical potential, as it is at lower energy, leaving an empty place behind that is replaced by electrons from the other contact. As a consequence, there is a continuous flow of electrons that causes the current [5]. However, filled bands do not conduct because the levels under the gap are far below of the Fermi level of the contacts, μ_1 and μ_2, so they just stay full.

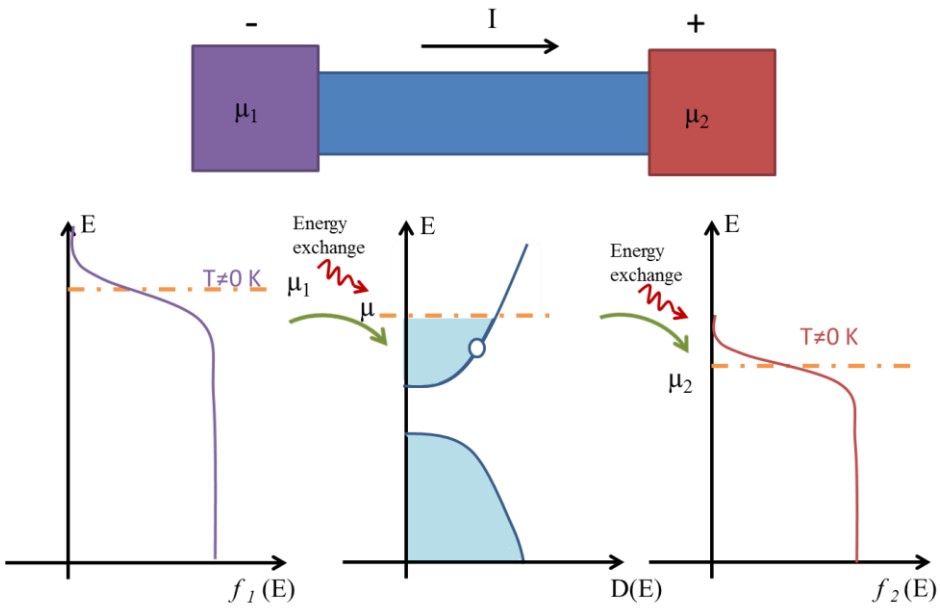

Figure 1.2. Band diagram out of the equilibrium of a conductor with contacts at the ends.

In macroscopic devices, this flow of electrons produces a dissipation of energy, called Joule heat, which is mathematically

described as, $P=I^2 \cdot R$, where P is the dissipated power, I is the electrical current and R the resistance of the material. Nevertheless, in small conductors, the heating effect can be localized specifically at the contacts. If one considers that electrons go from one contact to the other without practically exchanging energy, i.e. elastically, all the energy dissipates at the contacts as the electrons lose energy due to their transition to lower energy levels. The presence of large contacts assures a big dissipation of heat at the contacts avoiding nanostructures, like nanotubes or nanowires, to burn out.

Mathematically the current equation for the simplest case, i.e. an elastic resistor[5], can be expressed as,

$$I = \int dE \cdot m \cdot (f_1 - f_2) \tag{1.4}$$

where f_1 and f_2 are the Fermi functions at the two ends of the material, E is the energy and m is a constant. In order to get the expression for conductance at low voltages, one can use the approximation $(f_1 - f_2) \approx -\frac{\partial f_0}{\partial E} \cdot (\mu_1 - \mu_2) = -\frac{\partial f_0}{\partial E} \cdot qV$, where $\frac{\partial f_0}{\partial E}$ is the derivative of the Fermi function, q is the electron charge and V is the voltage applied. Therefore, the conductance can be expressed as,

$$G = \frac{I}{V} = \int dE \cdot m \cdot \left(-\frac{\partial f_0}{\partial E}\right) q \tag{1.5}$$

The constant m indicates how easily the electrons can flow at a given energy. In a simplified way, one can consider m as the time that an electron takes to flow across the material which also depends on the energy levels or density of states at the energy range between the Fermi levels of the material and contacts, i.e. $\frac{q}{t} D(E) \cdot dE$. However, one must take into account that when current flows half of the electrons are going in one direction, but holes are going in the other direction, as a consequence one must consider half of the density of states. Moreover, time can be described with a classic expression, in the ballistic conductance [5], as the length of the material, L, divided by the velocity of the electrons, v. Then, the constant m can be written as, $= \frac{q}{L} \frac{vD(E)}{2} \cdot dE$. As a consequence, one can obtain a semi-classical expression for the conductance of the material,

$$G = \int dE \cdot \frac{q^2 D(E) v}{2L} \cdot \left(-\frac{\partial f_0}{\partial E}\right) \tag{1.6}$$

In a quantum model, the term $\frac{D(E)v}{2L}$ must be substituted by $\frac{M(E)}{h}$ where h is the Planck constant while $M(E)$ is the number of modes, which is one in one-dimensional conductor, but in a three-dimensional conductor it is equal to the number of wave-lengths that fit into the cross section . As a result, the next expression is obtained [5],

$$G = \int dE \cdot \frac{q^2 M(E)}{h} \cdot \left(-\frac{\partial f_0}{\partial E}\right) \tag{1.7}$$

Equation 1.7 shows the equation for a ballistic conductance. However, if the conductance is diffusive with the exchange of momentum, but in an elastic regime, i.e. without losing energy, the Equation 1.7 should be modified to be [5]

$$G = \int dE \cdot \frac{q^2 M(E)}{h} \cdot \left(-\frac{\partial f_0}{\partial E}\right) \cdot \frac{m_{fp}}{L+m_{fp}} \tag{1.8}$$

where m_{fp} is the mean free path that indicates how long can go an electron before being scattered. If the material is very small, then $\frac{m_{fp}}{L+m_{fp}} \sim \frac{m_{fp}}{m_{fp}} = 1$ and Equation 1.8 approaches to the semi-classical one (Equation 1.7). On the contrary, if the conductor is long, the term $\frac{m_{fp}}{L+m_{fp}} \sim \frac{m_{fp}}{L}$ and Equation 1.8 approaches to Ohm's law, $G = \frac{\sigma A}{L}$, where A is the area and L is the length of the conductor.

So far, with this approach one is able to get Equation 1.8, which is similar to the standard expression obtained from the Boltzmann Equation with less mathematical effort, as it has been considered elastic effect and the decoupling of the mechanical part from the heat dissipation part. In the following section, we are going to study a current driven by a temperature difference.

1.1.2. Elastic resistor. Current driven by a temperature difference.

The Fermi function is described by the equation,

$$f(E) = \frac{1}{e^{(E-\mu)/KT}+1} \tag{1.9}$$

where K is the Boltzman constant, *E* is the energy, μ is the electrochemical potential and *T* the temperature. Therefore, if substitute it in Equation 1.4 a difference between the Fermi functions of the electrodes can happen owing to a difference of temperature. Figure 1.3 shows schematically this effect when contacts are connected as a closed circuit, which makes them to stay at the same electrochemical potential, and one contact is at 0 K while the other is at a temperature difference.

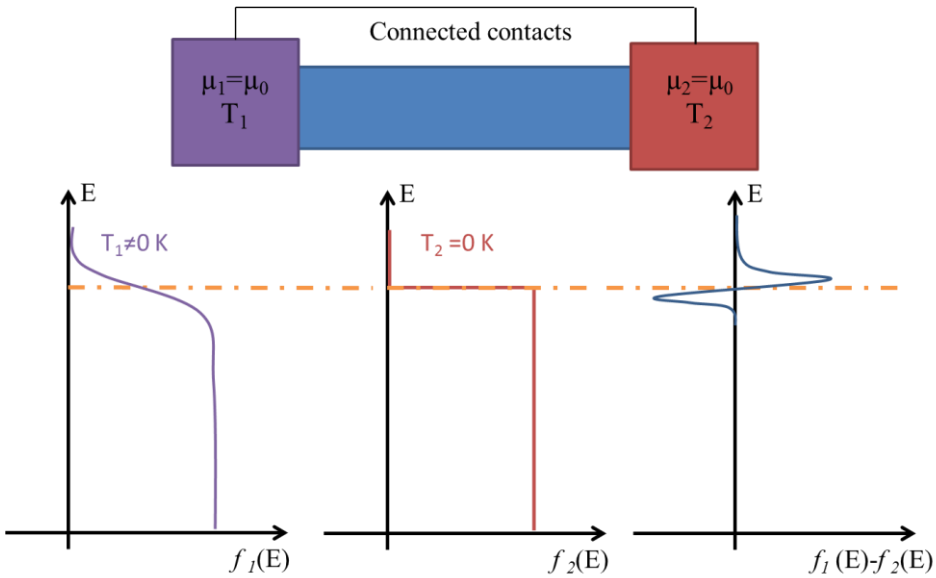

Figure 1.3. Fermi functions and its difference when contacts at different temperatures and electrically connected are presented.

For energy above electrochemical potential, electrons will flow from contact one to two, while for energies below electrochemical potential will be the other way around[5]. If both ways conduct equally well, it would involve no net current, but the truth is that the density of states is not the same above and below the Fermi level. As a consequence, one has a net flow, which can be observed in Figure 1.4. For a density of states that increase above the Fermi level the conductance goes from hot to cold side, Figure 1.4a, while if it is the other way around the conductance goes from cold to hot side, Figure 1.4b. This is usually named as n-type and p-type conductors, respectively [5]. The current generated by this effect is called thermoelectric current.

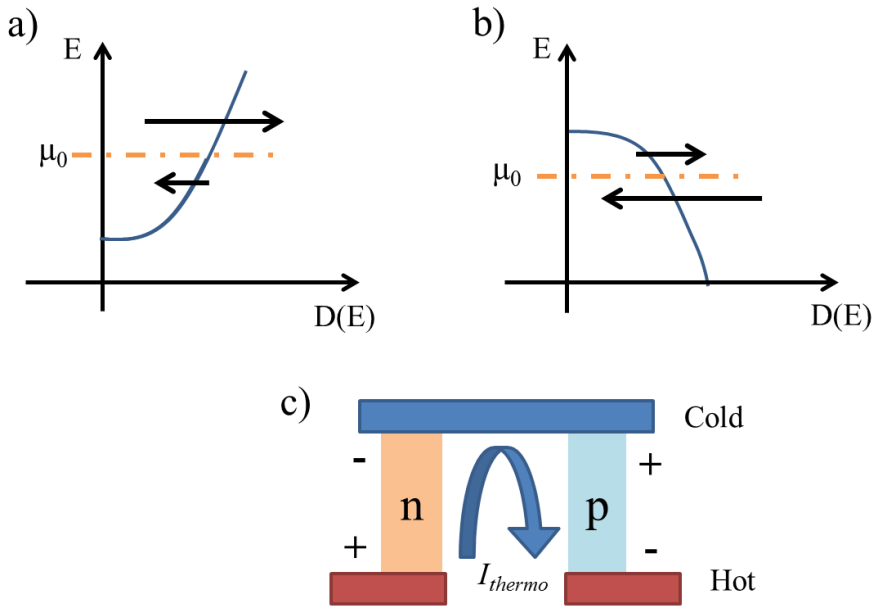

Figure 1.4. Net current obtained from a) an increase of DOS above, n-type material, and b) below the Fermi level, p-type material, which gives an opposite current direction. c) Thermoelectric generator used to generate a thermo-current.

If the circuit is opened, i.e. no current flows, and a difference of temperature is applied, the n-type material will pile up electrons in cold side charging it negatively while the hot side will be charged positively. The p-type material will act in an opposite way, charging positively the cold side and negatively the hot side. The material acts as a battery generating a voltage difference from a temperature difference[1 6]. Thermoelectric generators are based on this principle, which allows the extraction of current from a difference of temperature by combining n- and p-type materials, as can be seen in Figure 1.4c. In both power generation and cooling, a thermoelectric module is an array of many couples, n- and p-type pellets, connected electrically in series, but thermally in parallel. Whilst one couple, n- and p-type pellets junction, only gives few millivolts for a particular temperature difference, connecting several of them in series brings the voltage closer to that found in typical DC power sources for the same difference of temperature applied.

1.1.3. Seebeck coefficient.

As it was observed in Equation 1.9, the Fermi function not only depends on the electrochemical potential and energy but also on the temperature, (E, μ, T) . Therefore, the current equation can be re-written as [5],

$$I = \frac{1}{q}\int dE\, G(E)(f_1(E,\mu_1,T_1) - f_2(E,\mu_2,T_2)) \qquad (1.10)$$

where $f_1(E,\mu_1,T_1) - f_2(E,\mu_2,T_2)$ can be approximated to $\frac{\partial f}{\partial \mu}(\mu_1 - \mu_2) + \frac{\partial f}{\partial T}(T_1 - T_2)$, which as a result gives an expression for current equals to,

$$I \cong G\left(\frac{\mu_1-\mu_2}{q}\right) + G_s(T_1 - T_2) \qquad (1.11)$$

where $G = \int dE\, G(E)\left(-\frac{\partial f}{\partial E}\right)$ and $G_s = \int dE\, G(E)\left(-\frac{\partial f}{\partial E}\right)\frac{E-\mu}{qT}$.

As a consequence, an extra term, G_s, for the current appears in Equation 1.11 that can change the sign depending on the energy. If the energy is above the electrochemical potential, the term $\frac{E-\mu}{qT}$ will be positive while it will be negative if the contrary.

Equation 1.11 can be re-written as,

$$I \cong G\Delta V + G_s\Delta T \qquad (1.12)$$

where ΔV and ΔT are the voltage and temperature difference, respectively [5]. In an open circuit, the voltage generated from a difference of temperature is called the Seebeck coefficient [1], *S*, and mathematically can be expressed using Equation 1.12 under the assumption of having an open circuit ($I=0A$), that is

$$S = -\frac{G_s}{G} = \frac{\Delta V}{\Delta T} \qquad (1.13)$$

1.1.4. Thermoelectric refrigeration. Electronic Heat current. Peltier coefficient.

As it was mentioned above, the transition of electrons to the energy levels of the contacts involve an exchange of energy. This involves a loss of energy that is usually dissipated as heat [5] (Figure 1.2).

Let's consider now the situation at which the energy level of a n-type conductor, at room temperature and under an electrical field applied, is higher than the electrochemical potentials of the contacts, μ_1 and μ_2, as shown schematically in Figure 1.5. The electrons go down to the electrochemical potential of contact 2 which will involve heat dissipation. However, in order the current flow from contact 1 to contact 2, the electrons from contact 1 must gain energy and they do it from the heat absorption from the surroundings. Therefore, one side is cool down while the other is heated up [5]. This effect is known as Peltier effect [1].

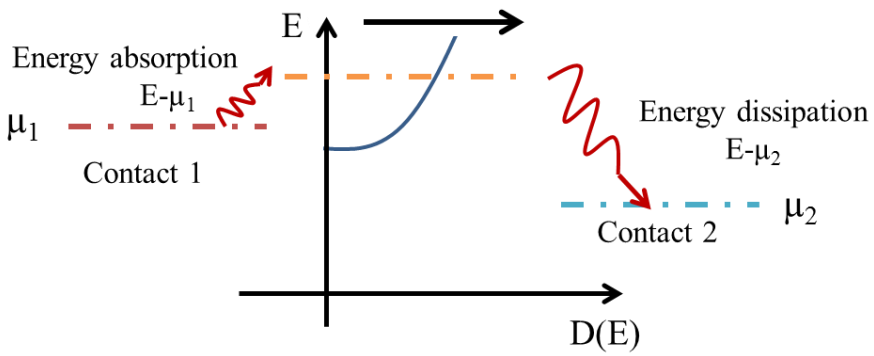

Figure 1.5. Heat current for an energy level higher than the electrochemical potentials of both contacts.

The Seebeck and Peltier effects are related and can be obtained using the expression above and considering new ones. For that purpose, similar to the electrical current obtained in Equation 1.11, an equation for the heat current can be obtained,

$$I_Q = \frac{1}{q}\int dE\,\frac{E-\mu}{q}\,G(E)(f_1 - f_2) \cong G_p\left(\frac{\mu_1-\mu_2}{q}\right) + G_Q(T_1 - T_2) \quad (1.14)$$

where $G_p = \int dE\, G(E) \left(-\frac{\partial f}{\partial E}\right) \frac{E-\mu}{q}$ and $G_Q = \int dE\, G(E) \left(-\frac{\partial f}{\partial E}\right) \left(\frac{E-\mu}{q}\right)^2 \frac{1}{T}$. This equation basically represents the total amount of heat that is carried out by electrons.

Equation 1.11 and Equation 1.14 give us a set of conductance coefficients[5] that are summarized in Table 1.I and that corresponds to electrical and heat currents.

Table 1.I. Summary of conductance coefficients.

Conductance Coefficient	Common term	Multiplying factor
G	$\frac{1}{q}\int dE\, G(E)\left(-\frac{\partial f}{\partial E}\right) *$	1
G_s		$\frac{E-\mu}{qT}$
G_p		$\frac{E-\mu}{q}$
G_Q		$\left(\frac{E-\mu}{q}\right)^2$

In order to obtain the electrical current in terms of the voltage difference, Equation 1.11 can be re-writen into $\Delta V \cong \frac{1}{G} I - \frac{G_S}{G} \Delta T = \left(\frac{\mu_1 - \mu_2}{q}\right)$. Then, using this term, the heat current (Equation 1.14) can be expressed as,

$$I_Q = \frac{G_p}{G} I + \left(G_Q - \frac{G_p G_s}{G}\right) \Delta T \qquad (1.15)$$

The Peltier coefficient is defined as $\Pi = \frac{G_p}{G}$, which indicates how much heat current is carried for a certain amount of electrical current under no temperature difference. The Seebeck and Peltier coefficients are related through the equation ,

$$\Pi = S \cdot T \qquad (1.16)$$

1.1.5. Landauer-Boltzmann approach. Thermoelectric transport parameters.

So far, these equations have been extracted considering only electronic terms and using a simplified model based on elastic resistor. With this approach is possible to find the Seebeck and Peltier coefficients and its relation. However, one important term missing here is the influence of the lattice thermal conductivity and for that purpose the Landauer-Boltzmann approach must be consider [7].

Using this formalism, one arrives to the next set of equations:

$$\varepsilon_x = \rho J_x + S\frac{dT}{dx} \tag{1.17}$$

Electrical current

$$J_{Qx} = \Pi J_x - k_e\frac{dT}{dx} \tag{1.18}$$

Heat current (electronic)

$$q_x = -k_L\left(\frac{dT}{dx}\right) \tag{1.19}$$

Heat current (lattice)

$$J_{Qx} = \Pi J_x - (k_e + k_L)\frac{dT}{dx} \tag{1.20}$$

Complete heat equation

whose terms are described by,

$$\sigma' = \frac{2q^2}{h}\cdot m_{fp\ electrons}(E)\cdot\left(\frac{M_{electrons}(E)}{A}\right)\cdot\left(-\frac{\partial f_0}{\partial E}\right) \tag{1.21}$$

Differential electrical conductivity

$$\sigma = \frac{1}{\rho} = \int_{-\infty}^{\infty} dE\cdot\sigma'(E) \tag{1.22}$$

Electrical conductivity

$$S = -\frac{1}{q}\frac{\int_{-\infty}^{\infty} dE\cdot(E-\mu)\cdot\sigma'(E)}{\int_{-\infty}^{\infty} dE\cdot\sigma'(E)} \tag{1.23}$$

Seebeck coefficient

$$\Pi = S\cdot T$$

Peltier coefficient

$$k_e = k_0 - T\sigma S^2\ ;\ \ k_0 = \frac{1}{q^2T}\int_{-\infty}^{\infty} dE\cdot(E-\mu)^2\cdot\sigma'(E) \tag{1.24}$$

Thermal conductivity (electrical)

$$k_L = \frac{\pi^2 {k_B}^2 T}{3h} \int_{-\infty}^{\infty} d(\hbar\omega) \cdot m_{fp\ phonons}(\hbar\omega) \cdot \frac{M_{phonons}(\hbar\omega)}{A} \cdot W_{phonons}(\hbar\omega) \quad (1.25)$$

$$W_{phonons}(\hbar\omega) = \left\{ \frac{3}{\pi^2} \cdot \left(\frac{\hbar\omega}{k_B T} \right)^2 \left(-\frac{\partial n_0}{\partial(\hbar\omega)} \right) \right\}$$

Thermal conductivity (lattice)

The equations for the lattice thermal conductivity are obtained using the Landauer-Boltzman approximation, but under certain considerations [7]. The heat flow in lattice thermal conductivity is now expressed in terms of $\hbar\omega$ and instead of the Fermi direct factor it has Bose-Einstein occupation factors, as it has phonons instead of electrons [7]. Both electrons and lattice vibration carry heat and this last term and the heat equation must consider both terms. In metals, heat conduction by electrons dominates, $k_e >> k_L$, while in semiconductors lattice vibrations dominate, $k_L >> k_e$. [7]

To conclude, it is important mentioning that the mean free path of the phonons is influenced by point defects and impurities, boundaries and surfaces and the phonon-phonon scattering, while electrons also scatter from defects, phonons, surface and boundaries and other electrons [1, 7]. Therefore, under this consideration the transport properties of the material can be modified by engineering adequately the material.

1.1.6. Thermoelectric efficiency.

The efficiency of a thermoelectric material [1] is proportional to its Figure of Merit, *zT*. This parameter is defined in terms of the Seebeck coefficient, *S*, and the electrical, σ, and thermal, *k*, conductivities,

$$zT = \frac{S^2 \sigma}{k_e + k_L} \cdot T \quad (1.26)$$

In a thermoelectric material, the power that one can extract depends on the term $S^2\sigma$, which is usually defined as the power factor (PF). Moreover, in terms of efficiency, the capacity of the material to keep the temperature difference depends on the thermal conductivity, $k = k_e + k_L$. A good thermoelectric has a high power factor and low thermal conductivity, which in the best scenario is defined as "phonon-glass electron-crystal" material [1, 8, 9]. As a consequence, semiconductors look

the more convenient materials to achieve this goal[10], as it can be seen in Figure 1.6. Figure of merits with values around 1 are considered to be good performance thermoelectrics and make them available for different applications such as coolers or power generators (TEG) [1,11]. However, if this value could be increased by a factor of 3 it would develop a wider range of applications, but unfortunatelly, to date, for bulk thermoelectric materials the maximum *zT* achieved is around 2 [12]. Therefore, there is a need of keep working to enhance the thermoelectric figure of merit.

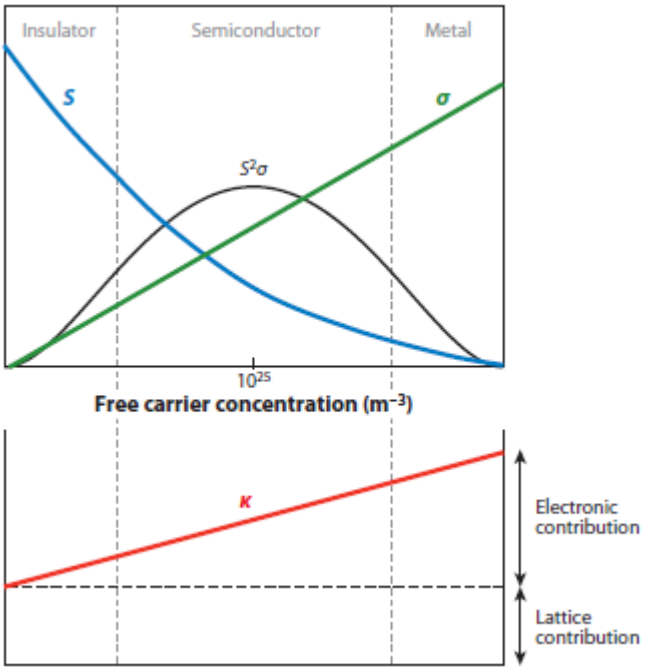

Figure 1.6. Seebeck coefficient (*S*), electrical conductivity (σ) and thermal conductivity (*k*) versus the number of free carriers from insulators to metals. Figure taken from reference[10].

There are two possible strategies [1, 9] to increase the efficiency of thermoelectric materials: a) increasing the power factor, $S^2\sigma$, or b) decreasing the thermal conductivity of the material, k.

If one considers the first approach, in order to have a large electrical conductivity in, e.g., a n-type semiconductor, one is interested in having a large mean free path and the Fermi level close to the conduction band ($E>>\mu$). On the contrary, the Seebeck coefficient is proportional to the factor $(E-\mu)$, Equation 1.23, and in order to increase

it one needs the Fermi level to be closed to valence band ($\mu << E$). Figure 1.7a shows the n-type and p-type Seebeck coefficient versus the electrical conductivity based on Equation 1.23. Figure 1.7b shows the electrical conductivity and Seebeck coefficient of a n-type material versus the Fermi level, where observe that the maximum power factor is achieved when μ is near the band edge. Therefore, the main strategy usually consists of doping the material in order to have the Fermi level close to the band edge [5].

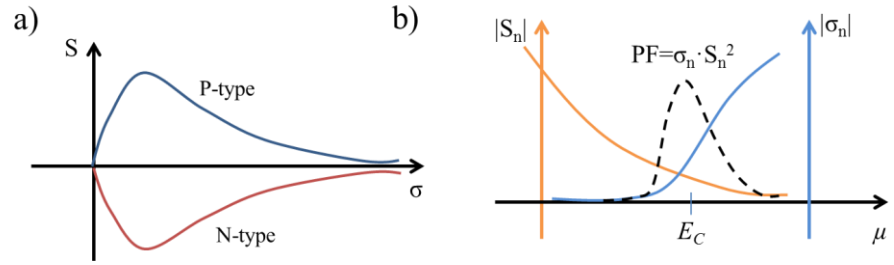

Figure 1.7. a) Seebeck coefficient versus the electrical conductivity for a n-type and p-type material. b) The dependence of the Seebeck coefficient, electrical conductivity and power factor of a n-type material with the location of the Fermi energy.

Nevertheless, recent progress in the enhancement of the figure of merit has focused on nano-engineering materials in order to reduce the lattice thermal conductivity [1, 13]. The goal consists of reducing the mean free path of phonons without affecting too much the mean free path of electrons. For that purpose, many different approaches can be carried out, but the most important ones are: a) the nano-structuration of the material through the incursion of scattering centers, the increase of boundaries, the generation of defects or superlattice materials, among others[13], and the reduction of the dimensionality of the material [13], which results in thin films (2D-structures), nanowires (1D-structures) or quantum dots (0D-structures).

1.1.7. Thermoelectric materials.

There are a wide variety of materials that have been used successfully in thermoelectric applications. Some of the most traditional ones are Bi_2Te_3, PbTe, $CoSb_3$ or SiGe, among others [14]. Each one of them present an optimum range of temperature in which they are more efficient, as can be seen in Figure 1.8 for both p and n type.

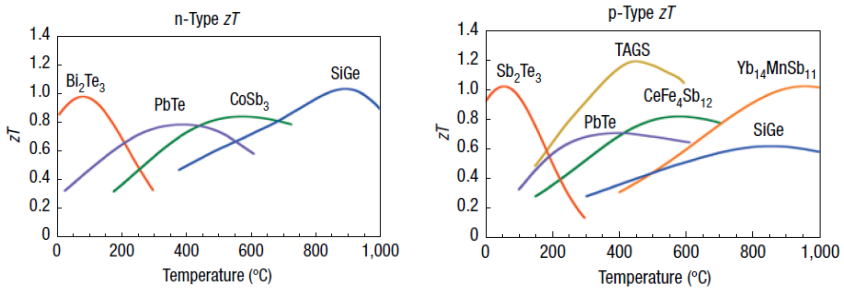

Figure 1.8. Some of the most known n- and p-type thermoelectric materials and the optimum working temperature at which they present maximum *zT*. Figure taken from reference [14].

This work mainly focus on those materials whose *zT* is maximum close to room temperature (300K). As an example, despite the fact that the properties of Bi_2Te_3 were discovered a long time ago, it is still the material used in commertial devices [1]. In order to increase the figure of merit of this material based on the nano-structuration described above, thin films and nanowires have been grown through different methods in order to obtain better physical properties in comparison to the bulk. Moreover, new materials that are attracting attention from the thermoelectric point of view, which combine the strategies described above to enhance the figure of merit, are Skutterudites, Oxides or Half-Heusler materials, among others [15, 16]. On the organic side, polymers are especially interesting as they present low thermal conductivity and they are expected to increase the power factor when doping, without affecting much the thermal conductivity [17]. As in the case of inorganic materials, their dimensionality has been also reduced in order to modify their physical properties [18].

Despite the fact that nano-structures, such as thin films or nanowires, can be grown through a wide variety of techniques, the measurement of their properties is still a challenge especially as its dimension reduces. The smaller the structure is, the more local techniques to measure their intrinsic electrical and thermal properties individually are required, and these parameters are essential to determine accurately its figure of merit.

1.2. Measuring techniques for determining physical properties at the nano-scale.

In this section, it is differenciated between measurements of physical properties of 2D-structures, thin films, and 1D-structures, nanowires. Accurate measurements of the electrical and thermal conductivity, as well as the Seebeck coefficient, are crucial to determine the figure of merit (zT) of thermoelectric materials.

1.2.1. Transport property measurements of thin films.

Thin films are 2D- structures that can be grown through many different techniques, such as electrodeposition[19] or sputtering[20], among others. Depending on the material, the electrical and thermal properties can be different depending if one is measuring in-plane or cross plane direction. These materials are defined as anisotropic. A classic example in thermoelectricity of anisotropic material is the Bi_2Te_3 [21]. On the other hand, if those properties are kept in both directions, the material is considered to be isotropic, like SiGe [22].

This section, summarizes some of the most used techniques to measure the electrical and thermal conductivities and the Seebeck coefficient of films either in-plane or cross-plane directions.

1.2.1.1. In-plane measurements.

This section summarizes the most used techniques to measure transport properties of the films in their in-plane direction.

1.2.1.1.1. Electrical conductivity measurements.

Measurements of the electrical conductivity along a thin film, or in its in-plane direction, become more complex than for bulk materials. Most of these complications arise on the substrate over which the films are grown, as they are usually conductors or semiconductors. The use of an isolating substrate or its removal is required when carried out these type of measurements. This detaching procedure might concern certain complexity, depending on the cases. After this step is done, two- or four-probes [23, 24] or Van der Pauw[25] techniques are the most used ones. In the two-probe technique [26], one contacts two probes at the sides of the surface of the sample and while passing a current between

them the voltage is measured. However, in this method the influence of the contacts and parasitic resistances must be considered, which becomes increasingly important as the electrical conductivity of the film increases. To remove this influence, the four probe method can be used (Figure 1.9a). In this method, while two probes are employed for passing current across the sample, the other two measure its voltage drop. For films with large areas and not extremely thin, or for bulk samples, the four probes are spaced equally and the separation distance must be much smaller than the sample size, otherwise correction factors must be included in the data reduction. The Van der Pauw method[25] is another technique commonly used (Figure 1.9b). It uses four probes that are placed at the edges of an arbitrary shape film or bulk sample for in plane measurements of the sheet resistance. The current is first passed across probes 1-2 while the probes 3-4 measure the voltage, then the current is passed across probes 1-4 and the voltage is measured across probes 3-2 (Figure 1.9b). The electrical conductivity is then determined from the sheet resistance, knowing the sample thickness.

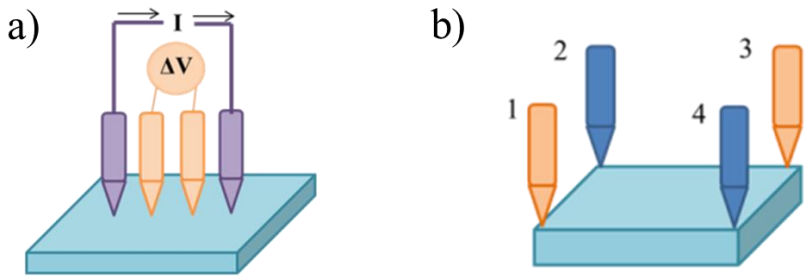

Figure 1.9. a) Four probe point technique and b) Van der Pauw method to measure the electrical conductivity of the films in its in plane direction.

1.2.1.1.2. Thermal conductivity measurements.

One of the major difficulties when measuring the in-plane thermal conductivity is the proper estimation of the heat transfer rate along the thin film. To address this issue, several strategies have been developed, such as depositing films on thin substrates with low thermal conductivity, making freestanding films by removing the substrate, using micro-heaters and temperature sensors and/or special sample configurations to sense the lateral heat spreading in the film[27]. Some of the most used techniques are based on the first two strategies by making suspended structures, which are the membrane and bridge techniques [27].

The membrane method[27] (Figure 1.10a) consists of a freestanding or thin film on a thin substrate structure suspended between two massive heat sinks. In this situation, a heater is placed in the middle of the membrane and the heat spreads to the heat sinks while its temperature profile is detected by one or more thermometers situated at different locations of the membrane. In the steady state method [27], the in-plane thermal conductivity of the film, under the assumption of 1D model, can be determined as

$$k = \frac{pL}{wt(T_h - T_s)} \tag{1.27}$$

where p/w is power dissipated in the heater per unit length, L is the distance from the heater to the heat sink, T_h is the heater temperature rise and T_s is the temperature of the sink. It is also possible to measure the thermal conductivity of the film using transient heating methods [27], which employs a heat pulse induced by passing an electric current pulse through the heating strip. The method measures the transient temperature profile of the sensor position during and after the heat pulse. If the specific heat and density of the sample are known, the thermal diffusivity or the thermal conductivity can be determined by fitting the experimental temperature profile with the corresponding equation.

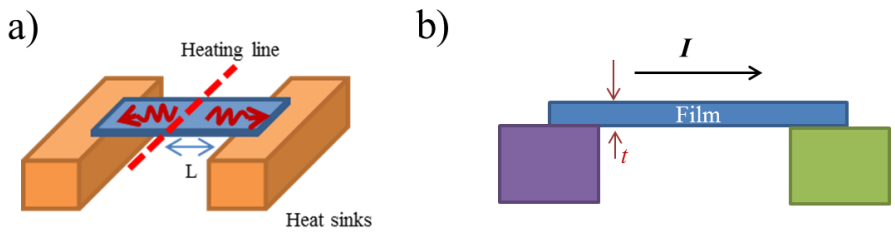

Figure 1.10. a) Membrane and b) bridge methods to determine the thermal conductivity of the films in their in plane direction.

The bridge method[27] (Figure 1.10b) is another way of measuring the in-plane thermal conductivity of thin films. In this case, the film bridges two heat sinks and a current is applied across it. The film then is heated as the current passes through it, acting as a heater and temperature sensor itself. The temperature rise of the heater is determined by measuring the change in its electrical resistance. The temperature response of the standing film under steady-state, pulsed

and modulation heating, coupled with appropriate heat transport modeling, can be used to determine the thermal conductivity, thermal diffusivity and heat capacity of the film[28]. Either in the membrane or bridge method, the experiment is usually carried out in vacuum to minimize the effect of heat convection.

1.2.1.1.3. Seebeck coefficient measurements.

The in-plane Seebeck coefficient is defined as the voltage (ΔV) generated by the thin film when it is subjected to a gradient of temperature (ΔT) along its plane, $S = -\frac{\Delta V}{\Delta T}$. This property is independent of the size or geometry of the film. When the Seebeck is negative the material is n-type, while it is positive when it is p-type. The traditional way of measuring consists of having a suspended film and positioning it between two heaters (Figure 1.11). Then, two electrical probes are placed on top of the film to measure the voltage generated by the film when it is subjected to a temperature difference, while two thermocouples are in charge of measuring the temperature difference across the film. Using this experimental set up, there are two possible ways [29] of measuring either the integral method [30] or the differential method [31, 32]. In the integral method, one end of the samples is kept at the same temperature while the other is varied continuously. The voltage and temperature difference is recorded and at each point one obtains the derivative of the voltage-temperature curve, $S = -\frac{dV}{dT}$. However, the trend might not be linear and the consideration of no delay between the voltage and temperature measurements could not be very accurate. On the other hand, the differential method consists of applying small gradients along the thin film, at the surrounding temperature of interest, while recording lots of data points in this interval. The linear trend of the voltage-temperature curve and its standard deviation give us the Seebeck coefficient and its corresponding experimental error, respectively. In both methods, it is very important to take them under steady-state conditions and heat flow are one-dimensional considering the finite sizes of the thermocouple junctions and probe tips. Thin thermocouples will help to minimize the heat loss from the sample surface through the thermocouple leads. Moreover, it is important to take into account that the two-probe voltage measured will include parasitic Seebeck voltages from the probes which should be considered in the data reduction or just

consider probes with low Seebeck coefficients, which in any case will require of a careful calibration.

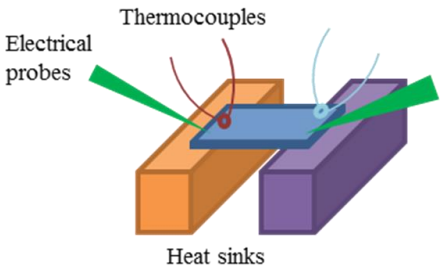

Figure 1.11. Free standing film measurements for the determination of the Seebeck coefficient in plane.

It is worth mentioning that under the right experimental set up [29], it is possible to carry simultaneous measurements of the Seebeck coefficient and the electrical conductivity with four probes based on the techniques described above.

1.2.1.2. Cross-plane measurements.

This section summarizes the most used techniques to measure transport properties of the films in their cross-plane direction.

1.2.1.2.1. Electrical conductivity measurements.

Cross-plane measurements are usually more complicated than in-plane as the films are usually very thin. Typical techniques to measure the electrical conductivity like four probe or Van der Pauw are difficult to use in these structures. However, lithographic methods make possible to fabricate thin metal probe lines that are in charge of injecting current and sensing voltage to determine electrical conductivity of the film using four probes technique [29]. This method usually employs a mesa structure for the film and the fabrication of contacts via lithography process (Figure 1.12a). However, in this technique, there might be a non-uniform spreading of the current across the film and within electrodes, and the influence of the contact resistances between the interfaces requires a careful analysis of the electric transport in the sample. Other methods used to determine the electrical conductivity of thin films out of plane is the modified transmission line model [33, 34] (TLM), which originally was conceived to measure contact resistances [35]. This technique requires electrodes on

top of structures etched in the film, which are separated by different distances (Figure 1.12b). The resistance measured between structures increases linearly with spacing while the vertical non-etched structures' resistance remains unchanged. This makes possible the determination of the out of plane electrical conductivity of the film. Another out of plane method that was originally used to measure contact resistances was presented by Cox and Strack [36]. This method consisted of having an array of circular contacts on top of a sample, while its backside was contacted by a large surface area electrode. This experimental set up makes possible the separation of the spreading, contact and residual resistances from the total resistance measured (Figure 1.12c).

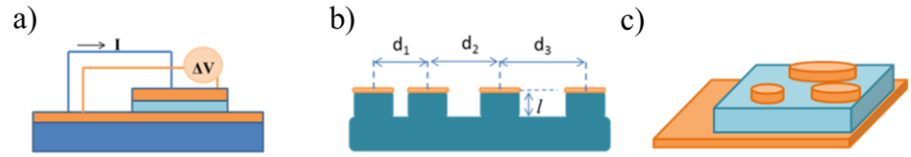

Figure 1.12. a) Four probe technique with patterned electrodes, b) Transmission Line Model (TLM) and c) Cox and Strack methods to measure the electrical conductivity out of plane.

1.2.1.2.2. Thermal conductivity measurements.

Thermal conductivity measurements of films in the cross-plane direction can be based on electrical techniques, like the 3ω-method or steady-state method, or optical methods, like Time Domain Thermo-Reflectance (TDTR)[37], photoacoustic (PA)[38] or photothermal (PT)[39] methods.

The 3ω-method is one of the most popular techniques to measure the cross-plane thermal conductivity of films, and it has recently been adapted to measurements of the in-plane and cross-plane directions[27] (Figure 1.13a). In this method a metallic strip is deposited onto the sample surface to act as both heater and temperature sensor. When one applies an AC current across it, $I=I_0 \cdot \cos(\omega t)$, the strip heats as a consequence of Joule effect, as described in Equation 1.28. The temperature rise in the heater is a superposition of a DC component and 2ω modulated AC component, $T(t)=T_{DC}+\Delta T_{2\omega,}$ where $\Delta T_{2\omega} = \Delta T_0 \cos(2\omega t)$. As the electrical resistance of the heater depends on the temperature, there is also a 2ω variation in the resistance of the heater, which goes like $R(t)=R_0(1+TCR \cdot T(t))$, where TCR is the temperature coefficient of the heater. The voltage is described as, $V(t)=I(t) \cdot R(t)$,

whose third harmonic, $V_{3\omega}$, is correlated with the thermal properties of the thin film measured. Instead of using a metallic strip it is also possible to use another heating element, like a Wollastone probe, which is basically a micro-point-heater.

Another electrical based technique is the steady-state method [27], which basically consists of using two or three strips onto the film which is held on a substrate. One large strip is in charge of heating and measuring the temperature at the surface of the film, while the second thermometer provides the temperature rise of the film at a particular distance from the other heater. If one uses a two-dimensional heat conduction model and a known thermal conductivity of the substrate, one can infer the temperature rise of the substrate at the heater location from the temperature rise of the second thermometer. In case the thermal conductivity of the substrate is unknown, a third thermocouple must be used in order to determine it. From this temperature rise and the use of the proper heat conduction model one can determine the thermal conductivity of the film.

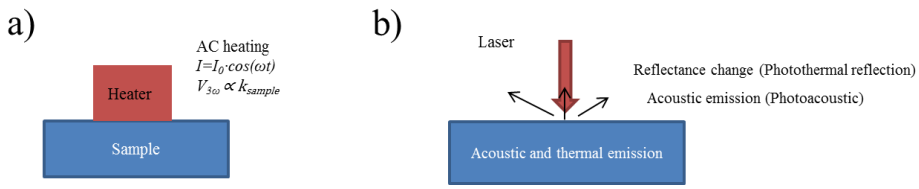

Figure 1.13. a) 3ω-method and b) optical based techniques to measure the thermal conductivity of the films out of plane.

Regarding optical based techniques, photoacoustic (PA), time domain thermoreflectance (TDTR), or photothermal (PT) methods are the most used [27] (Figure 1.13b). The first one, PA technique, is based on monitoring acoustic waves that are generated by a pulsed laser. The pulsed laser heats the surface of the sample. As a consequence, it generates acoustic waves in the surrounding gas that are recorded by a microphone. The phase shift between the acoustic waves and laser signals contains information of the thermal properties of the sample under study. In the TDTR technique, a probe laser heats up the sample and changes in the reflectance of the sample relate to its thermal properties. Regarding photothermal methods, there are several types, like reflectance, emission or deflection methods, but the most known is

the photothermal reflection. This method in the frequency domain is completed by periodically modulating a continuous-wave heating laser and detecting the small periodic change in the intensity of the reflected beam of a continuous-wave probe laser. This reflectance modulation is due to the temperature dependence of the refractive index. This technique has been used to measure the thermal diffusivity of films[27].

1.2.1.2.3. Seebeck coefficient measurements.

In order to measure the Seebeck coefficient in the cross plane direction one needs to measure the voltage generated and the temperature gradient across the thin film, which becomes more complex than in-plane measurements. The use of thermocouples to measure the difference of temperature across the film cannot be used because of the difficulty to make a good thermal contact between the surface of the film and the thermocouple. To overcome this problem, micro-devices that can work as heaters and as a temperature and voltage sensors is the most used technique to obtain the Seebeck coefficient of the films [29]. The micro-heater applies a temperature difference across the mesa film, which is also recorded, and the electrodes on the film or the ones of the micro-device are in charge of measuring the generated voltage (Figure 1.14).

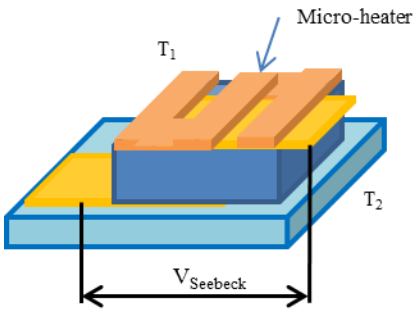

Figure 1.14. Microheater based techniques to measure the Seebeck coefficient of films in its out of plane direction.

Another method to obtain the Seebeck coefficient is the 2ω-method[29]. This technique consists of applying an AC current, with 1ω frequency, to the micro-heater, $I=I_0 \cdot cos(\omega t)$, whose temperature increases proportionally to Joule heating, that is

$$P_{Joule} = I^2 \cdot R = \frac{I_0^2 R_0}{2} + \frac{I_0^2 R_0}{2} \cdot \cos(2\omega t) \qquad (1.28)$$

where R_0 is the resistance of the heater line. The first term corresponds to the DC contribution while the second term indicates the fluctuations of temperature with time with 2ω frequency, i.e. $T(t)=T_{DC}+\Delta T_{2\omega}$. The $\Delta T_{2\omega}$ term can be described as $\Delta T_{2\omega} = \Delta T_0 \cos(2\omega t)$, where ΔT_0 is the magnitude of the temperature fluctuation. The electrical resistance of the heater depends on the temperature and as a consequence, it also varies with 2ω frequency. The temperature variation, ΔT_0, can be correlated with the 3ω electrical voltage, $V_{3\omega}$, response of the heater as $\Delta T_0 = V_{3\omega} \frac{2}{I_0 R_0} \cdot \frac{1}{TCR}$, where TCR is the temperature coefficient of the resistance of the heater. The Seebeck coefficient is then calculated from the equation,

$$S = -\frac{V_{2\omega}}{\Delta T_{2\omega}} \tag{1.29}$$

where $V_{2\omega}$ is the measured second harmonic of the voltage. The substrate where the film is held on might contribute to the Seebeck coefficient measured and it should be taken into account in the data reduction.

Table 1.II. Summary of the different techniques for measuring transport properties of films including advantages and disadvantages in brief.

Films

Electrical conductivity measurements

In-plane	***Out of plane***
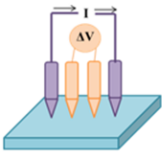 **-Four probe measurements** (*I-V* curves). MERITS -Easy achievement of electrical contact or fabrication of contact electrodes. -Influence of contact and other parasitic resistances is removed. DEMERITS - Separation between probes must be much smaller than sample size. - Correction factors must be considered in data reduction, especially for thin films. - An isolating substrate is needed.	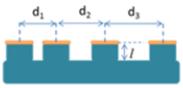 **-Modified Transmission Line model (TLM).** MERITS - Easy achievement of electrical electrodes. - Accounts for electrical contact Resistance. DEMERITS - Mesa attack or etching are required which might damage the sample.
	 **-Cox and Strack method.** MERITS - Easy achievement of electrical electrodes. - Accounts for electrical contact resistance and spreading of the current. DEMERITS - Some equations must be used to careful separate the current spreading, contact and residual resistance from total resistance measured.
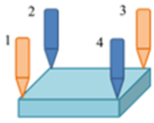 **-Van der Pauw method.** MERITS -Samples with arbitrary shape can be measured. -Influence of contact and other parasitic resistances is removed. -High accuracy. DEMERITS - Requires of proper estimation of the thickness of the film. - An isolating substrate is needed.	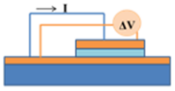 **-Four probe technique & Van der Pauw technique.** MERITS - Samples with arbitrary shape can be measured. - Accounts for electrical contact Resistance. DEMERITS - Time consuming as it might require of several lithographic steps. - Mesa attacks might be also needed which could damage the sample. - Non-uniform spreading of the current might happen.

Thermal conductivity measurements

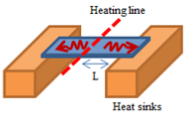

-Membrane method.

MERITS
- Steady state or transient methods can be used.
- Relatively simple experimental set up.

DEMERITS
- Difficulty to have a freestanding film.
- Transport modeling required.
- Vacuum conditions are desired.

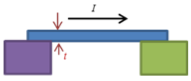

-Bridge method.

MERITS
-Steady state or transient methods can be used.
- Relatively simple experimental set up.

DEMERITS
- Difficulty to have a freestanding film.
- Transport modeling required.
- Vacuum conditions are desired.

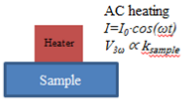

-3ω-method.

MERITS
- Electrical based technique successfully used to measure a wide variety of samples.
-Local resolution.

DEMERITS
- Thermal contact resistances must be consider carefully.

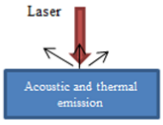

-Optical methods (TDTR , PA or PT).

MERITS
-Non-invasive or destructive techniques.
-Local resolution.

DEMERITS
-Complicated mathematical model must be used to determine the thermal conductivity of the film.
- Thermal contact resistances and substrate underneath the sample should be considered.

Seebeck coefficient measurements

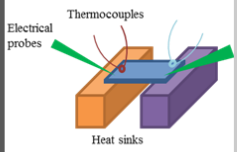

-Integral or differential method.

MERITS
-Temperature and voltage measurements with high accuracy.
- Electrical conductance measurements can be also carried out.

DEMERITS
- Difficulty of having a freestanding film.
- Very thin thermocouples are required to minimize heat loss.

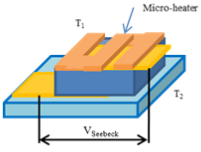

-Microheaters (steady state or 2ω method).

MERITS
- Voltage and temperature measurements taken with high accuracy.

DEMERITS
- Fabrication of the microchips that can act as both heater and thermometer.

1.2.1.3. Direct determination of the figure of merit. Harman technique.

The Harman method is an electrical based technique that has been proven to measure well and with only one experimental set up the figure of merit of bulk thermoelectric materials in its cross-plane direction. However, its application to thin film or nanowires structures is challenging and it requires specific considerations because of the heat losses and heat generation through the leads, as well as electrical parasitic effects.

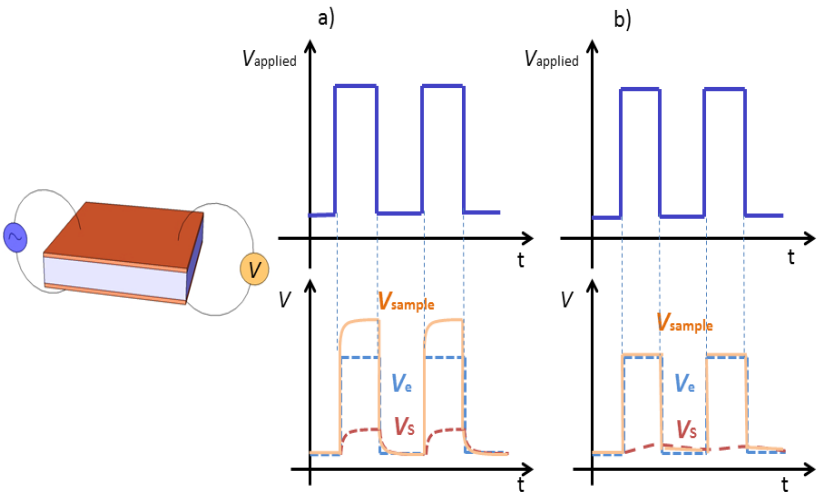

Figure 1.15. Schematic view of the signals measured with the Harman method at high and low frequencies. The left side illustrates the measurement setup: a freestanding thermoelectric thin film connected to a voltage source and a voltmeter. a) In the low frequency regime, a Seebeck voltage raise/decay is observed when the applied current is changing. b) In the high frequency regimes, temperature gradients cannot be established and thus the Seebeck voltage component is negligible. Figure taken from reference [40].

In the original Harman method [41], a DC current is applied through a thermoelectric sample subjected to one-dimensional (1D) electrical and heat conduction along its length and insulated adiabatically. The current generates a temperature gradient because of opposite Peltier effects (heating *versus* cooling) at the junctions between the thermoelectric sample and the two electrodes at the sample's ends. While Joule heating may occur within the sample, because of the

symmetric boundary conditions to heat transfer, it does not generate a temperature difference between the electrodes. At steady-state, the current is turned off, which results in an instantaneous drop in voltage, because the ohmic component of the voltage across the sample, V_e, vanishes. However, due to the fact that the response of heat transport is slower than the electrical transport, a temperature difference still remains across the sample that generates a Seebeck voltage, with initial value V_S. As the sample cool down, the temperature difference goes to zero and so the Seebeck voltage. The figure of merit is then calculated from the equation [41, 42] :

$$zT = \frac{V_s}{V_e} \quad . \tag{1.30}$$

Although, this method might look simple, for small zT samples or for nanostructures such as thin films or nanowires the measurement is non-trivial because they produce either small V_s or very fast decaying Seebeck signals. In order to increase the accuracy of Seebeck voltage measurement, the technique was modified from a transient signal to electrical resistance measurements under modulated (AC) currents. This is called the modified Harman method. There are two different regimes that can be distinguished: 1) a low frequency (LF or DC) regime, where the applied current produces a frequency independent steady temperature on account of Peltier effect, (Figure 1.15a), and 2) a high frequency (HF) regime (Figure 1.15b), where the applied voltage varies so fast that no AC temperature gradient can be generated. On the one hand, the voltage developed in the LF regime, V_{LF}, is composed of both the Seebeck and the ohmic voltage components. On the other hand, the voltage measured in the HF regime, V_{HF}, contains only the ohmic voltage. Therefore, the difference between V_{LF} and V_{HF} equals the thermoelectric voltage, $V_{LF} - V_{HF} = V_s$. Therefore, when the same current is utilized to perform AC and DC measurements, the figure of merit can be obtained from [43]

$$zT = \frac{V_{LF}}{V_{HF}} - 1 \tag{1.31}$$

Independently of the method used, either the original or the modified Harman methods, key to a successful measurement is the accurate determination of the generated Seebeck voltage. When measuring bulk samples with zT~1, which are adiabatically insulated and that have low resistance electrical contacts, the Seebeck voltage is of magnitude similar to the ohmic voltage and has a relatively low rate

of decay, which can be easily acquired by an oscilloscope. However, when the same methods are applied to nanostructured materials (films, etc), a small and fast decaying Seebeck voltage is typically generated, which requires voltage measurement equipment with specific technical characteristics such as: high sensitivity and high frequency response.

Because of all these inconveniences, the Harman methods, although they have been extensively used to measure the figure of merit of bulk samples [43-46], are hardly applied for thin film samples [34, 47-49] or nanowires. Although some works can be found in literature, there are very few manuscripts that measure the *zT* of films thinner than 6 µm through these methods [34, 49]. Moreover, an added challenge to these measurements is the complexity to ensure the validity of original conditions required by the original Harman technique (free standing, adiabatically insulated sample). As an example, measurements of thin film samples need the presence of a substrate underneath the sample. Depending on the kind of substrate used, as well as the quality of contact electrodes, the frequency, voltage and generated temperature gradient by the sample it might be affected significantly. As a consequence the measured, or extrinsic, *zT* can be very different from the real or intrinsic *zT* of the film.

1.2.2. Transport property measurements of single nanowires.

This section covers some relevant examples of the various devices and methodologies in use to measure electrical and thermal transport in single nanowires.

Adapting the measurement techniques currently in use for macroscopic materials to samples with nanometer dimensions often requires stringent technical demands. For contact based techniques, a miniaturization of the electrical contacts and/or the thermometers and heaters is mandatory and micro/nano-fabrication tools are required to build up specific microchips to enable thermoelectrical measurements in one dimensional structures. Single nanowire properties can also be measured by Scanning Probe Microscopy (SPM) and optical techniques. In the first case, different SPM modes and probes make possible an analysis of the electrical and thermal properties of single nanowires thanks to their nanometre resolution. A further advantage of these techniques is the possibility of measuring not only single nanowires, but also nanowires embedded in a matrix. In the case of optical

techniques, electrical and thermal conductivity of single nanowires have been measured by micro-Raman or micro-photoluminescence spectroscopy. In some cases, the use of an appropriate microchip to place the nanowire is required, but in general these optical techniques can be regarded as non-invasive.

1.2.2.1. Microchips designed to measure single nanowires.

The ceaseless progress of the microelectronic industry has provided a wide variety of well-established fabrication methods that have paved the way to miniaturization. This approach has been widely used and many specific microchip devices have been fabricated during the last decade [50]. In many cases, downscaling also allows the development of new measurement techniques that are specific to the nanoscale, as will be shown later.

The measurement of single nanowires employing microfabricated probes offers a powerful tool that, with the proper design, can determine not only one specific transport property but several of them. Therefore, microchips with the capacity of measuring electrical conductivity, thermal conductivity and/or Seebeck coefficient have been reported in the past years. [51, 52]

One of the main outcomes of microchip devices is that they make possible measurements on nanowires with very small diameters down to a few nanometers, where quantum size effects might rule transport properties[53, 54]. This size domain offers tremendous prospects for the realization of efficient thermoelectric materials but the thermoelectrical measurements are challenging on account of the required sensitivity. Additionally, at these very small size surface effects become so important, because of the increment of the surface to volume rate, that surface absorption of elements can induce variations in electrical transport along the nanowire [55].

In general, the manufacturing process is one of the principal difficulties of these microfabricated devices, because of the need of very specific equipment and installations to implement them. The experimenter faces the challenge of placing the nanowire at the right position and obtaining low electrical and thermal resistance[56]. When the nanowire cannot be grown directly in the microchip, there are two possible strategies. The first strategy consists of placing single

nanowires onto a substrate prior to the microchip fabrication. If the nanowires are grown inside a template, one must initially dissolve the matrix that contains the nanowires. In the case of free-standing nanowires, this procedure is obviously not necessary. In both cases, the nanowires are dispersed in a volatile solvent, such as ethanol. Then, a drop of this solution is poured onto the substrate, and the whole is let dry in air. Once the nanowires are placed in the substrate, a lithography process is carried out to define the microchip design, which is followed by the deposition of a certain metal in order to achieve electrical contacts at the ends of the nanowire. These contacts can act also as thermometers or heaters, depending on the requirements of the measurement configuration. These heaters regularly consist of two platinum *zig zag* heating lines that are connected to both ends of the nanowire. They will provide a way of controlling the temperature at the micrometer scale. Finally, in some cases where further isolation is necessary, a removal of the substrate under the nanowire can be carried out in order to have the nanowire suspended between the contacts and avoid leakage to the substrate. For instance, this process can be made via Reactive Ion Etching (RIE) [56]. The second strategy consists of fabricating the microchip with all its features, such as the heaters and contacts, prior to the positioning of the nanowire. This approach has the advantage that lithography steps are easily repeatable and a great number of identical microchips can be made at the same time, especially in single silicon wafers. The placement of the nanowires onto the chips is made by drop cast as it was mentioned previously, i.e. a solution of dispersed nanowires in a volatile solvent is dropped onto the wafer. Statistically, some of the nanowires will be placed precisely between the electrical/thermal contacts [56, 57], just where they should be. In some cases, one can also combine a focused ion beam (FIB) and a nano-manipulator to put the single nanowires on pre-patterned electrodes [58]. With this method, it is feasible to select specific nanowires as well as to locate the nanowire exactly on the electrode contacts. For this purpose, the desired nanowire is frequently pulled out from a hosting bundle with a tip (see Figure 1.16). When the metal tip is close to a nanowire, under the presence of an electrostatic force, the tip can attract a semiconducting nanowire. Once the tip touches the end of the nanowire, a local platinum deposition is made between the tip and the nanowire using an electron beam. Then, a strong "pull-out-force" is used to extract the nanowire from the bundle. Finally, using a nano-manipulator the "pulled" nanowire is located on four-point-probe electrodes and an ion beam is employed to cut the linkage between the nanowire and the tip. This offers a selective, reliable and highly

reproducible way of placing the nanowires in a desired location for specific applications. Nevertheless, on account of the time consuming procedure, it presents a clear disadvantage over the above mentioned procedure.

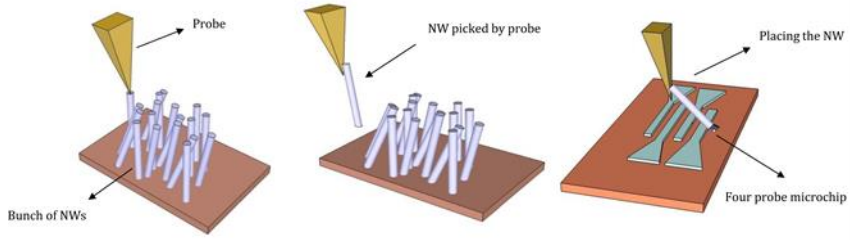

Figure 1.16. Schematic view of picking and placing a single nanowire for transport property measurements. Figure taken from reference [59].

1.2.2.1.1. Electrical conductivity measurements.

In any electrical measurement, achieving good electrical contacts is one of the first requirements. To this end, strategy mimics those used in the macroscopic domain, but with the need of spatial resolution imposed by the low dimensionality. In situations where quantum confinement plays a role, changes in the electronic density of states and energy levels of the carriers also have to be considered.

For nanowires located on top of insulating substrates or on substrates covered by thin isolation layers, electrical contacts can be obtained by different ways, as shown in Figure 1.17. If the metal contacts are patterned on the substrate before placing the nanowire, the contact can be performed mechanically, which requires use of sophisticated damped probe stations to minimize distortions due to vibrations, or by deposition of a contacting material, either by Focus Ion Beam (FIB) or Electron Beam Induced Deposition (EBID). In the first case, a hydrocarbon layer is grown by focusing the energetic electron beam of a SEM in the contact area between the nanowire and the tip. In the second case, platinum can be deposited with high accuracy on the selected region. The nanowires can also be dispersed on the substrate by drop cast and contacted afterwards by a lithographic process of adequate spatial accuracy to deposit, by standard evaporation methods, the metal contacts at the ends of the nanowire.

For semiconductor nanowires the strategy varies slightly because of the requirement to obtain satisfactory ohmic contacts. In all cases, the metal of the electrical contact should be carefully selected, with a work function that allows alignment of the Fermi levels and easy injection of the carriers within the nanowires.

The resistance of the nanowire at a certain temperature, $R(T_0)$, can be determined in a straightforward measurement. This can be done by injecting a very low current (in order to avoid self-heating by Joule effect) into the nanowire through the electrical contacts and measuring the voltage drop [51] or taking *I-V* curves to obtain the electrical resistance [60-64]. Once the resistance is determined, the electrical conductivity can be derived, as far as the size and geometry of the nanowires are measured with enough accuracy. It is important to mention that due to the large impedance associated with individual nanowire, voltmeters with large input impedances and low current precision sources are required for very sensitive and accurate measurements.

Two probes [65] can be used to obtain *I-V* curves, but in this case the influence of the contact resistances must be considered as it may affect the validity of the measurements. Using four electrical contacts instead of two improves the accuracy of the measurements by removing the influence of the contacts, probes and spreading resistance[66, 67]. The basis of the measurement is the same that in the *I-V* curves, but in this case the current is applied through the sample with two probes while the voltage drop is measured with other two. Four probe measurements can be performed with suspended probes[67-69] or with particular designs of the metal probes on a substrate (see Figure 1.17 for a specific example)[70-76]. Although the design of this kind of microchips (usually called four-probe microchips) can be quite complex, a broad variety of nanowires have been fully characterized by them. Furthermore, with a slight change in their design, this kind of microchips can measure the dependence of the electrical resistivity with temperature. For that purpose, micro-heaters should be located in one or both ends of the nanowire[60, 77, 78]. In some cases, the observation of semimetal-semiconductor transitions in nanowires can be also observed while performing those measurements. In order to study this kind of phenomenon in nanowires, models and techniques have been developed[79, 80]. The contact resistance can be evaluated by conducting electrical measurements at different points along the length of the

nanowire, such as those carried out on 50 nm NiFe/Pt multilayer nanowires [81].

These types of microchips have also been used to modify the number of charge carriers[82]. For that purpose, the end contacts of the nanowire serve as a source and a drain, and the number of carriers flowing through it can be manipulated by the gate voltage, V_g, which is applied to the back of the substrate. Therefore, the carrier density induced by the gate voltage can be studied and the mobility of electrons (μ_e) in the nanowires calculated. To this end, one should use the equation $I_{sd} = I_0(V_{sd}) + \left(\mu_e C V_{sd} / L^2 \right) V_g$ where C is the capacitance of the nanowire and I_{sd} is the current through the nanowire, that takes into account two components, the conventional current I_0, and the current induced by V_g. Nevertheless, even in the case of Si, there is no consensus if the mobility in nanowires is smaller or larger than in bulk Si. This is due to the fact that many factors, including nanowire diameter, crystalline orientation, surface termination or dopant concentration influence the mobility of the carriers[83]. Moreover, with a similar microchip design, it is also possible to obtain the dopant profile along the nanowire length. This can be achieved by taking low and high frequency capacitance-voltage measurements [84], from which one can obtain the carrier density profile of the nanowire.

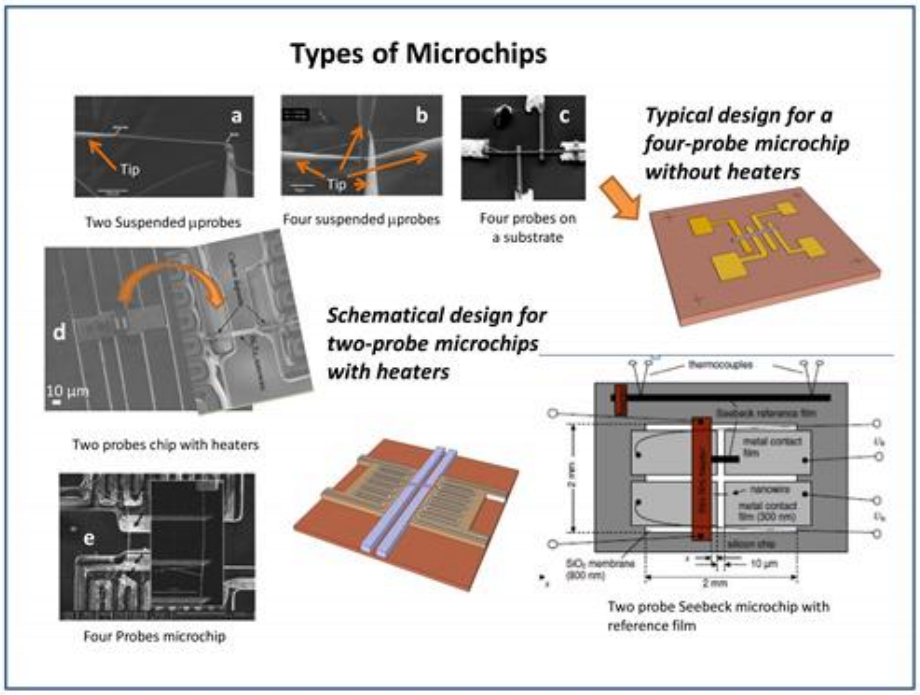

Figure 1.17. Illustration the main microchips types used to measure transport properties. The design of the microchip and the technique and methodology of choice highly depend on the transport property to be measured (electrical, thermal or thermoelectrical), on the material characteristics (metal, semiconductor or insulating) and on the fabrication of the nanowire. Figure taken from reference [59].

Regarding accuracy and sensitivity of the technique, different values in literature can be found when measuring electrical conductivity in metallic and semiconducting single nanowires with the aid of microchips. For example, Völklein *et al.*[51] measured transport properties of Pt, Au, Cu or Bi free standing nanowires of around 200 nm diameter and 20 µm length with a two probe microchip, obtaining for the Pt nanowire an electrical conductivity of $4 \cdot 10^6 (\Omega \cdot \mathrm{m})^{-1}$ with an error of less than $\pm 0.4 \cdot 10^6 (\Omega \cdot \mathrm{m})^{-1}$, and a thermal conductivity of $20 \mathrm{W/K \cdot m}$ with an error of ± 4 W/K·m at room temperature. Nowadays, measurements with high accuracy have been carried out with other microchips, mainly with four probe ones, that are able to detect electrical currents through the nanowire of few nano-amperes[70] and thermal conductivities of few $\mathrm{W/K \cdot m}$ [60].

1.2.2.1.2. Thermal conductivity measurements.

Accurate thermal conductivity measurements of single nanowires are particularly challenging since the effective thermal barriers are not readily available and heat can diffuse through any media. In small or medium diameter nanowires, where phonon transport is drastically reduced because of the scattering with the boundaries, the energy transfer between the two extremes of a nanowire held at different temperatures is really small and heat losses with the surroundings need to be notably diminished to perform reliable measurements. Only in the case of conducting nanowires simpler approaches can be conceived.

For conducting nanowires, which are electrically isolated from the substrate (like those shown in Figure 1.17 (a-b-c)). The nanowire itself can be used as a heater and the thermal conductivity can be derived using the 3ω method, which is well established in the case of bulk materials and thin films [85-88]. This method consists of applying an alternating voltage signal to a heater while the third harmonic (3ω) signal response is measured. This 3ω-voltage can be related to the thermal conductivity of the sample. In the four-probe 3ω-method used for the measurement of single nanowires [58, 89], an alternating (AC) current is applied through the nanowire at frequency ω. Then, the 3ω-voltage response of the nanowire is measured with the two other electrodes. This 3ω-signal correlates with the thermal conductivity of the nanowire according to the equation [58],

$$V_{3\omega} \approx \frac{\sqrt{2}\cdot I^3\cdot R\cdot R'\cdot L}{\pi^4\cdot k\cdot A} \tag{1.32}$$

where L, $R = R_0 + R'(T - T_0)$ and A are length, electrical resistance and cross sectional area of the nanowire, respectively. R' is the resistance change with temperature at room temperature defined as $(\partial R/\partial T)_T$ and k is the thermal conductivity of the nanowire.

In general, suspended structures, in which the influence of the substrate on the thermal signature is minimized, are considered for thermal measurements on single nanowires. Figure 1.17d shows a SEM micrograph of the central part of a typical suspended structure designed to measure thermal and/or electrical conductivities and the Seebeck coefficient of individual nanowires. Despite the fact that a variety of designs can be found in the literature, most of them consist of two

suspended platforms, each around 15 μm^2. Every platform consists of a zigzag heater made of Pt that is deposited on top of a SiN_x membrane. This one can be used as a heater or temperature sensor [90, 91]. Two additional electrodes make possible electrical contacts of the nanowire under study. Both platforms are suspended by long (200-to-400 μm) and narrow (2-4 μm) SiN_x arms connected to the Si frame. With this geometry the thermal conductance between the platforms and the Si frame is ~80 nW/K at 300 K under high vacuum conditions. The nanowire is located bridging the gap between the sensing and heating membranes. In order to perform the measurement, the temperature of one of the platinum heaters is increased while the temperature change of the opposite electrode is recorded. By a proper analysis of the heat losses through the beams, the thermal conductivity can be determined through a simple one dimensional analysis [56, 57, 60, 64, 92-96].

The lower limit of sensitivity of these devices to measure thermal conductance is in the order of 1 nW/K at room temperature. Among the different factors that limit the sensitivity of standard four-point measurements on these type of structures, the temperature stability of the cryostat and its influence on the electrical measurements are probably the most relevant. It is important mentioning that very small diameter nanowires with thermal conductivities of the order of 1 W/mK will have thermal conductances as low as 10 pW/K, and therefore sensitivity improvements are needed. In order to fulfil this requirement, the use of an on-chip Wheatstone bridge circuit has recently enabled a significant reduction of the noise in conductance to values of ~10 pW/K, at room temperature [97]. On the one hand, using this setup, Chen *et al*[98] have demonstrated the importance of phonon confinement in the reduction of the thermal conductivity in Ge-Si core shell nanowires with core diameters below 20 nm. On the other hand, when working with highly conductive samples bridging the two platforms, such as membranes, carbon nanotubes or graphene, it becomes essential to consider the modification of the temperature distribution on the platforms. In this case, if the standard 1D solution of the heat equation is used, errors around 25% can be made. Finite element modelling can be very helpful to provide insights into the variations of the temperature profile of the suspended platforms. Thermal losses by radiation can be another source of error in the determination of the thermal conductivity of nanowires. In this respect, the use of low temperature differences between the heater and the sensing platforms and the use of appropriate radiation shields can be considered for accurate measurements. Another source of uncertainty

is the presence of an unknown thermal contact resistance between the nanowire and the heating/sensing platforms. Therefore, a remaining challenge is to adequately take into consideration or reduce this contact resistance. Recently, Yang *et al*[99] performed measurements of thermal resistance versus the length of multi-walled carbon nanotubes and concluded that 50% of the thermal resistance of the nanotube could be on account of the contact resistance. Using electron beam induced deposition (EBID) or focus ion beam (FIB) may help to improve the contact by locally growing thermally conducting layers, but does not reduce it completely.

Suspended structures have been used to measure thermal conductance in an assortment of nanowires, with different diameters, doping levels and roughness[100, 101], including: single- (SWCN) and multi-walled carbon nano-tubes[99], Si, SiC, Si/SiGe[70, 95, 100, 101], Bi, Bi_2Te_3[56], InAs[100], PbS, PbSe, PbTe[64] and ZnO[76] nanowires, among others.

Although it has been theoretically predicted a deviation of classical transport models due to the appearance of quantum confinement effects on the thermal conductivity of nanowires, experimental evidences of clear deviations are still scarce. For instance, the measurements of the thermal conductance of Ge-Si core-shell ultrathin nanowires is an example in which the theoretically predicted phonon coherent resonance effect has been experimentally demonstrated[98]. Further developments of the techniques are needed to unveil the quantum size regime in nanowires, only a few nm in diameter.

In metals, the Wiedemann-Franz law can be used to determine the thermal conductivity from the electrical conductivity. This relationship establishes that in a metal the rate between the electrical and thermal conductivity is proportional to the temperature and a proportionality constant, L, known as Lorentz number. This expression is written as: $k_e/\sigma = LT$. Using the thermal and electrical conductivities of a bulk reference sample, and under the assumption of constant temperature conditions, it is possible to use the Wiedemann-Franz law to determine the electrical and thermal conductivity of metallic nanowires,

$$k/k_{bulk} = \sigma/\sigma_{bulk} \tag{1.33}$$

This assumption is only valid when the lattice part of the thermal conductivity is negligible in comparison to the electronic part[102-104]. A topic of actual interest is whether the Lorentz number shows size effects when the mean free path of the carriers is comparable to or smaller than the characteristic size of the nanowire. Recently, measurements of electrical conductivity and thermal conductivity on metallic Pt nanowires have found smaller Lorentz numbers than those obtained in the bulk [102]. Further developments of thermal measurements will permit testing these results in other small diameter metallic nanowires.

1.2.2.1.3. Seebeck coefficient measurement.

Regarding the thermoelectric capabilities of the nanowires, to fully characterize them, one needs to measure their Seebeck coefficient and this can also be done with the aid of different microchip designs. For instance, the suspended structure described in Figure 1.17d allows a simple way of performing this measurement, by controlling the temperature difference between both ends of the nanowire and measuring the voltage drop across the nanowire [60, 62, 63]. The Seebeck coefficient is defined as the ratio between the voltage produced and the temperature gradient present in the sample, that is, $S = \Delta V/\Delta T$, where ΔV is the voltage variation and ΔT the temperature difference. In this microchip set up these quantities are both measurable and so the Seebeck coefficient can be obtained. It is also important to take into account the contribution of the Seebeck coefficient of the wires connected to the sample in order to obtain accurate values of S_{sample}.

It is important to note that the measurement of the Seebeck coefficient is associated with at least two experimental challenges in the case of nanowires: 1) the generation of a temperature gradient and 2) the exact determination of the temperature at the nanowire contacts. In reference [51, 52], one possible approach to overcome these limitations is described. The basis of the microchip design used in this case (see Figure 1.17e) is the comparison between the nanowire under study and a known reference film. The microchip is composed of two identical pairs of metallic contacts: 1) a suspended nanowire is placed between two of them, and 2) a film with a known Seebeck coefficient, S_R, among the others. In order to generate the same temperature difference through the film and the nanowire, ΔT, this microchip also holds a thin-film heater, deposited onto the bottom side of the sample. If one takes

into account the Seebeck coefficient of the contacts, S_c, the temperature difference can be determined as $\Delta T = U_R /(S_R - S_c)$. Then, the voltage drop across the nanowire, U_N, created by the same temperature difference, can be obtained according to $S_N - S_c = U_N / \Delta T = U_N /[U_R /(S_R - S_c)]$.

The Seebeck coefficient can be also obtained using the 2ω technique with a four-probe microchip as described in reference[105]. In this method, an AC current at frequency ω is applied, which is in charge of producing a Joule heating in the microheater at a 2ω frequency. The heat produced causes a temperature oscillation that propagates through the nanowire. Using the four-probe technique, the temperature gradient between both ends of the nanowire can be measured, $\Delta T(2\omega)$, along with the voltage drop $\Delta V(2\omega)$, across the nanowire. Therefore, the Seebeck coefficient can be obtained from $S = \Delta V(2\omega) / \Delta T(2\omega)$. The electrical conductivity of the nanowire in reference [105] was measured within the same microchip via *I-V* curves, as it was explained before, which makes possible the determination of the Power Factor of single nanowires using the same chip.

The Seebeck coefficient is expected to increase when reducing the diameter of the nanowires on account of a higher density of states near the Fermi level[79, 106, 107]. In order to observe this effect these microchips have been extensively used to compare nanowire behavior with bulk[54, 56, 60, 96]. In practice, the modification of the electronic density of states is expected to appear for very small diameter nanowires. The work of Heath *et al* shows a substantial Seebeck enhancement with respect to bulk samples for 20 nm doped Si nanowires. Shi and coworkers have also observed an enhancement on 50 nm Bi_2Te_3 nanowires. Undoubtedly, the improvement of measurement techniques to characterize nanowires of smaller diameter will stimulate further experimental and theoretical investigations of the influence of quantum size effects on the thermoelectricity of nanowires.

1.2.2.2. Single nanowire measurements with Scanning Probe Microscope techniques.

Scanning Probe Microscopy (SPM) techniques is an alternative to the measurement of single nanowires with microchips (see previous section). In this case, a tip or probe scans the nanowires with nanometric resolution. These techniques provide some advantages and

shortcomings with respect to measurements performed with microchips. Among the first, SPM techniques are able to provide a morphological image of the surface of the sample from the interaction between the probe and the surface. Moreover, different physical properties can also be measured with local resolution by using an adequate probe in each case and by taking advantage of the high spatial resolution of SPM techniques. To this end, the use of thermal (for thermal conductivity measurement) and/or conductive probes (for electrical conductivity measurement), which are commercially available, along with slight modifications to the SPM microscopes set up; make possible the measurement of the transport properties of single nanowires inside and outside the templates. The nanowires outside the matrix should be placed onto a substrate in a similar way as they are done in the microchips. When the nanowires are inside of a matrix, it is important that the tips of the nanowires can be touchable by the AFM tip. The measurements of the nanowires inside the matrix present an advantage versus microchips since no oxidation is produced in the nanowire surface and the nanowire is not exposed to any chemical that can damage the wire.

Among the potential drawbacks of SPM technique, one can note the restriction to measure nanowire of diameters smaller than the size of the tip, which vary in the nanometer scale depending of the kind of measurement, and the need of certain expertise to obtain reliable data. This thorough understanding of the particular SPM technique not only does it play a role in the performance of the measurement, but also in understanding the results. The reason is that in most cases one does not obtain a direct measurement of the property, however it is necessary to use theoretical models and/or simulations from which the property has to be extracted.

1.2.2.2.1. Electrical conductivity measurements.

Regarding a standard AFM microscope, it is possible to obtain a topographic image of nanowires embedded in a template. If the tip is conductive, it can be positioned and contacted on top of a nanowire (see Figure 1.18) and then, with it, one can pass current through the nanowire and measure its voltage difference. A statistical study of electrical resistance of the nanowires can be carried out by taking several *I-V* curves of different nanowires. After that, by knowing the geometrical dimensions of them, it is possible to determine their

electrical conductivity [108]. Like in two probe microchips, the main drawback of this technique is the influence of the contact, probe and spreading resistances, which influence the accuracy of the electrical conductivity measurements. Depending on the diameter of the nanowires, the size of the tip must be properly selected. The smaller the diameters of the nanowires are, the more difficult the positioning of the tip on top of the nanowires is.

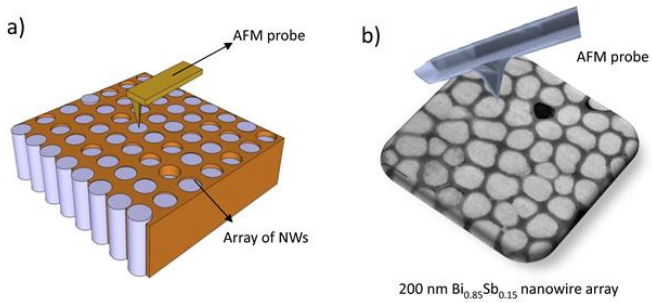

Figure 1.18. a) Schematics of the positioning of the AFM tip on top of an array of nanowires to enable electrical conductivity and Seebeck coefficient measurements. b) Illustration of an AFM probe scanning 200nm diameter $Bi_{0.85}Sb_{0.15}$ nanowire array. Figure taken from reference [59].

Among the different SPM techniques that have been modified to be applied to the study of nanowires, the Scanning Tunneling Microscopy (STM) is a powerful one. This kind of microscope is able to take images of sample surfaces at the atomic level based on the concept of quantum tunneling. This effect takes place under vacuum conditions when a bias is applied between the tip and the surface to be examined (both must be conductive) and they are brought close enough to allow electrons to tunnel between them. The current resulting from those electrons is a function of tip position, the applied voltage, and the local density of states. For instance, considering all this information recorded by the STM, the electrical conductivity and density of states and Fermi level of silicon oxide nanowires have been obtained via STM measurements. Moreover, if a voltage is applied between the ends of the nanowire, it is possible to observe the decay of the voltage along its length by scanning the nanowire with the STM tip [109]. From this measurement, and using the geometrical dimensions of the nanowire, the electrical conductivity can be determined. Another possibility

consists of taking *I-V* curves with the STM tip when the nanowire is placed between two electrodes [110].

The STM technique present some disadvantages like a slower scan speed compared to other techniques, that it is mainly used to analyze conducting materials and that it is very sensitive to mechanical and acoustical vibrations. The requirement of high vacuum conditions adds complexity to the overall setup.

Another SPM technique that has been used for measurements of nanowires is the Kelvin Probe Force Microscopy (KPFM), which maps the surface potential of a sample at atomic or molecular scales in non-contact mode with the use of a conductive tip. The surface potential measured by KPFM is related to the work function of the sample, from which many different surface phenomena can be studied. The work function is measured from the interaction of the electrostatic forces between the sample surface and the conductive AFM tip. A voltage difference, consisting of a DC bias, U_{dc} , and an AC-voltage, $U_{AC}\sin(wt)$, is applied between the surface of the sample and the tip. As a consequence, an electrostatic force is produced, whose force can be written as,

$$F = \frac{1}{2}\frac{\partial C}{\partial z}U^2 \tag{1.34}$$

where $U = U_{dc} + U_{ac}\sin(wt)$ is the total potential applied and *C* is the capacitance of the sample-probe system. The capacitance includes geometrical and dielectric properties of the sample-probe system. A local change in the dielectric properties would produce a change in the force signal. The force equation can be split in different terms, when substituting *U*, according to the Equation 1.34,

$$F = F_{dc} + F_w\sin(wt) + F_{2w}\sin(2wt) \tag{1.35}$$

The first term, F_{dc} contributes to the topographical surface image while the third term, F_{2w}, is related to the dielectric properties of the sample. The second term, F_w , is in charge of giving us information about the surface potential of the sample. This term depends on the DC voltage and the AC voltage applied. It can be written as,

$$F_w = \frac{\partial C}{\partial z}U_{ac}U_{dc} \tag{1.36}$$

The DC voltage is composed of two terms, $U_{dc} = U_{ext} - U_{surf}$ where U_{ext} is the external DC voltage applied whilst U_{surf} is the surface potential. Therefore, in order to measure the surface potential, the condition $F_w = 0$ must be fulfilled. If the external DC voltage is adjusted to the surface potential, $U_{ext} = U_{surf}$, one can obtain a surface potential to map the sample with a KPFM [111].

Consequently, the KPFM image gives information about the composition and electronic states of the local structures of the surface and it has been used to carry out electrical analysis of single nanowires[112-114]. This technique can also be applied to the study of the doping of a nanowire, the local voltage drop along the nanowire or electrical conductivity or the resistance of a single nanowire. KPFM measurements of the nanowire are performed with and without an external applied bias to study how the voltage drops along the nanowire and so the resistance and electrical conductivity of the nanowire can be determined. The subtraction of the data obtained from the unbiased and biased cases allows the deduction of the electrical resistance of the nanowire. In case one knows the mobility and the charge of the carriers, it is possible to determine the carrier concentration in semiconducting nanowires, using the equation $\sigma = qn\mu$ [113, 114]. Koren *et al.*[112] employed this technique to measure the non-uniform doping profiles of Si nanowires. The dopant distribution along the nanowire length ranged from $1.25 \cdot 10^{19}(\mathrm{cm}^{-3})$ up to $2.25 \cdot 10^{19}(\mathrm{cm}^{-3})$ over a distance of 10 µm.

The KPFM requires of particular expertise to achieve accurate measurements of the surface potential of the sample. It involves complex probe fittings while measuring, such as the fit of the phase or amplitude of the first and second harmonic signals from the probe. In order to avoid distortion of the surface potential image, special care is needed to prevent touching the tip with the surface when carrying out KPFM measurements. Afterwards, the information given by the KPFM image is related to the work function of the different materials of the sample and must be properly evaluated.

1.2.2.2.2. Thermal conductivity measurements.

Scanning Thermal Microscopy (SThM) combined with the 3ω method has been used to perform measurements of thermal properties of single nanowires with SPM.

The SThM uses thermoresistive probes that are in charge of making a thermal map of a sample surface. Some of the most used tips in SThM are the Wollaston probes, which basically consist of a platinum (Pt) wire. Another sort of probes are constituted of an integrated palladium film on a substrate. In both cases, when a heated tip gets in contact with different thermal conductivity areas of the sample it results in different heat exchanges. It involves variations in the tip temperature, which influence also its electrical resistance due to the thermoresistive character of the probe. These changes are recorded and from them a qualitative thermal mapping can be obtained for the sample surface.

In order to determine quantitatively the thermal conductivity of a sample the SThM can work in combination with the 3ω method. In this technique, the tip is in contact with the surface of the sample and the application of an alternating signal to the SThM tip warms it up owing to Joule effect. Thus, a heat flux from the tip to the sample is dissipated. The rate of heat flux dissipated to the sample depends on the different thermal conductivities of the composite. This effect generates a 3ω electrical signal response in the tip that can be measured. From the 3ω voltage measurements and the use of thermal models, it is possible to determine the thermal conductivity of nanowires.

As an example, the thermal conductivity of Si single nanowires, with diameters ranging from 250 nm to 4 μm and embedded in a matrix, has been measured using a Wollaston probe mounted on a nanopositioning stage[115]. This stage was mounted inside a Scanning Electron Microscopy (SEM), which was used to help to position the tip on top of the nanowires. The probe is used as both heating element and thermometer by measuring its 3ω electrical response when contacting a nanowire [116, 117]. As it has been previously found by other authors, the thermal conductivity shows a decrease for lower diameter Si nanowires. The uncertainty of these measurements, ~30%, mainly induced by the small heat impedance of the Wollastone probe, obscures detail physical analysis of the size dependence.

A relatively new thermoresistive probe made of palladium with a spatial resolution below one hundred nanometers has been used in references[118-120]. This probe makes possible the measurement of nanowires with smaller diameters than the Wollastone probe. Puyoo *et al.*[119] and M.M. Rojo *et al.*[120] performed thermal imaging of individual Si and Bi_2Te_3 nanowires, respectively, with a spatial resolution around 100 nm. Using these tips with a SThM in 3ω mode configuration, the thermal conductivity of single Si and Bi_2Te_3 nanowires of around 200 nm in diameter were determined to be near to that of the bulk material. As it was outlined in ref.[119, 120], the thermal contact resistances between the tip and the nanowire or the nanowire to the substrate resistance must be carefully considered in order to obtain reliable values of the thermal conductivity of the nanowires. Moreover, the use of theoretical models and a proper calibration of the probe must be considered if one wants to obtain an accurate value of the thermal conductivity of the nanowires.

Thermal conductivity values of around 1.3 W/K·m for 200nm diameter Bi_2Te_3 nanowires and around 128 W/K·m for 200 nm diameter Si nanowires have been determined by SThM. Recently, thermal conductivity measurements of organic nanowires have been carried out with this technique, which also includes a deep study of why the thermal conductivity of these nanowires depends on their diameter size[18]. When determining the thermal conductivity of the nanowires properly, it is very important to consider the right approach and evaluate properly of the nanowire/matrix influence[120]. SPM techniques are non-destructive and therefore allow post-measurements of other properties of the nanowires, like the electrical conductivity or the Seebeck coefficient, using complementary techniques. Further developments, especially in the design of the tip may soon enable sub-100 nm resolution, which would make these techniques ideally suited to investigate size effects in small diameter single nanowires embedded in matrices.

1.2.2.3. Single nanowire measurements by optical techniques.

Optical measurements in bulk samples are usually characterized by being non-invasive and quite versatile techniques. Their maximal resolution is restricted to sizes comparable to the wavelength of the light used through the Abbe diffraction limit. Nevertheless, this limit of

resolution was overcome some time ago and nowadays sub-wavelength studies can be performed with different optical techniques, like Scanning Near Field Optical Microscopy (SNOM). This is particularly important in the case of aiming directly to single nanowires, which would not be detected by optical means otherwise.

Considering that an isolated nanowire is placed onto an appropriate substrate in such a way that it is easily detectable, classical optical techniques can also be used to measure a wide variety of properties of single nanowires. It is important to mention that this is usually achieved with the aid of microchip devices, similar to those presented in Section 1.2.2.1.. Moreover, it is possible to combine the use of microchips with optical techniques, which provides a broader range of measurement possibilities. For instance, light can be used to excite carriers in a nanowire and study the current that is created under an external field (photocurrent). The microchip then can be in charge of detecting and measuring this current. Light can be also used to heat locally the sample with a focused laser beam or to excite photoluminescence in a certain point of the nanowire. Temperature changes of a nanowire can be also detected by optical means using Raman Thermography or microphotoluminiscence.

One of the main drawbacks in the application of optical techniques for the characterization of single nanowires is this necessity of combining optical means and microchips. This is due to the fact that, firstly, the required equipment is increased, because not only the appropriate optical equipment (such as lasers, optical microscopes, detectors) has to be available, but it is also mandatory to have the facilities and expertise to design and fabricate the microchips. Moreover, the placement of the nanowire along with the performance of the electrical contacts at the end of the nanowire is also of crucial importance, as it was in the case of microchip devices.

1.2.2.3.1. Electrical properties analysis of single nanowire.

In order to study the electrical transport properties of a nanowire, one can use light to locally generate an excess of carriers, which induces an electrical current (known as photocurrent). The Scanning Photocurrent Microscopy (SPCM), which is in charge of studying the electrostatic potential, has been used to carry out electrical analysis of single nanowires. It is important mentioning that this is not an exclusively optical technique, because it involves the measurement of

the current created along the nanowire under illumination, and thus implies the location of the single nanowire in an appropriate microchip with electrical contacts. Then, a laser beam is focused into the nanowire, which generates a local photocurrent that is highly sensitive to the electric field. With this technique, one can obtain information about interfaces, inhomogeneities, carriers or dopants. For instance, in ref.[121] the potential profiles of phosphorous doped silicon nanowires were quantitatively measured and the effective concentrations of the carriers were also determined. For these measurements the silicon nanowires were mounted into four-probe microchips, and these were placed on a piezoelectric scanning stage. Then a 532 nm wavelength laser was focused into the nanowires using a confocal microscope. The drift of the free carriers excited by illumination in the presence of an electric field generates the photocurrent. The surface doping of a nanowire can be studied from the different photocurrents obtained in grown and etched nanowires. SPCM has also been used to determine the minority carrier mobility of CdS nanowires, obtaining that the electron transport ($\mu_e\tau_e \approx 5\cdot10^{-7}$ cm^2/V) was more efficient than the hole transport ($\mu_h\tau_h \approx 1\cdot10^{-7}$ cm^2/V) [122]. For these measurements, a chopped 457 nm wavelength laser was focused to a ~ 400 nm spot and the nanowire was placed onto a microchip with contacts at both ends of the nanowire. Then, a bias voltage was applied between the contacts and the photocurrent generated by the illumination was determined as a function of the position of the beam.

Given that the quantities measured by SCPM can be also measured by Kelvin Probe Force Microscopy (See Section 1.2.2.2.1.), these results can be cross-checked with KPFM. The SPCM provides an alternative where the light does not induce any perturbation to the device while supplying a high spatial resolution, which gives insight to the transport processes[121].

1.2.2.3.2. Light-based thermal conductivity measurements.

Photoluminescence is a spectroscopic technique that has been adapted to the measurement of the thermal conductivity of nanowires. As it was said before, the isolated nanowires have to be easily found with classical optical techniques. As an example, in reference [123] single CdS nanowires with diameters ranging from 200 to 400 nm were partially suspended on a silicon substrate with stripes and trenches between these stripes. Once the nanowire was located, it was irradiated with a laser beam focused with a confocal configuration (see Figure

1.19), which caused at the same time local heating and the excitation of the fluorescence of the sample. The actual temperature rise can be determined knowing the laser power and the thermal conduction of the nanowires, which can be characterized through the micro-photoluminescence of the nanowire under the excitation of the laser. It is possible to study different micro-photoluminescence spectra recorded at different temperatures, which makes possible the extraction of the temperature at the different positions of the suspended nanowires[123]. The thermal conductivity of the nanowire can be obtained from the temperature gradient along with the length of the nanowire section between two silicon stripes. For that purpose, one must use the theoretical equation of heat conduction through a solid rod:

$$k = \frac{L}{4A} \cdot \left(\frac{\Delta P}{(T_1 - T_0)}\right) = \frac{L}{4A} \cdot \left(\frac{\Delta P}{\Delta T}\right) \tag{1.37}$$

where L is the length of the nanowire suspended between two stripes, x is the position where the laser hits the nanowire, A is the cross sectional area of the nanowire and ΔP is the calculated energy absorbed by the nanowire considering the parameters of the laser (spot profile and diameter) and the absorptivity of the surface of the nanowire. Finally, ΔT is the temperature increment caused by the local heating of the laser. From these measurements, a thermal conductivity of 4.9 – 6.2 W/m·K was obtained for these CdS nanowires.

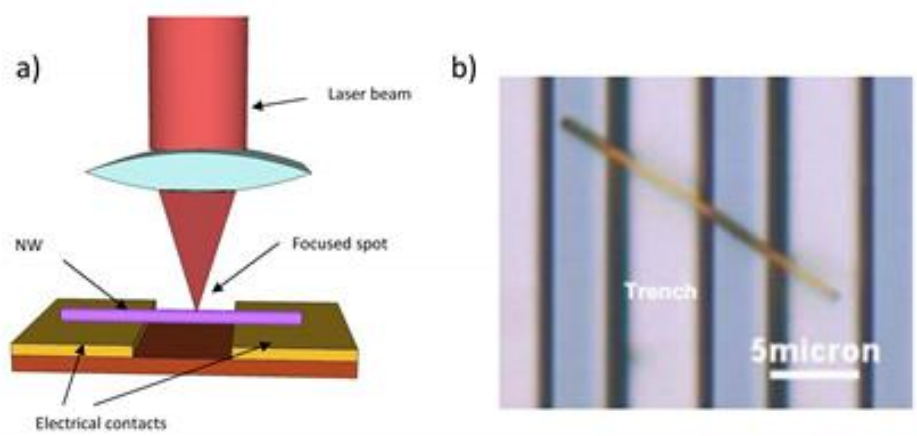

Figure 1.19. a) Schematic view of the experimental setup used for microphotoluminiscence. b) Optical image of a suspended CdS nanowire where microphoto-luminescence spectroscopy takes place. Figure taken from reference [59].

Micro-Raman is another spectroscopic technique which has been used for obtaining the thermal conductivity of single nanowires. The experimental setup is almost the same as the one presented in Figure 1.19, with the nanowire suspended between two contacts or fixed on one side. Then, the excited Raman modes have to be spatially resolved to make a map of the temperature along the nanowire. Some examples of this technique applied to nanowires can be found in references [124, 125] where a thermal conductivity of $\kappa \sim 8 - 36$ W/m·K in GaAs nanowires of 150 – 170 nm in diameter, and $\kappa \sim 25 - 75$ W/m·K in a Si nanowires of 80 to 30 nm in diameter were measured. In these works, a nanowire is locally heated with a focused laser beam and then, the local temperature of the nanowire is obtained via the Raman spectra at the micrometric scale. This can be achieved thanks to the linear relation of the shift of the transverse optical phonon frequency ν with temperature. In other words, there is a shift in the position of the Raman peaks that depends on the temperature of the sample. Then, from the theoretical model that describes the expected experimental temperature profile of a suspended nanowire [126], the thermal conductivity can be calculated as,

$$\Delta T(x) = \frac{P_{abs}}{kA}\left(\frac{x^2}{L} - \frac{L}{4}\right) = -B_1 x^2 + \Delta T_{\max} \qquad (1.38)$$

where P_{abs} is the power absorbed inside the nanowire (extracted from simulations), L is the length of the suspended part, A the cross sectional area, and B_1 the curvature.

1.2.3. Transport property measurements of nanowire arrays.

This far it has been discussed different methods to measure the properties of single nanowires, independently of their fabrication procedure. Nevertheless, it is important noting that the most common way of producing thermoelectric nanowires implies the growth of an array of nanowires embedded in a certain matrix or free standing nanowires on a substrate. As an example, anodic alumina templates, or polymeric membranes, are broadly used to fabricate nanowires of a variety of materials via electrochemistry processes [127-131]. Obtaining efficient thermoelectric devices with sufficient power-output per unit area for a given temperature difference require assembling a large amount of nanowires electrically connected in parallel within the

individual n and p-type legs of the device. This configuration allows enhancing the output current and provides increased mechanical stability. Therefore, nanowire arrays embedded in templates offer potential prospects for integration into real thermoelectric devices [132, 133]. As a consequence, techniques that allow measurements of the whole structure need to be developed, as far as thermoelectric efficiency is concerned. This section presents measurement techniques that are able to determine the transport properties of arrays of nanowires with the matrix as a whole, and then, if the contribution of the matrix can be independently determined, it would make possible the characterization of the nanowire array.

As it was previously mentioned, these techniques present not only some practical advantages compared to single nanowire measurements, like an easier preparation of the samples, but also prevent the degradation of the nanowires during the process of dissolving the matrix or when exposed to air. It has been reported that for nanowires whose surface can easily oxidize, their measurement as single nanowires with the aid of microchips show the effect of the oxidation, modifying their transport properties[134]. Surface oxidation adds complexity to the electrical measurements, and the need to locally remove the oxide layer prior to adding the metallic contacts, in order to obtain reliable data. Moreover, some disadvantages regarding the measurement of nanowire arrays include growing a dense array of nanowires to properly fill the matrix, the possibility of achieving good thermal and electrical contacts to reduce the influence of the contact resistances and granting a suitable access to the top of the nanowires in order to assure that the whole array is measured.

1.2.3.1. Experimental setups for both electrical conductivity and Seebeck coefficient measurements.

Measurements of the electrical conductivity and Seebeck coefficient of a nanowire array can be carried out in a direct and simple way. The only requirement of the sample is that nanowires must protrude the matrix at both ends of the matrix in order to ensure a good electrical contact. When the nanowires are grown inside a matrix by electrochemical deposition, the electrical contact between what one could call “the bottom side” of the matrix and the nanowires is ensured. On the other hand, the “top side” of the nanowires can be contacted by evaporating or electrochemically growing a gold layer, for instance. The Seebeck coefficient is then measured by applying a difference of

temperature between both sides of the nanowire template while simultaneously measuring the Seebeck voltage generated between the top and bottom sides. The Seebeck coefficient can be calculated using the equation, $S = \Delta V / \Delta T$ [108, 135-137]. A slightly different arrangement is presented in ref. [138], where a set up made of a heater and heat sink sandwiching a nanowire array sample was used to measure the Seebeck coefficient of the array.

Taking advantage of the previous setup configuration, the electrical conductivity of the nanowire array can also be measured. Now, an electrical current is applied through the nanowire array while the voltage drop across the nanowires is measured. Through the *I-V* curves obtained, the electrical resistance of the nanowire array can be determined[136]. Two probe measurements can be used to take *I-V* curves on several nanowires of the nanowire array, but the estimation of the number of nanowires selected in each measurement is quite complex[139]. For that purpose, there are several software programs that can help with this estimation to determine it more precisely. As it is a two probe measurement, the main disadvantage of this technique comes from the influence of the spreading and contact resistances.

A special set up, consisting of a thin film sample of randomly aligned nanowires on a substrate can be also used to measure the electrical conductivity and Seebeck coefficient of different nanowire arrays. Usually this thin film is fabricated by nanowire casting and pressing processes until it gets dense and solid [140, 141]. On the one hand, a heat sink and a heater are placed on top of the sides of the thin film. Two thermocouples are in contact with the thin film in order to determine the temperature difference generated by the heaters. On the other hand, two electrodes used to measure the voltage drop are pressed on the thin film sample between the heaters. Once the film has been fabricated and the electrical contacts have been made, the sample is ready for electrical conductivity and Seebeck coefficient measurements (see Figure 1.20).

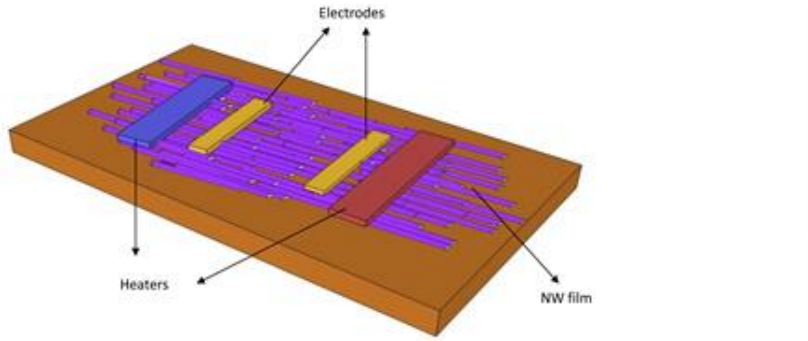

Figure 1.20. Schematic set up for electrical conductivity and Seebeck coefficient measurement of thermoelectric nanowires. Figure taken from reference [59].

The measurement of the electrical conductivity of these nanowire films can be performed with a setup configuration similar to the four-probe system using the heaters as electrodes, given the fact that they are in close contact with the sample and made of a conductive material. In this situation, the voltage drop along the thin film is measured when an electrical current is applied. The electrical conductivity of the nanowires can be obtained from the current-voltage curves (*I*-*V* curves), the thickness estimation of the thin film from Scanning Electron Images (SEM) and the use of a theoretical transport model that takes into account the electrical transport in nanowires. Using the same set up, the Seebeck coefficient of the nanowires can be determined. For that purpose, using the heaters, it is possible to apply a difference of temperature along the thin film. Then, with the aid of the electrodes, the Seebeck voltage generated in the film as a consequence of such temperature difference can be measured. Thus, the Seebeck coefficient of the nanowires can be calculated from $S = \Delta V / \Delta T$.

An advantage of this system compared to others is the possibility of fabricating the nanowires thin film and making the electrical contacts with more simple processes. Moreover, this technique is based on the four probe method, which avoids the contact and spreading resistance of the system. This set-up makes possible to measure not only the electrical conductivity, but the Seebeck coefficient of the whole film, from which later on the properties of single nanowires can be determined. However, one-dimensional electrical transport model must be used to obtain the properties of the nanowire, which can be complex, as well as the proper estimation of the film thickness.

1.2.3.2. Experimental setups for thermal conductivity measurements.

The measurement of the thermal conductivity of template-embedded arrays of nanowires can, in principle, be accomplished by a variety of methods, which range from steady state to AC current methods. Despite it is a very important area of research, it is still in its infancy and there is room for improvement through the development of new methodologies and/or through modifications of existing tools already in use for thin films or single-nanowires.

An approach recently used consists of determining the thermal conductivity of an array of Si nanowires from the Seebeck voltage of pressure-joined chip stacks. The device structure is composed by two stacks. The first one is made of a nanowire array composite pressed between metallic blocks. The second one is a bulk Si substrate of similar composition and size in the same configuration [115] (see Figure 1.21).

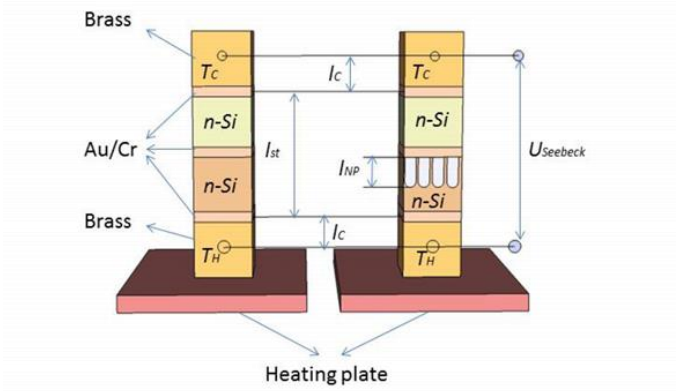

Figure 1.21. Schematic view of the experimental setup for Seebeck coefficient measurements of nanowire arrays. Figure taken from reference [59].

Then, both structures are placed on a heating plate that generates a temperature difference $T_H - T_C$ between the brass blocks of the stacks. When the temperature gradient is constant along the stacks, it is possible to measure the Seebeck voltage, $U_{Seebeck}$, generated by thermoelectric effects. A temperature loss is produced on account of the brass block and contact layers in the stacks. It causes a reduction in the

residual temperature gradient within the stack and therefore a reduced Seebeck voltage is expected according to,

$$\frac{U_{Seebeck}}{T_H - T_C} = \frac{S_{bulk}}{1 + 2\frac{k_{st}}{k_C}\frac{l_C}{l_{st}}} \tag{1.39}$$

where S_{bulk} is the Seebeck coefficient of the bulk sample, k_{st} and l_{st} the thermal conductivity and length of the stack, respectively, and k_C and l_C the thermal conductivity and length of the brass, respectively. Neglecting the thermal contact resistances between the blocks of the system and measuring $U_{Seebeck}/(T_H - T_C)$, the thermal resistance of the nanowire composite stack and bulk stack, l_{st}/k_{st} can be calculated.

Under the approximation of no heat conduction through the room temperature air and from the well-known bulk thermal conductivity, the thermal resistance of the nanowire array composite stack can be determined from the next equation,

$$\frac{l_{st}}{k_{st}} = \frac{l_{NW}}{\theta_{NW} k_{NW}} + \frac{l_{st} - l_{NW}}{k_{bulk}} \tag{1.40}$$

where l_{NW} is the length compression of the nano-wires and θ_{NW} is the coverage of the stack area fraction. From this expression, the thermal conductivity of the nano-wires, k_{NW} , is calculated. This setup configuration was employed to measure the thermal conductivity and Seebeck coefficient of arrays of silicon nanowires of 250 nm - 4 μm diameter at different temperature ranges. The thermal conductivity obtained for the nanowires was compared to the one measured with the 3ω-technique, made with a Wollastone tip. It was observed in both cases a reduction of less than 30% of the thermal conductivity in comparison to bulk silicon. The main drawback of this technique comes from the fact that different terms must be evaluated as carefully as possible, like the coverage of the it, evaluating stack area fractions or the compressed length of the nanowires, as they appear in Equation 1.40.

There is another approach, similar to the one described above, that was recently developed by Völklein *et al* [50]. It uses microfabricated structures in order to measure the cross-plane thermal conductivity of arrays of Bi nanowires. Electrodeposition was used to

grow Bi nanowires on top of a highly thermally conductive substrate. On top of the sample a thin dielectric layer is deposited ensuring the isolation to permit the patterning of electrical heaters and thermometers. In steady state conditions, the heaters are used to apply a temperature gradient with respect to the substrate, which is used as a heat sink. The ratio between the power released by the heater and the temperature difference across the sample represent the total thermal resistance which accounts for: the thermal resistance of the substrate, the thermal link introduced by the electrical leads used to contact the heaters and thermometers, the thermal boundary resistance between the different interfaces and, of course, the thermal resistance of the sample (both the template and the nanowires filling the pores). The thermal conductivity of the nanowires can be evaluated using a suitable reference that contains the empty template (air at atmospheric pressure filling the nano-channels). Complete suppression of the various interface resistances, to evaluate with sufficient accuracy the thermal conductivity of the nanowires, remains a challenge. Although these measurements can also be accomplished with the 3ω method, in general the steady-state method requires much lower electrical power density for the heater/thermometer and a less expensive/complex electrical measuring setup.

1.2.3.3. Direct measurement of the figure of merit of nanowire arrays.

As it was mentioned before, the efficiency of thermoelectric materials is associated to its figure of merit, z*T*, which is expressed as $zT = \frac{S^2\sigma}{k}T$, where S is the Seebeck coefficient, σ is the electrical conductivity; k is the thermal conductivity and T the absolute temperature.

The figure of merit of nanowire arrays can be measured with a single experimental setup using the approach developed by Harman[41, 42]. In the Harman method. The AC resistance (R_{ac}) of the composite and the DC voltage (V_{dc}) are measured when a low current (I_{dc}) is applied through the system. After that, the figure of merit of the sample can be determined through the equation $ZT = (V_{dc}/I_{dc} - R_{ac})/R_{ac}$. To carry out this experiment in nanowire arrays, a hybrid device, as shown in Figure 1.22, can be fabricated [142]. This device consists of a sample made of a nanowire array embedded in a matrix connected to a bulk element, of

similar size and composition of that of the nanowires, by a metal tab. It is usually preferable not to fill the whole length of the matrix with the thermoelectric material under study but instead deposit some metal on top of the nanowires that fill completely the matrix, so one can assure good electrical contact of the nanowires with the tab. Finally, voltage and current wires are soldered at the top and bottom sides of the metallic pads, which were added to the bulk and nanowire array samples (see Figure 1.22). Two thermocouples measure the temperature on the top and bottom of the nanowire array sample. The AC resistance of the composite is obtained from the nanowire composite-bulk AC resistance measurements after being extrapolated from the known properties of the bulk component[142].

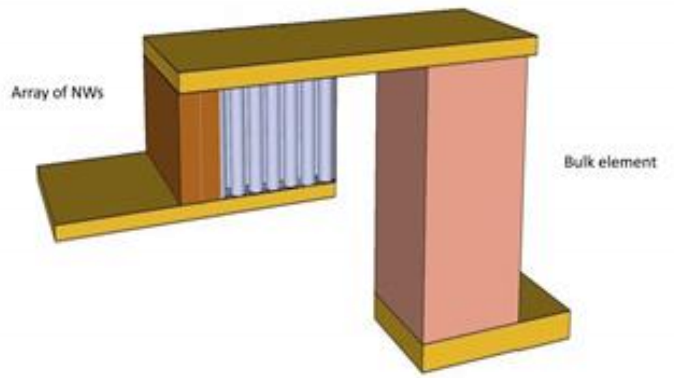

Figure 1.22. Schematic view of the hybrid nanowire-bulk device. Figure taken from reference [59].

The main disadvantage of this technique comes from the fact that one must fill most of the pores of the matrix, manage growing uniform length nanowires, and achieve good electrical contact simultaneously in all nanowires.

1.2.3.4. Nanowire arrays measurements by optical techniques.

In section 1.2.2.3. it was shown that in order to characterize single nanowire with optical techniques, it requires the placement of the nanowire in an appropriate microchip with electrical contacts at both ends of the nanowire in most cases. However, the measurement of nanowire arrays with optical techniques is more similar to bulk optical techniques, in which the main feature is that they provide a non-contact and non-destructive way for obtaining information about the material.

Furthermore, the experimental setups necessary for these kind of measurements are usually the same needed for standard bulk optical measurements without further adaptations. Due to the fact that in this situation the nanowire arrays do not require of electrical contacts or surface treatments, they can be measured without any extra preparation.

Nevertheless, the main disadvantage of these optical measurements is that certain characteristics of the nanowire array have to be known, like the optical absorption or the influence of the containing matrix in the measurement, among others. In general, it is also necessary to study an empty template and then a filled one to take into account the characteristics of the matrix. But in some cases, this is not enough, because it is also important to understand the interaction between the nanowire and the matrix. As a consequence, complex physical models to extract the actual parameters of the nanowires are needed, which leads in most cases to complex mathematical systems that have to be solved.

1.2.3.4.1. Thermal conductivity measurements.

The photo-acoustic is an optical technique that is based on the generation of acoustic waves in a medium caused by the absorption of modulated or pulsed electromagnetic radiation in a material. This absorbed radiation is then converted into thermal energy, provoking the material to warm up and cool down. As a consequence, it produces acoustic waves in the surrounding media. From the analysis of the amplitude and phase of this photo-acoustic signal, thermal parameters of the sample can be obtained. This optical technique is non-destructive or invasive and offers a direct way to measure thermal properties of the sample.

The photo-acoustic technique has been used to determine the thermal conductivity of bulk materials, films, and without any setup modification, nanowire arrays. However, the mathematical model used to obtain the thermal conductivity of the films or the nanowire arrays are complex and this can be considered as the main problem of the photo-acoustic technique. There are several parameters that must be carefully taken into account, such as the geometry of the structure that is being measured, the thermal and optical properties of the components of the sample and the thermal contact resistances between different layers of the structure. This theory must be applied to all the samples.

In the case of nanowire arrays, one can take the nanowire plus the matrix as an effective medium for the mathematical treatment of the data[38, 143, 144]. For instance, in reference[132] an array of Bi_2Te_3 nanowires embedded into a matrix (SU8 or alumina) is placed inside of a sealed acoustic chamber to be measured with the photo-acoustic technique (see Figure 1.23). In general, this chamber is filled with a certain gas, such as helium. A modulated laser is in charge of transferring thermal energy to the sample and its warming and cooling generates acoustic waves inside the chamber. Sometimes, the samples can be coated with a thin metal layer to increment the energy absorption of the laser radiation, but this is not compulsory. Then, the phase shift between the laser heating pulse and the acoustic response of the sample is measured with a microphone mounted in the side of the wall, which carries information of the thermal conductivity of the sample. The amplitude and phase shift of the measured signal have to be analyzed using a one dimensional thermal model in order to determine the thermal conductivity of the sample under study. In this particular case, values of 1.4 ± 0.07 W/m·K and 1.1 ±0.06 W/m·K were obtained for Bi_2Te_3 nanowire arrays embedded in alumina and SU8, respectively. This thermal conductivity results corresponds to the matrix plus nanowire medium. Getting the actual value of the thermal conductivity of the Bi_2Te_3 nanowires is not a straightforward step and it requires of the use of the effective medium theory. The parameters that one has to take into account to use this theory are the matrix thermal conductivity and its porosity, the filling factor (that is, how many pores are filled with a nanowire). Using this theory the thermal conductivity of the nanowires was determined to be 1.4±0.1 W/m·K.

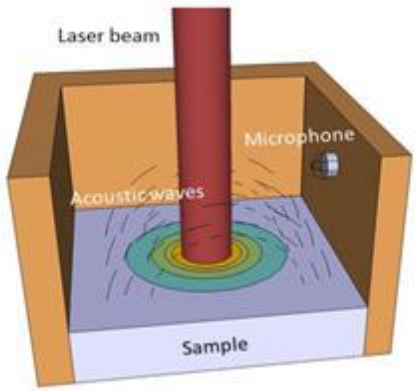

Figure 1.23. Schematic set up of the photo-acoustic technique. Figure taken from reference [59].

The photo-thermoelectric technique[145-147] is another optical technique that makes possible to obtain the thermal diffusivity coefficient of nanowire arrays embedded in a matrix. The basis is very similar to the photo-acoustic technique, that is, a modulated laser warms the surface of a sample and the temperature changes at its backside are recorded (see Figure 1.24). In the case of nanowire arrays measurement, one side of the nanowire array is hit by the laser while in the other side a thermocouple junction is formed between this surface and a constantan wire. A metallic layer, such as gold, is deposited on the backside of the sample in order to ensure good temperature measurements at the backside of the nanowire array, and therefore good thermocouple connection. Then, the amplitude and phase of the thermocouple voltage are measured.

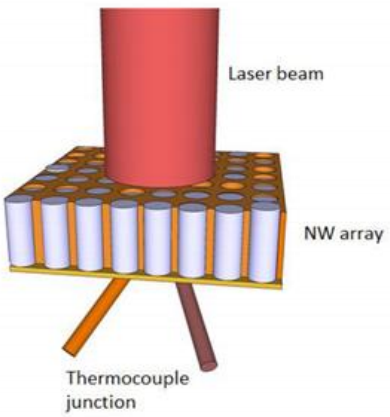

Figure 1.24. Schematic view of the photo-thermoelectric set up. Figure taken from reference [59].

In order to determine the thermal conductivity of the nanowires, the experimental data are fitted with a two dimensional heat conduction model and the heat capacity of the sample is obtained from effective medium theory, where the contribution from the alumina, the pore density and the filling factor must be considered. Therefore, unfilled alumina templates were also measured to determine their heat capacity and then the thermal diffusivity of the nanowires. However, if the thermal diffusivity of the nanowires and the matrix are similar, as it is the case for Bi_2Te_3 nanowires embedded in alumina matrices[145], this does not lead to reliable measurements and the uncertainty associated with the resulting values might be quite high.

Table 1.III. Summary of the different techniques for measuring transport properties of single nanowires and nanowire arrays with advantages and disadvantages.Taken from reference [59].

<table>
<tr><td rowspan="3">Electrical based</td><td rowspan="2">Single NW</td><td>μ-chips on substrates</td><td>2 point contacts</td><td>4point contacts</td></tr>
<tr><td></td><td> 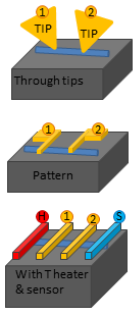

-Electrical Conductance through IV curves.
-Thermal conductivity indirects estimation: Wiedemann Franz law.
-Seebeck coefficient using Steady State method.

MERITS
-Easy achievement of electrical contact or fabrication of contact electrodes.

DEMERITS
-Do not discriminate for electrical contact resistance.
- Only electrical & high thermal conductive NW compared to substrate conductivity.</td><td> 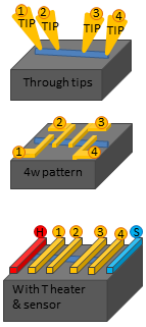

-Electrical Conductance through IV curves.
-Thermal conductivity using AC methods.
-Seebeck coefficient using Steady State method.

MERITS
-Easy achievement of electrical contact or fabrication of contact electrodes.
- Accounts for electrical contact Resistance.

DEMERITS
- Difficult to evaluate Thermal boundaries Resistances at the contacts.
- Only electrical & high thermal conductive NW compared to substrate conductivity.</td></tr>
<tr><td>μ-Chips Suspended Structures</td><td> 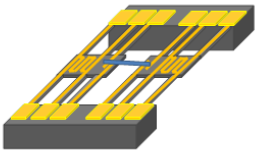
 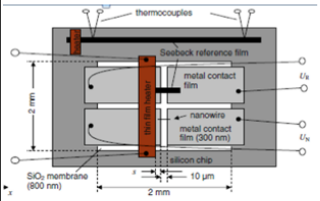
</td><td colspan="2">-Electrical Conductance through IV curves.
-Thermal conductivity using steady state.
-Seebeck coefficient using steady state methods or ac method.

MERITS
-Good configuration to measure electrical conductance evaluating electrical contact.
- Very good thermal isolation to achieve ultra-high sensitivities in measuring thermal conductivities (10pW/K).

DEMERITS
- Very complex microfabricated structures.
- Difficult sample placement.
- Requires deposition of extra materials on the contacts to reduced electrical contact resistance and thermal boundary resistances.
- Thermal boundary resistance suppression requires systematic studies as function of NW length.</td></tr>
<tr><td>Arrays</td><td> 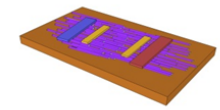
 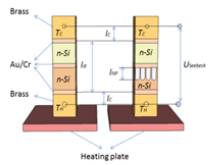

 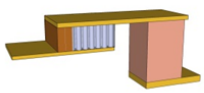 </td><td colspan="2">-Electrical Conductance through IV curves.
-Thermal conductivity using both steady state or ac methods.
-Seebeck coefficient using steady state methods.

MERITS
- Electrical conductance and Seebeck coefficient measurements may be achived with a simple configuration.
- A wide variety of alternative set-ups that provide other ways of measuring NW arrays transport properties.
- Hybrid nanowire-bulk device permits the direct measurement of the nanowire array.

DEMERITS
- Extraction of the NW transport properties from NW estimations a posterior and using 1D transport model.
- Considerable influence of interface and contact resistances in some set-ups.
- Hybrid nanowire-bulk device requires of uniform length nanowires and good electrical contact in all of them.</td></tr>
</table>

SPMs based

Single NW out of the matrix

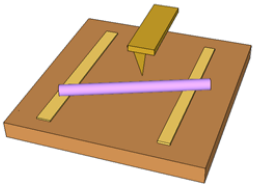

-**Electrical Conductance** through the study of the voltage drop along the NW length with KPM or STM.

-**Density of states and Fermi level** with a STM.

MERITS
- High spatial resolution to examine samples at the atomic level.
- Localized and specific measurements with high accuracy.

DEMERITS
- STM technique requires of low scan speed, conducting samples, very sensitive to mechanical and acoustic vibrations and a high vacuum chamber.
- KPM technique involve complex probe fittings when measuring and signal distortion when tip touches the surface.

Single NW inside the matrix

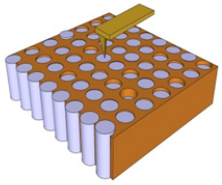

-**Electrical Conductance** through IV curves with an AFM.

-**Thermal conductivity** using SThM .

MERITS
- Avoidance of effects of oxidation or chemical exposure of the nanowire
- High spatial resolution and high accurate measurements.
- Non destructive techniques.

DEMERITS
- Properties of the NW are extracted mostly with theoretical models.
- Electrical and thermal contact resistances must be properly considered.

Optical based

Single NW

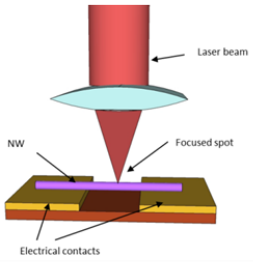

-**Electrical Conductance** measuring the current created under illumination.

-**Thermal conductivity.** A laser beam heats locally the sample and throught microluminscence or microraman a map of the temperature at the surface of the nanowire is made .

MERITS
- Non invasive.
- Local resolution.

DEMERITS
- Necessary to place the single nanowires onto microchips.
- Electrical contacts have to be made.

Arrays

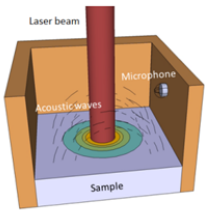

-**Thermal conductivity** with the photo-acoustic technique or the photo-thermal technique.

MERITS
- Non-invasive.
- Same set-up for bulk, films or nanowire array measurement.

DEMERITS
- Complicated mathematical model that takes into account many material parameters from both the NWs and the matrix.
- The effective medium theory has to be used, taking into account the pore density, filling factor, and so on to extract information from the NWs themselves.

1.3. Thesis objectives.

This PhD work is focused on the determination and understanding of the electrical and thermal properties of thin films, nanowires and other nanostructures with thermoelectric properties.

The main objective is to study how the reduction in the dimensionality of the material affects its transport properties in inorganic and organic materials. For that purpose, the scanning probe microscopy has been used as the main working instrument to measure experimentally and locally the transport properties of those nanostructures. Nevertheless, other techniques, such as the four probe station or the Seebeck Microprobe were also used. In most cases the candidate has carried out simulations in order to support, understand and/or validate my experimental measurements. The results of the transport properties obtained for nanostructures with different shapes and sizes required of physical explanations that were carefully considered in each case. In Chapter 2 all the experimental techniques used to fabricate, structurally characterize and measure experimentally the transport properties of the different nanostructures are shown. Finally, in Chapter 3 and Chapter 4, the thermal and electrical conductivity of those samples are presented within a deep physical explanation for such particular transport properties, respectively.

References

1. D. M. Rowe, *CRC Thermoelectrics Handbook: Macro to Nano.*, CRC Press, Broken Sound Parkway NW, 2005.
2. D. J. Griffiths, *Introduction to Electrodynamics*, Prentice Hall, 1999.
3. G. D. Mahan and J. O. Sofo, *Proceedings of the National Academy of Sciences*, 1996, **93**, 7436-7439.
4. C. Kittel, *Introduction to Solid State Physics*, Wiley, 2004.
5. S. Datta, *Lessons from Nanoelectronics: A New Perspective on Transport*, World Scientific Publishing Company, 2012.
6. H. Bottner, J. Nurnus, A. Gavrikov, G. Kuhner, M. Jagle, C. Kunzel, D. Eberhard, G. Plescher, A. Schubert and K. H. Schlereth, *Journal of Microelectromechanical Systems*, 2004, **13**, 414-420.
7. M. Lundstrom, C. Jeong and R. Kim, *Near-equilibrium Transport: Fundamentals and Applications*, World Scientific, 2013.
8. T. Tritt, *Advances in Thermoelectric Materials I*, Elsevier Science, 2000.
9. T. M. Tritt and M. A. Subramanian, *MRS Bulletin*, 2006, **31**, 188-198.
10. A. Shakouri, *Annual Review of Materials Research*, 2011, **41**, 399-431.
11. M. D. Rowe, G. Min and K. S. Williams, *An up-date on the thermoelectric recovery of low temperature waste heat*, World renewable energy congress (GBR), Pergamon, Amsterdam, PAYS-BAS, 2000.
12. K. Biswas, J. He, I. D. Blum, C.-I. Wu, T. P. Hogan, D. N. Seidman, V. P. Dravid and M. G. Kanatzidis, *Nature*, 2012, **489**, 414-418.
13. M. M.-González, O. C.-Calero and P. D.-Chao, *Renewable and Sustainable Energy Reviews*, 2013, **24**, 288-305.
14. G. J. Snyder and E. S. Toberer, *Nature Materials*, 2008, **7**, 105-114.
15. A. P. Gonçalves and C. Godart, *Eur. Phys. J. B*, 2014, **87**, 1-29.
16. Z.-G. Chen, G. Han, L. Yang, L. Cheng and J. Zou, *Progress in Natural Science: Materials International*, 2012, **22**, 535-549.
17. M. Culebras, C. M. Gómez and A. Cantarero, *Materials*, 2014, **7**, 6701-6732.

18. M. M. Rojo, J. Martin, S. Grauby, T. Borca-Tasciuc, S. Dilhaire and M. Martin-Gonzalez, *Nanoscale*, 2014, **6**, 7858-7865.
19. C. V. Manzano, A. Rojas, M. Decepida, B. Abad, Y. Feliz, O. Caballero-Calero, D. A. Borca-Tasciuc and M. Martin-Gonzalez, *J Solid State Electrochem*, 2013, **17**, 2071-2078.
20. H.-J. Kim, H.-B. Bae, Y. Park, K. Lee and S. H. Choi, *Journal of Crystal Growth*, 2012, **353**, 124-128.
21. A. Jacquot, N. Farag, M. Jaegle, M. Bobeth, J. Schmidt, D. Ebling and H. Böttner, *Journal of Electronic Materials*, 2010, **39**, 1861-1868.
22. G. Joshi, H. Lee, Y. Lan, X. Wang, G. Zhu, D. Wang, R. W. Gould, D. C. Cuff, M. Y. Tang, M. S. Dresselhaus, G. Chen and Z. Ren, *Nano Letters*, 2008, **8**, 4670-4674.
23. P. V. Pesavento, R. J. Chesterfield, C. R. Newman and C. D. Frisbie, *Journal of Applied Physics*, 2004, **96**, 7312-7324.
24. A. Mavrokefalos, M. T. Pettes, F. Zhou and L. Shi, *Review of Scientific Instruments*, 2007, **78**, 034901.
25. A. A. Ramadan, R. D. Gould and A. Ashour, *Thin Solid Films*, 1994, **239**, 272-275.
26. Y. SINGH, *International Journal of Modern Physics: Conference Series*, 2013, **22**, 745-756.
27. T. M. Tritt, *Thermal Conductivity: Theory, Properties, and Applications*, Springer2004.
28. F. Völklein and E. Kessler, *physica status solidi (a)*, 1984, **81**, 585-596.
29. J.-H. Bahk, T. Favaloro and A. Shakouri, *Annual Review of Heat Transfer*, 2013, **16,** 51-99.
30. S. R. Sarath Kumar and S. Kasiviswanathan, *Review of Scientific Instruments*, 2008, **79**, 024302.
31. O. Boffoué, A. Jacquot, A. Dauscher, B. Lenoir and M. Stölzer, *Review of Scientific Instruments*, 2005, **76**, 053907.
32. J. Ravichandran, J. T. Kardel, M. L. Scullin, J.-H. Bahk, H. Heijmerikx, J. E. Bowers and A. Majumdar, *Review of Scientific Instruments*, 2011, **82**, 015108.
33. B. Yang, W. L. Liu, J. L. Liu, K. L. Wang and G. Chen, *Applied Physics Letters*, 2002, **81**, 3588-3590.
34. R. Venkatasubramanian, E. Siivola, T. Colpitts and B. O'Quinn, *Nature*, 2001, **413**, 597-602.
35. H. H. Berger, *Solid-State Electronics*, 1972, **15**, 145-158.
36. R. H. Cox and H. Strack, *Solid-State Electronics*, 1967, **10**, 1213-1218.

37. L. M. Surhone, M. T. Timpledon and S. F. Marseken, *Time-Domain Thermoreflectance*, VDM Publishing, 2010.
38. H. Hu, X. Wang and X. Xu, *Journal of Applied Physics*, 1999, **86**, 3953-3958.
39. D. P. Almond and P. Patel, *Photothermal Science and Techniques*, Springer, 1996.
40. M. Muñoz Rojo, J. J. Romero, D. Ramos, D.-A. Borca-Tasciuc, T. Borca-Tasciuc and M. Martín Gonzalez, *International Journal of Thermal Sciences*, 2015, **89**, 193-202.
41. T. C. Harman and Harman, *Journal of applied physics*, 1958, **29**, 1373-1374.
42. T. C. Harman and Harman, *Journal of applied physics*, 1958, **29**, 1471-1473.
43. H. Iwasaki and H. Hori, *24th International Conference on Thermoelectrics*, 2005, 501-504.
44. H. Iwasaki, M. Koyano and H. Hori, *Japanese journal of applied physics*, 2002, **41**, 6606-6609.
45. H. Iwasaki, S. Y. Yokoyama, T. Tsukui, M. Koyano and H. Hori, *Japanese journal of applied physics*, 2003, **42**, 3707-3708.
46. S. Fujimoto, H. Kaibe, S. Sano and T. Kajitani, *Japanese journal of applied physics*, 2006, **45**, 8805-8809.
47. E. Castillo, C. Hapenciuc and T. Borca Tasciuc, *Review of scientific instruments*, 2010, **81**, 044902.
48. R. Singh, Z. Bian, A. Shakouri, G. Zeng and J.-H. Bahk, *Applied physics letters*, 2009, **94**, 212508.
49. R. Singh, Z. Bian, G. Zeng, J. Zide and J. Christofferson, *Materials Research society symposium proceedings*, 2006, **886**, 123-128.
50. D. Huzel, H. Reith, M. C. Schmitt, O. Picht, S. Müller, M. E. Toimil-Molares and F. Völklein, in *Nanowires - Implementations and Applications*, ed. A. Hashim, Intech2011, vol. 1, ch. 14.
51. F. Völklein, H. Reith, M. C. Schmitt, M. Huth, M. Rauber and R. Neumann, *Journal of Electronic Materials*, 2010, **39**, 1950-1956.
52. F. Völklein, M. Schmitt, T. W. Cornelius, O. Picht, S. Müller and R. Neumann, *Journal of Electronic Materials*, 2009, **38**, 1109-1115.
53. Y. Tian, M. R. Sakr, J. M. Kinder, D. Liang, M. J. MacDonald, R. L. J. Qiu, H.-J. Gao and X. P. A. Gao, *Nano Letters*, 2012, **12**, 6492-6497.

54. J. Heremans and C. M. Thrush, *Physical Review B*, 1999, **59**, 12579-12583.
55. C. Li, E. Krali, K. Fobelets, B. Cheng and Q. Wang, *Applied Physics Letters*, 2012, **101**, 222101-222103.
56. L. Deyu, A. L. Prieto, W. Yiying, M. S. Martin-Gonzalez, A. Stacy, T. Sands, R. Gronsky, Y. Peidong and A. Majumdar, Measurements of Bi_2Te_3 nanowire thermal conductivity and Seebeck coefficient, 2002, 333-336.
57. A. I. Boukai, Y. Bunimovich, J. Tahir-Kheli, J.-K. Yu, W. A. Goddard Iii and J. R. Heath, *Nature*, 2008, **451**, 168-171.
58. K. M. Lee, T. Y. Choi, S. K. Lee and D. Poulikakos, *Nanotechnology*, 2010, **21**, 125301.
59. M. Muñoz Rojo, O. Caballero Calero, A. F. Lopeandia, J. Rodriguez-Viejo and M. Martin-Gonzalez, *Nanoscale*, 2013, **5**, 11526-11544.
60. J. Zhou, C. Jin, J. H. Seol, X. Li and L. Shi, *Applied Physics Letters*, 2005, **87**, 133109.
61. J. H. Seol, A. L. Moore, S. K. Saha, F. Zhou, L. Shi, Q. L. Ye, R. Scheffler, N. Mingo and T. Yamada, *Journal of Applied Physics*, 2007, **101**, 023706.
62. W. Liang, O. Rabin, A. Hochbaum, M. Fardy, M. Zhang and P. Yang, *Nano Res.*, 2009, **2**, 394-399.
63. A. I. Hochbaum, R. Chen, R. D. Delgado, W. Liang, E. C. Garnett, M. Najarian, A. Majumdar and P. Yang, *Nature*, 2008, **451**, 163-167.
64. M. Fardy, A. I. Hochbaum, J. Goldberger, M. M. Zhang and P. Yang, *Advanced Materials*, 2007, **19**, 3047-3051.
65. Y. Long, Z. Chen, W. Wang, F. Bai, A. Jin and C. Gu, *Applied Physics Letters*, 2005, **86**, 153102.
66. A. Boukai, K. Xu and J. R. Heath, *Advanced Materials*, 2006, **18**, 864-869.
67. Y. Long, J. Duvail, M. Li, C. Gu, Z. Liu and S. Ringer, *Nanoscale Res Lett*, 2010, **5**, 237-242.
68. H. Suzuki, H. Araki, M. Tosa and T. Noda, *Chemical Physics Letters*, 2009, **468**, 211-215.
69. A. S. Walton, C. S. Allen, K. Critchley, M. L. Górzny, J. E. M. c. Kendry, R. M. D. Brydson, B. J. Hickey and S. D. Evans, *Nanotechnology*, 2007, **18**, 065204.
70. K.-K. Lew, L. Pan, T. E. Bogart, S. M. Dilts, E. C. Dickey, J. M. Redwing, Y. Wang, M. Cabassi, T. S. Mayer and S. W. Novak, *Applied Physics Letters*, 2004, **85**, 3101-3103.

71. S. B. Cronin, Y.-M. Lin, O. Rabin, M. R. Black, J. Y. Ying, M. S. Dresselhaus, P. L. Gai, J.-P. Minet and J.-P. Issi, *Nanotechnology*, 2002, **13**, 653.
72. X. Duan, Y. Huang, Y. Cui, J. Wang and C. M. Lieber, *Nature*, 2001, **409**, 66-69.
73. F. Zhiyong, M. Xiaoliang, L. Chengfei, Y. Yan, W. Dawei, C. Guorong and J. G. Lu, *Nanotechnology, IEEE Transactions on*, 2005, **4**, 238-241.
74. M. T. Chang, L. J. Chou, C. H. Hsieh, Y. L. Chueh, Z. L. Wang, Y. Murakami and D. Shindo, *Advanced Materials*, 2007, **19**, 2290-2294.
75. A. L. Schmitt, L. Zhu, D. Schmeiβer, F. J. Himpsel and S. Jin, *The Journal of Physical Chemistry B*, 2006, **110**, 18142-18146.
76. S. C. Andrews, M. A. Fardy, M. C. Moore, S. Aloni, M. Zhang, V. Radmilovic and P. Yang, *Chemical Science*, 2011, **2**, 706-714.
77. Y. M. Zuev, J. S. Lee, C. m. Galloy, H. Park and P. Kim, *Nano Letters*, 2010, **10**, 3037-3040.
78. C.-H. Lee, G.-C. Yi, Y. M. Zuev and P. Kim, *Applied Physics Letters*, 2009, **94**, 022106-022103.
79. Y.-M. Lin, O. Rabin, S. B. Cronin, J. Y. Ying and M. S. Dresselhaus, *Applied Physics Letters*, 2002, **81**, 2403-2405.
80. L. Li, Y. W. Yang, X. H. Huang, G. H. Li, R. Ang and L. D. Zhang, *Applied Physics Letters*, 2006, **88**, 103119-103113.
81. M. Elawayeb, Y. Peng, K. Briston and B. Inkson, *Journal of applied physics*, 2012, **111**, 034306.
82. M. Sakurai, Y. G. Wang, T. Uemura and M. Aono, *Nanotechnology*, 2009, **20**, 155203.
83. X. Ou, P. Das Kanungo, R. Koegler, P. Werner, U. Goesele, P. Kanungo, R. Kagler, U. Gasele, W. Skorupa and X. Wang, *Advanced materials*, 2010, **22**, 4020-4024.
84. E. C. Garnett, Y.-C. Tseng, D. R. Khanal, J. Wu, J. Bokor and P. Yang, *Nature Nanotechnology*, 2009, **4**, 311-314.
85. D. G. Cahill and R. O. Pohl, *Physical Review B*, 1987, **35**, 4067-4073.
86. D. G. Cahill and Cahill, *Review of scientific instruments*, 1990, **61**, 802-808.
87. D. G. Cahill, M. Katiyar and J. R. Abelson, *Physical Review B*, 1994, **50**, 6077-6081.
88. T. Tong and A. Majumdar, *Review of Scientific Instruments*, 2006, **77**, 104902.

89. L. Lu, W. Yi and D. L. Zhang, *Review of Scientific Instruments*, 2001, **72**, 2996-3003.
90. L. Shi, D. Li, C. Yu, W. Jang, D. Kim, Z. Yao, P. Kim and A. Majumdar, *Journal of Heat Transfer*, 2003, **125**, 881-888.
91. E. K. Lee, L. Yin, Y. Lee, J. W. Lee, S. J. Lee, J. Lee, S. N. Cha, D. Whang, G. S. Hwang, K. Hippalgaonkar, A. Majumdar, C. Yu, B. L. Choi, J. M. Kim and K. Kim, *Nano Letters*, 2012, **12**, 2918-2923.
92. D. Li, Y. Wu, P. Kim, L. Shi, P. Yang and A. Majumdar, *Applied Physics Letters*, 2003, **83**, 2934-2936.
93. J. W. Roh, S. Y. Jang, J. Kang, S. Lee, J.-S. Noh, W. Kim, J. Park and W. Lee, *Applied Physics Letters*, 2010, **96**, 103101-103103.
94. A. L. Moore, M. T. Pettes, F. Zhou and L. Shi, *Journal of Applied Physics*, 2009, **106**, 034310-034317.
95. R. Chen, A. I. Hochbaum, P. Murphy, J. Moore, P. Yang and A. Majumdar, *Physical Review Letters*, 2008, **101**, 105501.
96. F. Zhou, J. Szczech, M. T. Pettes, A. L. Moore, S. Jin and L. Shi, *Nano Letters*, 2007, **7**, 1649-1654.
97. M. Wingert, S. Kwon, J. Xiang and R. Chen, *Review of Scientific Instruments*, 2012, **83**, 024901.
98. J. Chen, G. Zhang and B. Li, *The Journal of Chemical Physics*, 2011, **135**, 104508.
99. J. Yang, S. Waltermire, Y. Chen, A. Zinn and T. Xu, *Applied Physics Letters*, 2010, **96**, 023109.
100. F. Zhou, A. L. Moore, J. Bolinsson, A. Persson, L. Fröberg, M. T. Pettes, H. Kong, L. Rabenberg, P. Caroff, D. A. Stewart, N. Mingo, K. A. Dick, L. Samuelson, H. Linke and L. Shi, *Physical Review B*, 2011, **83**, 205416.
101. Y.-H. Park, J. Kim, H. Kim, I. Kim, K.-Y. Lee, D. Seo, H.-J. Choi and W. Kim, *Appl. Phys. A*, 2011, **104**, 7-14.
102. F. Völklein, H. Reith, T. W. Cornelius, M. Rauber and R. Neumann, *Nanotechnology*, 2009, **20**, 325706.
103. N. Stojanovic, J. M. Berg and M. Holtz, *Applied Physics Letters*, 2009, **95**, 091905.
104. P. D. C. O. Caballero Calero, Marisol Martín Gonzalez, *Renewable & Sustainable Energy Reviews,* 2013, **24,** 288-305.
105. K. Kirihara, T. Sasaki, N. Koshizaki and K. Kimura, *Applied Physics Express*, 2011, **4**, 041201.
106. L. D. Hicks and M. S. Dresselhaus, *Physical Review B*, 1993, **47**, 12727-12731.

107. M. S. Dresselhaus, G. Chen, M. Y. Tang, R. G. Yang, H. Lee, D. Z. Wang, Z. F. Ren, J. P. Fleurial and P. Gogna, *Advanced Materials*, 2007, **19**, 1043-1053.
108. Y. Kim, L. Cagnon, U. Goesele and J. Lee, *Physica Status Solidi. Rapid research letters*, 2010, **4**, 43-45.
109. D. D. D. Ma, C. S. Lee and S. T. Lee, *Applied Physics Letters*, 2001, **79**, 2468-2470.
110. J. G. Park, S. H. Lee, B. Kim and Y. W. Park, *Applied Physics Letters*, 2002, **81**, 4625-4627.
111. J. Colchero, A. Gil and A. M. Baró, *Physical Review B*, 2001, **64**, 245403.
112. E. Koren, Y. Rosenwaks, J. E. Allen, E. R. Hemesath and L. J. Lauhon, *Applied Physics Letters*, 2009, **95**, 092105-092103.
113. S. Vinaji, A. Lochthofen, W. Mertin, I. Regolin, C. Gutsche, K. Blekker, W. Prost, F. J. Tegude and G. Bacher, *AIP Conference Proceedings*, 2010, **1199**, 329-330.
114. S. Vinaji, A. Lochthofen, W. Mertin, I. Regolin and C. Gutsche, *Nanotechnology*, 2009, **20**, 385702.
115. A. Stranz, *Journal of Materials Research*, 2011, **26**, 1958.
116. S. Lefèvre, S. Volz and P.-O. Chapuis, *International Journal of Heat and Mass Transfer*, 2006, **49**, 251-258.
117. D. G. Cahill, *Review of Scientific Instruments*, 2002, **73**, 3701-3701.
118. E. Puyoo, S. Grauby, J.-M. Rampnoux, E. Rouviere and S. Dilhaire, *Review of Scientific Instruments*, 2010, **81**, 073701-073705.
119. E. Puyoo, S. Grauby, J.-M. Rampnoux, E. Rouviere and S. Dilhaire, *Journal of Applied Physics*, 2011, **109**, 024302-024309.
120. M. Muñoz-Rojo, S. Grauby, J. M. Rampnoux, O. Caballero-Calero, M. Martin-Gonzalez and S. Dilhaire, *Journal of Applied Physics*, 2013, **113**, 054308-054307.
121. J. E. Allen, D. E. Perea, E. R. Hemesath and L. J. Lauhon, *Advanced Materials*, 2009, **21**, 3067-3072.
122. Y. Gu, J. P. Romankiewicz, J. K. David, J. L. Lensch and L. J. Lauhon, *Nano Letters*, 2006, **6**, 948-952.
123. X. F. Liu, R. Wang, Y. P. Jiang, Q. Zhang, X. Y. Shan and X. H. Qiu, *Journal of Applied Physics*, 2010, **108**, 054310-054314.
124. M. Soini, I. Zardo, E. Uccelli, S. Funk, G. Koblmuller, A. Fontcuberta i Morral and G. Abstreiter, *Applied Physics Letters*, 2010, **97**, 263107-263103.

125. G. S. Doerk, C. Carraro and R. Maboudian, *ACS Nano*, 2010, **4**, 4908-4914.
126. I. K. Hsu, R. Kumar, A. Bushmaker, S. B. Cronin, M. T. Pettes, L. Shi, T. Brintlinger, M. S. Fuhrer and J. Cumings, *Applied Physics Letters*, 2008, **92**, 063119-063113.
127. M. Martín-González, A. L. Prieto, R. Gronsky, T. Sands and A. M. Stacy, *Advanced Materials*, 2003, **15**, 1003-1006.
128. M. Martín-González, A. L. Prieto, M. S. Knox, R. Gronsky, T. Sands and A. M. Stacy, *Chemistry of Materials*, 2003, **15**, 1676-1681.
129. M. Martín-González, G. J. Snyder, A. L. Prieto, R. Gronsky, T. Sands and A. M. Stacy, *Nano Letters*, 2003, **3**, 973-977.
130. C.-L. Chen, Y.-Y. Chen, S.-J. Lin, J. C. Ho, P.-C. Lee, C.-D. Chen and S. R. Harutyunyan, *The Journal of Physical Chemistry C*, 2010, **114**, 3385-3389.
131. I. Enculescu, Z. Siwy, D. Dobrev, C. Trautmann, M. E. Toimil Molares, R. Neumann, K. Hjort, L. Westerberg and R. Spohr, *Appl. Phys. A*, 2003, **77**, 751-755.
132. K. G. Biswas, T. D. Sands, B. A. Cola and X. Xu, *Applied Physics Letters*, 2009, **94**, 223116-223113.
133. W. Wang, F. Jia, Q. Huang and J. Zhang, *Microelectronic Engineering*, 2005, **77**, 223-229.
134. E. J. Menke, M. A. Brown, Q. Li, J. C. Hemminger and R. M. Penner, *Langmuir*, 2006, **22**, 10564-10574.
135. J. Sommerlatte, L. Cagnon, D. Bourgault, U. Gosele and K. Nielsch, Ordered nanowires based on V-VI materials: From synthesis in organic electrolytes to electrical characterization, 2007.
136. F. Xiao, B. Yoo, K.-H. Lee and N. Myung, *Nanotechnology*, 2007, **18**, 335203.
137. W. Wang, Q. Huang, F. Jia and J. Zhu, *Journal of Applied Physics*, 2004, **96**, 615-618.
138. B. Xu, C. Li, K. Thielemans, M. Myronov and K. Fobelets, *IEEE Transactions on Electron Devices*, 2012, **59**, 3193-3198.
139. L. Li, Y. Yang, X. Huang, G. Li and L. Zhang, *Nanotechnology*, 2006, **17**, 1706.
140. G. Tai, W. Guo and Z. Zhang, *Crystal Growth & Design*, 2008, **8**, 2906-2911.
141. G. a. Tai, B. Zhou and W. Guo, *The Journal of Physical Chemistry C*, 2008, **112**, 11314-11318.

142. J. Keyani, A. M. Stacy and J. Sharp, *Applied Physics Letters*, 2006, **89**, 233106-233103.
143. X. W. Wang, H. P. Hu and X. F. Xu, *Journal of Heat Transfer*, 2001, **123**, 138-144.
144. B. A. Cola, J. Xu, C. Cheng, X. Xu, T. S. Fisher and H. Hu, *Journal of Applied Physics*, 2007, **101**, 054313-054319.
145. D. A. Borca-Tasciuc, G. Chen, A. Prieto, M. S. Martin-Gonzalez, A. Stacy, T. Sands, M. A. Ryan and J. P. Fleurial, *Applied Physics Letters*, 2004, **85**, 6001-6003.
146. D.-A. Borca-Tasciuc, G. Chen, M. S. Martin-Gonzales, A. L. Prieto, A. Stacy and T. Sands, *ASME Conference Proceedings*, 2002, **2**, 193-194.
147. T. Borca-Tasciuc, D. A. Borca-Tasciuc and C. Gang, *A photo-thermoelectric technique for anisotropic thermal diffusivity characterization of nanowire/nanotube composites*, Symposium IEEE, 2005.

Chapter 2

Experimental Methodology

This chapter is divided into two sections. The first one (section 2.1.) is focused on the fabrication, preparation and structural characterization techniques that were used to obtain films, nanowires and other nano-structures, whose physical properties are of interest. Secondly, (section 2.2.) the techniques used to measure the transport properties of those structures are explained.

2.1. Samples fabrication, preparation and structural characterization techniques.

2.1.1. Fabrication techniques.

In this work, the samples that are going to be the subject of our study are: a) Bi_2Te_3 films and nanowires, b) Silicon Germanium films and c) Polymeric films and nanowires. This section summarizes the techniques used to grow them. The samples growth work was carried out by different members of our group at the Instituto de Microelectrónica de Madrid (IMM-CSIC). But it has been considered important to summarize all the techniques used for sample growth in this chapter, since their growth parameters will be used to understand the thermoelectric measurements.

2.1.1.1. Electrodeposition.

Electrodeposition[1] is an electro-chemical process in which the ions from a solution (electrolyte) are reduced when enough voltage is applied across two electrodes. This reduction causes the deposition of the ions, M, on a conductive substrate (cathode) according to the reaction, $M^{n+} + ne^{-} \leftrightarrow M$.

For that purpose, it was used an electrochemical cell that consists of three electrodes: a) working-electrode (WE), b) counter-electrode (CE) and c) the reference-electrode (RE). The working electrode is a conductive substrate and acts like the cathode, and in our case it will be made of gold (Au), platinum (Pt) or Fluorine doped Tin Oxide (FTO), depending on the samples. The counter-electrode is Pt that acts as anode. The reference-electrode is Ag/AgCl (saturated KCl) and it is used to control the applied voltage. Figure 2.1a and 2.1b shows a schematic view of the electrochemical cell used and the reaction involved.

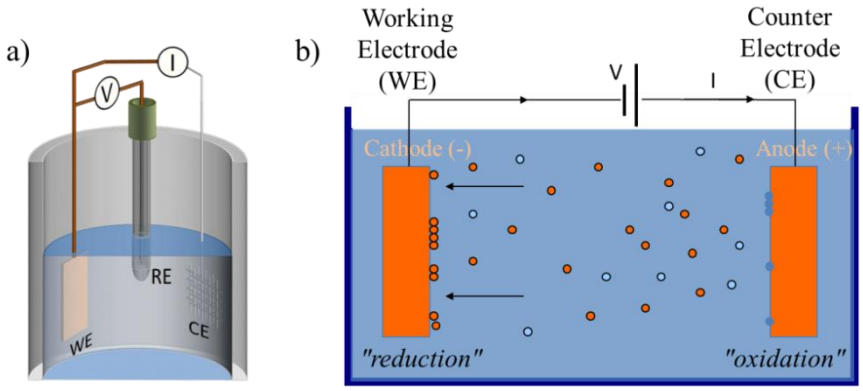

Figure 2.1. a) Electrochemical cell used to grow films, nanowires and other structures. b) Simplified schematic description of the reaction carried out in an electrochemical cell.

There are two electrodeposition working modes: a) potentiostatic, which consists of controlling the voltage applied and measured the current, or b) galvanostatic, in which the amplitude of the current applied is controlled and the voltage is measured. The potentiostatic mode was the one used to grow Bi_2Te_3 samples measured in this work. The nanostructuration of the material has been carried out by using porous alumina templates and photoresists. When using AAOs, the electrodeposition was template-assisted, using the pores of the AAOs as individual electrochemical nano-cell in which the nanowires grew. The samples presented were optimized by Dra. Cristina Vicente and Dra. Olga Caballero from our group. Other nano-structures were made using the photoresist templates, which were fabricated by me using lithography processes similar to those presented in Section 2.1.2.1.

2.1.1.2. Sputtering.

The sputtering [2] is a physical deposition method that consists of bombarding a target with energetic particles, i.e. plasma, which involves an ejection of atoms that are then deposited on a selected substrate. It is commonly used for etching, thin film deposition and analytical techniques.

This technique was used to grow Silicon Germanium films. For that purpose, a target of Silicon Germanium (SiGe), which works as anode, is blasted with inert gas ions (Ar 99.999% pure) on a vacuum chamber at high pressures (10^{-9} mbar). The SiGe atoms ejected from the target are deposited on a substrate resulting in a thin film. The plasma was activated with voltage of 720V and 80mA at a pressure of $7 \cdot 10^{-3}$ mbar. The substrates were pre-cleaned in deionized water and were located at 10cm from the target. Underneath the substrate there is a heater that can be used to heat it up during the growth. The samples were optimized by Jaime Andres Pérez from our group.

2.1.1.3. Polymer films and nanowires growth.

Polymeric films of poly [N-9'-heptadecanyl-2,7carbazole-alt-5,5-(4',7'-di-2-thienyl-2',1',3-benzothiadizole)] (PCDTBT) were grown by drop cast. This polymer was supplied by Solaris Chem Inc., with an average molecular weight (M_w) of 53000 g/mol and a polydispersity index of 1.5. For that purpose, the polymer was dissolved in chloroform at room temperature to produce a 50 mg/mL solution. Afterwards, the polymer solution was drop-casted on the glass surface and chloroform was allowed to evaporate at room temperature for 24h. Figure 2.2a shows a schematic of the process. As a consequence, a PCDTBT film can be fabricated. Films of this polymer doped with iron atoms (Fe) were also fabricated in order to improve its electrical properties. In this second case, the growing process is identical to the previous one, but now the chloroform solution has different concentrations of $FeCl_3$. These samples were grown by Dr. Jon Maiz from our group.

Polymeric nanowires of poly (3-hexylthiophene) (P3HT) were grown via infiltration method from melting. This polymer was supplied by Aldrich Ltd. with a average molecular weight (M_w) of 33405 g/mol and a polydispersity index of 1.5. For that purpose, a bulk piece of P3HT was placed on top of porous alumina templates with different diameters and then the polymer was melted. The melted polymer infiltrated on the porous of the template creating P3HT nanowires. Figure 2.2b shows a schematic of the process. These samples were grown by Dr. Jaime Martín from our group.

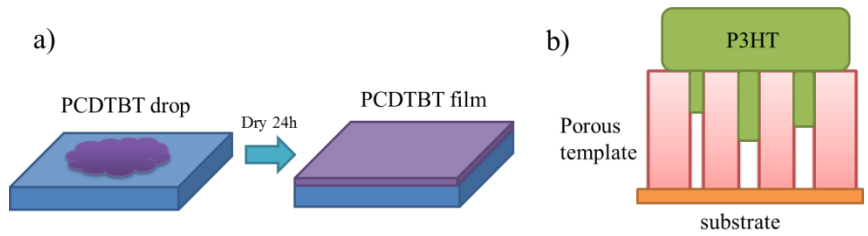

Figure 2.2. a) PCDTBT film growth via drop cast. b) Growing of P3HT nanowires inside the pores of the template through the infiltration process from melting.

2.1.2. Sample preparation for transport properties measurement.

In this section some of the most used techniques to prepare our samples for transport properties measurements are summarized. Some of these techniques have been used with the help of the technicians of the MINA lab of the "Insituto de Microelectrónica de Madrid (IMM-CSIC)". I want to emphasize the *photo-lithography, mechanical polishing and electrical contacting* as the ones that the candidate has been enrolled more directly.

2.1.2.1. Photolithography.

The Photo-lithography[3] is a method that consists on the optical microfabrication of patterns on a substrate. For that purpose, one must use a photoresist, which is light-sensitive. A drop of liquid photoresist is dispensed on a cleaned substrate and it is spin coated to spread it uniformly on the surface of a substrate (Figure 2.3a). Depending on the spinning time and revolutions per minutes (r.p.m.) used, one can obtain a resist film of a particular thickness, often ranging from 0.2 μm to 2.5 μm depending on the photo-resist used. A pre-baking is carried out to drive off the excess photoresist solvent, typically at 100º for 60 seconds on a hotplate. Afterwards, a photomask, which is an opaque plate with a transparent pattern that allows light to shine across, is aligned on the surface of the sample (Figure 2.3b). Then, the sample is exposed to light, usually ultra-violet light (UV) (Figure 2.3c). This exposure to light causes a chemical change in the polymerization of the photoresist that allows some of the photoresist to be removed by a special solution called "developer". If the photoresist is positive, the exposed part of the photoresist becomes soluble, while if it is negative, unexposed regions are soluble in the developer (Figure 2.3d). A post-exposure bake is carried out to help reduce standing wave phenomena caused by the destructive and constructive interference patterns of the incident light. The areas that are not protected by the photoresist can be etched to remove part of the substrate, or used to deposit other materials. Finally,

after the photoresist is no longer needed, one can remove it with a "remover" liquid solution.

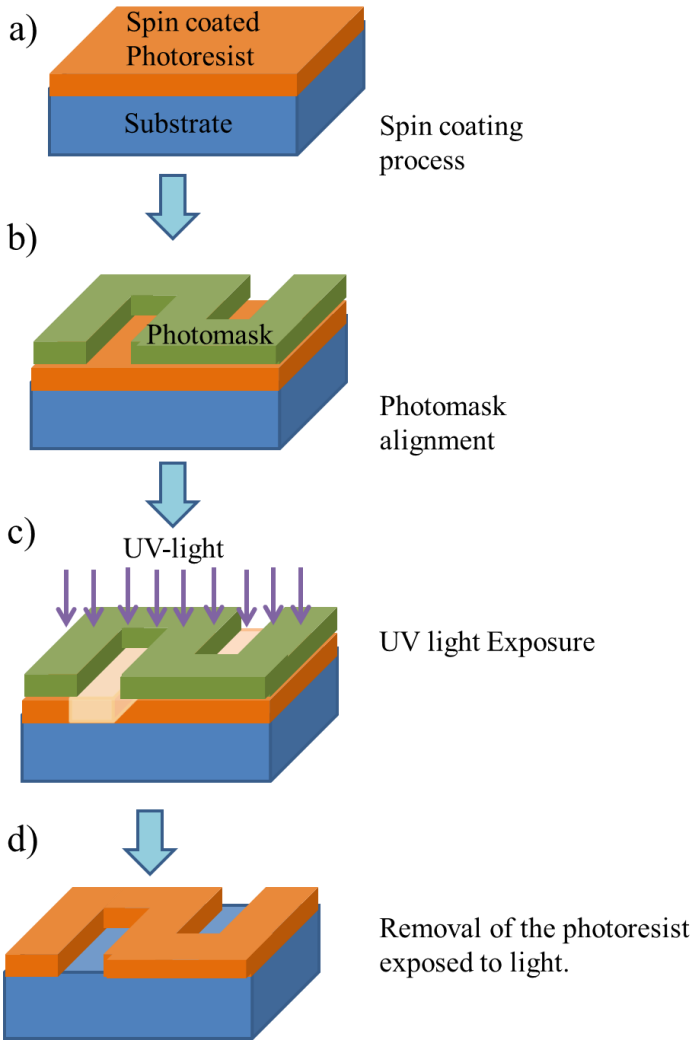

Figure 2.3. a) Spin coated photoresist on top of a substrate surface. b) Photomask alignment on top of the photoresist. c) Light exposure of the photoresist. d) Pattern formed after the photoresist is exposed to light using a photomask.

This process was used to fabricate special motifs, like discs in the micro-meter range thickness, fabricate specific shape electrical contacts. This process was carried out at the clean-room of the Instituto de Microelectrónica de Madrid (IMM-CSIC).

2.1.2.2. Electron beam evaporator.

The electron beam evaporator[4] is a physical process that can deposit metals, like Au, Cr or Pt, on top of different substrates. For that purpose, one applies voltage to a filament, which in our case it is made of tungsten, inside of a vacuum chamber. It produces an emission of electrons that are targeted, with the help of magnets, to the metal that one is interested to deposit on a substrate. The metal is heated up as a consequence of the bombarding of the electrons, which produces its evaporation on the vacuum chamber and so it deposits on the desired substrate. The thickness of the film is controlled by a quartz oscillator.

The working electrodes or cathodes of the electrodeposition process were fabricated through the deposition of Au or Pt on Si (100) wafer. Moreover, in several occasions, Au was evaporated on top of electrodeposited samples to provide electrical connections on the surface.

2.1.2.3. Mechanical polishing.

The mechanical polishing[5] improves the surface conditions of the sample making them flatter. In this process, a disk plate with grid sandpapers is used to polish the sample. The sample is glued on a metallic holder and placed on the arm of the polisher, making it spinning continuously onto the sandpaper.

This technique was used to polish Bi_2Te_3 nanowires embedded in alumina templates in order to get a flat surface with the tips of the nanowires putting out the matrix. For that purpose, polishing cloths and alumina powders with particle size of 1 μm, 0.5 μm and 0.03 μm were used. During this process, it was progressively changed the size of alumina particles from the largest to the smallest ones, achieving surfaces with roughness lower than 20 nm.

2.1.2.4. Focused Ion Beam (FIB).

The Focused Ion Beam[6] (FIB) is used for local metal deposition and ablation of different materials. The FIB employs a focused beam of ions, usually gallium (Ga) that can be in charge of etching local parts of the sample. The FIB can be used as micro-scale machining device and can fabricate particular patterns on a substrate. On the other hand, a FIB can also be used to deposit material via ion beam induced deposition. FIB-assisted chemical vapor deposition occurs when a gas, such as tungsten hexacarbonyl ($W(CO)_6$), is introduced in the vacuum chamber and allowed to chemisorb onto the sample. By scanning an area with the Ga^+ beam, the precursor gas will be decomposed into volatile and non-volatile components. The non-volatile component, such as tungsten, remains on the surface of deposition.

This technique was used to fabricate microchips and for the fabrication of metallic contacts on single Bi_2Te_3 nanowires. Their electrical properties and the surface effects were studied by Kelvin probe microscopy and two and four-point probes techniques.

2.1.2.5. Plasma-enhanced chemical vapor deposition (PECVD).

Plasma enhanced chemical vapor deposition[7] (PECVD) is a process used to deposit thin films at low temperature from a gas state (vapor) to a solid state on a substrate. This process involves chemical reactions that occur after creation of plasma of the reacting gases. In order to generate the plasma two electrodes are used, whose space between is filled with the desired reacting gases, and apply radio-frequencies (RF) or a direct current (DC) discharge between them.

This technique was used during the fabrication of electrical microchips. The goal was depositing a silicon oxide layer on top of the substrate, which in our case is Si (100) wafer, in order to isolate the electrical contacts that are fabricated on top of it. With this process, the

electrical measurements are not affected by the substrate due to the presence of this isolating layer in between.

2.1.2.6. Electrical Contacts.

Once a sample was grown, and depending of the experiment that one wants to carry out, there might be a need of having wires that contact the sample to external devices for microelectronic purposes[8]. Techniques such as the electro-soldering or tin (Sn) soldering are not adequate for samples whose sizes are in the range of micro-meters. It is required the presence of small contacts and wires. In order to achieve this goal, two processes were used: silver conductive epoxy or ball bonding.

The silver epoxy paste is a conductive adhesive with good electrical and thermal conductivities. It bounds very well in a variety of surfaces. With this paste and the help of a small probe one can bound an electrical gold wire on top of the surface of a sample, with contact sizes on the micro-meter range. On the other hand, the ball bonding technique is a type of wire bonding also working in the micro-meter range. In this technique, a needle, usually called capillary, is fed with a gold wire. Then, a high-voltage charge is applied to the wire to melt it at the tip of the capillary. The tip then forms a ball because of the surface tension of the molten metal. The capillary lowered on the surface of the sample and the ball rapidly solidifies. This is usually called ball bond. Then, the wire is passed out through the capillary and the machine moves over a few millimeters. The wire can be connected to an electrical pad by making a second ball bond on it.

These two processes were used to make electrical contacts at the surface of Bi_2Te_3 films as well as on the surface of microchips used to measure electrical properties of nanowires.

2.1.2.7. Thermal treatments.

Thermal treatments were carried out in a rapid thermal annealing system[9] (RTA). It consists of heating the sample under study through an infrared lamp that heats up the sample rapidly and uniformly. The RTA chamber is filled with forming gas, a mixture of 95% of nitrogen (N) and 5% of hydrogen (H), to avoid the surface of the sample to oxidize. The holder of the sample is a glass substrate.

The RTA system was used for thermal annealing of SiGe films.

2.1.3. Structural characterization.

After the samples were grown, a study of their structural properties is required to determine their chemical and physical quality. Most of the equipment used for these purpose needs of a technician to manipulate them. Nevertheless, in most of the cases, the post-analysis of the data was independently analyzed.

2.1.3.1. X-Ray diffraction (XRD).

The X-Ray diffraction[10, 11](XRD) gives information about the crystal orientation of the sample under study. A beam of X-Rays impacts in a crystalline sample and as a result a diffraction pattern occurs. A constructive interference from crystal planes spacing at distance, *s*, happens. To satisfy it, the angle of incidence of the beam, θ, is varied. This effect is called Bragg's law and it can be expressed mathematically through the equation,

$$n \cdot \lambda = 2 \cdot s \cdot sen\theta \qquad (2.1)$$

where λ is the wavelength of the X-Ray beam, n is an integer number, d is the spacing between crystalline planes and θ is the angle between the incident beam and the dispersive planes. If the sample is crystalline, after carrying a scan over a range of angles, a particular number of

peaks will be obtained. These peaks correspond to an interplanar distance, whose Miller-index or crystal direction is obtained from standard tables depending of the angle at which this diffraction is found.

The equipment used is an X-Ray diffract-meter of high resolution of Philips (X'Pert Pro) that can be found at the "Insituto de Microelectrónica de Madrid (IMM-CSIC)". The emitter of X-Rays consists of a copper anode that works in the Bragg-Brentano configuration (θ-2θ) with a wavelength of 1.5418 Å.

In order to scan the crystalline orientation of all our films, a fixed a scanning step of 0.02º and a scanning time of 1 second was used, while for our nanowires the same step was fixed but a time of 16 seconds was applied to increase the ratio signal versus noise. The XRD shown in this work were performed by the expert of our group that optimized each sample type.

2.1.3.2. Energy dispersive X-Ray spectroscopy (EDX).

Energy dispersive X-ray spectroscopy[10, 11] (EDX) is an analytical technique used for the elemental analysis or chemical characterization of a sample. This is based on the principle that each element has a unique atom structure allowing unique set of peaks on its X-ray emission spectrum. To obtain this spectrum, a high-energy beam of electrons or X-rays beam is focused onto the sample. At the ground state of an atom, the electrons are found in discrete energy levels or electron shells bound to the nucleus. However, when the incident beam interacts with them, it may involve an excitation of an electron from its inner shell, leaving a hole behind. An electron from an outer shell can fill this hole releasing energy in form of an X-Ray. The number and energy of X-Ray emitted from the specimen due to this phenomenon can be measured by an energy-dispersive spectrometer. The energy of the X-Ray is characteristic of the difference in energy between the two shells and of the atomic structure of the element. This allows knowing the elemental composition of the sample under study.

The equipment used for the compositional study of all our samples was S-3000N, which can be found at the "SIdI" department (Servicio Inter-departamental de Investigación) of the Universidad Autónoma de Madrid (UAM).

2.1.3.3. Scanning electron microscopy (SEM).

The Scanning Electron Microscopy[11] (SEM) makes possible the morphologic characterization of the sample under study by scanning its surface with a focused beam of electrons. A beam of electrons is generated from a filament that is subjected to a voltage. These electrons interact with the sample producing secondary electrons (SE), back-scattered electrons (BSE), characteristic X-rays, light (cathodoluminescence, CL), specimen current and transmitted electrons (TE). The secondary electrons result from the interaction of the electron beam with atoms at or near the surface of the sample, yielding high-resolution images of the sample surface.

A SEM Philips XL305-FEG of ultra-high resolution was used to characterize the morphology of our films and nanowires. This system can be found at the "SIdI" department (Servicio Inter-departamental de Investigación) of the Universidad Autónoma de Madrid (UAM).

2.1.3.4. Transmission electron microscopy (TEM).

The Transmission Electron Microscopy[11] (TEM) analyzes the transmitted electrons when a sample is subjected to a focused beam of electrons. The analysis of those electrons makes possible to obtain images with resolution in the order of Armstrongs, which able the observation of even individual atoms. However, in order to take these images, one needs ultra-thin samples, otherwise one would not be able to collect transmitted electrons.

TEM pictures of nanowires, which are shown in this work, were taken at the Molecular Foundry of the Lawrence Berkeley National Laboratory (USA).

2.1.3.5. Wide Angle X-Ray Scattering (WAXS).

The wide-angle X-ray scattering (WAXS) is an X-Ray diffraction technique, refereed to the analysis of Bragg peaks scattered to wide angles caused by nanometer-sized structures. It was use to characterize structural properties of polymer P3HT nanowires (Section 3.3.2). Firstly, the experiments in a geometry in which the wave vector, *Q*, was parallel to the long axis of P3HT NWs were carried out in reflection geometry using a Philips X'Pert diffractometer, as it is shown in Figure 2.4a. Moreover, WAXS experiments were also performed in transmission geometry with the X-ray beam traveling along the direction perpendicular to the template surface (Figure 2.4b) using a Bruker AXS Nanostar X-ray scattering instrument. So that *Q* was nearly perpendicular to the long axis of NWs. The underlying Al substrate was chemically etched from the AAO templates for transmission measurements. The scattered X-rays were detected using a two dimensional multiwire area detector (Bruker Hi-Star). The data were then converted to one-dimensional scattering profiles by radial averaging along the azimuthal direction. The sample to detector distance was 10 cm. Both instruments use Cu K_α radiation (1.54 Å). The fabrication and structural characterization were carried out by Dr. Jaime Martín from our group.

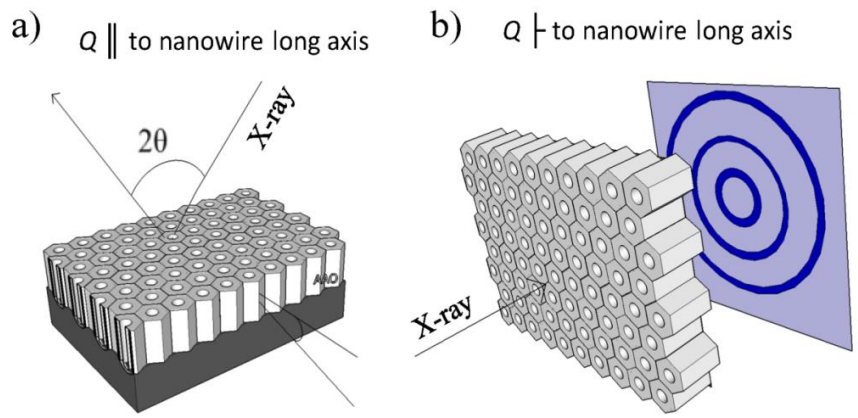

Figure 2.4**.** Schematic representations of WAXS experiments: a) Experiment in reflection geometry in which the wave vector *Q* is parallel to pore long axis. b) Experiment in transmission geometry. The

X-ray beam travels along the direction perpendicular to the template surface, in such a way that *Q* is nearly perpendicular to the pore long axis. Figure taken from supporting information of reference [12].

2.1.3.6. Raman spectroscopy.

Raman spectroscopy[13] indicates the vibrational, rotational and other lower-frequency modes of the material under study. It can be used as a fingerprint by which molecules or elements can be identified. In this technique, the sample is impinged with a laser that interacts with molecular vibrations, phonons or other excitations, resulting in the energy of the laser photons being shifted up or down. This shift in energy gives information about the vibrational modes in the system. There are two possible inelastic emitted/scattered photons, Stokes or anti-Stokes, which happens at lower or higher energy than the incoming photon, respectively. With the information obtained from this technique, one can determine the elements or molecules that are present in the material under study.

Raman spectroscopy analysis was carried out in our films and nanowires using a micro-Raman spectrometer of high resolution (Horiba Jobin Yvon ®) available in our group.

2.1.3.7. Profilometer.

The profilometer consists of a micrometer probe that scans, when bringing it into contact with the surface, the step sample-substrate giving information of its thickness, as well as it gives a rough estimation of the roughness of the sample surface. The profilometer used for that purpose is a commercial Veeco® Dektak Stylus that can be found at the clean room of the Instituto de Microeletrónica de Madrid (IMM-CSIC). The thicknesses of all our films were determined using this instrument.

2.2. Transport properties measurement techniques.

This section summarizes the techniques that the PhD candidate has used to measure transport properties of films, nanowires and other nanostructures. Most of the measurements have been carried out at a local scale with Atomic Force Microscopy techniques, although some other techniques have been used to double check or gain additional information about the samples. Finally, it is also shown the software that the candidate has become to be an expert during this PhD work, COMSOL Multiphysics®. This modelling tool has been used to understand some of the experimental data obtained.

2.2.1. Atomic Force Microscopy (AFM).

The Atomic Force Microscopy (AFM) is a type of Scanning Probe Technique (SPM) that makes possible to study the surface of a sample at an atomic scale[14 15]. Almost any sample can be imaged with this technique, those that are very hard, like ceramic material or a dispersion of metallic particles, or very soft, such as flexible polymers, individual molecules of DNA or human cells, among others[14].

Differently to other microscopes that form an image by focusing light or electrons onto a surface, like an optical or electron microscope, an AFM physically "feels" the sample surface with a sharp probe, building a height map of it. While in the other microscopes a 2D-image of the sample surface is obtained, the AFM obtains a 3D-map of it. The working principle of an AFM is based on a physical interaction of the probe with the sample surface. When an AFM probe is brought into proximity of a sample surface, the forces between the tip and the sample lead to a deflection of the cantilever. Typically, the deflection is measured using a laser spot reflected from the top surface of the cantilever in an array of photodiodes. Then, a feedback circuit is in charge of driving the *z*-axis of a piezoelectric element in order to keep the sample-probe distance at a fixed value, while the *x* and *y* movement

of the piezoelectric can scan the surface horizontally. Figure 2.5 shows a schematic of an AFM system. The primary modes of the AFM are:

a) Contact mode, at which the tip is dragged across the surface of the sample and the contours of the surface are measured either using the deflection of the cantilever directly or using the feedback signal required to keep the cantilever at a constant position.

b) Non-contact mode, at which the tip of the cantilever oscillates near or just above its resonant frequency. When the tip is near to the sample surface, the decrease in the resonant frequency due to the interacting forces, usually Van der Waals when the tip is oscillating very close to the surface (between 1nm or 10nm), combined with the feedback loop system maintains a constant oscillation amplitude (Amplitude Modulation Mode) or frequency (Frequency Modulation Mode) by adjusting the average tip to sample distance.

c) Tapping mode or dynamic mode, at which the cantilever is driven to oscillate at near its resonance frequency, similar to non-contact mode, but now it touches intermittently the sample surface while scanning. The interaction of forces acting on the cantilever when the tip comes close to the surface, Van der Waals forces, dipole-dipole interactions, electrostatic forces, etc. cause the amplitude of oscillation to decrease as the tip gets closer to the sample.

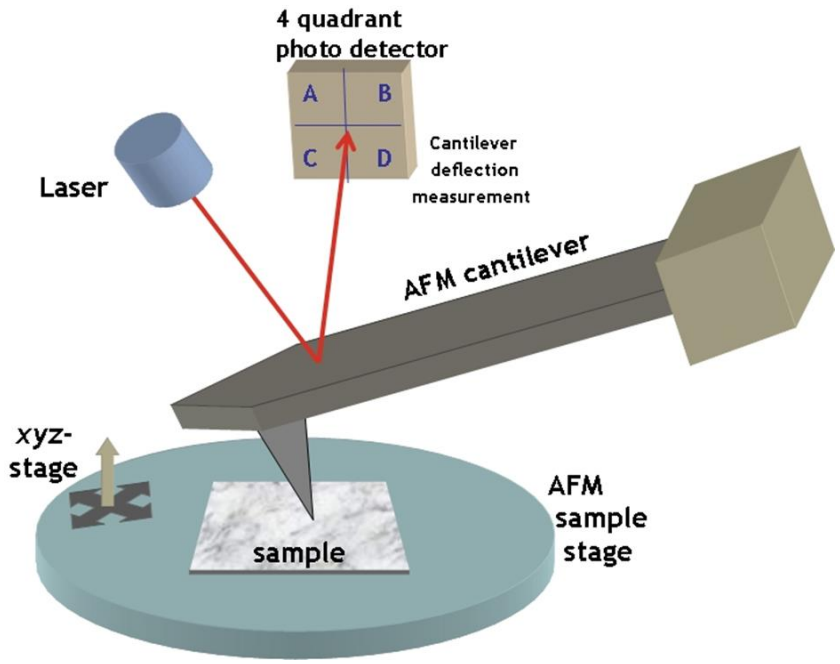

Figure 2.5. Schematic of an Atomic Force Microscope.

Depending on the tip used and the AFM mode at which one is working on, the force measured can be different and the map obtained can give information about certain properties of the sample. As a consequence, the AFM has various "spectroscopic" modes that measure physical properties of the sample at the nanometer scale[14]. Table 2.I summarizes some of the most typical modes that can be used to determine different properties of the sample. Furthermore, the AFM can be also used as nano-tool to manipulate particles, to make nano-patterns, using for example local oxidation, or just to measure other properties, like the Young modulus.

Table 2.I. Summary of the most typical modes that are used with an AFM. Adapted from reference[14].

Scanning Probe Techniques		
Primary AFM modes	Tapping Mode	AFM tip oscillates at its fundamental resonance frequency. The tip intermittently touches the sample, which reduces the amplitude of oscillation. This is fixed to a predetermined level to carry out the scan.
	Contact mode	Tip and sample are in direct contact throughout the scan. A detector measures the deflection of the cantilever, giving a topographic map.
	Non-Contact mode	An AFM tip is oscillating close to surface of the sample while it scans. The force interactions are measured through changes in the amplitude at constant frequency just off resonance (amplitude modulation) or by measuring the change in resonant frequency (frequency modulation) using a feedback circuit (PLL).
Other SPM Modes	Magnetic Force (MFM)	A magnetic probe is used to observe magnetic domains at the sample. Depending if the sample is repulsed or attracted, one can determine the magnetic domains of the sample.
	Electrostatic Force (EFM)	In this mode an electrostatic force is probed. This force comes from the attraction or repulsion of the charges of the sample.
	Kelvin Probe (KPM)	The surface potential or work function of surfaces can be observed at atomic or molecular scales. It is measured from the force interaction of tip-sample when we combine an AC and DC voltages on the probe.
	Scanning Tunneling (STM)	It is based on the concept of quantum tunneling. A sharp conducting tip is brought very neat to the surface and a bias is applied between the two. A tunnel current is obtained that depends of tip position, applied voltage and local density of states of the sample. The sample measured must be conducting.
	Scanning Capacitance (SCM)	A narrow probe electrode is held just above the surface of a sample and scanned along it. This technique uses the information obtained from the change in electrostatic capacitance between the surface and the probe.
	Conductive (C-AFM)	An electrical probe in contact with a sample and under the application of a bias voltage between the two, uses the electrical current to construct the surface electrical conductive profile of the sample.
	Scanning Thermal (SThM)	It maps the local temperature and thermal conductivity at the surface of a sample. The probe is sensitive to local temperatures providing a nanoscale thermometer.

An Atomic Force Microscope from Nanotec® Company was used to carry out transport properties measurements in inorganic and organic films and nanowires at Instituto de Microelectrónica de Madrid (IMM-CSIC). Other electrical and thermal properties of nanowires were measured in an Aligent® AFM at group of Prof. Miquel Salmeron from the Lawrence Berkeley National Laboratory (USA) and with a Veeco® AFM at the group of Prof. Stefan Dilhaire from the University of Bordeaux (France).

2.2.1.1. Topographic analysis.

The topographic analysis of the surface of a sample was carried out mostly in non-contact under the amplitude modulation mode, as explained previously. This technique was used to analyze the surface of all our films, whose roughness could change depending on the growing conditions either in electrodeposition or sputtering process, as well as to observe nanowires embedded in a matrix.

2.2.1.2. Kelvin Probe Microsocopy (KPM): Surface potential measurements.

Kelvin Probe Microscopy [16] (KPM or KPFM) is a non-contact mode of the AFM that allows the study of the surface potential or work function of the sample under study.

This technique works by applying an adjustable bias voltage (U_{dc}) and alternating voltage (U_{ac}) between a conductive tip and the sample. Therefore, from the theoretical point of view, the force acting on the tip in KPM measurements can be described as,

$$F = \frac{1}{2}\frac{\partial C}{\partial z}U^2 \tag{2.2}$$

where C is the capacitance of the probe-sample system and $U = U_{dc} + U_{ac}\sin(\omega t)$ is the total potential applied. A local change in the dielectric properties would produce a change in the force signal. The resulting equation for the total force can be split in different terms,

$$F = F_{dc} + F_{\omega}\sin(wt) + F_{2\omega}\sin(2\omega t) \tag{2.3}$$

where the *dc* term of the force, expressed as $F_{dc} = \frac{1}{2}\frac{\partial C}{\partial z}\left(U_{dc}^2 + \frac{1}{2}U_{ac}^2\right)$, is related to the topographic image of the surface of the sample, while F_{ω} and $F_{2\omega}$ are related to the surface potential and dielectric properties of the sample, respectively.

The first harmonic of the *ac* signal, F_ω, can be written as,

$$F_\omega = \frac{\partial C}{\partial z} U_{ac} U_{dc} \tag{2.4}$$

Then, the *dc* voltage can be expressed as, $U_{dc} = U_{feedback} - \phi$, where ϕ is the surface potential and the $U_{feedback}$ is the *dc* voltage applied by the AFM in order to fulfil the $F_\omega = 0$ condition, so it can measure the sample surface potential [17].

Additionally, the second harmonic of the ac signal, $F_{2\omega}$, can be written as,

$$F_{2\omega} = -\frac{1}{4}\frac{\partial C}{\partial z} U_{ac}^2 \tag{2.5}$$

This term does not depend on the constant potential, U_{dc}, but it is proportional to the square of the alternate potential, U_{ac}, which is fixed during the experiment as well as the derivative of the capacitance respect to the distance. This derivative changes with the tip to sample distance and also with the dielectric properties of the sample. As consequence, the study of this term can yield the dielectric properties of the sample as long as the probe-sample system geometry is constant along the surface.

The Kelvin Probe Microscopy measures simultaneously the topography and electrostatic signal. In the experiments, surface potential measurements were carried out by using the Force Gradient as interaction signal instead of the Force together with a low frequency range (7 kHz) for the oscillating bias voltage, as it enhances the sensitivity of the measurement. The surface potential of Bi_2Te_3 films and nanowires samples was measured by this technique. Some of these measurements were also performed in a KPM system at Lawrence Berkeley National Laboratory.

2.2.1.3. Conductive AFM (*I-V* curves): Electrical conductivity measurements.

The conductive AFM[18] (C-AFM) works in contact mode and can be considered as a type of current spectroscopy. It consists of using

a conductive tip, which is brought into contact with the sample surface. Then, a bias voltage is applied between them and the current is measured. One can use it to obtain a current versus voltage (*I*-*V*) curves on different locations of the sample to determine its electrical resistance. Moreover, if applying a constant voltage during a scan, one can get simultaneously a topographic and a current map of the sample.

This technique was used to obtain current maps and to determine the electrical conductivity through *I*-*V* curves of Bi_2Te_3 nanowires.

2.2.1.4. Scannning Thermal Microsocopy (SThM): Thermal conductivity measurements.

The Scanning Thermal Microscopy[11] (SThM) is a type of scanning probe microscopy (SPM) that maps the local temperature and thermal conductivity of an interface[19]. The probe in a scanning thermal microscope is sensitive to local temperatures, changing its electrical resistance with temperature, providing a nanoscale thermometer. There are two operating modes: a) active mode, in which the tip is heated up and a heat flux is exchanged from the tip to the surface of the sample. The change in the electrical resistance of the tip is related to thermal properties of the sample; b) passive mode, in which the surface heats up and the changes in the tip electrical resistance are consequence of different heat flux from local areas of the sample to the tip. The most used one is the active mode, which is the one that I have used.

For a thermoresistor probe the change in probe temperature is extracted from the change in its electrical resistance using the expression,

$$T_p - T_0 = \frac{R_p - R_0}{R_0 \cdot (TCR)} \tag{2.6}$$

where TCR is the temperature coefficient of resistance of the probe, R_p and T_p are the electrical resistance of the probe and its average temperature, respectively, and R_0 is the probe resistance under the ambient temperature, T_0. It is possible to directly measure the electrical

resistance of the probe just by measuring the voltage drop across the probe when a current is passed through it or by monitoring the changes in resistance using a Wheatstone bridge setup. In case one use a Wheatstone bridge, one must first balance it at ambient conditions, where $R_p = R_0$. If then it is energized by a voltage V_a, changes in the electrical resistance are related to the bridge voltage, V_b, that come from the variation in the electrical resistance of the probe and the bridge resistor. It can be expressed mathematically through the equation,

$$R_p - R_0 = \frac{V_b}{V_a} \cdot \frac{(R_b+R_0)^2}{R_b} \tag{2.7}$$

Using DC, AC or a combination of AC and DC modes, the thermoresistor probes can be used for heating or sensing. If one considers the DC mode, the average DC temperature rise and probe thermal resistance can be extracted by directly using Equation 2.6 and Equation 2.7. In the AC mode, a temperature profile is established both a DC and an AC contribution and it requires the use of more complex equations. Both modes of operation, within the help of heat transfer models, have been used to perform thermal characterization.

When one applies an AC current, with 1ω frequency, to the probe, $I(t)=I_a \cdot \cos(\omega t)$, its temperature increases proportionally to Joule heating, that is

$$P_{Joule} = I_a^2 \cdot R_p \cdot (\cos(\omega t))^2 = \frac{I_a^2 R_p}{2} + \frac{I_a^2 R_p}{2} \cdot \cos(2\omega t) \tag{2.8}$$

The first term corresponds to the DC contribution while the second one is the AC contribution. As a consequence, both DC an AC components contribute to the probe temperature, which is averaged along the probe length, can be written as,

$$T_p(t) = T_{DC} + \Delta T_{2\omega} \tag{2.9}$$

where $\Delta T_{2\omega}$ corresponds to the fluctuation of temperature of the probe due to the AC component, which is defined as $\Delta T_{2\omega} = T_{2\omega}\cos(2\omega t)$ where $T_{2\omega}$ is the magnitude of the temperature fluctuation. The electrical resistance of the probe under heating is,

$$R_p = R_0[1 + TCR \cdot (T_{DC} + \Delta T_{2\omega})] =$$

$$R_0 \cdot (1 + TCR \cdot T_{DC}) + (R_0 \cdot TCR \cdot T_{2\omega} \cos(2\omega t)) \quad (2.10)$$

The voltage across the probe is a superposition of a DC an AC term that can be obtained from the equation,

$$V(t) = I(t) \cdot R_p(t) = [I_a \cdot R_0 \cdot (1 + TCR \cdot T_{DC}) \cdot \cos(\omega t)] +$$

$$\left(\frac{I_a \cdot R_0 \cdot TCR \cdot T_{2\omega}}{2} \cos(\omega t)\right) + \left(\frac{I_a \cdot R_0 \cdot TCR \cdot T_{2\omega}}{2} \cos(3\omega t)\right) \quad (2.11)$$

The temperature amplitude, $T_{2\omega}$, can be obtained using the Equation 2.11,

$$T_{2\omega} = \frac{2 \cdot V_{3\omega}}{I_a \cdot R_0 \cdot TCR} = \frac{2 \cdot V_{3\omega}}{TCR \cdot V_{1\omega}} \quad (2.12)$$

where $V_{1\omega}$, that was approximated to $I_a \cdot R_0$, and $V_{3\omega}$ are the first and third harmonic of the voltage response of the probe, respectively.

2.2.1.4.1. Experimental working modes and heat transfer modelling.

In order to determine the thermal conductivity of the sample, the use of analytical models is mandatory for rapid data reduction and simple interpretation of the physical parameters. In this section, the typical models[19] used for DC and AC heating methods are introduced. On the one hand, the DC method with a thermos-resistor called Wollaston probe is used to measure films and arrays of nanowires. On the other hand, the AC method was used with a new commercial thermo-resistive Pd/SiO_2 probe in order to map and measure the thermal conductivity of individual nanowires.

2.2.1.4.1. 1. DC heating methods: Wollaston thermo-resistive probe.

a) Wollaston probe and experimental set-up.

The DC method[19] has been used with a Wollaston micro-probe, which consists of 5µm diameter Pt-Rh cores clad with 75µm diameter silver shell. The micro-wire is bent into a V-shape and etched in the central part to expose its Pt-Rh core over a length of typically 200µm. This micro-probe is mounted in an AFM from Nanotec®, which is used as a micro-positioner. For this purpose, it was necessary to fabricate a new holder to set the probe in the AFM head and to achieve a proper reflection from the probe to the center of the AFM photodetector. With the AFM one is able to approach the Wollaston probe to the surface of the sample in a very accurate way. This probe has a topographic lateral resolution of around 1µm and a thermal lateral resolution of around 2-3 µm. Figure 2.6 shows a SEM picture of a Wollaston probe.

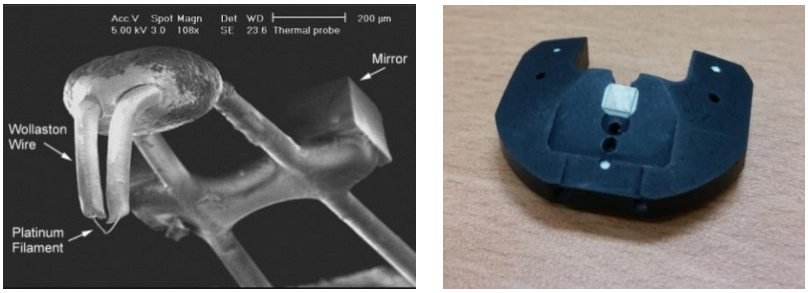

Figure 2.6. a)SEM pictures of a Wollaston probe. Image are taken from reference [20]. b) Specially designed and fabricated holder to set the Wollaston probe in the AFM head.

The local thermal properties of bulk, films and nanowires arrays can be obtained using this probe, but a thermal map of nanostructures cannot be taken due to its poor lateral resolution. In the Chapter 3, one will see that new commercial probes can be used to take topographic and thermal maps of nanowires samples because of their nanometer lateral resolution. In summary, one uses the Wollaston probes to measure locally the thermal properties of a film or nanowire arrays

samples. Figure 2.7 shows a schematic view of the experimental setup that was lab-made at the Instituto de Microelectrónica de Madrid (IMM-CSIC) and that counted on the collaboration with the Prof. Theodorian Borca-Tasciuc group at the Reensselaer Polytechnic Institute (RPI) from New York (USA) to develop the mathematical model.

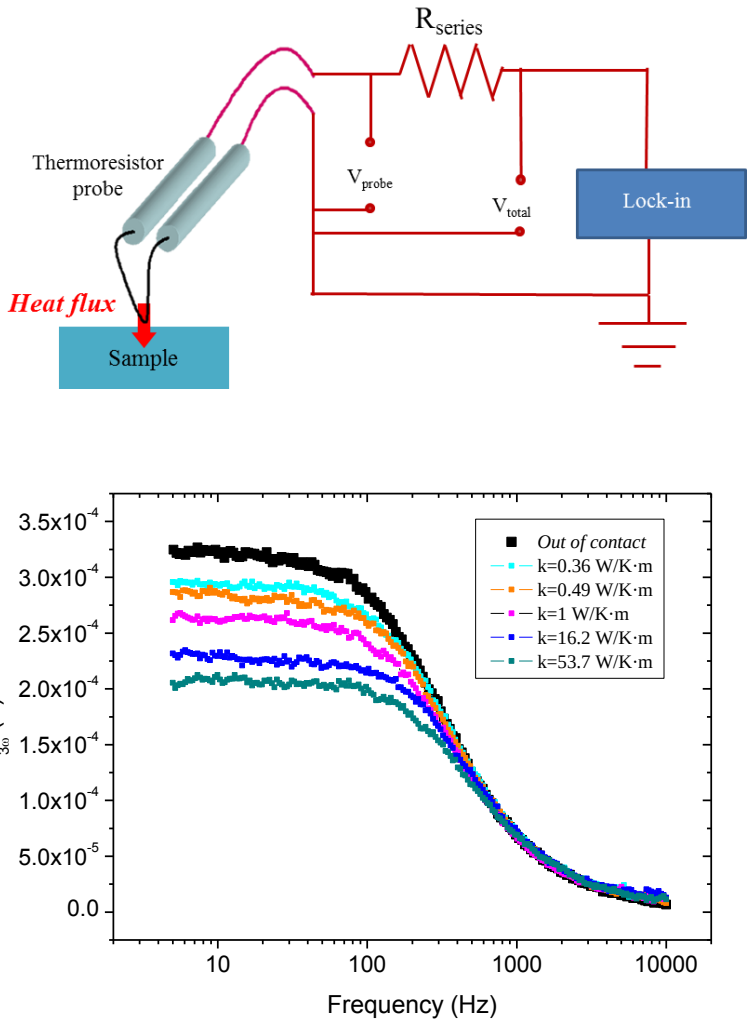

Figure 2.7. a) Schematic view of the experimental set-up for a Wollaston probe working in DC heating mode. b) 3ω voltage versus frequency. In order to work in DC mode the data at 10 Hz has been considered.

Our experimental setup consists of a 10Ω resistor connected in series with the Wollaston probe, which is mounted in a Nanotec® AFM system. A lock-in amplifier from Zurich Instruments® is used to apply an AC bias voltage across the system while measuring simultaneously the total voltage drop, $V_{1\omega,total}$, (series resistor plus thermos-resistive probe) and the voltage drop only across the thermos-resistive probe, $V_{1\omega,probe}$. The current across the probe can be determined as, $I_a = \frac{V_{1\omega,total} - V_{1\omega,probe}}{R_{series}}$, where R_{series} is the series resistor.

b) 3ω-voltage signal.

Figure 2.7b shows the 3ω voltage signal obtained from the probe when it is *out of contact* and *in contact* with different thermal conductivity samples versus frequency. As one is going to work in DC mode, one is only interested in the probe response at low-frequency range, around 10Hz (AC fluctuations are negligible). In the DC mode, the measurement of the 3ω voltage of the probe, $V_{3\omega,probe}$, is needed in order to determine the 2ω temperature amplitude, $T_{2\omega}$, (Equation 2.12). This term influences the electrical resistance of the probe under heating and must be taken into account, as can be seen in Equation 2.10.

c) DC thermal model.

In the DC method[19], the heat transfer equation for a probe, like the Wollaston one under the assumption that it behaves as a Joule heated fin of length L (half of the probe length), with probe electrical resistivity ρ_0 at ambient temperature T_0, is given by

$$\frac{\partial^2 T_p^*}{\partial x^2} - \left(\frac{h\mathrm{p}}{k_p A_p} - \frac{I^2 \cdot \rho_0 \cdot TCR}{k_p A_p^2} + \frac{4 \cdot \epsilon \cdot \sigma \cdot \mathrm{p} \cdot T_0^3}{k_p A_p} \right) \cdot T_p^* = -\frac{I^2 \cdot \rho_0}{k_p A_p^2} \qquad (2.13)$$

where k_p is the probe thermal conductivity, h is the effective convective heat transfer coefficient, I the electrical current through the probe, $T_p^* = T_p(x) - T_0$ and $T_p(x)$ is the probe temperature at location x, and ϵ, r p and $A_p$are the probe emissivity, probe radius and the

perimeter of the cross-section and the cross-sectional area of the probe, respectively. The first term refers to the heat conduction along the probe while the second term in parenthesis includes the convective heat transfer with the surrounding through an effective heat transfer coefficient, the Joule heating in the probe, and the radiative heat transfer. This equation assumes that the probe does not undergo heat transfer with the sample, other than in the tip region, which is considered as a boundary condition. If the probes present a small height, in which the cantilever beams are in close proximity with the substrate, might involve tip-sample heat transfer in regions away from the tip and this approximation might not be longer valid.

d) Sorting out the DC heat equation.

In order to solve the heat transfer equation, the next boundaries conditions are assumed for a probe similar to the Wollaston one:

a) The first boundary equation[19] takes into account that, due to the large diameter and thermal conductivity of the Ag coating, the ends of the heated probe region remain at ambient temperature, that is:

$$T_p^*|_0 = 0 \tag{2.14}$$

It considers that the heat transfer between the sample and the surface occurs only in the tip region. This assumption is believed to hold because the tip-sample heat transfer terms through the air gap are significant only if the gap is in the microns range, which is comparable to the wire diameter of the Wollaston probe.

b) The second boundary equation[19] accounts for the heat transfer rate Q_s between the tip of the probe and the sample surface. The heat transfer is assumed to occur through an effective heat transfer radius, *b*. For Wollaston probes, the temperature of the probe tip is uniform over the region that undergoes the heat transfer with the sample [21]. The energy balance at the tip can be written as,

$$-k_p A_p \left.\frac{\partial^2 T_p^*}{\partial x^2}\right|_{x=L-b} + \frac{I^2 \cdot \rho_0 \cdot b}{A_p}\left(1 + TCR \cdot T_p^*|_{x=L-b}\right) - hpb \cdot$$

$$T_p^*|_{x=L-b} = \frac{Q_s}{2} \qquad (2.15)$$

These boundary conditions lead to a semi-analytical solution of the heat transfer model. The first term of the equation refers to the heat conduction in the probe wire, the second term corresponds to the Joule heating, while the third term is the convection heat transfer for the probe area undergoing heat transfer with the sample. When the probe is in contact with the surface of the sample and due to the twofold symmetry V shaped thermoresistor probes, the right hand side of this equation accounts for half of the heat transfer rate between the probe and the sample. If the probe is not in contact, this term becomes null.

The term Q_s can be written in terms of the effective conductance through the sample, G_{eq}, that is,

$$Q_s = G_{eq} \cdot T_p^*|_{x=L-b} \qquad (2.16)$$

The effective conductance can be also expressed in terms of the tip-sample thermal contact conductance, G_c, and the thermal conductance of the sample, G_s, as follows

$$G_{eq} = \frac{G_c \cdot G_s}{G_c + G_s} \qquad (2.17)$$

Under the assumption of these boundary conditions, the solution to the differential Equation 2.13 is

$$T_p^* = Ne^{\Upsilon x} + Oe^{-\Upsilon x} + \frac{\Gamma}{\Upsilon^2} \qquad (2.18)$$

where N and O are constants can be determined using Equations 2.14 and 2.15, while $\Upsilon = \left(\frac{hp}{k_p A_p} - \frac{I^2 \cdot \rho_0 \cdot TCR}{k_p A_p^2} + \frac{4 \cdot \epsilon \cdot \sigma \cdot p \cdot T_0^3}{k_p A_p}\right)^{1/2}$ and $\Gamma = \frac{I^2 \cdot \rho_0}{k_p A_p^2}$. The average temperature of the probe along its length is obtained by integration over the probe length,

$$T_{p\,ave}^* = \frac{1}{L}\int_0^L T_p^*\, dx = T_{DC\,ave} - T_0 \qquad (2.19)$$

Then, the effective probe thermal resistance is obtained from

$$R_{probe}^{th} = \frac{T_p^* ave}{I^2 \cdot R_p} \tag{2.20}$$

The experimentally measured probe thermal resistance $R_{probe,exp}^{th}$ can be then compared with Equation 2.20 to extract unknown thermal properties of the sample, contact or even probe.

Mathematically, the probe thermal resistance can be correlated to the intrinsic thermal resistance of the probe using the expression:

$$R_{probe,exp}^{th} = R_{sample}^{th} + R_C^{th} \tag{2.21}$$

where R_{sample}^{th} is the intrinsic thermal resistance of the sample and R_C^{th} is the contact resistance between the probe and the sample.

When a Wollaston probe, with a thermal exchange radius *b*, is in contact with the sample surface, if the sample heat transfer can be assumed to be equivalent to semi-infinite conduction from a uniformly heated disk on its surface, the thermal conductance of the sample G_s becomes [19],

$$G_s = 4 \cdot k \cdot b \tag{2.22}$$

where *k* is the thermal conductivity of the sample under study. The inverse of the thermal conductance for a semi-infinite medium, G_s, is related to the thermal resistance of the sample according to the equation,

$$R_{sample}^{th} = \frac{1}{G_s} = \frac{1}{4 \cdot k \cdot b} \tag{2.23}$$

These equations were used to determine the thermal conductivity of films, nanowires and nano-structures, as it is shown in Chapter 3. It is very important to note here that for non-semi-infinite mediums (2D- or 1D-samples) additional terms must be considered in Equation 2.22. For a thin film on a substrate, the heat transfer occurs not only along the film, but along the multilayered structure. If one could assume the simplest case and one-dimensional (1D) heat conduction across the film thickness, *t*, the sample conductance could

be written as a thermal resistance network with the film and substrate connected in series, i.e. $\frac{1}{G_s} = \frac{t}{k_{film} \cdot \pi \cdot b^2} + \frac{1}{4 \cdot k_{subst} \cdot b}$ where k_{film} and k_{subst} are the thermal conductivities of the film and substrate respectively. However, in reality, most of the cases approach to the two-dimensional (2D) case and in order to calculate the total thermal resistance of the film and the substrate, one must use a 2D heat conduction model. For that purpose, heat conduction models for laser heating[22] can be adapted to this case. If the thermal exchange radius and the thermal conductivity of the substrate is known, the thermal resistance of the sample, R^{th}_{sample}, can be obtained by simulating a disc-shape heat source of uniform heat flux on this multilayered structure. In Section 3.2.2.1., a COMSOL Multiphysic® simulation based on this method was developed to determine the thermal resistance of the films under study.

2.2.1.4.1. 2. AC heating methods: Pd/SiO_2 thermo-resistive probe.

a) **Pd/SiO_2** *probe and experimental setup.*

The AC heating method[19] has been used with a new commercial thermo-resistive probe made of palladium (Pd) film on a silicon oxide substrate (SiO_2), which offers a nanometric topographic lateral resolution (~60 nm) and a typical 100 nm thermal lateral resolution. The thin Pd layer (~10 nm) acts as the thermos-resistive element. It also possesses NiCr current limiters for tip protection. Figure 2.8 shows a SEM image of the Pd/SiO_2 probe. Apart from its high spatial and thermal resolution, this probe also has a higher thermal cut-off, which makes possible to take thermal images quicker and the use of a wider band of frequencies in comparison to the Wollaston probe. Table 2.II shows a quantitative comparison between the Pd/SiO_2 and the Wollaston probes.

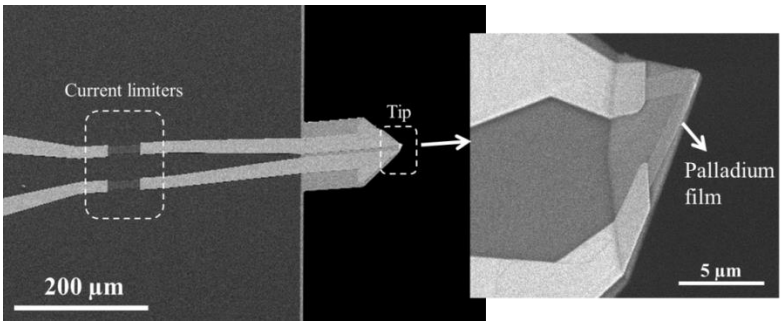

Figure 2.8. SEM images of a Pd/SiO_2 commercial probe from Veeco®.

Table 2.II. Quantitative comparison between the Pd/SiO_2 and the Wollaston probes.

Probe	Pd/SiO_2	Wollaston
Thermal cut-off frequency $2f_c$ (Hz)	2750	250
Maximal electrical frequency f (Hz)	1375	125
Minimum 256×256 points image acquisition time (s)	4	44
Spatial resolution	1-2µm	60-100nm

The setup used to measure in AC heating mode with Pd/SiO_2 probes is shown in Figure 2.9. It consists of a Wheatstone bridge, where the probe is considered as one of the resistors of the bridge, a function generator, a lock-in amplifier and an amplification system. The probe was mounted in an AFM system, which is used to scan the topography and thermal properties of a sample surface. The function generator is in charge of applying an AC signal, $I(t)=I_a \cdot \cos(\omega t)$, to the system while the electrical response of the probe is measured with a lock-in amplifier. An amplification system is used to amplify the signal.

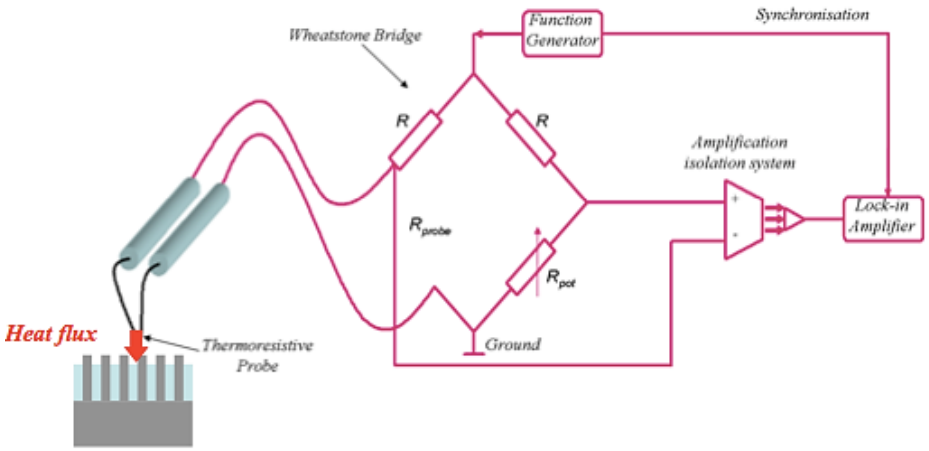

Figure 2.9. Schematic view of the experimental set-up of the AC heating mode of a SThM in 3ω configuration. Figure taken from reference [23].

This system was originally built in a Veeco® AFM at the University of Bordeaux in the group of Prof. Stefan Dilhaire, where I was able to carry out measurements of nanowires inside alumina matrix. A similar system was implemented in our Nanotec® AFM "Insituto de Microelectrónica de Madrid (IMM-CSIC)".

b) 3ω- voltage signal.

As it was explained previously in section 2.2.1.4., the 3ω-voltage signal of the tip is related to the 2ω-temperature variations of the probe (Equation 2.11).

However, it is important to take into account that in real experimental conditions the 3ω voltage measured does not come only from the probe, but also, from the system itself. Corrections to the 3ω-voltage must include the influence of the current limiters of the probe as well as the distortion of the 3ω signal. These terms are expressed as,

$$(V_{3\omega})_{Limiters} = \frac{G}{1+i\frac{\omega}{\omega_c}} \qquad (V_{3\omega})_{Distortion} = V_D exp(i\emptyset_D) \qquad (2.24)$$

where G is the static voltage of the 3ω-signal by the probe limiters, ω_c is the cut-off frequency, V_D and $\emptyset_D$ are the amplitude and phase of the 3ω distortional signal. Then, the 3ω-voltage signal that is going to be measured for the new commercial tip depends on the following terms [23],

$$V_{3\omega} = (V_{3\omega})_{tip} + (V_{3\omega})_{limiters} + (V_{3\omega})_{Distortion} =$$

$$K_{ampli}(\omega = 0)\frac{R_{Tip}\alpha_{Tip}I_a}{2} < T_{2\omega}(\omega) > + \frac{G}{1+i\frac{\omega}{\omega_c}} + V_D exp(i\emptyset_D) \quad (2.25)$$

As one can observe in Equation 2.25, even the radius R_{Tip}, thermal coefficient α_{Tip} or current through the tip I_a, as well as the amplification gain of our system K_{ampli}, are important parameters when calculating the actual 3ω-voltage.

Figure 2.10 shows how the theoretical curves obtained for amplitude and phase of the 3ω-signal change when these terms are taken into account[23].

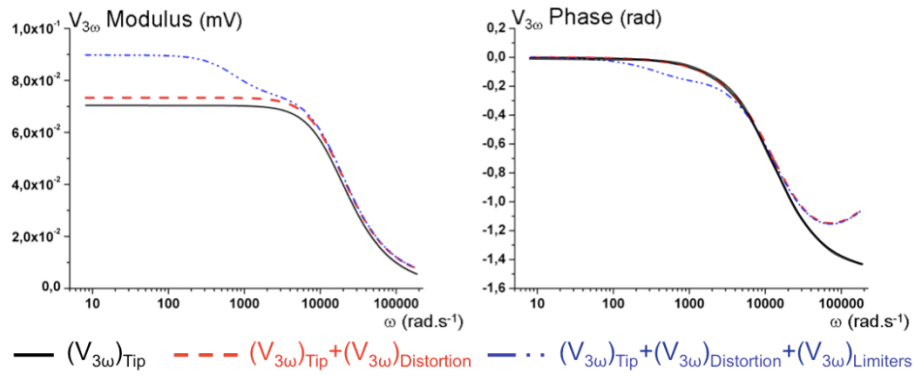

Figure 2.10. Theoretical simulation of the 3ω curves when adding to the 3ω voltage of the tip the influence of the probe limiters and signal distortion. Figures taken from reference [23].

Before performing the measurements, the SThM system has to be fully characterized. The first analysis concerns the study of the changes of the resistance of the probe when the tip is heated or cooled. For this purpose, one heats the tip in an oven from room temperature to approximately 70° C while measuring the probe resistance. Then, one switches off the oven to observe the behaviour of the resistance of the tip while cooling down. From the cooling or heating slopes, one obtains the dependence of the resistance of the probe with the temperature, which will be used in our measurements. Figure 2.11 shows the electrical resistance of the probe versus temperature.

In order to extract the resistance of the probe, a linear fit of the data obtained for the cooling curve was done, where $R_{probe} = slope \cdot \Delta T + (R_{probe})_{T=0}$.

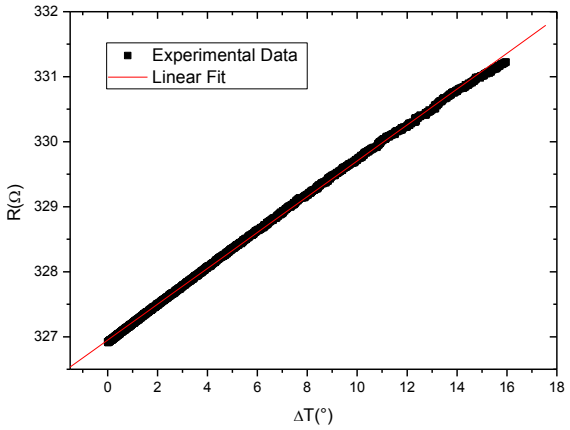

Figure 2.11. Linear fitting of the electrical resistance of the probe versus temperature.

From the fitting one obtains, $R_{probe} = (0.27 \pm 0.01) \cdot \Delta T + (326.95 \pm 0.01)\Omega$ where $(R_{probe})_{\Delta T=0} = (326.95 \pm 0.01)\Omega$ and the slope is $(0.27 \pm 0.01)\Omega \cdot K^{-1}$. However, the tip resistance measured from this fitting includes also the influence of the current limiters. Indeed, the probe resistance is considered as,

$$R_{probe} = (R_{NiCr} + R_{Pd}) + (R_{NiCr}\alpha_{NiCr} + R_{Pd}\alpha_{Pd})\Delta T \qquad (2.26)$$

where R_{NiCr} and α_{NiCr} are the resistance and thermal coefficient of the NiCr limiters and R_{Pd} and α_{Pd} are the resistance and thermal coefficient of the palladium tip. The palladium resistance of the probe, or tip resistance, is the one of interest because it is in charge of measuring the temperature variations on the surface sample. In order to measure the resistance of the NiCr limiters a specific platform was used, where the probe was held, a multi-meter and an optical microscope. The optical microscope was used to locate the NiCr limiters and assure good electrical contact with the multi-meter's probes. A value of $R_{NiCr} = (181.0 \pm 0.1)\Omega$ was found in such a way whilst the thermal coefficient was given in the data sheet of the probe, being $\alpha_{NiCr} = (2.4 \cdot 10^{-4} \pm 0.1 \cdot 10^{-4})K^{-1}$. Substituting these values into the Equation 2.26 given for the probe, one can determine the

resistance and thermal coefficient of the palladium tip, $R_{tip} = R_{Pd} = (145.9 \pm 0.1)\Omega$, and $\alpha_{tip} = \alpha_{Pd} = (1.59 \cdot 10^{-3} \pm 0.07 \cdot 10^{-3})\mathrm{K}^{-1}$.

Once the probe resistance is obtained, one should determine the current amplitude, I_a that passes through the tip. To this end, an equivalent electrical circuit (see Figure 2.12) that involves all the resistances found in the Wheatstone bridge is considered and is solved using the Kirchoff rules.

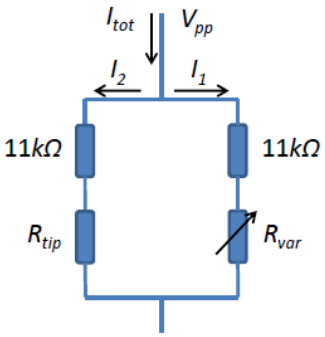

Figure 2.12. Equivalent electrical circuit of the Wheatstone bridge.

The Wheatstone bridge consists of two resistors of $11 \pm 0.1\mathrm{k}\Omega$, a potentiometer and the probe itself, which acts as another resistor. The potentiometer is set at the same value as the tip resistance, which was previously calculated, i.e., $R_{probe} = R_{potentiometer} = (326.95 \pm 0.01)\Omega$. Therefore, the currents at both branches are equal, $\mathrm{I}_1 = \mathrm{I}_2$, and the total resistance of the circuit is, $R_{total} = \frac{(R_{probe} + 11\mathrm{k}\Omega)^2}{2(R_{probe} + 11\mathrm{k}\Omega)}$. Then, the total current is $I = 2 \cdot I_1 = \frac{V}{R_{total}} = (811.5 \pm 0.3)\mu\mathrm{A}$. The current passing through the tip is then $I_0 = I_1 = (405.7 \pm 0.3)\mu\mathrm{A}$.

In order to calculate the amplification gain of the system, one substitutes the tip for a single wire at the Wheatstone bridge and a fixed resistor of $400 \pm 0.1\Omega$ is used instead of the potentiometer. The new equivalent circuit is shown in Figure 2.13.

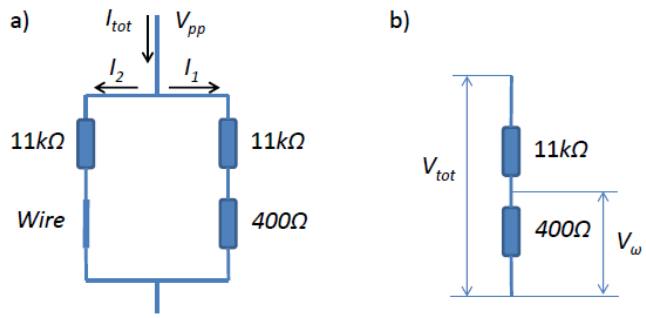

Figure 2.13. a) Equivalent electrical circuit of the Wheatstone bridge when substituting the SThM tip for a wire. b) Branch of the equivalent electrical circuit that involves the $(400\pm0.1)\Omega$ resistor and a $(11\pm0.1)\text{k}\Omega$ resistor.

The amplification is basically calculated from the relation, $K_{ampli} = \frac{(V_\omega)_{\text{measured}}}{(V_\omega)_{\text{theoretical}}}$, where $(V_\omega)_{\text{measured}}$ is the voltage measured for different ω whilst the $(\text{V}_\omega)_{\text{theoretical}}$ is the voltage expected. The theoretical value of the voltage is calculated from $(V_\omega)_{\text{theoretical}} = V_{\text{total}} \cdot \left(\frac{R_2}{R_1+R_2}\right)$ where R_2 is the $400\pm0.1\Omega$ resistor and R_1 is the $11\pm0.1\text{k}\Omega$ resistor.

Figure 2.14 shows the amplification module and phase shifts for different frequencies. This is important to determine the regions where the amplifier works without any attenuation of the signal, as well as the real amplification of the system and the phase shift of the signal.

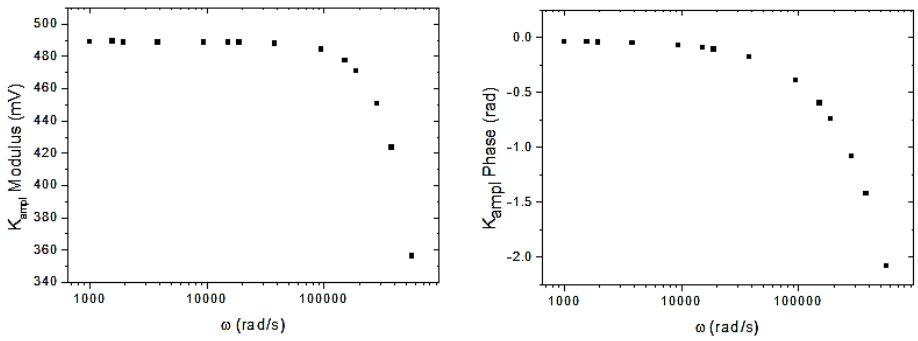

Figure 2.14. a) Module of the amplification system. b) Phase of the amplification system. In both graphs, the attenuation regime is clearly observed.

c) AC thermal model.

In the AC heating mode, an AC current, $I(t)=I_a \cdot \cos(\omega t)$, is passing through the probe and both a DC and AC temperature profile is developed. The DC contribution can be explained by the equations given in in section 2.2.1.4.1.1. However, one is now interested in operating in the AC regime.

In order to develop the AC heat transfer model for our Pd/SiO_2 probes, one first needs to know the geometrical, electrical and thermal properties of the tip. The geometrical characteristics of the tip can be simplified by considering the tip as a parallelepiped semi-infinite probe and due to its symmetry, only half of the tip (one arm) is studied. Moreover, regarding the thermal parameters, the heat diffusion length at the frequencies one uses is much larger than the thickness of the SiO_2 layer, which simplifies the thermal model. Figure 2.15a and 2.15b show SEM images of the shape of the tip, while Figure 2.15c is a drawing that corresponds to a simple representation of the Pd/SiO_2 layer.

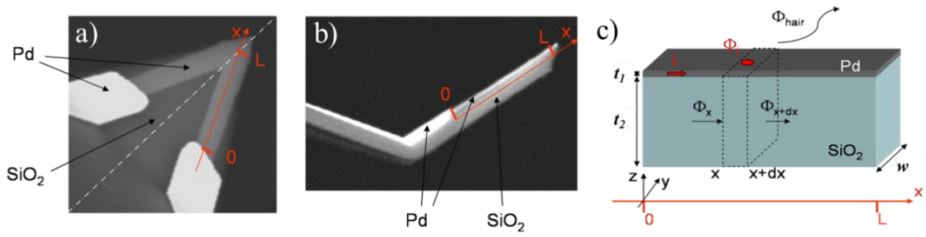

Figure 2.15. a) Front view of the Pd/SiO_2 tip. b) Lateral view of the tip. c) Schematic view of the Pd and SiO_2 layers of the tip and the parameters involved in the thermal probe characterization calculus. Figures taken from reference [23].

When the probe is heated due to the flowing current, it is assumed the temperature to be uniform at the probe and the system to be isothermal in the *y* and *z* directions. The Joule dissipation term on the tip is described as,

$$\phi_{Joule} = \frac{\rho_{ele1} \cdot dx \cdot I^2(t)}{A_1} \tag{2.27}$$

where ρ_{ele1} and A_1 are the electrical resistivity and the section of the Pd layer, respectively.

Then, it is considered a diffusive term referred to SiO_2 layer on the two sections at positions *x* and *x+dx* (see Figure 2.15c)

$$\emptyset_x = -k_2 A_2 \frac{\partial T}{\partial x}(x) \qquad \emptyset_{x+dx} = -k_2 A_2 \frac{\partial T}{\partial x}(x + dx) \tag{2.28}$$

where k_2 and A_2 are the thermal conductivity and the section of the SiO_2 film, respectively. The heat diffusion in the Pd film is voluntary neglected since it is very thin (about ten nanometers) and represents a barrier to heat diffusion compared to the 1µm thick SiO_2 layer.

The air convective heat losses are expressed as,

$$\phi_h = h_{air} \cdot p_2 \cdot dx \cdot \mathrm{T} \tag{2.29}$$

where h_{air} are the air convection losses coefficient and p_2 the SiO_2 layer perimeter.

Finally, the heat transfer model for the alternative (AC) regime part of the heat equation can be solved in Fourier space[23],

$$\frac{d^2T_{2\omega}}{dx^2} - \left(\frac{2i\omega}{a_2} + \frac{h_{air}\rho_2}{k_2A_2}\right)T_{2\omega} = -\frac{\rho_{ele1}I_a^2}{2k_2A_1A_2} \qquad (2.30)$$

where ω is the signal frequency and a_2 is the thermal diffusivity of the SiO_2 film, respectively.

Once the alternative heat equation for the tip is obtained, one can distinguish two different boundary conditions[23] for the two possible configurations; one when the probe is out of surface contact and another when the probe is in contact with the surface. This boundary conditions are summarized in Table 2.III.

Table 2.III. Boundary conditions for the probe.

Boundary Conditions	
Probe out of contact	Probe in contact
$\mathbf{T_{2\omega}(x=0)=0}$ $\mathbf{\frac{\partial T_{2\omega}}{\partial x}(x=L)=0}$	$-k_2A_2\frac{\partial T_{2\omega}}{\partial x}(x=L) = \frac{T_{2\omega}(x=L)}{R_{eq}}$

d) Sorting out the AC thermal equation.

In order to fulfill the first boundary condition, one must have the tip out of contact. This implies that the variation of temperature of the tip along the palladium film is null.

From solving the heat equation for these conditions one obtains the averaged 2ω-temperature of the probe,

$$< T_{2\omega} >= \frac{R_{tip}I_a^2}{4L^2k_2A_2}\frac{[-exp(2Lm)+1+Lm+Lm\,exp(2Lm)]}{Lm^3[1+exp(2Lm)]} \qquad (2.31)$$

where $m^2 = \left(\frac{2i\omega}{a_2}\right) + \left(\frac{h_{air}p_2}{k_2A_2}\right)$, L is the length of the tip and R_{tip} is the electrical resistance of the tip. Some of the parameters are well characterized but others, like the tip length or section, can change slightly between similar probes. Usually, the tip data sheet expresses

them as a range of values. However, the exact values are required for exact determination of the 3ω-voltage.

Experimentally, when the tip is *out of contact* from the surface of the sample, these probe parameters can be extracted via a two steps procedure[23]. In the first step, the probe is in vacuum, which means that $h_{air} = 0$, and the experimental data of the 3ω voltage amplitude and phase are obtained for different frequencies. Then, these experimental data are fitted with the theoretical model explained previously in section 2.2.1.4.1.2.b, including the limiters and signal distortion corrections. From this fitting, parameters related to the geometry, electrical and thermal properties of the tip are extracted. In the second step, the tip is kept under atmospheric conditions and experimental data of the 3ω voltage amplitude and phase are taken again. Using the probe parameters identified in the previous step and fitting the experimental data with the theoretical values, it is possible to obtain the convection coefficient of the air, h_{air}. Figure 2.16 shows the results of the theoretical fitting of the experimental data corresponding to the phase and amplitude of the 3ω signal are shown. Table 2.IV summarizes the parameters that can be identified with this code as well as the values that were measured experimentally or obtained from literature.

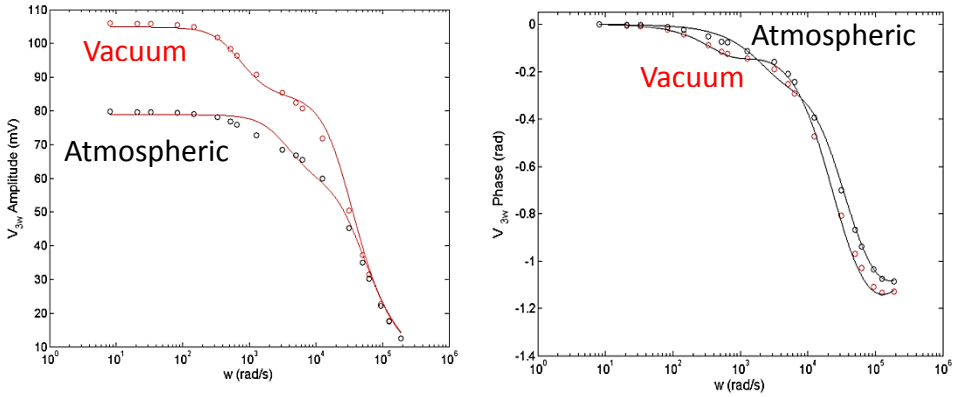

Figure 2.16. Experimental $V_{3\omega}$ modulus and phase experimental curves and fits under vacuum (P=10^{-5} Torr) and under atmospheric conditions: circles are used for experimental data and continuous lines for the theoretical fittings.

Table 2.IV. Summary of the results obtained for geometrical, electrical and thermal parameters of our Pd/SiO_2 probe. Some of them are measured (meas.) and other identified (id.) with the code and others are taken from literature (lit.).

Elements	Symbol	Parameter	Atmospheric	Vacuum	Determination
Pd/SiO_2 probe	L	SiO_2 Length (m)	$6.5\cdot10^{-6}$		Id.
	w	SiO_2 Width (m)	$5.9\cdot10^{-6}$		Id.
	t	SiO_2 Thickness(m)	$1\cdot10^{-6}$		Meas.
	k_2	SiO_2-Thermal Conductivity ($W\cdot K^{-1}\cdot m^{-1}$)	1.3		Lit.
	a_2	SiO_2-Diffusivity ($m^2\cdot s^{-1}$)	$8.6\cdot10^{-7}$		Lit.
	h_{air}	Heat Transfer Coefficient ($W\cdot K^{-1}\cdot m^{-2}$)	16000	0	Id.
	I_a	Current amplitude (A)	$405\cdot10^{-6}$		Meas.
	R_{tip}	Pd resistance (Ω)	145.95		Meas.
	TCR	Pd temperature coefficient (K^{-1})	$1.6\cdot10^{-3}$		Meas.
Current limiters	G	Gain (V)	0.03		Id.
	ω_c	Cut off pulsation ($rad\cdot s^{-1}$)	3500	800	Id.
Generator distortion	V_D	Distortion modulus (V)	0.006		Id.
	Φ_D	Distortion phase (rad)	-0.5		Id.

Once the different tip parameters are obtained, one must solve the heat equation considering the second boundary equations. This boundary condition corresponds to the situation of the tip *in contact* with the surface of the sample. The solution of the averaged 2ω-temperature is then expressed as [23],

$$< T_{2\omega} >= \frac{R_{tip} I_a^2}{4L^2 k_2 A_2} \frac{\frac{[4\,exp(mL)-2+Lm\,exp(2Lm)-Lm-2\,exp(2mL)\,]}{R_{eq} m k_2 A_2}+[mL+mL\,exp(2mL)-exp(2mL)+1]}{\frac{[exp(2Lm)-1]}{R_{eq} m k_2 A_2}+1+exp(2mL)} \quad (2.32)$$

Once this averaged 2ω-temperature is substituted into the 3ω-voltage equation, the $V_{3\omega} = K_{ampli}(\omega = 0)\frac{R_{Tip}\cdot TCR\cdot I_a}{2} < T_{2\omega}(\omega) > + \frac{G}{1+i\frac{\omega}{\omega_c}} + V_D exp(i\emptyset_D)$, is obtained, in which the correlation of the 3ω

voltage signal detected by SThM with the equivalent thermal resistance, R_{eq}, of the sample is expressed. Figure 2.17 shows this correlation when one uses a frequency of 1 kHz, which is the one that has been selected during the experiments.

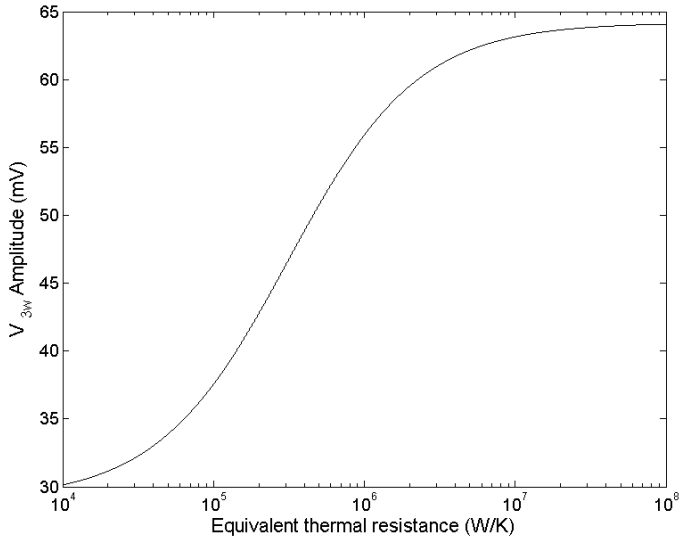

Figure 2.17. 3ω bridge voltage $V_{3\omega}$ as a function of the equivalent thermal resistance, R_{eq}.

Similar to the Wollaston probe case, once the thermal resistance of the sample and the thermal exchange radius *b* of the probe are known, if the sample heat transfer can be assumed to be equivalent to semi-infinite conduction from a uniformly heated disk on its surface, the thermal conductance of the sample is given by Equation 2.22.

This method was used to measure the thermal conductivity of individual organic and inorganic nanowires and get a thermal map of them, as it is shown in Chapter 3.

2.2.2. Four Probe Station: Electrical conductivity measurements.

A four probe station[9] is used to determine the resistance of a specimen by passing current across two probes while measuring the voltage drop across the other two. These probes can be micro-positioned to be located precisely at specific areas of the sample. This method can determine the resistance of films in both in- and cross-plane directions without the influence of the contact resistances between probes and sample and other parasitic resistances from the system. However, other effects such as the non-uniform spreading of the current across the film and within electrodes, and the influence of the contact resistances between the interfaces must be taken into account, which requires a careful analysis of the electric transport in the sample.

This technique has been used to measure the electrical conductivity of Bi_2Te_3 films in cross-plane configuration.

2.2.3. Seebeck microprobe: Seebeck coefficient measurements.

The Seebeck microprobe[24] is an instrument to measure the Seebeck coefficient with spatial resolution. This Seebeck coefficient map gives information on the homogeneity or distribution of the components over a certain area.

In this system, a heated probe tip is positioned onto the surface of a sample, as shown in Figure 2.18. The probe is a thermocouple type-T (Cu-CuNi) that measures the temperature at the top of the sample. An identical thermocouple is in charge of measuring the temperature underneath the sample. The sample is in good electrical and thermal contact with the probe and a heat sink underneath it. If one connects the copper wires (Cu-Cu) and the constantan (CuNi-CuNi) wires that come from the thermocouple of the probe and the one underneath the sample, one can measure the voltages U_0 and U_1 (Figure 2.18).

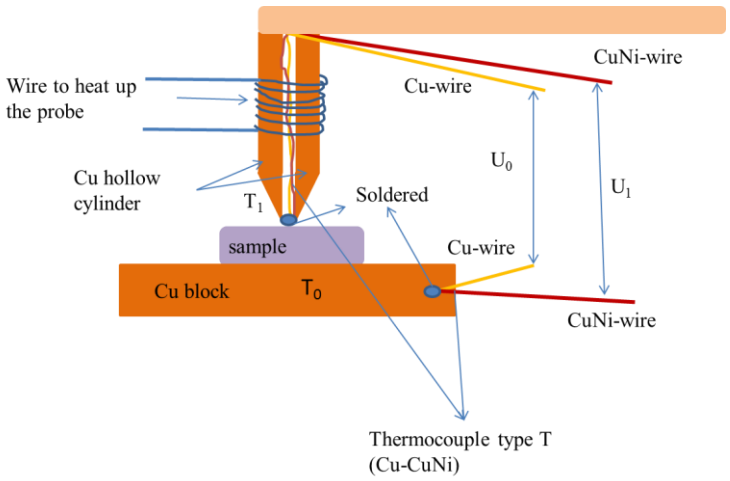

Figure 2.18. Schematic view of the Seebeck microprobe. Figure adapted from reference [24].

These voltages can be expressed in terms of the Seebeck coefficients of the sample, S_{sample} , copper, S_{Cu}, and the constantant, S_{CuNi}, through the expression,

$$U_0 = \left(S_{sample} - S_{Cu}\right) \cdot (T_1 - T_2) \tag{2.35}$$

$$U_1 = \left(S_{sample} - S_{CuNi}\right) \cdot (T_1 - T_2) \tag{2.36}$$

Using these equations one can yield to an expression for the Seebeck coefficient of the sample,

$$S_{sample} = \frac{U_0}{U_1 - U_0}(S_{Cu} - S_{CuNi}) + S_{Cu} \tag{2.37}$$

Mounting this probe into a three dimensional micro-positioning system allows the determination of the Seebeck coefficient of a sample at local areas. As a result, a two dimensional image of the Seebeck coefficient of the sample surface can be obtained.

A commercial Seebeck Microprobe from the Polytechnic University of Barcelona was used to measure the Seebeck coefficient of films.

2.2.4. COMSOL/Matlab software to support experimental results.

Some experimental measurements required of specific analysis that concerned the use of simulating software in order to extract accurate results. COMSOL® Multiphysics[25] is a finite element analysis, solver and simulation software for various physics and engineering applications, especially coupled phenomena or multiphysics. This tool within the help of a data sheet platform, like Origin® or Excel®, and multi-paradigm numerical computing environment and programming language, like Matlab® [26], were very useful to determine and validate thermal and electrical properties of films and nanowires as well as to obtain theoretically specific details of the conditions and parameters to measure for certain complex experiments, such as the Harman technique (Chapter 4) or the development of a 2D heat transfer model to determine the thermal resistance of the sample under study with SThM (Chapter 3). The use of programs such as COMSOL® requires of a full understanding of the theory and physics that accompanies complex experimental measurements. One must take into account all the details, like the possible presence of thermal or electrical contact resistances, particular boundary equations, introduction of complex partial differential equations to simulate particular effects, combination of different physical phenomenon, etc.

References

1. S. N. S. R.K. Pandey, S. Chandra, *Handbook of Semiconductor Electrodeposition*, Taylor & Francis, 1996.
2. K. Wasa, *Handbook of Sputter Deposition Technology: Fundamentals and Applications for Functional Thin Films, Nano-materials and MEMS*, William Andrew, 2012.
3. R. Leuschner and G. Pawlowski, in *Handbook of Semiconductor Technology*, Wiley-VCH Verlag GmbH, 2008, pp. 177-263.
4. D. M. Mattox, *Handbook of Physical Vapor Deposition (PVD) Processing*, Elsevier Science, 2010.
5. I. D. Marinescu, E. Uhlmann and T. Doi, *Handbook of Lapping and Polishing*, CRC Press, 2015.
6. J. Orloff, L. Swanson and M. Utlaut, *High Resolution Focused Ion Beams: FIB and its Applications: Fib and Its Applications : The Physics of Liquid Metal Ion Sources and Ion Optics and Their Application to Focused Ion Beam Technology*, Springer US, 2003.
7. H. O. Pierson, *Handbook of Chemical Vapor Deposition, 2nd Edition: Principles, Technology and Applications*, Elsevier Science, 1999.
8. G. Harman and D. DESIGN, *Wire Bonding in Microelectronics 3 Edition By George Harman: Wire Bonding in Microelectronics, Third Edition*, McGraw-Hill, 2010.
9. Y. Nishi and R. Doering, *Handbook of Semiconductor Manufacturing Technology, Second Edition*, CRC Press, 2007.
10. J. Cazes, *Analytical Instrumentation Handbook, Third Edition*, CRC Press, 2004.
11. N. Yao and Z. L. Wang, *Handbook of Microscopy for Nanotechnology*, Kluwer Academic Publishers, 2006.
12. M. M. Rojo, J. Martin, S. Grauby, T. Borca-Tasciuc, S. Dilhaire and M. Martin-Gonzalez, *Nanoscale*, 2014, **6**, 7858-7865.
13. I. R. Lewis and H. Edwards, *Handbook of Raman Spectroscopy: From the Research Laboratory to the Process Line*, CRC Press, 2001.
14. P. J. Eaton and P. West, *Atomic force microscopy*, Oxford University Press Oxford, 2010.
15. L. A. Bottomley, *Analytical chemistry*, 1998, **70**, 425R-475R.
16. B. Bhushan and M. B. Palacio, in *Encyclopedia of Nanotechnology*, B. Bhushan, Springer Netherlands, 2012, 150, 1173-1179.

17. J. Colchero, A. Gil and A. M. Baró, *Physical Review B*, 2001, **64**, 245403.
18. S. E. Lyshevski, *Nano and Molecular Electronics Handbook*, CRC Press, 2007.
19. T. Borca Tasciuc, *Annual Review of Heat Transfer*, 2013, **16**, 211-258.
20. P. G. Royall, D. Q. M. Craig and D. B. Grandy, *Thermochimica Acta*, 2001, **380**, 165-173.
21. Y. Zhang, *Applied Physics Letters*, 2010, **96**, 062107-062103.
22. T. Borca-Tasciuc, D. A. Borca-Tasciuc and G. Chen, *A photo-thermoelectric technique for anisotropic thermal diffusivity characterization of nanowire/nanotube composites*, Symposium IEEE, 2005.
23. E. Puyoo, S. Grauby, J.-M. Rampnoux, E. Rouviere and S. Dilhaire, *Journal of Applied Physics*, 2011, **109**, 024302-024309.
24. G. K. D. Platzek, C. Drasar, E. Müller, *Materials Science Forum*, 2005, **492-493**, 587-592.
25. R. W. Pryor, *Multiphysics Modeling Using COMSOL: A First Principles Approach*, Jones & Bartlett Learning, 2011.
26. S. Attaway, *Matlab: A Practical Introduction to Programming and Problem Solving*, Elsevier Science, 2013.

Chapter 3

Thermal Transport Measurements of Nanostructures

The interest of determining the thermal conductivity of different materials resides in their wide variety of technological applications that range from thermoelectrics to thermal insulation, among others. In thermoelectricity, the efficiency is related to the figure of merit, zT, which is inversely proportional to the thermal conductivity, k, of the thermoelectric material. Therefore, the lower the thermal conductivity, the higher the efficiency of the material is. As it was mentioned in the Introduction Chapter, in order to reduce the thermal conductivity of the material, one strategy consists of reducing its spatial dimensionality through the nanostructuration, obtaining structures such as thin films (2D) or nanowires (1D). The thermal conductivity reduction can be explained by the alteration of the phonon transport at the nanometric scale because there appear several effects, such as changes in phonon dispersion relation and increased phonon boundary scattering[1, 2, 3, 4].

The thermal characterization of those nano-structures is of major importance and requires of techniques able to reach nano-metric lateral spatial resolution. Optical methods, such as infrared thermometry, visible thermos-reflectance or interferometry, which are diffraction limited, cannot reach this resolution. Since its invention in 1986[5], the scanning thermal microscopy (SThM) [6, 7, 8] is presented as one of the most efficient techniques to study thermal transport in nano-objects and nano-materials.

In this chapter, a SThM working in DC and AC modes is used to determine the thermal conductivity of films, nanowires and other nano-structures.

3.1. Thermoresistor probe calibration: thermal exchange radius and contact resistance.

In SThM measurements, there are two critical parameters that must be obtained in order to determine the thermal conductivity of the sample under study. These parameters are the thermal exchange radius, b (Equation 2.23), and the thermal contact resistance, R_C^{th}, between the probe and the sample (Equation 2.21). It is important to take into account that the thermal exchange radius also indicates the thermal lateral resolution of the probe, which is essential to determine the smallest thermal features that one can observe with a particular probe.

3.1.1. Wollaston thermoresistor probe.

In order to obtain the thermal exchange radius and the contact resistance of a Wollaston probe, it is first necessary to characterize certain geometrical, electrical and thermal parameters of the probe. Some of these parameters were extracted from literature, like the thermal conductivity or temperature coefficient of resistance, but others can be experimentally measured, like the length, diameter, heat transfer

coefficient and nominal resistance of the probe. Table 3.I shows these results and how they were obtained for two Wollaston probes, probe 1 and probe 2.

Table 3.I. Summary of the results obtained for geometrical, electrical and thermal parameters of two Wollaston probes used in this chapter.

Parameter	Probe 1	Probe 2	Obtained from
Length (l_p)	206.48 µm	212.00 µm	SEM image
Diameter (d_p)	4.96 µm	4.90 µm	SEM image
Thermal Conductivity (κ_p)	38.0 $W \cdot m^{-1} \cdot K^{-1}$	38.0 $W \cdot m^{-1} \cdot K^{-1}$	Manufacturer data-sheet
Heat Transfer Coefficient (h)	5233 $W \cdot m^{-2} \cdot K^{-1}$	2047 $W \cdot m^{-2} \cdot K^{-1}$	Experiment
Temperature Coefficient of Resistance (TCR)	0.00165 K^{-1}	0.00165 K^{-1}	Manufacturer data-sheet /Experiment
Nominal Electrical Resistance (R_0)	2.19 Ω	2.10 Ω	Experiment

After, we measured the 3ω voltage response of the Wollaston probe at 10 Hz when it is in contact with different calibration samples, whose thermal conductivities range from 0.36 to 1.1 $W \cdot K^{-1} \cdot m^{-1}$. The measured reference samples are poly(3,4-ethylenedioxythiophene) (also known as PEDOT, with κ = 0.36 $W \cdot K^{-1} \cdot m^{-1}$), polyaniline (PANI) with 5% and 7% graphene nano-platelets (κ = 0.49 $W \cdot K^{-1} \cdot m^{-1}$and 0.65 $W \cdot K^{-1} \cdot m^{-1}$, respectively)[23], p-type bulk Bi_2Te_3 (doped with Sb to ensure p-type formation) with κ = 1.0 $W \cdot K^{-1} \cdot m^{-1}$, and borosilicate glass with κ = 1.1 $W \cdot K^{-1} \cdot m^{-1}$. We call them reference samples, because they have been measured by other lab and different techniques and their thermal conductivity values are well known. Figure 2.7b showed the kind of curves that were obtained. Using the equations presented in the Chapter 2 for the DC heating transfer model (Equation 2.23), the thermal resistance of the sample can be calculated. If the thermal conductivity of the sample under study is known, one can

use this value of k within an algorithm to determine the probe thermal exchange radius, b, and the thermal contact resistance between the probe and the sample, R_C^{th}, for a set of samples enclosed in a particular range of thermal conductivities. Figure 3.1 shows the representation of these values, one versus the other, for the calibration samples described above. The intersection of the curves of well-known thermal conductivity samples gives the b and R_C^{th} values [9]. The fact that samples with thermal conductivities that go from 0.36 to 1.1 $W \cdot K^{-1} \cdot m^{-1}$ intersect in the same point in Figure 3.1, supports the assumption that R_C^{th} and b remain constant for low thermal conductivity samples. Generally, the range at which this premise can be considered valid goes from 0.1 to 2.5 $W \cdot K^{-1} \cdot m^{-1}$ [10]. In this Chapter, all the samples studied lie within these range of thermal conductivities. However, if one would be interested in measure a sample with a thermal conductivity higher than this range, a new intersection between b and R_C^{th} should be found in a similar way to those presented in Figure 3.1, but now considering a set of calibration samples that fit within the new higher thermal conductivity [11].

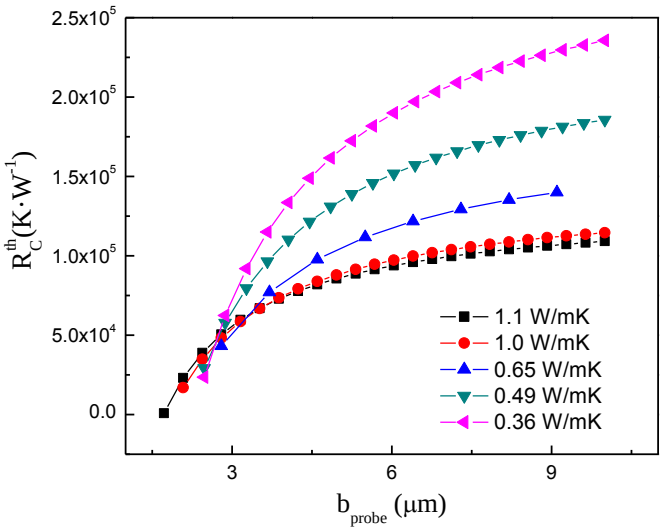

Figure 3.1. R_C^{th} and b for several calibration samples in thermal conductivity range of interest.

The Wollaston probe calibration for probe 1 of Figure 3.1 shows that the curves intersect around $b = 2.8 \pm 0.3$ μm and this corresponds to $R_C^{th} = 47500 \pm 3600\ \mathrm{K \cdot W^{-1}}$. These parameters might vary slightly for different Wollaston probes due mainly to their geometrical differences. Similarly to probe 1, the thermal exchange radius and contact resistance were determined for probe 2, those values were $b = (2.72 \pm 0.08)$ μm and $R_C^{th} = (197035 \pm 1400)\mathrm{K \cdot W^{-1}}$. The experimental error for both the thermal exchange radius and the contact resistance was calculated from the deviation of the crossing points between calibration sample curves, as can be seen in Figure 3.1.

The thermal measurements carried out with the Wollaston probe have been performed in DC mode at room temperature, as explained in Section 2.2.1.4.1.1., at the Instituto de Microelectrónica de Madrid (IMM-CSIC) under the collaboration of the group of Professor Theodorian Borca Tasciuc of the Rensselaer Polytechnic Institute (RPI-USA).

3.1.2. Pd/SiO_2 thermoresistor probe.

As in the Wollaston probe, the thermal exchange radius and the contact thermal resistance of Pd/SiO_2 probes are critical parameters that must be considered in order to determine the thermal conductivity of the sample under study.

The experimental procedure used to obtain the thermal exchange radius of the Pd/SiO_2 probe is different to the Wollaston one, although it could be used for both. It consists of making a thermal scan with the Pd/SiO_2 probe on an abrupt step made of a 200 nm thick oxide layer on a Si substrate[12]. When the probe placed upon the oxide layer is shifted towards the step, the tip-to-sample thermal exchange surface is truncated, which causes an increase of the tip's temperature variations until a maximum value is reached when the contact point is at the edge of the step. Measuring the distance from the position for which the $V_{3\omega}$ signal starts to increase to the position for which the signal is maximal leads to the tip-to-sample thermal exchange radius, b. This value can vary from one probe to another and must be studied prior to each thermal scan. Figure 3.2 shows a schematic view of this process even for a Pd/SiO_2 and a Wollaston probes [12]. In this figure, it is clearly seen that the thermal resolution is higher for a Pd/SiO_2 probe than for a Wollaston one, because it has a smaller thermal exchange radius. While Wollaston probes present thermal exchange radius in the range of a few micrometers (Section 3.1.1.), measurements on different Pd/SiO_2 probes resulted in values between ~80 nm to ~200 nm. As a consequence, Pd/SiO_2 probes make a possible analysis of thermal regions in the range of nanometers and they can be used to obtain thermal maps of nanowires, as it will be shown in the next sections.

Even though the methods used to calculate b for the Wollaston and Pd/SiO_2 probes are different, both are complementary and can be considered for any thermal probe. The advantage of this method in comparison with the one previously used for the Wollaston probe is the possibility of measuring the thermal exchange radius from a quick thermal scan, without the need of measuring several calibration samples. On the contrary, the other method determines accurately, and

for a particular range of thermal conductivities, the thermal exchange radius and the thermal contact resistance, simultaneously.

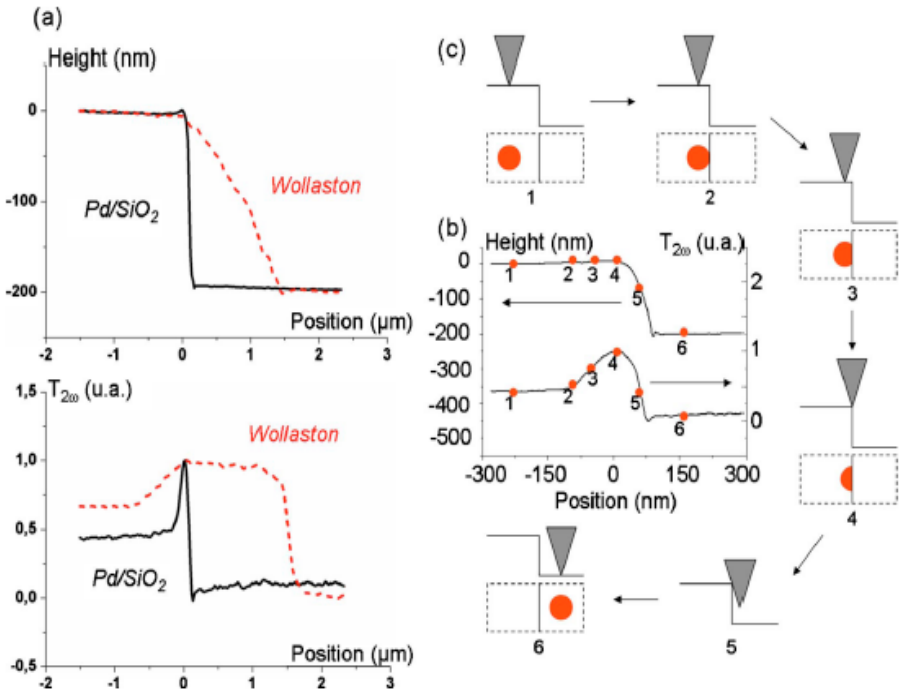

Figure 3.2. Topographic and thermal profiles obtained with the two different probes scanning an abrupt oxide on silicon step. (a) Comparison of the profiles: the dotted line and the full line correspond to the profiles obtained respectively with the Wollaston and the Pd/SiO_2 probes. (b) Zoom on profiles obtained with the Pd/SiO_2 probe. (c) Schematic side view of the probe and schematic top view of the thermal exchange radius. Figure taken from reference [12].

Once the thermal exchange radius is known, the thermal contact resistance between the Pd/SiO_2 probe and the sample can be determined from a reference sample with a well-known thermal conductivity, $k_{reference}$, using the Equation 2.21 as follows,

$$R_C^{th} = R_{probe,exp}^{th} - R_{sample\ reference}^{th} \quad (3.1)$$

where $R_{sample\ reference}^{th} = \frac{1}{4 \cdot k_{reference} \cdot b}$. The thermal exchange radius error is determined from the deviation obtained for several profiles obtained at the step, while the contact resistance is obtained from standard deviation of this value measured at different location of the reference sample.

The thermal measurements carried out with the Pd/SiO_2 probe have been performed in AC mode at room temperature, as explained in Section 2.2.1.4.1.2., at the University of Bordeaux in the group of Professor Stefan Dilhaire.

3.1.3. Technique accuracy.

Regarding the Wollaston probe (DC mode), in order to determine the thermal resistance of the sample under study, the probe is located at different positions of the sample. At that point, a 3ω voltage curve versus frequency, similar to those presented in Figure 2.7b, were taken. Then, these signals were analyzed at 10 Hz using the equations given by the DC mode, as at this low AC frequencies the DC mode is a good approximation (Section 2.2.1.4.1.1.). Next, the experimental thermal resistance at each location was obtained. From these three measurements, a mean experimental thermal resistance was determined, while the deviation between them indicate the experimental error. Finally, the thermal conductivity of the sample is obtained from Equation 2.23, while its experimental error is calculated from propagation of errors of the averaged thermal resistance within the error of the thermal exchange radius.

Regarding the Pd/SiO_2 probe (AC mode), it was used to carry out thermal or 3ω-voltage (usually around 1 kHz) maps of nanowires embedded in a matrix. From the 3ω-voltage data obtained from the maps and using the Equations presented in Section 2.2.1.4.1.2. for AC mode, a mean thermal resistance within its standard deviation can be obtained from a statistical study over several nanowires. Then, the thermal conductivity of the sample can be determined from Equation 2.23 within its error calculated from propagation of errors.

In both techniques, the error presented for these thermal measurements is around 10% approximately. This error is in the range of magnitude of other thermal measurement techniques. Moreover, most of the measurements obtained in this PhD work with SThM were cross-checked with other techniques, such as the photoacoustic (PA) or time domain thermoreflectance (TDTR), resulting in good agreement with differences below 15%.

3.2. Thermal conductivity measurements of films.

Thermal conductivity measurements of films were carried out using a Wollaston probe working in DC mode (see Section 2.2.4.1.1.). Following the calibration procedure described in section 3.1.1., the thermal exchange radius and contact resistance of probe 1 was found. With this probe, we were able to determine the thermal conductivity of inorganic films, like SiGe, and organic films, like PCDTBT.

3.2.2.1. Inorganic films: SiGe films.

In this section, the thermal conductivity of silicon germanium (SiGe) films are studied with the SThM. Silicon is one of the most abundant semiconductors in the world, with a low manufacturing cost and non-toxic properties, and its combination with germanium make it to present improvements in terms of transport properties or efficiency, among others. Regarding the transport properties for SiGe[13] bulk and films, it presents a low band gap (~1-2 eV) at room temperature with high electrical conductivity and Seebeck coefficient and a relatively low thermal conductivity. Compared to bulk or films made of silicon, it presents the advantage of presenting a much lower thermal conductivity without modifying much the electrical conductivity[13]. Photovoltaic[14], metal-oxide-semiconductor field-effect transistors (MOSFETs)[14] or thermoelectric applications[13] are some of the most known ones for this material. From the point of view of thermoelectricity, it can present high figures of merit especially at high working temperatures (800 K - 1000 K).

The SiGe is polycrystalline, with a cubic and isotropic structure. In reference[13] is shown that the nano-composite that results in lowest thermal conductivity values presents an optimum stoichiometry of $Si_{0.8}Ge_{0.2}$ and a crystalline orientation of [1 1 1]. Although pure $Si_{0.8}Ge_{0.2}$ presents a very low electrical conductivity, it can be doped with a low proportion of boron or phosphorous that result in p- and n-type $Si_{0.8}Ge_{0.2}$ films with higher electrical conductivities while keeping low thermal conductivities. Most of the techniques used to obtain p-

and n- type materials, such as molecular beam epitaxial growth (MBE)[15] or chemical vapor deposition (CVD)[16], require of high temperature or mixture of gases which make difficult the doping. Consequently, it becomes challenging to keep the proper level of doping when growing high quality films from the point of view of the stoichiometry and the crystalline orientation. Rowe *et al* [13] reported values of the thermal conductivity between 4 - 5 $W \cdot K^{-1} \cdot m^{-1}$ at room temperature for p- and n- type $Si_{0.8}Ge_{0.2}$ films grown through spark plasma sintering (SPS), showing a drastic reduction in comparison to bulk silicon at room temperature (~150 $W \cdot K^{-1} \cdot m^{-1}$)[17].

In order to overcome these difficulties, two p-types $Si_{0.8}Ge_{0.2}$ films doped with boron, were grown via metal induced crystallization (MIC) through sputtering process[18]. For that purpose, a glass substrate with 25 nm of gold on top was used to grow a $Si_{0.8}Ge_{0.2}$ film by sputtering. The metal induces the crystallization of the film when it migrates across the silicon-germanium layers through thermal processes. The main advantage of the MIC process comes from the reduction of the needed temperature for crystallizing the material. This avoids the loss of the doping. The thermal treatments of the two films grown under the MIC technique were different. While in one of them the substrate was heated at 500 ºC during the deposition of the film (*in-situ* thermal treatment), the other one was thermal annealed at 500 ºC in a controlled atmosphere furnace (rapid thermal annealing, RTA) after it was grown (*ex-situ* thermal treatment). This way of growing $Si_{0.8}Ge_{0.2}$ films and the different thermal treatments are expected to influence its thermal conductivity[18]. The mean roughness of the flattest part of the films were measured by taking topographic images with an atomic force microscopy (AFM), resulting in around 15 nm and 6 nm for the *in-situ* and *ex-situ* films, respectively. During the MIC growing process, phase segregation is produced. Figure 3.3a and 3.3b a topographic AFM images of the clusters formed in the *in-situ* and ex-situ films, respectively. The diameters of the clusters vary from 1 µm to 5 µm, while its height from 100 nm to 350 nm.

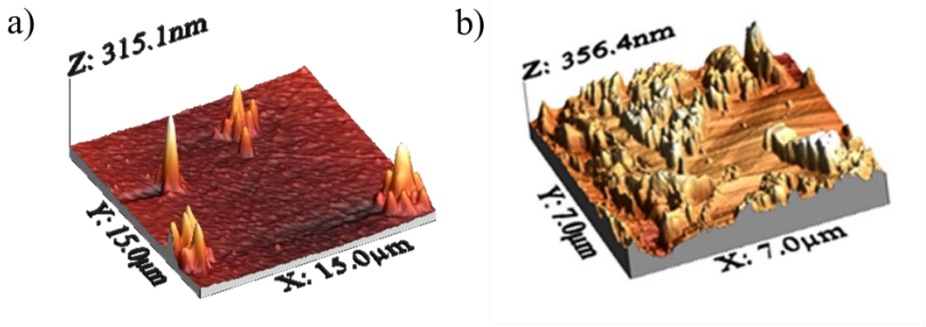

Figure 3.3. a) and b) show three dimensional AFM topographic images of the *in-situ* and *ex-situ* thermal treated $Si_{0.8}Ge_{0.2}$ films, respectively, where clusters in shape of mountains can be observed.

In order to measure the thermal conductivity of those samples, we approached our Wollaston probe 1 (Section 3.1.1.) to three different locations of the sample surface. In these three locations, we took a 3ω voltage curve versus frequency, similar to those presented in Figure 2.7b and analyze the data obtained at 10 Hz. Using the equations given in the DC mode the experimental averaged thermal resistance with their standard deviations was determined. In order to get the thermal resistance of the intrinsic sample, once the measured thermal resistance was obtained, we used Equation 2.21 and subtracted to it the thermal contact resistance for probe 1 determined in Section 3.1.1. It gave a result of $R^{th}_{sample} = 65612 \pm 5885\ \mathrm{K \cdot W^{-1}}$and $R^{th}_{sample} = 59674 \pm 3228\ \mathrm{K \cdot W^{-1}}$ for the *in-situ* and *ex-situ* thermal treated samples, respectively. The thicknesses of the films were 1.4 μm for the *in-situ,* while 1.8 μm for *ex-situ sample*, respectively. For these thicknesses the obtained thermal resistance might be influenced by the substrate presence (see end of Section 2.2.1.4.1. 1.). Consequently, Equation 2.23 cannot be directly applied and instead a heat transfer model that considers the effects of the substrate must be used.

For that purpose, a finite element modeling with COMSOL Multiphysics® was developed to determine the thermal conductivity of the $Si_{0.8}Ge_{0.2}$ films. From the geometrical point of view, a total sample area of 25 μm^2 was considered for the film and the substrate, but in order to increase the simulation speed, the symmetry of the sample

facilitate the simulation as only a fourth of the total sample area can be considered (Figure 3.4a). Then, symmetry boundary conditions were selected in its internal walls while in the external wall, open boundary domain. Then, the thickness of the $Si_{0.8}Ge_{0.2}$ film was set according to the ones measured for *in-situ* and *ex-situ* cases, while the length of the substrate remained fixed to 10 µm and its bottom temperature set to room temperature (293.15 K). The thermal resistance at the interface between the film and the substrate can be considered negligible, because of the good wet-out and flat surface achieved at the interface by the MIC processes [19]. A convection heat coefficient on the sample top surface of $h = 5\ W \cdot K^{-1} \cdot m^{-2}$ was used to simulate the effects of the surrounding air. Regarding the material properties, the thermal conductivity of the glass substrate underneath the sample was known and fixed to $1.1\ W \cdot K^{-1} \cdot m^{-1}$, while the thermal conductivity of the $Si_{0.8}Ge_{0.2}$ film was varied.

In order to simulate the heating of the SThM probe, a circular Gaussian heat source, in similitude with the realness, with an applied power of $1 \cdot 10^{-5}$ W was defined on top of the film. As in the experiment, the same thermal exchange radius as the one given for Wollaston probe 1 was used. Then, by determining the maximum temperature, T_{max}, reached at the center of the disc heat source for the different thermal conductivities of the sample, the thermal resistance of the $Si_{0.8}Ge_{0.2}$ film can be obtained from the expression, $R_{therm}^{simul} = \frac{T_{max} - T_{room}}{\dot{Q}}$, where T_{room} is the room temperature and $\dot{Q}$ is the heat power applied in the simulation. To perform this simulation, the "Heat Transfer in Solids" module in COMSOL Multiphysics® was used in order to solve the stationary equation of heat for solids. Figure 3.4a shows the 3D heat transfer graphical simulation obtained for the for *ex-situ* $Si_{0.8}Ge_{0.2}$ film with film thickness 1.8 µm on a glass substrate. Figure 3.4b and Figure 3.4c represents the simulated (red line) and experimental (black line) thermal resistances of the *in-situ* and *ex-situ* $Si_{0.8}Ge_{0.2}$ films, whose line crossing determines their thermal conductivities.

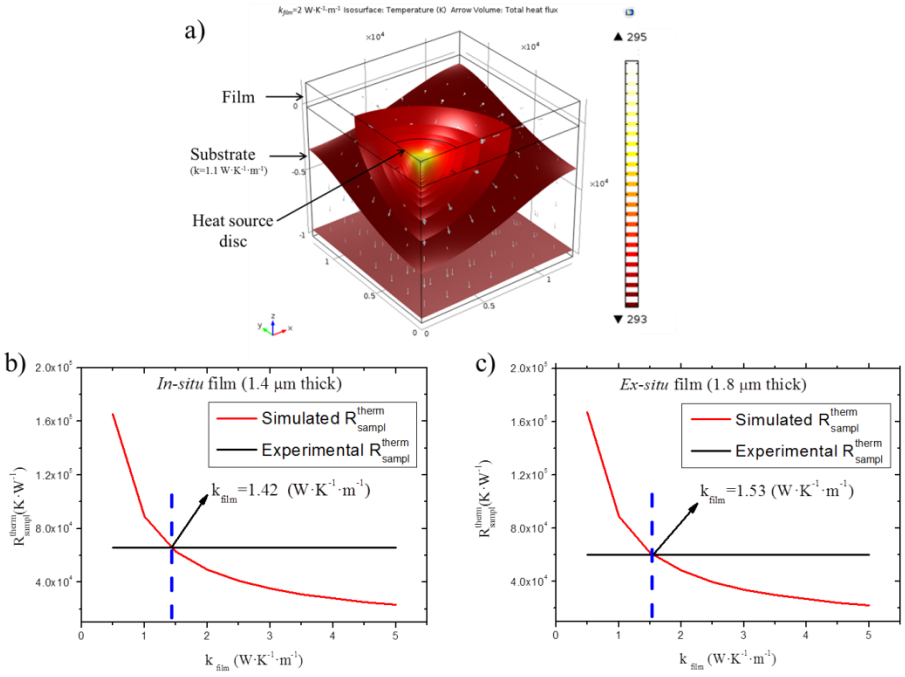

Figure 3.4. a) Temperature iso-surfaces and total heat flow (arrows) when a heat source with a radius similar to the thermal exchange radius is positioned on top of the film. b) and c) show the R^{th}_{sample} obtained from the simulation for different film thermal conductivities (red line) versus the R^{th}_{sample} experimental (black line) for both *in*- and *ex*-situ thermal treated films, respectively. The crossing point between the lines gives the value of the thermal conductivity of the film[11].

Finally, the results for the thermal conductivity of *in-situ* and *ex-situ* $Si_{0.8}Ge_{0.2}$ films, within their errors and taking into account the influence of the substrate, are summarized in Table 3.II.

Table 3.II. Thermal conductivity results for *in-situ* and *ex-situ* $Si_{0.8}Ge_{0.2}$ films.

Thermal treatment (500 ºC)	Thickness (µm)	Thermal conductivity ($W \cdot K^{-1} \cdot m^{-1}$) (Room Temperature)
In-situ	1.4±0.1	1.42 ± 0.12
Ex-situ	1.8±0.2	1.53 ± 0.31

The results of thermal conductivity seem to be lower than those reported in the literature (4 - 5 $W \cdot K^{-1} \cdot m^{-1}$) [13] for other $Si_{0.8}Ge_{0.2}$ thin films. However, recent works on SiGe nanowires have shown values of thermal conductivity ~ 1.2 $W \cdot K^{-1} \cdot m^{-1}$, which are similar to our results for films. This reduction of thermal conductivity in NW was associated to the high-frequency phonons that are scattered by the Ge atoms behaving as impurities in addition to the low-frequency phonon boundary scattering, which were associated to the size confinement of the material. Nevertheless, in our case, it is believed that this reduction on the thermal conductivity is related to the increase of phonon scattering at grain boundaries occurring due to the presence of clusters produced during the metal induced crystallization process, as it was detected by AFM topographic images, as shown in Figure 3.3a and 3.3b, and confirmed by Raman spectroscopy, Figure 3.5a and 3.5b.

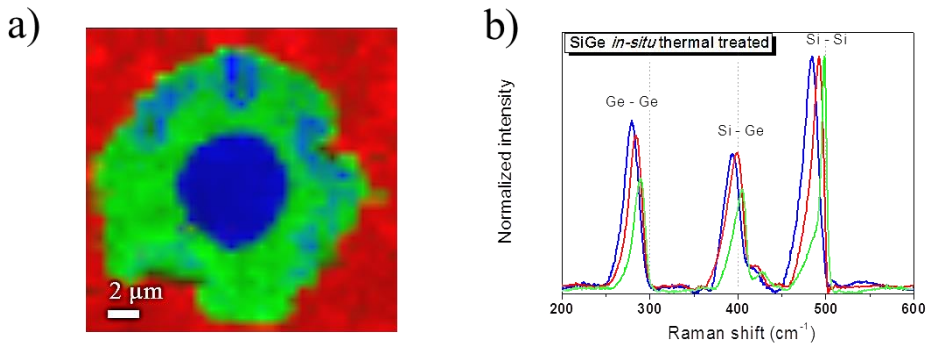

Figure 3.5. a) and b) show a Raman 2D-map and its spectra profile in the cluster zone. The colors of the Raman spectra are correlated with the colors of the 2-D map.

In summary, measurements with SThM were able to show that the thermal conductivity of $Si_{0.8}Ge_{0.2}$ films grown by metal induced deposition presented lower thermal conductivity values in comparison to those films grown with other techniques, which was associated to an increment of phonon scattering at grain boundaries of the clusters. This reduction observed in the thermal conductivity versus bulk samples will contribute positively to enhance the efficiency of this thermoelectric material.

3.2.2.2. Organic films: PCDTBT polymer.

In this Section, the thermal conductivity of films made of a polymer called poly[N - 9' - heptadecanyl - 2, 7 carbazole - alt - 5, 5 - (4',7'- di - 2 - thienyl - 2',1',3 benzothiadizole)] (PCDTBT) were investigated. This type of polymer is of interest in thermoelectric applications due to its large Seebeck coefficient, *S*, and low thermal conductivity, *k*, at room temperature. However, the electrical conductivity, σ, of the polymer is very low. Nevertheless, it can be doped with iron (Fe) atoms in order to increase its power factor ($\sigma \cdot S^2$) without altering much its thermal conductivity. The growing of the doped and undoped PCDTBT films were done via drop cast as it was explained in Chapter 2.1.1.3. and present similar crystalline orientation in the [1 0 0] direction.

The thermal conductivity of these films was measured following the same procedure as explained for inorganic $Si_{0.8}Ge_{0.2}$ films (Section 3.2.2.1.). In this case, the films presented a mean roughness of ~100 nm and thickness of 3 µm or larger, which are thick enough to not include the effects of the substrate, as the heat only spreads along the sample. This was cross-checked with a COMSOL Multiphysic® simulation, where the thickness of the sample was varied from 5 µm to 2.5 µm. No changes in the thermal resistance were observed, as it behaves as a bulk sample. Therefore, after taking measurements with Wollaston probe 1 in three different locations, the averaged thermal resistances with its standard deviations were determined for all the polymer samples. Then, using each of the R_{sample}^{th}, one can directly use Equation 2.23 to obtain the thermal conductivity of the undoped and doped polymer films.

Figure 3.6a shows the thermal conductivity dependence of the polymer films with the doping level.

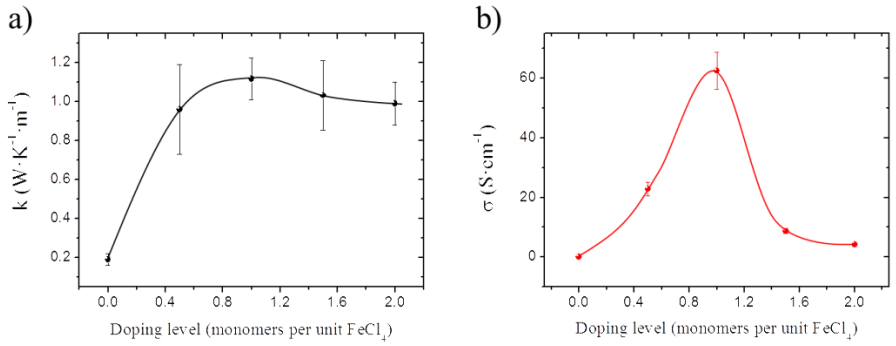

Figure 3.6. a) Evolution of thermal conductivity versus doping level measured by SThM technique. b) Electrical conductivity versus doping level [20].

The value for the undoped film is 0.19 ± 0.02 $W \cdot K^{-1} \cdot m^{-1}$, which agrees well with the cross-check measurement taken by PA (0.20 ± 0.03 $W \cdot K^{-1} \cdot m^{-1}$). In the undoped polymer, its thermal conductivity is mainly dominated by phonons, $k \approx k_{lattice}$, and it is expected to be low, mainly because of the typical structural characteristics of the polymers. However, when doping the PCDTBT with $FeCl_3$, not only the lattice, but also the electronic terms contribute to the total thermal conductivity, $k = k_{electronic} + k_{lattice}$. It is important noting that for semicrystalline polymers, like PCDTBT, thermal conductivity might also depend on both the orientation and the degree of crystallinity of their structural elements [21]. However, the undoped and doped PCDTBT films do not present strong changes in its crystal orientation [20]. Therefore, effects related with orientation shouldn't be the main cause for this thermal conductivity variation. In order to better understand the trend of Figure 3.6a, it is important to also study the variation of the electrical conductivity for the different doping.

Figure 3.6b shows that the maximum electrical conductivity is given for 1:1 doping, i.e. one unit of polymer monomer by unit of

$FeCl_3$ respectively, while for lower (1:1.5 and 1:2) or higher (0.5:1) doping it becomes smaller. At lower doping, this implies that the level of doping is not enough. As a consequence, there is an optimum doping at which the electrical conductivity is maximum but afterwards, the electrical conductivity becomes reduced. Different theories have been proposed to explain such phenomenom, such as trapping [22] or typical semiconductor transport in intrinsic regime (bipolar transport) [23, 24].

Similarly to what happen with the electrical conductivity (Figure 3.6b), the 1:1 doping shows the maximum thermal conductivity, around 1.2 $W \cdot K^{-1} \cdot m^{-1}$. However, although the trend in the total thermal co nductivity for higher doping levels become slightly smaller than for the 1:1 doping, it is not that drastically reduced as for the electrical conductivity case. The total thermal conductivity of doped samples remain very similar. After doping the polymer, the influence of the electrical term to the total thermal conductivity have a major influence due to the presence of the electron carriers, but also, the presence of the Fe ions in the polymer might also affect the lattice thermal conductivity. It is expected that at the highest value of σ (doping 1:1), the $k_{electronic}$ becomes larger, while for other dopings in which σ is reduced (1:1.5 and 1:2) the conservation of the total thermal conductivity is expected to be affected by the $k_{lattice}$ mainly. These two terms combine in such a way that the different dopings result a similar thermal conductivity, as can be observed in Figure 3.6a.

In summary, this work makes possible to understand the heat transport mechanisms in undoped and doped films: a) in the undoped PCDTBT polymer, the thermal conductivity is mainly dominated by the lattice term (phonon scattering); b) in the doped PCDTBT films, not only does the lattice term contribute to the total thermal conductivity, but also the influence of the electronic term. The electrons also carry heat, becoming a very important heat transfer mechanisms in doped polymers. Moreover, the presence of dopant atoms have also a contribuition to the lattice term of the thermal conductivity. In this particular case, it has been observed that the larger number of dopant atoms in the polymer is, the higher its influence to the lattice term is.

3.3. Thermal conductivity measurements of nanowires.

In this section, the thermal conductivity of organic and inorganic nanowires (NW) is determined. The NWs (one-dimensional structures) are expected to suffer changes in their thermal properties due to the reduction in the dimensionality of the material, which are one and two dimension less than thin films and bulk, respectively. In order to study these effects, the nanowires must be carefully characterized which due to its small size becomes challenging. For that purpose, both the Pd/SiO_2 and the Wollaston probe working in AC and DC mode, respectively, were used.

3.3.1. Inorganic nanowires: Bi_2Te_3.

Among the different possible inorganic nanowires, Bi_2Te_3 ones have been chosen especially for its potential thermoelectric applications. Bi_2Te_3 nanowires with different diameters can be grown via template assisted electrodeposition (See Chapter 1, Introduction, and Chapter 2, about the technique). Thermal maps and properties of nanowires embedded in the template can be obtained with SThM measurements.

In Section 3.3.1.1., it is shown how to obtain a thermal and topographic map, and determine the thermal conductivity of Bi_2Te_3 nanowires with 300 nm diameter embedded in alumina matrix with SThM working in AC heating mode and using a Pd/SiO_2 probe. Then, in Section 3.3.1.2., a Wollaston probe working in DC heating mode was used to measure Bi_2Te_3 nanowire arrays embedded in alumina with different diameters, ranging from 300 nm to 45 nm, in order to study how the thermal conductivity becomes affected as the nanowire diameter size is reduced.

3.3.1.1. 300 nm diameter Bi_2Te_3 Nanowires. AC heating mode: Pd/SiO_2 probe.

In this section, the thermal conductivity of a composite sample made of a Bi_2Te_3 NWs array with 300 nm diameter embedded in an alumina matrix was measured by SThM working in AC mode, usually called 3ω-SThM, using a Pd/SiO_2 probe. To date, most of the NW thermal conductivity measurements have been performed for single NWs on microchips (See Chapter 1, Introduction). However, many future NW devices will be based on a large number of NWs embedded in a matrix. Therefore, thermal properties of an array of NWs might be different to single ones because of the matrix-NWs interaction and by the fact that by releasing the nanowires from the templates their surface can be oxidized. These changes in the thermal conductivity depend on the NW diameter and the geometry of the array as well as the character of the NW/matrix interface and the presence of additional components.

These measurements were carried out in the group of Stefan Dilhaire in the Laboratoire Ondes et Matière d'Aquitaine (LOMA) at the University of Bordeaux (France).

Nanowires fabrication embedded in a matrix

The nanowires were grown inside Whatman© anodic alumina oxide (AAO) with a mean porous diameter of 300 nm. This matrix was selected because there are already studies in the literature about these particular type of samples. The growing process was carried out in an electrodeposition cell with three electrodes, similar to the one described in [25, 26, 27] (See Chapter 2.1.1.1.). One surface of the AAO templates was deposited with 5 nm of Cr and 150 nm of gold by e-beam evaporation in order to act as working electrode. During the electrodeposition, the pores of the alumina template were filled with Bi_2Te_3, giving rise to NWs embedded in a matrix.

For this particular samples, the deposition was carried out at continuous potential at -20 mV versus Ag/AgCl and during 12 hours. Due to the longtime of deposit, the Bi_2Te_3 nanowires grew until they

reached the alumina template surface. Afterwards, the sample was polished using 50 nm alumina nanoparticles. The mechanical polishing is very important in order to achieve that mos of the tips of the nanowires can appear on the surface. Then, the sample was treated afterwards with 10% weight in volume concentration of KOH in order to eliminate the possible excess of alumina nanoparticles from the polishing, as well as for etching the template selectively.

After this process, Bi_2Te_3 NWs with diameters ranging from 200 to 400 nm and 37 µm long were finally obtained to be measured by SThM in adequate conditions. In Figure 3.7 SEM (Scanning Electron Microscopy) images of the sample are presented. Figure 3.7a shows a top view of the sample surface where one can see that not every pore is filled with a NW. This is due to the fact that some of the NWs are not long enough to reach the surface of the matrix, as can be seen in Figure 3.7b. However, given that the measurements are made using a SThM tip with nanometer resolution, it would be possible to be selective, accessing and analyzing only the NWs jutting out above the matrix.

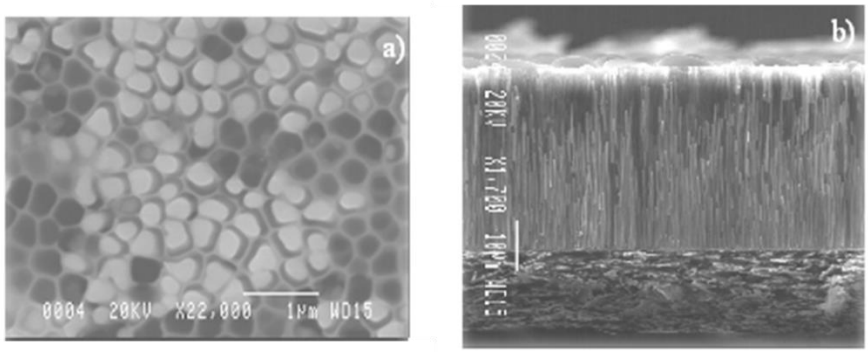

Figure 3.7. Sample SEM pictures: a) Top view of the commercial Whatman alumina matrix after polishing. The pore are partially filled with Bi_2Te_3 nanowires whose diameter ranges between 200nm and 400nm, b) Cross Section view of the sample before polishing. Figure taken from reference [28].

The experimental set-up used to measure this sample consisted of a Pd/SiO_2 probe working in AC heating mode and it was described in

Section 2.2.1.4.1.2. As it was mentioned, this technique makes possible to obtain simultaneously a topographic and thermal map of the sample. As it can be observed in the first term of Equation 2.25, when the tip gets in contact with a material, a heat flow goes from the tip to the sample and this flow depends on the thermal conductance of the sample. As a consequence, the tip temperature variations, $< T_{2\omega} >$, depend on the equivalent thermal resistance R_{eq} between the tip and the sample. The higher the thermal conductivity of the sample is, the lower the 2ω thermal variations are. For that reason, this configuration is sometimes called conductivity contrast imaging. Experimentally, the tip scans the sample and we measure the 3ω tip voltage $(V_{3\omega})_{tip}$ using a lock-in amplifier. From the $(V_{3\omega})_{tip}$ image, a tip temperature variations, $< T_{2\omega} >$, map can be deduced and hence an equivalent tip-sample thermal resistance R_{eq} image [28].

It is important to underline that, for a sample constituted of several NWs or a NW "carpet", this experimental method enables to simultaneously measure R_{eq} on each NW of the thermal image. Therefore, a statistical data processing can be performed in order to deduce a mean thermal conductivity with its associated standard deviation.

Prior to thermal measurements of the sample, the tip-to-sample thermal exchange radius, *b*, must be estimated. This radius can be assimilated here to the circular constriction radius[12]. The experimental procedure to do it was explained in Section 3.1. 2. For the probe that we used in this experiment, a value of *b* = 230 nm was determined. As we mentioned before, this value has double importance: on the one hand, the thermal lateral resolution depends on it and, on the other hand, it constitutes an essential value in our method to determine the NW thermal conductivity as presented in the following section.

3ω-SThM measurements. NWs equivalent thermal resistance evaluation.

Figure 3.8 shows 3 µm × 3 µm topographical and $(V_{3\omega})_{tip}$ images obtained simultaneously using the 3ω-SThM technique

described above at a 927 Hz fundamental frequency (ω = 5825 rad/s) [28]. The NWs jutting out above the matrix (bright parts in Figure 3.8a) offer a lower 3ω voltage (dark parts in Figure 3.8b) than the alumina matrix, consequently a lower 2ω temperature variation. This can be explained by an increase of the heat flux passing from the tip to the sample in this region. As a consequence, the equivalent thermal resistance is lower on the NWs than on the alumina.

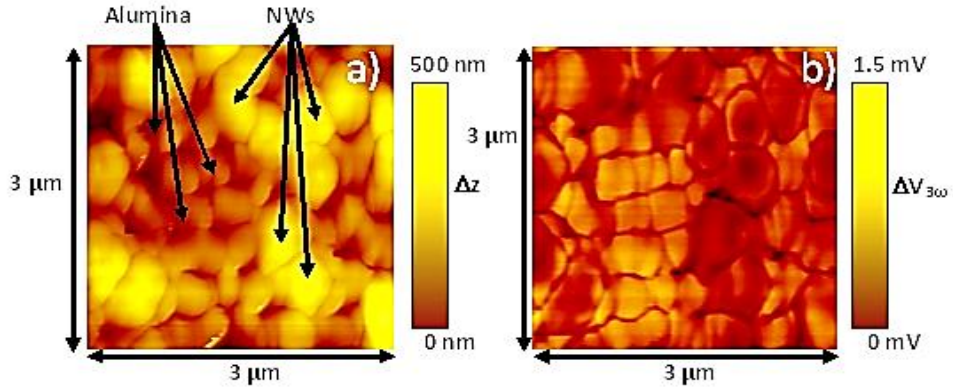

Figure 3.8. SThM imaging of Bi_2Te_3 nanowires embedded in an alumina matrix. a) Topographic image. Yellow spots in this figure reveal the presence of nanowires. b) $(V_{3\omega})_{tip}$ image. The centers of the nanowires show a lower $(V_{3\omega})_{tip}$ signal due to an increase of the heat flux in this region. Figure taken from reference [28].

Figure 3.9 shows the distribution of the equivalent thermal resistances measured on the alumina part of the sample and on the Bi_2Te_3 NWs that were obtained from the $(V_{3\omega})_{tip}$ image (Figure 3.8b). In this figure, two separate distributions can be distinguished. The mean equivalent thermal resistance value is $\langle (R_{eq})_{NW} \rangle = (1.53 \pm 0.05) \times 10^6$ $K \cdot W^{-1}$ on the NWs and $\langle (R_{eq})_{Alu} \rangle = (1.75 \pm 0.02) \times 10^6$ $K \cdot W^{-1}$ on the alumina. The mean equivalent thermal resistance is higher on the alumina than on the NWs, which points out that thermal conductivity of the alumina is lower than the NW one.

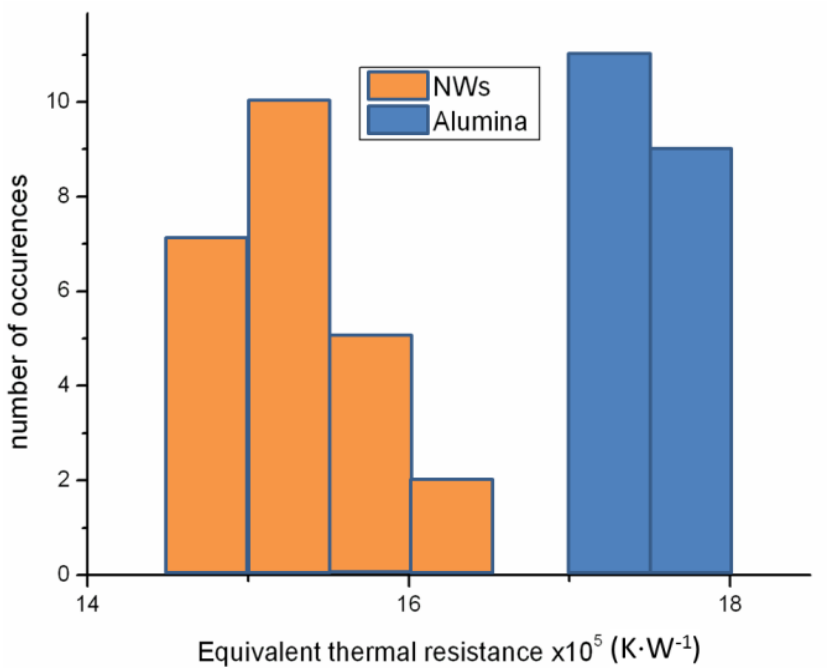

Figure 3.9. Equivalent thermal resistance distribution on the alumina and NWs parts of the sample. Figure taken from reference [28].

The evaluation of the mean thermal conductivity of the nanowire requires of these mean equivalent thermal resistance values. Figure 3.10 shows schematically how a 3ω-SThM measurement was taken for a NW. The tip is positioned on top of the NW and then the thermal resistance is measured. A SEM image of the tip is presented in the top left part of the Figure 3.10.

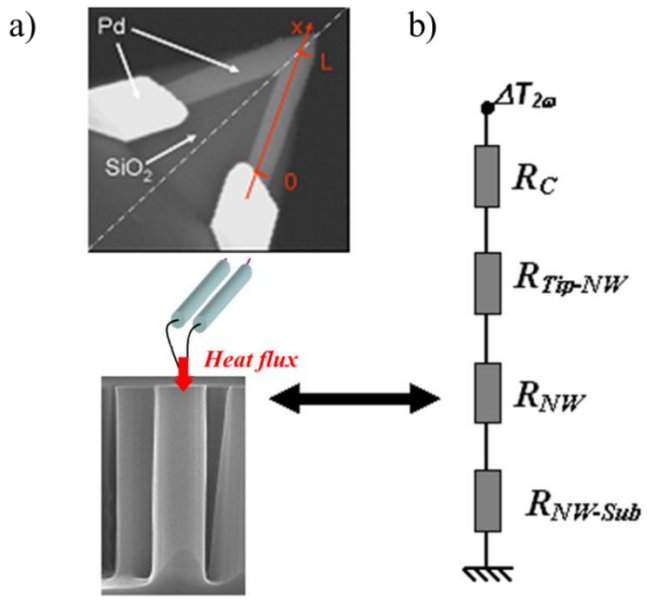

Figure 3.10. a) Tip image (top left) and its location on top of a nanowire and b) equivalent thermal schema of the thermal flux passing from the tip to a NW. Figure taken from reference [28].

The NW equivalent thermal resistance $(R_{eq})_{NW}$ can be represented by four thermal resistances in series, which are defined as: the tip-to-sample contact thermal resistance R_c, the constriction resistance R_{Tip-NW} of the heat flux between the tip and the NW, the sample intrinsic thermal resistance R_{NW} and the constriction resistance R_{NW-Sub} of the heat flux between the NW and the substrate on which the NW is deposited. It can be expressed mathematically as,

$$(R_{eq})_{NW} = R_{Tip-NW} + R_c + R_{NW} + R_{NW-Sub}. \qquad (3.2)$$

Then, in order to extract the mean NW thermal conductivity, which is given by the intrinsic thermal resistance R_{NW}, one must determine the values of the three thermal resistances R_{Tip-NW}, R_c, and R_{NW-Sub} as well as the expression of the NW intrinsic thermal resistance R_{NW}, as a function of its thermal conductivity k_{NW}.

The constriction resistance R_{Tip-NW}, between the tip and the NW is negligible as the thermal exchange surface is bigger than the NWs section, as the diameter , d_{NW} ,of the probed NWs varying from 200 nm to 400 nm. Regarding the constriction resistance between the NW and the substrate, it can be written as [28],

$$R_{NW-Sub} = \frac{1}{2 \cdot k_{Sub} \cdot d_{NW}} \tag{3.3}$$

where k_{Sub} is the substrate thermal conductivity. As the NWs were deposited on Cr/Au electrode, the mean value of this thermal resistance is of the order of ~104 $K \cdot W^{-1}$, depending on the NW diameter value. Consequently, this term is negligible compared to the mean equivalent thermal resistance $\langle (R_{eq})_{NW} \rangle$ measured on the NWs.

As the thermal conductivity of the porous alumina (AAO) is known, the contact thermal resistance between the tip and the sample, R_c, can be evaluated measuring the equivalent thermal resistance on the porous alumina part of the thermal image [7 9 29]. The mean equivalent thermal resistance of the porous alumina, $\langle (R_{eq})_{Alu} \rangle$ = (1.75±0.02)×10^6 $K \cdot W^{-1}$, was deduced from a statistical study of around twenty values (Figure 3.9). This resistance (Equation 3.1) is the addition of the mean contact thermal resistance $\langle R_c \rangle$ and of the constriction resistance between the tip and the porous alumina, which can be written as,

$$R_{Tip-Alu} = \frac{1}{4 \cdot k_{AAO} \cdot b} \tag{3.4}$$

where k_{AAO} is the thermal conductivity of the porous alumina (AAO) whose value was reported in reference [30] to be 1.3 $W \cdot K^{-1} \cdot m^{-1}$. Using Equation 3.1, the mean contact resistance can be estimated to be

$\langle R_c \rangle = (9.1 \pm 0.2) \times 10^5\ \mathrm{K \cdot W^{-1}}$. The low value of the uncertainty, which is calculated from the standard deviation of the values measured on the twenty locations, involves that the contact resistance does not vary much from one point to another. Finally, considering the measured NW equivalent thermal resistances $(R_{eq})_{NW}$ and the obtained contact resistance, the mean intrinsic thermal resistance was determined from Equation 3.2 to be $\langle R_{NW} \rangle = (6.01 \pm 0.41) \times 10^5\ \mathrm{K \cdot W^{-1}}$. Once this result was obtained, it was proceeded with the deduction of an estimation of the mean NW thermal conductivity $\langle k_{NW} \rangle$. For that purpose, different approaches were considered in order to correlate the NW thermal resistance R_{NW} as a function of k_{NW}.

NW composite thermal model and thermal conductivity

From a classical point of view, R_{NW} can be assumed to be given by the conductive thermal resistance of a thermal conductor of length *L* and section *A*, which can be expressed mathematically as,

$$R_{NW} = \frac{1}{k_{NW}} \cdot \frac{L}{A} \tag{3.5}$$

In this case, given the fact that the NWs have the same length, but a large diameter distribution, R_{NW} should only vary from one NW to another depending on the NW section. Nevertheless, this behavior was not observed since when dividing the section by a factor of two, the R_{NW} remains practically unaltered. The same conclusion can be reached, noting that the dispersion on the R_{NW} value is relatively low (7%) for a population with a 25% section dispersion.

The use of Equation 3.5 to determine the thermal conductivity of the measured NWs would lead to a ridiculous value of 410 $\mathrm{W \cdot K^{-1} \cdot m^{-1}}$. Therefore, this expression might not be suitable for our configuration. As a result, two different hypotheses were taken under

consideration. The first one considered that the length *L* appearing in Equation 3.5 was not correctly evaluated. Indeed, the NWs are relatively long (37 µm) and the thermal diffusion length in this material at 927 Hz is only 11 µm, which was calculated taking into account a 6.9×10^{-7} $m^2 \cdot s^{-1}$ thermal diffusivity of such NWs identified by Borca-Tasciuc *et al* [31]. Then, it can be assumed the heat only diffuses over the thermal diffusion length and not along the total NW length. Consequently, instead of using the real length of the NW, the thermal diffusion length (effective length) should be considered in Equation 3.5.

However, even in this situation, the NW mean thermal conductivity remains very high. In addition, since the thermal diffusion length depends on the frequency, the measured R_{NW} should also depend on it. In order to check it, thermal images at a frequency of 309 Hz were performed. Since the frequency has been divided by three, the thermal diffusion length has increased to 19 µm and the mean NW thermal resistance R_{NW} should then be expected to vary by a factor $\sqrt{3}$. However, it only changed from $\langle R_{NW} \rangle = (6.01 \pm 0.41) \times 10^5$ $K \cdot W^{-1}$ at 927 Hz to $\langle R_{NW} \rangle = (5.80 \pm 0.44) \times 10^5$ $K \cdot W^{-1}$ at 309 Hz. Measurements performed at two other frequencies (103 Hz and 2781 Hz) confirmed that this hypothesis does not seem to work as expected.

In the second hypothesis, the NWs are not considered as individual elements, but as part of a composite made of Bi_2Te_3 NWs and the alumina matrix. This can be supported by the fact that the NWs are not isolated from the matrix, but in contact. As it was observed in the SEM images of Figure 3.7. Moreover, the thermal conductivities of the NWs and the alumina are expected to be of the same order. Therefore, when the tip is in contact with a NW, part of the heat flux that is being propagated along a NW passes from the NW to the matrix. In addition, the thermal exchange surface is larger than the NWs section. Then, the tip heats not only the NW, but also the surrounding alumina matrix at the same time. Under these circumstances, the thermal resistance measured when scanning a NW is not given by the

Equation 3.5, as might be originally though, but by the expression of a constriction resistance on a semi-infinite effective medium, as was explained in Section 2.2.1.4.1,

$$R_{NW} = \frac{1}{4 \cdot k_c \cdot b} \tag{3.6}$$

where k_c is the composite thermal conductivity. Using this theory and the measurements of R_{NW} taken at different frequencies, the thermal conductivity of the composite can be determined, $\langle k_c \rangle$=(1.68 ± 0.20) $W \cdot K^{-1} \cdot m^{-1}$. In order to obtain this value, a statistical study was carried out of the measurements made on 49 NWs whose thermal conductivity distribution is presented in Figure 3.11.

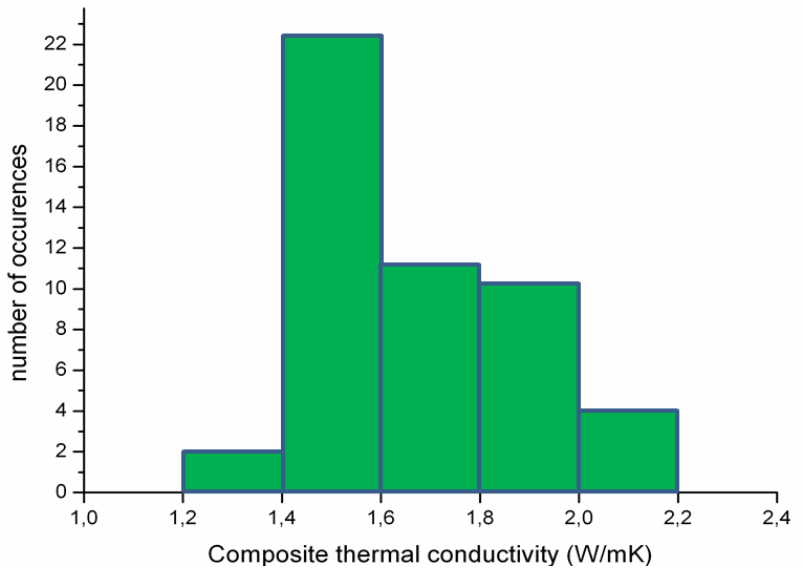

Figure 3.11. Composite thermal conductivity distribution on around 50 NWs. Figure taken from reference [28].

A low uncertainty can be noted due to the low dispersion on the measurements. As expected from Figure 3.9, this thermal conductivity is higher than the one of the porous alumina. This value, which is of great importance since it constitutes the thermal conductivity of the

functional device, could be reduced if using another matrix with a lower thermal conductivity. As an example, Biswas *et al* [32] showed that using epoxy resin SU-8 instead of porous anodic alumina, the composite thermal conductivity of 200 nm diameter Bi_2Te_3 NWs/matrix could be reduced from 1.4 $W \cdot K^{-1} \cdot m^{-1}$ with the alumina matrix to 1.1 $W \cdot K^{-1} \cdot m^{-1}$ with the SU-8 matrix.

Nanowires thermal conductivity and discussion

From the composite thermal conductivity, we can now evaluate the NW thermal conductivity using the effective medium theory [33]. The thermal resistance at the alumina/NW interface can be neglected since the NWs are in contact with the alumina and the fact that both media are expected to have close thermal conductivity values. Then, the thermal conductivity of the composite made of the NW array and the matrix can be estimated by the effective medium theory as [32 33],

$$k_c = x \cdot k_{NW} + (1-x) \cdot k_{Alu} \tag{3.7}$$

where x is the areal packing density of the NW array, k_{NW} and k_{Alu} are respectively the thermal conductivities of the NWs and matrix. The percentage of NWs and alumina were determined by analyzing five different SEM pictures, using image processing with ImageJ®, resulting to be 41% and 59%, respectively. The thermal conductivity of the solid alumina matrix was reported in reference [30] to be k_{Alu} = 1.9 $W \cdot K^{-1} \cdot m^{-1}$ at room temperature. From this measurement and using Equation 3.7, the thermal conductivity of the nanowire was determined to be k_{NW} = (1.37 ± 0.20) $W \cdot K^{-1} \cdot m^{-1}$.

Table 3.III. Summary of thermal conductivity measurements in Bi_2Te_3 nanowire arrays. T-ED stands for Template-assisted Electrodeposition. AAO stands for Anodic Aluminium Oxide template. SThM is Scanning Thermal Microscopy. EMT is Effective Medium Theory. NW is nanowire.

Bi_2Te_3 Sample	**Fabrication method**	**Measurement method**	**c-axis orientation**	**$\kappa_{composite}$** ($W \cdot K^{-1} \cdot m^{-1}$)	**$\kappa_{nanowire}$** ($W \cdot K^{-1} \cdot m^{-1}$)	**Ref.**
Bulk	Bridgman	Comparative method	c ⊥	-	2.2	34,35, 36,
Bulk	Bridgman	Comparative method	c //	-	0.79	34,35, 36,
300 nm NW	T-ED in AAO	SThM + EMT	c ⊥ nw length	1.68±0.2	1.37±0.20	This thesis work [28]
200 nm NW	T-ED in AAO	Photoacoustic technique + EMT	not shown	1.4±0.07	1.44±0.10	[32]
200 nm NW	T-ED in AAO + replacement of the AAO by an epoxy resist		not shown	1.1±0.06	1.45±0.09	
120 nm NW	T-ED in AAO	Laser Flash+EMT	c ⊥ nw length	Thermal diffusivity $0.41 \cdot 10^{-6}$ m^2/s	0.75	[37]
55 nm NW	T-ED in AAO	Microchip	c ⊥ nw length	-	1-3	[38]

As it was shown in the Introduction Chapter, there are other techniques that can be used to measure single NWs or whole arrays of NWs. When carrying out thermal conductivity measurements of single NWs, the NW is generally suspended onto the electrodes of a thermal microchip [39] [40] [38]. These experiments have reported data for Bi_2Te_3 at room temperature of 1-3 $W \cdot K^{-1} \cdot m^{-1}$ for 55 nm diameter NWs [38]. It is worth mentioning here that for this sort of experiments, the matrix must be dissolved and this process, having the NWs in air, leads to the oxidation of the surface of the NWs[41], which might affect its thermal transport properties. Other techniques [32] [33] [37] allow the measurement of the thermal conductivity of an array of NWs inside a matrix, obtaining the thermal conductivity of the whole structure. From this result, the NW thermal conductivity can be determined. Reported data for Bi_2Te_3 NWs measured with this technique are 0.75 $W \cdot K^{-1} \cdot m^{-1}$ for 120 nm diameter [37] and 1.44 $W \cdot K^{-1} \cdot m^{-1}$ for 200 nm diameter [32]. A summary of all the reported data found in literature is presented in Table 3.III.

The 3ω-SThM present an advantage in comparison to these techniques, which is the possibility of measuring the thermal conductivity of the composite locally as well as determining the thermal conductivity of the single NWs embedded in the matrix. Moreover, not only a thermal map, but also a topographic image of the surface of the sample can be obtained simultaneously to assure the local measurement. Regarding the thermal conductivity value obtained for the nanowires, it lies within the range of the reported data mentioned above. However, a rigorous comparison of these results cannot be done because of the differences within the techniques, the diameters, crystal orientation, crystallinity, etc. In fact, measurements with a thermal microchip and with 3ω-SThM must be compared with precaution for two main reasons: 1) the reported samples have diameters far smaller than ours; 2) the thermal microchip technique measures only one single isolated NW whereas 3ω-SThM probes an assembly of NWs embedded in a matrix. Nevertheless, as future prospects, the combination of both the 3ω-SThM and microchip techniques to measure identical nanowires could enable to study the influence of the surrounding matrix or the oxidation of the single NW outside the matrix. Comparing 3ω-SThM results with the values measured by the techniques based on the effective medium theory seems more appropriate since in both cases, the samples are embedded in a matrix. Although no identical sample (same NW length, NW diameter, matrix and growing process) has been reported in literature, our value is in particular good agreement with the value given in[32], 1.44 $W \cdot K^{-1} \cdot m^{-1}$, which corresponds to NWs with similar diameter and length than ours and that are also embedded in an alumina matrix.

These measurements show a small thermal conductivity reduction in comparison with the bulk Bi_2Te_3 value, as could be expected from nano-structuration. Molecular dynamics simulations [42] have also predicted a thermal conductivity reduction limited to 20% (in comparison with the bulk thermal conductivity), even for 30 nm diameter Bi_2Te_3 NWs. Compared to other materials, this thermal conductivity reduction is less pronounced, according to literature, than in for example Si in which the thermal conductivity of 56 nm diameter NWs has been measured to be around 25 $W \cdot K^{-1} \cdot m^{-1}$ [43]at room

temperature, that is, six times lower than the bulk thermal conductivity. The reason for such a huge reduction is the fact that the phonon mean free path (250 nm in bulk Si at 300 K) is higher than the NW diameter, which favors phonon boundary scattering and so, a thermal conductivity reduction. In bulk bismuth telluride, the lattice phonon mean free path is only 3 nm [38], which is much smaller than every diameter of the studied NWs. Therefore, the impact of phonon boundary scattering is in our case much smaller than in Si NWs, leading to a limited thermal conductivity reduction.

3.3.1.2. Thermal conductivity dependence with the diameter of Bi_2Te_3 Nanowires. DC heating mode: Wollaston probe.

In the previous Section 3.3.1.1., it was shown that there is not a strong reduction in the thermal conductivity of Bi_2Te_3 nanowires of 300 nm diameter in comparison to bulk. This was explained in terms of the small free path of the phonons of Bi_2Te_3, which is estimated to be around 3 nm [38]. However, one must take into account that this mean free path corresponds to the global average obtained from the different scattering mechanisms in bulk. In nanowires, as the diameter of the nanowire is reduced, this mean free path might enlarge because of the increase of certain scattering modes due to size confinement. In references [38] and [44], the suppresion of the thermal conductivity in Bi and Bi_2Te_3 NWs of small diameter, respectively, is explained by heat transport models that consider diffuse phonon-surface scattering, partially diffuse surface scattering of electrons and holes, and scattering of phonons and charge carries by ionized impurities, among others. Therefore, although a small reduction of the thermal conductivity is observed for 300 nm Bi_2Te_3 NWs, it is expected to observe larger reduction as the diameter of the nanowire becomes smaller.

In order to carry out the study of how the thermal transport is affected as the size of the nanowire is reduced, Bi_2Te_3 nanowires arrays with different mean diameters were grown via electrodeposition inside of alumina matrices in a similar way as it was explained in Section

3.3.1.2. and Chapter 2. For that purpose, four different porous alumina matrices with average diameters of 300 nm, 75 nm, 55 nm and 45 nm were fabricated with [1 1 0] crystal orientation and with good stoichiometry. Inside of them, nanowires were grown via pulsed voltage electrodeposition process, which resulted in an improvement of the quality and the orientation of the NWs in comparison to continuous voltage deposition. Afterwards, the sample was polished mechanically using a polishing cloth and different alumina nanoparticles sizes until a mean roughness of around 50 nm was achieved, as explained in Section 2.1.2.3. While in Section 3.3.1.1. the nanowire array sample shows some empty porous (Figure 3.6) after the polishing process, now the nanowires samples were polished much more until no empty porous were observed. Figure 3.12 shows SEM images of the top view of arrays of nanowires with standard diameters of 300 nm and 45 nm that show their NWs tip at the surface (intermediate contrast), jutting out of the matrix (brightest contrast) while practically no porous (a percentage below 5 %) were observed (darkest contrast). The length of the four nanowires arrays remained very long after polishing, whose values varied between 32 µm and 37 µm.

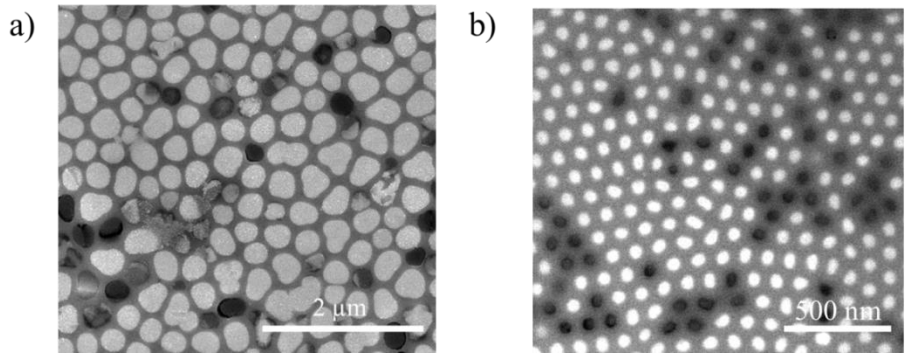

Figure 3.12. SEM images of a) 300 nm and b) 55 nm average diameter nanowires. The largest diameter ones were fabricated in a commertial Whatman® template (300 nm) and the rest were grown in laboratory-made porous alumina. In both images the nanowires jutting slightly out of the matrix are seen in white (brightest white dots) while some others that stay at the same level of the alumina surface present an intermediate contrast. There are very few empty porous, which show a high dark contrast.

Except for the 300 nm diameter Bi_2Te_3 nanowires, the diameters of the nanowires that want to be studied are very small to observe them individually in a thermal map with a Pd/SiO_2 probe. This is due to the fact that its thermal resolution is limited by its thermal exchange radius, which is generally of the order of few hundreds of nanometers. This makes impossible to detect and map individual nanowires of 75 nm, 55 nm or 45 nm diameters. Evidently, the Wollaston is neither a good candidate for thermal mapping because of its largest thermal exchange radius (in the order of few micrometers) compared to the Pd/SiO_2 probe. Under this circumstances, even though a thermal map similarly to those obtained in Section 3.3.1.1. for Bi_2Te_3 nanowires of 300 nm diameter cannot be imaged, one can perform local thermal measurement on the nanowire arrays. For that purpose, a larger probe tip (Wollaston probe) would be more appropriate in order to obtain average composite properties while a small probe tip (Pd/SiO_2 probe) might observe more local properties. The proper polishing of the sample, showing that around 95% of the nanowires appear on the surface (Figure 3.12) reduces the uncertainty of the measurements. In a similar way as the thermal properties of the films were measured (Section 3.2), the DC heating mode was used for the Wollaston probe in order to determine thermal resistance of the composites made of Bi_2Te_3 nanowires embedded in alumina with different diameters.

For that purpose, the Wollaston probe 2 was calibrated to obtain its thermal exchange radius and thermal contact resistance, as already explained in Section 3.1.1. Then, using our Nanotec® AFM system the Wollaston probe got in contact with the surface of the sample and measure the local thermal resistance of the composite at different locations. As in films (Section 3.2), the thermal resistance of the composite was obtained using the equations for DC heating working mode (Section 2.2.1.4.1.1.). Once the mean thermal resistance of the composite is determined, one can calculate the thermal conductivity of the composite, k_c, using Equation 3.6, in an identical way as it was calculated in the previous section for the 300 nm Bi_2Te_3 nanowire array embedded in the alumina matrix. Finally, the effective medium theory is also used in this case to obtain the thermal conductivity of the

nanowire using the obtained thermal conductivity of the composite, k_c, the thermal conductivity of the alumina matrix, k_{Alu}, and the areal packing density of the NW array, *x*, as it was mathematically expressed in Equation 3.7. The areal packing density of the different NWs samples was estimated from SEM pictures while the thermal conductivity of the laboratory-made alumina matrices was measured with the photoacoustic technique by Begoña Abad from our group. This was necessary for the proper determination of the thermal conductivity of the nanowires through the effective medium theory.

Table 3.IV summarizes the thermal resistances and thermal conductivities obtained for all the composites measured as well as the thermal conductivities determined from the effective medium theory for the different diameter nanowires. The experimental error is considerably large, but it is caused by the addition of the different errors obtained from the measurements of alumina matrix, the packing density and the composite thermal conductivity. Regarding the Bi_2Te_3 NWs with 300 nm diameter, one could be tempted to compare the result of its thermal conductivity with those obtained in Section 3.3.1.1. Nevertheless, one must take into account that the nanowires are not exactly the same. In this case, they have been grown with pulsed electrodeposition while in the previous section a continuous voltage was applied. The effects of pulsed electrodeposition result in an improvement of the crystalline orientation and robustness and compaction of the Bi_2Te_3 nanowire, which might facilitate the heat conduction along it because of the better structural properties. Because of that, the obtained thermal conductivities become a bit different, obtaining (1.37± 0.20) $W \cdot K^{-1} \cdot m^{-1}$ and (1.88± 0.40) $W \cdot K^{-1} \cdot m^{-1}$ for the continuous and pulsed electrodeposited nanowires, respectively. It is important to highlight this because it is stayed the influence of electrodeposition conditions on the thermal conductivity. This effect can explain the difference in results observed in Table 3.III. So, in order to really get a good study of the dependence of the thermal conductivity versus the NW diameter, it is very important to make sure that the NWs are optimized in composition, orientation, density, etc.

Table 3.IV. Summary of the thermal results obtained for Bi_2Te_3 nanowires with different diameter embedded in alumina matrix.

Nanowire diameters (nm)	Packing areal density of the NW array (%)	Thermal exchange radius (μm)	$(R_{ea})_{composite}$ $(K \cdot W^{-1})$	Composite thermal conductivity $(W \cdot K^{-1} \cdot m^{-1})$	Alumina matrix thermal conductivity $(W \cdot K^{-1} \cdot m^{-1})$	NW thermal conductivity $(W \cdot K^{-1} \cdot m^{-1})$
300	0.55±0.03	2.72±0.08	56563±8890	1.62±0.20	1.31±0.19	1.88±0.40
75	0.46±0.02	2.72±0.08	87332±9960	1.05±0.20	0.92±0.12	1.21±0.45
55	0.38±0.03	2.72±0.08	80450±7330	1.14±0.10	1.35±0.13	0.80±0.34
45	0.33±0.02	2.72±0.08	85741±8150	1.07±0.10	1.35±0.13	0.51±0.40

Figure 3.13 shows graphically how the thermal conductivity of the nanowires reduces when the diameter of the nanowire becomes smaller.

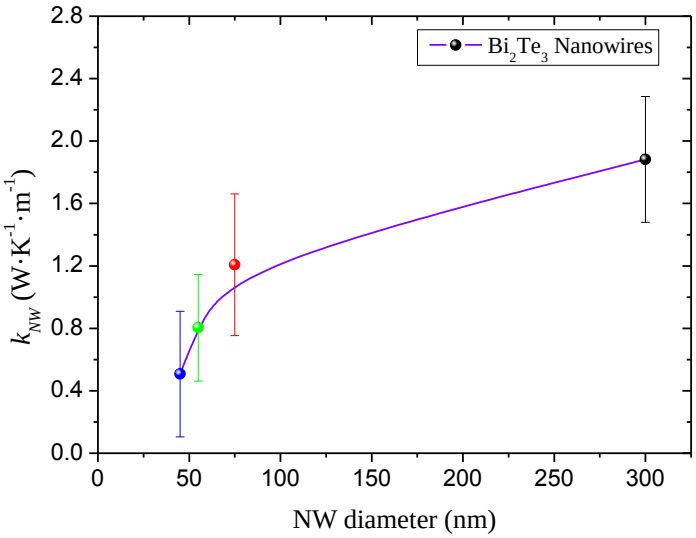

Figure 3.13. Thermal conductivity versus the diameter of the Bi_2Te_3 nanowires (1 1 0) oriented with perfect stoichiometry and high density and crystal quality.

Despite the fact that the phonon mean free path of the Bi_2Te_3 , around 3 nm [38], is much smaller than the studied NWs diameter a clear reduction in the thermal conductivity is observed in Figure 3.13. In order to explain this, the department of physics of the University of Barcelona, under the leadership of Dr. Xavier Àlvarez, provided a model to predict theoretically the thermal conductivity of bulk and nanostructures, such as nanowires, based on a Kinetic-Collective model in the framework of the Boltzmann transport equation as a generalization of the Guyer-Krumhansl model [45] [46]. Whereas most of the current models to predict the thermal conductivity of materials are based on the role of resistive scattering (Umklapp, impurities, boundaries), this model incorporates also the role of normal scattering on the phonon collective behavior. As a consequence, two different thermal transport regimes could be established, i.e. the kinetic and the collective, which depend on what scattering mechanism (resistive or normal) is dominating the transport. While in the kinetic regime each phonon contributes independently to the heat flux, in the collective regime the momentum is conserved and shared among the phononic modes (the phonons behave as a whole). The Kinetic-Collective model can be applied to any range of temperature and provide a new insight into the underlying physics of thermal transport, introducing thermodynamic perspective at mesoscopic level that allows the interpretation of the differences in phonon behavior in terms of the average of the phonon-phonon processes. This model was successfully tested in silicon samples[45] and recently applied to study group-IV materials. The Kinetic-Collective model was applied to study Bi_2Te_3 nanowires showing a reduction in the thermal conductivity as the diameter of the NW becomes smaller. This model is limited to a NW diameter of ~50 nm, which is similar to the lowest diameter measured experimentally and presented in Figure 3.13. The predicted lattice thermal conductivities for nanowires ranging from 350 nm to 50 nm diameter at different temperatures are presented in Figure 3.14. These predictions seem to be in agreement with the general trend of the experimental results presented in Figure 3.13 within the error. As the surface to volume rate is increased when the diameter of the nanowires is reduced, an increment of the phonon boundary scattering at the surface of the NW is also playing a role in the thermal conductivity

reduction. This effect has been considered in the Kinetic regime of the simulation.

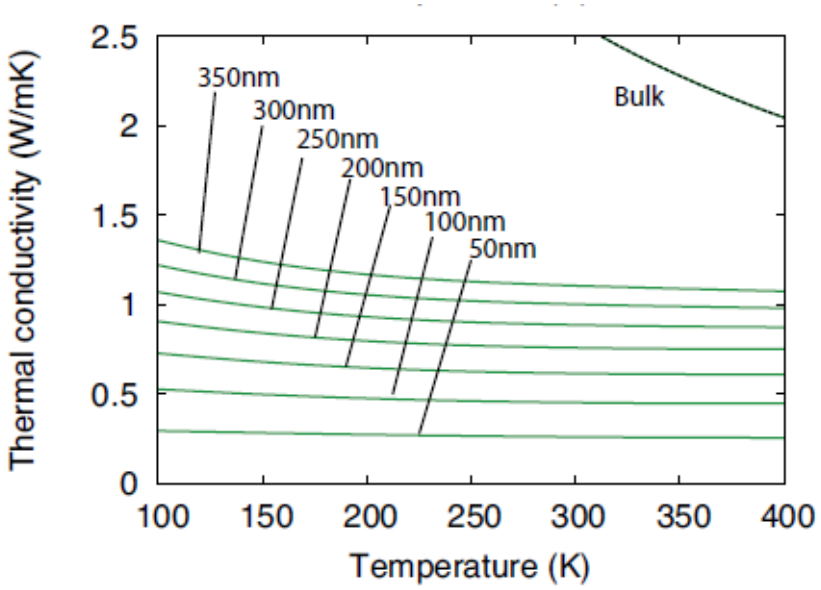

Figure 3.14. Thermal conductivity prediction with Kinetic-Collective model for Bi_2Te_3 NWs whose diameter range from 350 nm to 50 nm. Courtesy of Carla de Tomás from the University of Barcelona [46].

To conclude, the reduction of the thermal conductivity observed in Bi_2Te_3 nanowires when their diameter become smaller contributes positively to enhance the thermoelectric performance of these structures. The power factor estimated for these NWs is the same the measured in Bi_2Te_3 films prepared by electrodeposition with the same crystal orientation. Further advances must be performed in electrochemistry or the use of other growing techniques might be demanded in order to obtain larger figure of merits. But, it is demonstrated that for this diameter range a reduction is obtained in the thermal conductivity without affecting much the power factor of the electrodeposited material. As an example, if power factors of the films and nanowires obtained by electrodeposition were similar to those found in bulk Bi_2Te_3, while keeping the thermal conductivities predicted by the Kinetic-Collective model, figures of merits in the order of 2 might be achieved at room temperature. Figure 3.15a and 3.15b

show the figure of merit calculated from $zT = \frac{\sigma \cdot S^2}{k} \cdot T$, for nanowires with 350 nm and 100 nm diameters at different temperatures, whose power factor was taken from bulk and the thermal conductivity obtained from the Kinetic-Collective model. It is important to take into account that the large numbers in the figure of merit have not been observed experimentally and that it only correspond to an idealized case when considering the optimum transport properties for Bi_2Te_3 nanowires might be achieved.

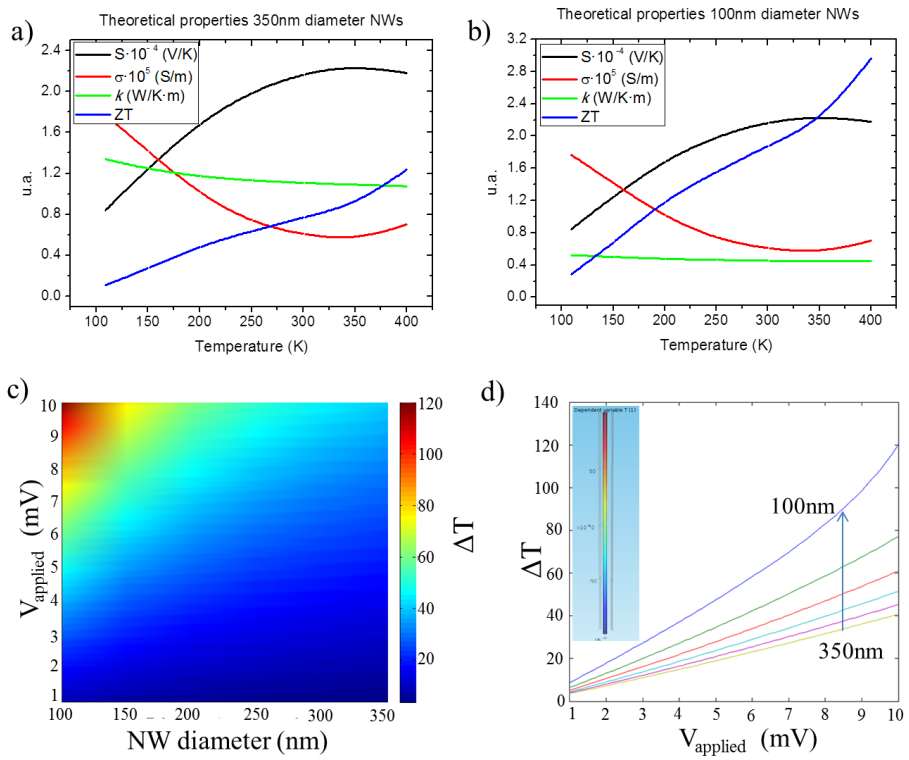

Figure 3.15. a) and b) show the transport properties (*S* and *σ* taken from bulk Bi_2Te_3 while *k* was obtained from the Kinetic-Collective model) and the figure of merit obtained for different temperatures. c) and d) show the temperature difference, ideally generated by nanowires with different diameters under ideal conditions when an electrical voltage is applied across it.

Moreover, with COMSOL Multiphysics® it was possible to simulate the temperature difference generated by Peltier effect when these kinds of ideal nanowires were subjected to an electrical voltage difference, in similitude to how a practical Peltier device made of NWs could work. For that purpose, the geometry of the model consisted of a cylinder with a length of 20 µm and a variable diameter ranging from 350 nm to 100 nm, in order to reproduce the NW shape. Then, to perform stationary thermoelectric simulations with COMSOL Multiphysics ®, it was necessary to use the partial differential module (PDE) to define and set the thermoelectric equations that govern the physics of nanowire, as explained in reference [47]. This model and its implementation for transient thermoelectric simulations is explained in detail in Chapter 4. The bottom of the nanowire was fixed at room temperature while temperature of the top part of the nanowire evolved freely. Figure 3.15c and 3.15d show the map and graph of the temperature difference generated by different diameter nanowires when it is subjected to various electrical voltage differences. Even though the simulation was carried out under ideal conditions, the relatively high temperatures achieved for the electrical voltages applied show the huge potential of the NWs as thermoelectric devices.

In summary, Bi_2Te_3 nanowires are excellent candidates to improve the thermoelectric efficiency of the material. A clear reduction in its thermal conductivity was observed experimentally and compared with theoretical models. Future prospects might be based on improving their electrical conductivity and Seebeck coefficient, either by improving the electrodeposition process or by growing them with other, techniques in order to achieve large numbers for the figure of merit.

3.3.2. Organic nanowires: P3HT.

So far, we have been able to measure the thermal conductivity of inorganic Bi_2Te_3 nanowires and observe how the thermal conductivity changes with diameter. However, little is known about how low dimensionality affects the thermal transport properties in semiconducting polymer materials. Although severe changes are also expected, because size-reduction is well known to induce structural and dynamical changes in nanoconfined polymers [48], it needs to be proved experimentally. In this section, the thermal conductivity of relevant semiconducting polymer nanowires with different diameters inside a matrix is studied in order to clarify the effect upon nanoconfinement in their thermal transport.

The first time that the thermal conductivity of polymer nanowires was performed was reported by Shen *et al* [49] for single ultra-drawn polyethylene (PE) NWs, in which a dramatic increase of the thermal conductivity of the NW was observed as reducing diameter. This effect was correlated to the molecular orientation and reduction of voids and defects. Likewise, Cao *et al* [50] reported the enhancement of thermal conductivity of PE NWs. However, in this case, the NWs thermal conductivity was determined from measurements of collapsed bundles of NWs. As a consequence, these measurements might be influenced by the different environments experienced by the NWs-NWs at interior positions of the bunch, from those at external positions, free NWs, etc. In order to understand the thermal behavior of NWs it is compulsory to study the thermal transport of isolated NW in well controlled boundary conditions. To carry out this study, poly(3-hexylthiophene) (P3HT) as model semiconducting polymer was selected. The reason are: a) it is one of the best characterized semiconducting polymers from a structural point of view[51]; and b), from the point of view of its thermoelectric properties, promising figures of merit at room temperature have been observed [52]. Thus, the characterization of the thermal conductivity of these material in the nanoscale is crucial to calculate its efficiency. Although little is known on the confinement effects on thermal properties of P3HT, the few works reported on

P3HT 2D thin films have shown anisotropy of the thermal conductivity along the different spatial dimensions[53, 54]. However, due to the high spatial resolution required to carry our measurements of individual NW, these measurements are extremely challenging and only very few techniques are able to do it with accuracy.

In this section, the SThM technique working in AC mode with a Pd/SiO_2 probe is used to carry out for the first time topographic and thermal mapping and local measurements of thermal conductivity on individual semiconducting polymer NWs made of P3HT embedded in a matrix. These measurements fill a gap in literature and constitute a step forward to the determination of how polymer materials behave at the nanoscale.

Samples fabrication

In order to observe how spatial confinement affects the thermal properties of polymers, we required of nanowires samples with different diameters. For that purpose, hexagonally ordered porous alumina (AAO) templates with pores of 120, 220, and 350 nm in diameter and 100 µm in length were synthesized by a two-step electrochemical anodization of aluminum and subsequent chemical etching. This process was carried out in a similar way as the one reported in the literature for templates with pore diameter in the 120-400 nm range [55, 56]. After that, for the fabrication of P3HT NWs, macroscopic pieces of commercial P3HT from Aldrich Ltd. (M_n=33405 g/mol, M_w/M_n=1.50, region regularity = 96%) were placed onto the surface of the AAO at 260 °C for 45 min in N_2 atmosphere[57]. Then the samples were taken out from the furnace, and quenched in ice-water, so that P3HT rapidly solidified. In order to remove the excess of P3HT at the AAO top surfaces a razor blade was used and the surface polished with diamond paste (3 µm, Buehler MetaDi II). Finally, the P3HT-infiltrated templates were annealed at 125 °C for 30 min. Figure 3.16 shows SEM images and an schematic view of the fabricated samples.

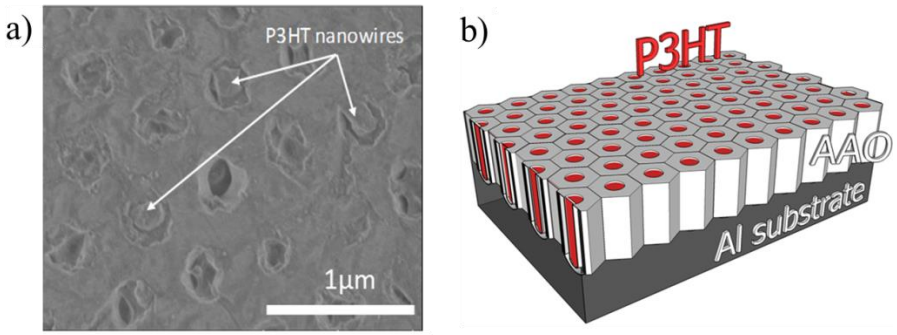

Figure 3.16. a) SEM image of surface of AAO templates having 120 nm in diameter pores. The nanopores have been infiltrated with P3HT and the excess of P3HT film located at the AAO surfaces have been removed with a razor blade and the sample polished with diamond paste (3 µm, Buehler MetaDi II). As can be observed all the pores are filled. (b) Schematic illustration of the samples look like after polishing. Figure taken from supporting information of reference [58].

In order to characterize the structural properties of the nanowires, wide-angle X-ray scattering (WAXS) experiments in a geometry in which the wave vector, *Q*, was considered first parallel and later perpendicular to the long axis of P3HT NWs, as it is shown in Chapter 2.1.3.5.

3ω-SThM measurements. NWs equivalent thermal resistance evaluation.

The SThM working in AC mode was applied to measure P3HT NWs with different diameters embedded in a porous alumina matrix, similarly as the measurements on 300 nm Bi_2Te_3 nanowires. It is important to remember that this experimental technique not only allows measurements of the thermal resistance, R_{eq}, of individual NW inside the matrix, but it also gives information of the R_{eq} of the whole composite [28]. As it was previously explained, this technique is based on a statistical data processing to determine the mean average of the equivalent thermal resistance of the NWs and the whole composite, with its associated standard deviation.

In Figure 3.17a Scanning Electron Microscopy (SEM) images of the top view of the un-filled porous alumina templates used to embed P3HT NW can be seen. Figure 3.17b and Figure 3.17c show the topographic and 3ω voltage ($(V_{3\omega})_{Tip}$) (or thermal) images of P3HT NWs with three different nanowire diameters size, 350 nm, 220 nm and 120 nm, respectively.

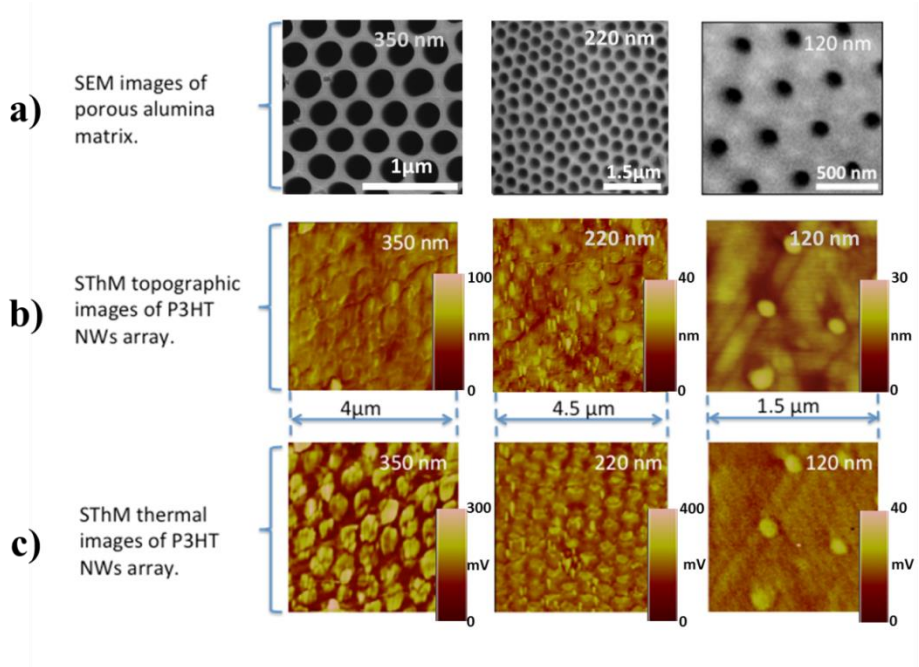

Figure 3.17.a) SEM pictures of the three different diameter size porous alumina matrix used to embedded P3HT NWs, b) topographic of the filled templates and c) $(V_{3\omega})_{Tip}$ or thermal images of P3HT NWs taken with a 3ω-SThM. Figure taken from reference [58].

According to the $(V_{3\omega})_{Tip}$ thermal images of P3HT NWs, we can differentiate two areas: 1) at which a high $V_{3\omega}$ signal area is observed, that corresponds with the NWs locations and 2) at which a low $V_{3\omega}$ signal area is found, which is related to the presence of anodized alumina (the template). From these images, the NW mean equivalent thermal resistances $(R_{eq})_{NW}$ for the three different diameters can be determined from the $V_{3\omega}$ value measured on each NW as it was done in

Section 3.3.1.1. The results are given in Table 3.V. It is important to notice that each $(R_{eq})_{NW}$ value presented in this table was obtained after an statistical study on measurements of 20 NWs (even for the 120nm NW sample for which a thermal image larger than the one in Figure 3.17c was used). The thermal exchange radius of the tip, *b*, for the Pd/SiO_2 probe used is also shown in this table whose value was specifically measured before each sample scan. As it was mentioned before, it is a key parameter not only in terms of spatial resolution, but also in the estimation of the thermal conductivity of some of the thermal resistances involved in the total equivalent resistance measured, as shown in Section 3.3.1.1.

The data reduction analysis was carried out using the Equations 3.2, 3.3 and 3.4. Similarly to what happened in Section 3.3.1.1 , Equation 3.2 can be reduced to,

$$(R_{eq})_{NW} = R_C + R_{Com} \tag{3.8}$$

where R_{Com} is the thermal resistance of the composite (nanowires plus alumina matrix) and R_C is the thermal contact resistance between the tip and the sample. The evaluation of R_C is mandatory to determine R_{Com} and subsequently k_{Com}. As reported by Lefevre *et al* [10] , this resistance takes into account not only the solid-solid conduction between tip and sample, but also the conduction through air and through the water meniscus, which constitutes the two other main heat transfer mechanisms under atmospheric conditions. It can be expressed as: $1/R_C=G_c=G_S+G_A+G_W$ where G_S, G_A and G_W are the conductance through solid-solid contact, through the air and through the water meniscus, respectively. The heat transfer mechanisms take place over a surface not defined by the contact-contact radius but by the thermal exchange radius *b*, hence the necessity to calibrate this parameter.

In the same way as in the Bi_2Te_3 nanowires measurements, to evaluate R_c we measure the equivalent thermal resistance on the alumina matrix [7, 28, 29, 59] . Indeed, in this case, the equivalent thermal resistance measured on the alumina is given by,

$$\left(R_{eq}\right)_{Alu} = R_C + R_{Tip-Alu} \tag{3.9}$$

where $R_{Tip-Alu}$ is the constriction resistance between the tip and the alumina matrix. If the matrix is considered as a semi-infinite medium because of its dimensions in comparison with the thermal exchange radius, b, the constriction resistance can be expressed as [59] $R_{Tip-Alu} = \frac{1}{4 \cdot k_{Alu} \cdot b}$ where k_{Alu} is the thermal conductivity of the alumina. R_{Com} can then be expressed as a constriction resistance on a semi-infinite effective medium, $R_{Com} = \frac{1}{4 \cdot k_{Com} \cdot b}$, where k_{Com} is the thermal conductivity of the composite. This thermal conductivity. k_{Com}, can be expressed in terms of the thermal conductivity of the NW, k_{NW}, and the alumina, k_{Alu}, using the effective medium theory [33] [28], $k_{Com} = x \cdot k_{NW} + (1 - x) \cdot k_{Alu}$, where x is the areal packing density of the NW array.

Table 3.V. Areal packing density of the NW array and alumina, thermal exchange radius, equivalent thermal resistance and thermal conductivities of the composite, alumina matrix and intrinsic NWs for three different composites made of P3HT NWs array embedded in alumina matrix. Table taken from reference [58].

NW diameter (nm)	Packing areal density of the NW array (%)	Thermal exchange radius (nm)	$(R_{eq})_{NW}$ $(K \cdot W^{-1})$ $\times 10^6$	$(R_{eq})_{Alumina}$ $(K \cdot W^{-1})$ $\times 10^6$	Composite thermal conductivity $(W \cdot K^{-1} \cdot m^{-1})$	Alumina matrix thermal conductivity $(W \cdot K^{-1} \cdot m^{-1})$	NW thermal conductivity $(W \cdot K^{-1} \cdot m^{-1})$
350	0.55±0.01	175±10	4.36±0.11	4.63±0.03	1.89±0.08	1.38±0.08	2.29±0.15
220	0.25±0.02	175±10	4.49±0.06	4.34±0.02	1.21±0.06	1.38±0.08	0.70±0.12
120	0.08±0.02	81±5	6.48±0.03	6.36±0.02	1.31±0.02	1.38±0.08	0.50±0.24

In order to determine the thermal resistance of the alumina, from the same $(V_{3\omega})_{Tip}$ image presented in Figure 3.17c we measured the $(V_{3\omega})_{Tip}$ signal on twenty locations on the alumina area for the three samples with porous size of 350 nm, 220 nm and 120 nm. The thermal conductivity of the alumina matrices was measured with an independent technique at the University of Barcelona giving a value of $k_{Alu} = 1.38 \pm 0.08\ W \cdot K^{-1} \cdot m^{-1}$, as shown in Table 3.V, for the three alumina templates. The thermal conductivity values show consistence since all the templates were prepared under the same

conditions; [55 57] the only difference is that the pores are widening by chemical etching and the porosity increase. With these values of the alumina the mean contact resistances were calculated using Equation 3.9 to be, R_C =3.60×10^6 K · W^{-1}, R_C =3.31×10^6 K · W^{-1} and R_C =4.12×10^6 K · W^{-1} for the alumina with 350 nm, 220 nm and 120 nm in diameter pores, respectively. Often, the contact resistance is determined by calibration on a material of well-known thermal conductivity [7 60]. It can be then assumed that R_C does not change from sample to sample and when measuring other materials. This was also checked in Section 3.1.1. where a thermoresistor probe showed an identical thermal exchange radius and contact resistance for a range of thermal conductivities that go from 0.1 to 2.5 W · K^{-1} · m^{-1} [10]. Despite of this fact, precautions need to be taken since this contact resistance may depend on various parameters such as the surface roughness or the tip-to-sample contact geometry. In this experiment, when measuring $(R_{eq})_{Alu}$ on the alumina part of the three samples, even if the tip is identical, three different values were measured (Table 3.V), which resulted in three different contact resistances. An original method was previously proposed in reference[29] to determine R_c accurately. It consists of deducing directly the thermal resistances measured directly on the NWs from the 3ω or thermal SThM images. In this approach, the classical Equation 3.5 is used, whose *y*-axis crossing of the experimental trend should give R_c. This method demands a sample with NWs offering wide diameter dispersion, which is not the case here. Nevertheless, in reference [29] it is also proposed to determine the mean contact resistance from a reference sample, similarly as we have calculated the contact resistance from the alumina matrix. The estimated values obtained by both methods differ by less than 1%. Therefore, measuring R_C on a part of a sample seems to give a reliable value that can be used on another part of the sample from a thermal image obtained during the same scan under the same experimental conditions. In particular, with a contact force between tip and sample maintained constant by the AFM feedback loop.

Afterwards, an estimated ±1% relative error must be considered in the contact resistance result. This value, which is also consistent with

the standard deviation evaluated on $(R_{eq})_{Alu}$ in Table 3.V and from which R_c is deduced, can appear small in comparison with classical mechanical contact resistance relative variations. Indeed, it only takes into account the repeatability error which is reduced because, from one image, twenty measurements were taken on the alumina part, reducing the standard deviation by almost five. With this ±1% possible error, the mean composite intrinsic thermal resistances, R_{Com}, were determined to be R_{Com}=(0.760 ± 0.036)×10^6 $K \cdot W^{-1}$, R_{Com}=(1.180 ± 0.033)×10^6 $K \cdot W^{-1}$ and R_{Com}=(2.36 ± 0.041)×10^6 $K \cdot W^{-1}$ for the P3HT NWs with 350 nm, 220 nm and 120 nm diameter, respectively.

Nanowires thermal conductivity and discussion

From Equation 3.9 and a low dispersion statistical study over 20 NWs, the local thermal conductivity of the composites was deduced to be $k_{Com} = 1.89 \pm 0.08\ W \cdot K^{-1} \cdot m^{-1}$, $k_{Com} = 1.21 \pm 0.06\ W \cdot K^{-1} \cdot m^{-1}$and $k_{Com} = 1.31 \pm 0.02\ W \cdot K^{-1} \cdot m^{-1}$, for composites made of P3HT NWs with 350 nm, 220 nm and 120 nm diameters embedded in porous alumina matrix, respectively. It is worth to mention that these results are extremely useful and relevant, as it constitutes the thermal conductivity values of future functional polymer nanowire devices as well as it involves the first measurements of the thermal conductivity of polymer nanowires.

A reduction of the thermal conductivity of individual P3HT, calculated from the effective medium theory, with its diameter is evidenced in Table 3.V.

For semicrystalline polymers, the thermal conductivity is known to depend on both the degree of crystallinity and its orientation of their structural elements, i.e. molecules, aggregates, crystals, etc. [21] Regarding crystallinity, the crystalline region of the polymers show intrinsically higher conductivity than its amorphous regions. For that reason, the thermal conductivity of semicrystalline polymers is usually higher than that of amorphous polymers. Regarding the degree of orientation, this leads to a large anisotropy in the thermal transport of semicrystalline polymers. It can be commonly understood considering that molecular chains in the crystallites are aligned in a certain

direction, thus offering little thermal resistance along this direction. P3HT is known to be a semicrystalline polymer and thus, the considerations explained above should be taken into account when studying its thermal transport. Recently, Feng *et al.* [61] have shown that thermal conductivity of P3HT does not depend significantly on density, which can be directly related to the degree of crystallinity of the polymer. An increase of only 12 % of the thermal conductivity was observed between P3HT films with density values around 1 g/ml (which according to Ro *et al* [62] corresponds to completely amorphous P3HT) and those having values around 1.6 g/ml (highly crystalline P3HT). This low dependence of the thermal conductivity with the crystallinity in polymers having medium degrees of crystallinity, like P3HT (the degree of crystallinity of bulk P3HT has been proposed to be somewhat below 50 % [63]), was suggested to be a consequence of the difference in elastic properties between amorphous and crystalline regions, which provokes a high thermal boundary resistance at the many interfaces existing between amorphous regions and crystals[21].

In contrast, orientation phenomena are likely to alter strongly the thermal conductivity of semicrystalline polymers and to induce a large anisotropy as a function of the crystallographic directions. For instance, Piraux *et al* [64] observed that the thermal conductivity of oriented polyacetylene films (another semicrystalline conjugated polymer) were 15 to 60 times larger than that of the non-oriented polyacetylene. Kiliam *et al* [65] reported that the thermal diffusivity in stretched polyethylene was 50 times higher along the drawing direction than along the perpendicular direction. Furthermore, this observation contrasts to the behavior of amorphous polyethylene, for which only a two fold increase was measured. These results indicates the special relevance of crystal orientation in semicrystalline polymers. Regarding P3HT films, Feng *et al* [53] have recently reported a strong anisotropic thermal transport along the three spatial dimensions.

2D-nanoconfinement, like the one imposed by the cylindrical nanopores of AAO templates, frequently produces a preferential orientation of the confined polymer crystals [66 67] . In order to study if there is a modification of the crystal orientation in our P3HT nanowires. WAXS measurements were carried out for two different

spatial directions, i.e. directions parallel and perpendicular to long nanowire axis, in order to elucidate whether changes in the orientation of P3HT crystals in the NWs may be at the origin of the observed reduction of their thermal conductivities. Note that, 2D patterns were collected in the direction perpendicular to NWs and then converted to one-dimensional scattering profiles by radial averaging along the azimuthal angle. All the samples showed diffraction rings in the perpendicular direction.

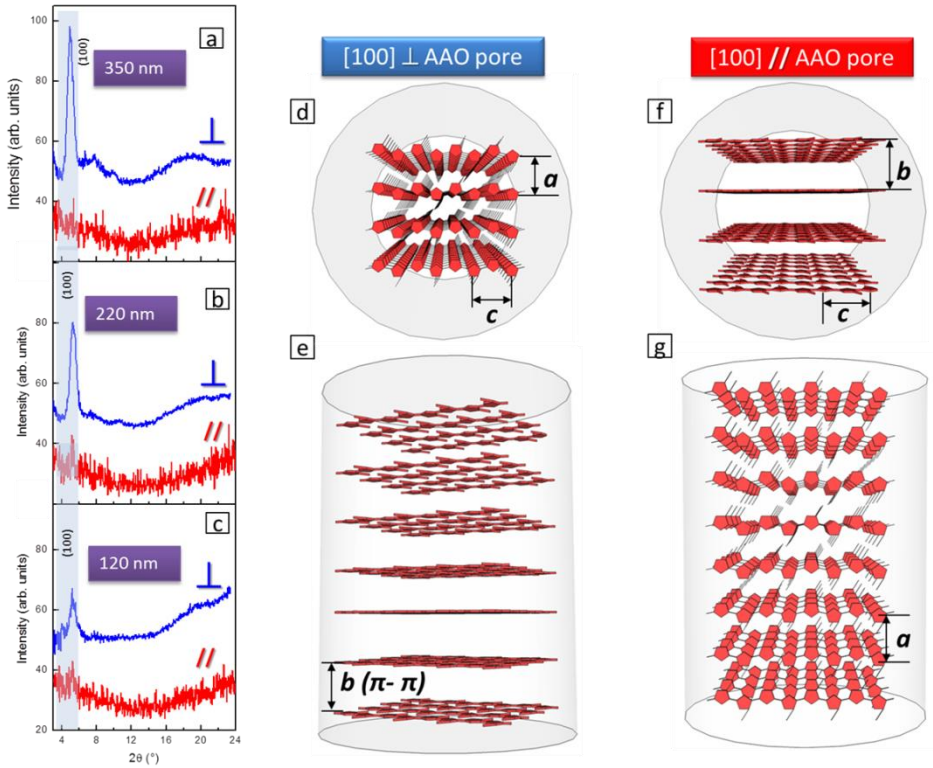

Figure 3.18. WAXS diffractograms of ensembles of P3HT NWs in which the wave vector, *Q*, was perpendicular to nanowires (lower red line with || symbol) and parallel to nanowires (upper blue line with ⊥ symbol) for (a) 350 nm, (b) 220 nm and (c) 120 nm NW arrays. Schematic illustrations of the 3 possible ideal spatial orientations of the P3HT crystallite within nanopores from up and transversal perspectives: (d and e) top and side view of the *b* axis of the crystal cell (π-π stacking direction) parallel to NW long axis which also

corresponds to [1 0 0] perpendicular, and (f and g) top and side view of the *a* axis of the crystal cell ([1 0 0] growth direction) parallel to NW long axis. Figure taken from reference [58].

In the experimental geometry in which the wave vector, *Q*, was perpendicular to nanowire long axis, the three samples (P3HT NWs of 350, 220 and 120 nm diameters) presented a diffraction maximum at 2θ = 5.2°. It corresponds to the stacking of the main chain/side-chain layered structure of the P3HT crystal along the *a* axis [68, 69] (Figure 3.18a, 3.18b and 3.18c). In general, in the three samples studied, crystals were preferentially oriented lying with their [1 0 0] crystallographic direction perpendicular to NW long axis and thus, the [0 1 0] direction (the π-π stacking direction) or the [0 0 1] directions arrange preferentially parallel to the NW axis (both type of stacking are ideally represented in Figure 3.18d and 3.18e). The most probable orientation is the one in which crystals lay with the π-π stacking direction parallel to nanowire long axis, as that orientation is the one fulfilling the Bridgeman mechanism [70, 71, 72] for orientations guided by kinetic aspects. This has been usually observed in commodity polymers confined in nanopores [71, 72]. Such mechanism dictates that the crystallographic direction with the fastest growth rate aligns parallel to the NW long axis. For P3HT crystal, π-π stacking direction is known to be the fastest growth direction [68, 73], and so it is expected to be parallel to NW long axis. The fact that most of the chains are oriented along that direction explain the high values of the thermal conductivity measured in the 350 nm samples. In this case, the phonons can travel easily from chain to chain using the π-π bounding. The diffraction peak exhibits a decrease in intensity and a broadening upon reduction of the diameter of the nanowires from 350 to 120 nm. It can be explained according to three main reasons: a) the porosity % of the alumina template is lower in the 120 nm (8%) than in 220 nm (25%) and 350 nm (55%), which means than the less amount of diffracting P3HT is in 120 nm sample (only 8% of the total surface); b) As the nanowire diameter is reduced, the crystal size becomes smaller, so the diffraction peaks become broader; and c), some of the P3HT crystals may rotate under confinement.

In the experimental geometry in which the wave vector, *Q*, was parallel to nanowire long axis, the (1 0 0) diffraction for *Q* parallel to NWs long axis was vanished in 350 nm nanowires, while weak (1 0 0) peaks become visible for 250 and 120 nm samples, being more intense in 120 nm nanowires. This means that as nanowire diameter is reduced, more crystals are tilt toward the [1 0 0] direction parallel to NWs axis. It is worth noting that in crystals with the [1 0 0] direction parallel to NWs axis, the [0 1 0] direction is almost perpendicular to the AAO pore walls. P3HT crystallites would tend to grow along that direction since the [0 1 0] direction is that of the fastest growth, but they impinge on the pore walls and die. As a consequence, this would lead these crystals to be considerably small, which would generate non-well-developed diffraction peaks when measuring in the geometry where *Q* is parallel to nanowire axis. This rotation of the polymer chain is ideally represented in Figure 3.18f and 3.18g.

An orientation parameter Γ, defined as $\Gamma = \gamma_{\perp} / 1.18\gamma_{\parallel}$, being $\gamma_{\perp}$ and $\gamma_{\parallel}$ the areas of the (1 0 0) peaks in direction perpendicular and parallel to the NW axis, respectively, was considered to perform a semi-quantitative analysis of the crystal orientation of P3HT NWs. A coefficient of 1.18 was determined from the ratio $\gamma_{\perp} / \gamma_{\parallel}$ of the bulk P3HT powder (the P3HT was powdered in an agate mortar), considering the fact that crystals must be oriented along all the directions in that sample and thus Γ must be equal to unity. In this way, Γ is closely correlated to the preferential orientation of the (1 0 0) planes in the nanowires. Since $\Gamma > 1$ for the three samples, crystals laid with their [1 0 0] crystallographic direction preferentially perpendicular to the NW axis and thus, [0 1 0] and/or [0 0 1] directions were preferentially parallel to the NW axis (Figure 3.18e and 3.18f). As it is shown Figure 3.19, Γ decreased as the pore diameter reduces, which suggest the presence of more and more crystals with [1 0 0] parallel to NWs, as ideally represented in Figure 3.18d. In other words, for the largest nanowire diameter (350 nm), a compact π-π stacking and strong covalent bonds ocurr parallel and perpendicular to the length of the nanowire, respectively, which facilitate the phonon transport along this direction. However, as the diameter of the P3HT nanowire reduces, this structure is not longer maintained and the π-π stacking becomes

disordered, involving a reduction in the thermal conductivity of the nanowire.

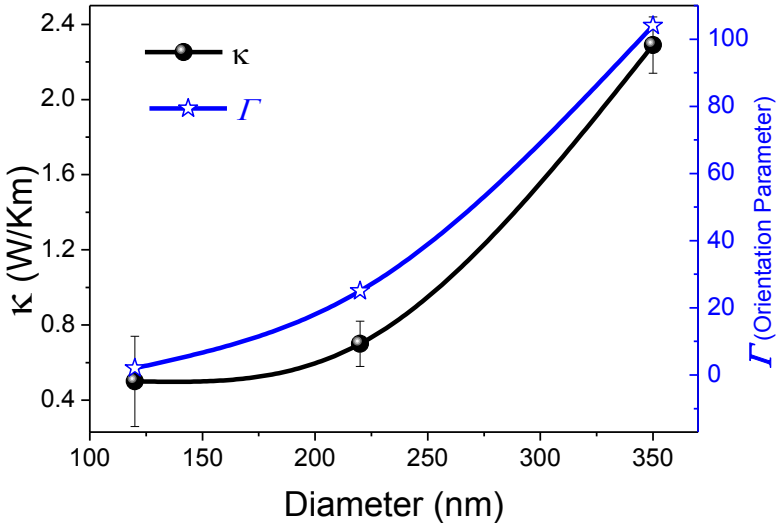

Figure 3.19. Plot of the thermal conductivity (black spheres) the orientation parameter, Γ, (blue stars) of P3HT NWs as a function of the NW diameter. $\Gamma = \gamma\perp / 1.18\gamma\parallel$, being $\gamma\perp$ and $\gamma\parallel$ the areas of the (100) peaks in direction perpendicular and parallel to the NWs axis, respectively. The coefficient 1.18 is extracted from the ratio $\gamma\perp / \gamma\parallel$ of the bulk P3HT. Figure taken from reference [58].

In Figure 3.19 the reduction of the thermal conductivity is observed when lowering the diameter size of the nanowire. These results show the potential of these nanowires for different application in thermal transport engineering because of choosing a particular diameter the changes in its thermal conductivity are appreciable. As a consequence, the heat flow across a device could be controlled with a certain magnitude by selecting the appropriate P3HT diameter nanowire.

In conclusion, the thermal conductivity of P3HT nanowires becomes seriously affected depending on the alignment of the polymer chains. When the confinement of the polymer NW is such that the π-π stacking is perpendicular to the length of the nanowire (350 nm

diameter), high values of thermal conductivity, $2.29 \pm 0.15\ W \cdot K^{-1} \cdot m^{-1}$, are found. This is consequence that the phonons can transport heat easily in this direction, because of the strong bonding. However, when the π-π stacking begins to disorder, as consequence of a stronger confinement of the polymer NWs (220 nm and 120 nm diameters), the thermal conductivity is drastically reduced up to $0.50 \pm 0.24\ W \cdot K^{-1} \cdot m^{-1}$. The conclusions of this work explain the wide variety of thermal conductivity results obtained for P3HT in literature and set the foundations for polymeric thermal transport engenieering.

3.3.3. Validation of the effective medium theory with Finite Element Modeling (COMSOL® Multiphysic's).

The effective medium theory is a theory that is normally applied to extract the thermal conductivity of the different materials inside a matrix. The validity of the effective medium theory used to quantify the thermal conductivity of P3HT, was also study using a COMSOL Multiphysic® simulation to analyze the experimental results. The measurements of the P3HT nanowires have been considered as a model example.

The simulation consists of three different P3HT nanowire arrays embedded in alumina with 350 nm, 220 nm and 120 nm diameters. From the geometrical point of view, the total sample area considered was 36 μm^2, but in order to increase the simulation speed, the symmetry of the sample has been taken as advantage. Hence, only a fourth of the total sample has been taken into account, but adding symmetry boundary conditions in its internal walls. The proper functioning of the symmetry was checked with a comparison of their results with the ones obtained for a full sample simulation. The exterior walls were considered as open boundaries that limit the modeling domain that extends in an open fashion within the temperature variable, *T*, obtained in this limit. The sample is 5μm long and its bottom temperature was fixed at room temperature (293.15 ºK). The areal packing density was kept identical to the ones considered in our

manuscript (see Table 3.V). A convection heat coefficient on the top surface of h = 5 $W \cdot K^{-1} \cdot m^{-2}$ to simulate the effects of the surrounding air was considered. Concerning the properties of the materials, the thermal conductivity of the solid part of the alumina was fixed to 1.38 $W \cdot K^{-1} \cdot m^{-1}$ while the thermal conductivity of the nanowires will be varied.

In order to simulate the heating of the SThM probe, a circular Gaussian heat source with an applied power of $1 \cdot 10^{-5}$ W was defined on top of the sample. A constant disc source was discarded as it does not approach to the reality and results in not very accurate values. The gaussian distribution of heat has been considered in similitude to the measurements of the thermal exchange radius given in reference [12]. The same thermal exchange radius as the ones given in Table 3.V were taken for each sample.

This heat source was placed on top of the nanowires and on the alumina matrix between the nanowires in similitude to the experimental measurements carried out with our SThM system. The maximum temperature reached at each location is considered and the thermal resistance for the nanowire, $R^{simul}_{therm\,NW}$, and the alumina, $R^{simul}_{therm\,AAO}$, are obtained by using the next equation,

$$R^{simul}_{therm} = \frac{T_{max} - T_{room}}{\dot{Q}} \tag{3.10}$$

This process was performed in each nanowire diameter sample. Figure 3.20 shows an example of the simulation obtained for 350 nm diameter nanowire array embedded in alumina matrix.

To perform this simulation, the "Heat Transfer in Solids" module in COMSOL Multiphysics® was used in order to solve the stationary equation of heat for solids. In order to run the simulation accurately, the mesh was refined in each nanowire array samples until no variation in the results was observed. The results are sensitive to the mesh, especially as the diameter of the nanowire is reduced.

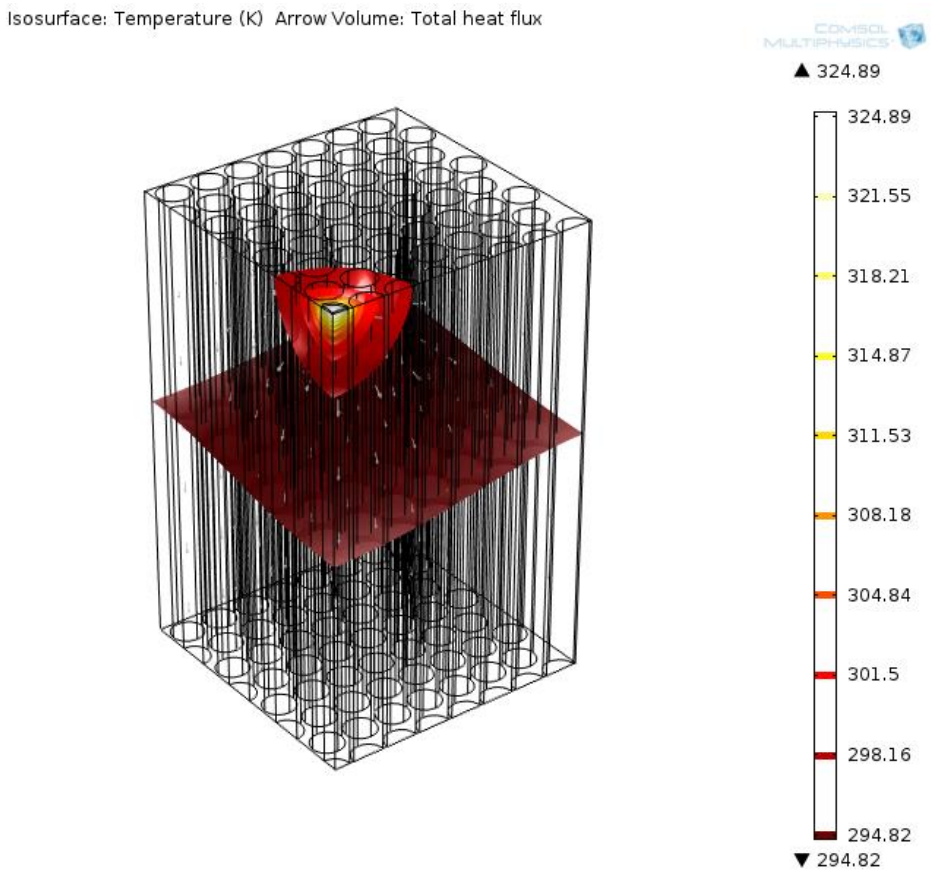

Figure 3.20. Temperature iso-surfaces and total heat flow (arrows) when the heat source is positioned on top of a 350 nm diameter nanowire.

First of all, validation of the model was carried out for a bulk sample with different thermal conductivities and a bulk sample with nanowires, having both the same thermal conductivity, using the equation: $R_{therm\ theory} = \frac{1}{4 \cdot b \cdot k}$. Table 3.VI shows that the model works properly, within 5% error maximum, for a thermal exchange radius of 175 nm and 81 nm.

Table 3.VI. Validation of the model. Simulated results versus the expected ones $R_{therm} = \frac{1}{4 \cdot b \cdot k}$ for b of 175 nm and 81 nm.

k_{bulk} (W/K·m)	b (nm)	$R_{therm\ simulated}$ (W/K)	$R_{therm\ theory}$ (W/K)
0.1	175	$1.42 \cdot 10^7$	$1.43 \cdot 10^7$
0.5	175	$2.83 \cdot 10^6$	$2.86 \cdot 10^6$
1	175	$1.42 \cdot 10^6$	$1.43 \cdot 10^6$
1.5	175	$9.44 \cdot 10^5$	$9.52 \cdot 10^5$
2	175	$7.08 \cdot 10^5$	$7.14 \cdot 10^5$
2.5	175	$5.66 \cdot 10^5$	$5.71 \cdot 10^5$
3	175	$4.71 \cdot 10^5$	$4.76 \cdot 10^5$
3.5	175	$4.04 \cdot 10^5$	$4.08 \cdot 10^5$
4	175	$3.53 \cdot 10^5$	$3.57 \cdot 10^5$
4.5	175	$3.14 \cdot 10^5$	$3.17 \cdot 10^5$
5	175	$2.83 \cdot 10^5$	$2.86 \cdot 10^5$
0.1	81	$3.00 \cdot 10^7$	$3.09 \cdot 10^7$
0.5	81	$5.99 \cdot 10^6$	$6.17 \cdot 10^6$
1	81	$3.00 \cdot 10^6$	$3.09 \cdot 10^6$
1.5	81	$2.00 \cdot 10^6$	$2.06 \cdot 10^6$
2	81	$1.50 \cdot 10^6$	$1.54 \cdot 10^6$
2.5	81	$1.20 \cdot 10^6$	$1.23 \cdot 10^6$
3	81	$9.98 \cdot 10^5$	$1.03 \cdot 10^6$
3.5	81	$8.55 \cdot 10^5$	$8.82 \cdot 10^5$
4	81	$7.48 \cdot 10^5$	$7.72 \cdot 10^5$
4.5	81	$6.65 \cdot 10^5$	$6.86 \cdot 10^5$
5	81	$5.99 \cdot 10^5$	$6.17 \cdot 10^5$

After the validation has been achieved, it was decided to analyze the thermal resistance obtained in the alumina matrix and on top of the nanowires. On the one hand, by subtracting the simulated equivalent thermal resistance of the alumina and the alumina experimental thermal resistance given in Table 3.V of the manuscript, the simulated contact resistance was obtained: $R_C^{simul} = R_{therm\ AAO}^{exper} - R_{therm\ AAO}^{simul}$. On the other hand, by subtracting the simulated contact resistance to the experimental nanowires resistance, $R_{therm\ NW}^{experm}$ of Table 3.VI of the manuscript, $R_{NW} = R_{therm\ NW}^{exper} - R_C^{simul}$, it would be possible to compare the simulated nanowire resistance with the one just calculated. By varying the thermal conductivity of the nanowire until we fit these thermal resistances, we would be able to determine the intrinsic thermal conductivity of the nanowire. The next tables and figures show the results given from the simulation and its comparison to the effective medium theory results for the three different NWs arrays samples, where $R_C^{exp.} = R_{AAO\ therm}^{experm} - R_{AAO\ therm}^{Simulated}$, $R_C^{mean\ eff.} = R_{AAO\ therm}^{experm} - 1/(4 \cdot k_{AAO} \cdot r_{th})$, $R_{NW\ therm}^{exp.+sim} = R_{NW\ therm}^{experm} - R_C^{exp.}$ and $R_{NW\ therm}^{mean\ eff.+sim} = R_{NW\ therm}^{experm} - R_C^{mean\ eff.}$.

Table 3.VII. Data results for the 350 nm diameter NW array sample. Thermal exchange radius used is 175 nm.

k_{NW} (W/K·m)	$R_{NW\ therm}^{Simulated}$ (W/K)	$R_{NW\ therm}^{effective}$ (W/K)	$R_{AAO\ therm}^{Simulated}$ (W/K)	$R_{NW\ therm}^{experm}$ (W/K)	$R_{AAO\ therm}^{experm}$ (W/K)	$R_{C}^{exp.}$ (W/K)	$R_{C}^{mean\ eff.}$ (W/K)	$R_{NW\ therm}^{exp.+sim}$ (W/K)	$R_{NW\ therm}^{mean\ eff.+}$ (W/K)
0.1	$2.50\cdot10^{6}$	$2.11\cdot10^{6}$	$1.24\cdot10^{6}$	$4.36\cdot10^{6}$	$4.63\cdot10^{6}$	$3.39\cdot10^{6}$	$3.59\cdot10^{6}$	$9.65\cdot10^{5}$	$7.65\cdot10^{5}$
0.5	$1.67\cdot10^{6}$	$1.59\cdot10^{6}$	$1.11\cdot10^{6}$	$4.36\cdot10^{6}$	$4.63\cdot10^{6}$	$3.52\cdot10^{6}$	$3.59\cdot10^{6}$	$8.40\cdot10^{5}$	$7.65\cdot10^{5}$
1	$1.22\cdot10^{6}$	$1.22\cdot10^{6}$	$1.05\cdot10^{6}$	$4.36\cdot10^{6}$	$4.63\cdot10^{6}$	$3.58\cdot10^{6}$	$3.59\cdot10^{6}$	$7.78\cdot10^{5}$	$7.65\cdot10^{5}$
2	$8.35\cdot10^{5}$	$8.30\cdot10^{5}$	$9.96\cdot10^{5}$	$4.36\cdot10^{6}$	$4.63\cdot10^{6}$	$3.63\cdot10^{6}$	$3.59\cdot10^{6}$	$7.26\cdot10^{5}$	$7.65\cdot10^{5}$
3	$6.55\cdot10^{5}$	$6.29\cdot10^{5}$	$9.73\cdot10^{5}$	$4.36\cdot10^{6}$	$4.63\cdot10^{6}$	$3.66\cdot10^{6}$	$3.59\cdot10^{6}$	$7.03\cdot10^{5}$	$7.65\cdot10^{5}$
4	$5.49\cdot10^{5}$	$5.06\cdot10^{5}$	$9.60\cdot10^{5}$	$4.36\cdot10^{6}$	$4.63\cdot10^{6}$	$3.67\cdot10^{6}$	$3.59\cdot10^{6}$	$6.90\cdot10^{5}$	$7.65\cdot10^{5}$
5	$4.79\cdot10^{5}$	$4.23\cdot10^{5}$	$9.52\cdot10^{5}$	$4.36\cdot10^{6}$	$4.63\cdot10^{6}$	$3.68\cdot10^{6}$	$3.59\cdot10^{6}$	$6.81\cdot10^{5}$	$7.65\cdot10^{5}$

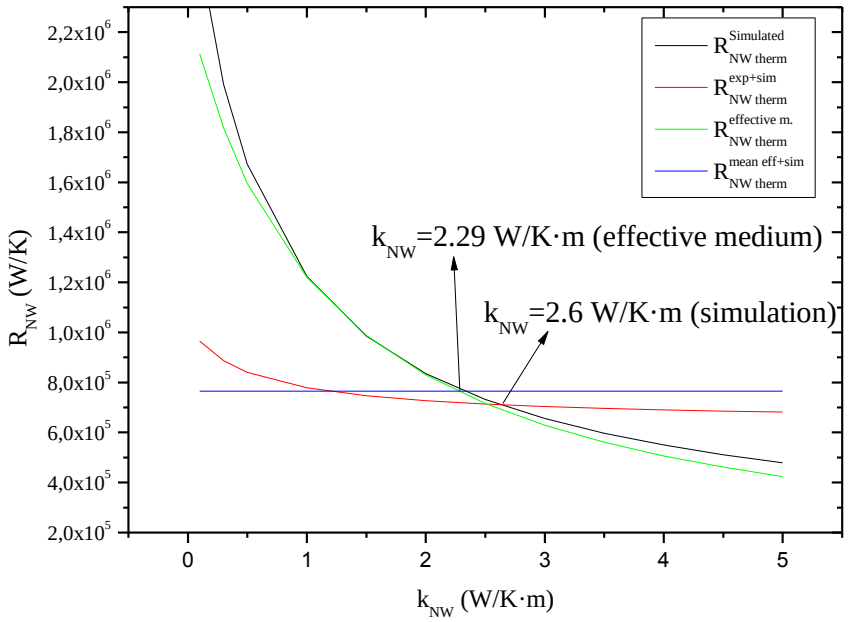

Figure 3.21. Simulation and effective medium results for 350 nm diameter NWs sample.

Table 3.VIII. Data results for the 220 nm diameter NW array sample. Thermal exchange radius used is 175 nm.

k_{NW} (W/K·m)	$R_{NW\ therm}^{Simulated}$ (W/K)	$R_{NW\ therm}^{effective}$ (W/K)	$R_{AAO\ therm}^{Simulated}$ (W/K)	$R_{NW\ therm}^{experm}$ (W/K)	$R_{AAO\ therm}^{experm}$ (W/K)	$R_C^{exp.}$ (W/K)	$R_C^{mean\ eff}$ (W/K)	$R_{NW\ therm}^{exp.+sim}$ (W/K)	$R_{NW\ therm}^{mean\ eff}$ (W/K)
0.1	$1.32\cdot10^6$	$1.35\cdot10^6$	$1.09\cdot10^6$	$4.49\cdot10^6$	$4.34\cdot10^6$	$3.25\cdot10^6$	$3.30\cdot10^6$	$1.24\cdot10^6$	$1.19\cdot10^6$
0.5	$1.20\cdot10^6$	$1.23\cdot10^6$	$1.05\cdot10^6$	$4.49\cdot10^6$	$4.34\cdot10^6$	$3.29\cdot10^6$	$3.30\cdot10^6$	$1.20\cdot10^6$	$1.19\cdot10^6$
1	$1.10\cdot10^6$	$1.11\cdot10^6$	$1.03\cdot10^6$	$4.49\cdot10^6$	$4.34\cdot10^6$	$3.31\cdot10^6$	$3.30\cdot10^6$	$1.18\cdot10^6$	$1.19\cdot10^6$
2	$9.60\cdot10^5$	$9.30\cdot10^5$	$9.96\cdot10^5$	$4.49\cdot10^6$	$4.34\cdot10^6$	$3.34\cdot10^6$	$3.30\cdot10^6$	$1.15\cdot10^6$	$1.19\cdot10^6$
3	$8.69\cdot10^5$	$8.00\cdot10^5$	$9.80\cdot10^5$	$4.49\cdot10^6$	$4.34\cdot10^6$	$3.36\cdot10^6$	$3.30\cdot10^6$	$1.13\cdot10^6$	$1.19\cdot10^6$
4	$8.02\cdot10^5$	$7.02\cdot10^5$	$9.69\cdot10^5$	$4.49\cdot10^6$	$4.34\cdot10^6$	$3.37\cdot10^6$	$3.30\cdot10^6$	$1.12\cdot10^6$	$1.19\cdot10^6$
5	$7.48\cdot10^5$	$6.25\cdot10^5$	$9.61\cdot10^5$	$4.49\cdot10^6$	$4.34\cdot10^6$	$3.38\cdot10^6$	$3.30\cdot10^6$	$1.11\cdot10^6$	$1.19\cdot10^6$

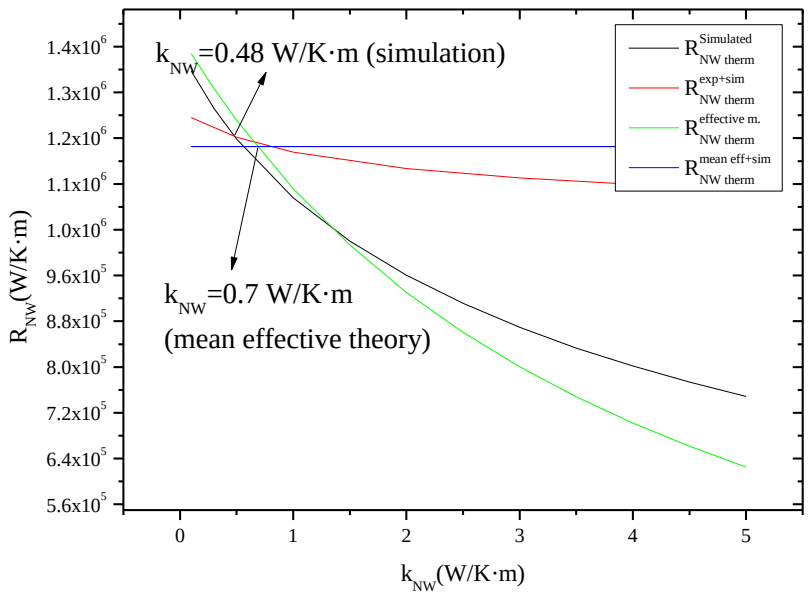

Figure 3.22. Simulation and effective medium results for 220 nm diameter NWs sample.

Table 3.IX. Data results for the 120 nm diameter NW array sample. Thermal exchange radius used is 81 nm.

k_{NW} (W/K·m)	$R_{NW\ therm}^{Simulate}$ (W/K)	$R_{NW\ therm}^{effectiv}$ (W/K)	$R_{AAO\ therm}^{Simulated}$ (W/K)	$R_{NW\ therm}^{experm}$ (W/K)	$R_{AAO\ ther}^{experm}$ (W/K)	$R_C^{exp.}$ (W/K)	$R_C^{mean\ ef}$ (W/K)	$R_{NW\ therm}^{exp.+sim}$ (W/K)	$R_{NW\ therm}^{mean\ eff.}$ (W/K)
0.1	$2.58\cdot10^6$	$2.42\cdot10^6$	$2.436\cdot10^6$	$6.48\cdot10^6$	$6.36\cdot10^6$	$3.924\cdot10^6$	$4.12\cdot10^6$	$2.556\cdot10^6$	$2.36\cdot10^6$
0.5	$2.42\cdot10^6$	$2.36\cdot10^6$	$2.428\cdot10^6$	$6.48\cdot10^6$	$6.36\cdot10^6$	$3.931\cdot10^6$	$4.12\cdot10^6$	$2.548\cdot10^6$	$2.36\cdot10^6$
1	$2.27\cdot10^6$	$2.29\cdot10^6$	$2.423\cdot10^6$	$6.48\cdot10^6$	$6.36\cdot10^6$	$3.937\cdot10^6$	$4.12\cdot10^6$	$2.543\cdot10^6$	$2.36\cdot10^6$
2	$2.04\cdot10^6$	$2.16\cdot10^6$	$2.415\cdot10^6$	$6.48\cdot10^6$	$6.36\cdot10^6$	$3.945\cdot10^6$	$4.12\cdot10^6$	$2.535\cdot10^6$	$2.36\cdot10^6$
3	$1.87\cdot10^6$	$2.04\cdot10^6$	$2.409\cdot10^6$	$6.48\cdot10^6$	$6.36\cdot10^6$	$3.950\cdot10^6$	$4.12\cdot10^6$	$2.529\cdot10^6$	$2.36\cdot10^6$
4	$1.75\cdot10^6$	$1.94\cdot10^6$	$2.406\cdot10^6$	$6.48\cdot10^6$	$6.36\cdot10^6$	$3.954\cdot10^6$	$4.12\cdot10^6$	$2.526\cdot10^6$	$2.36\cdot10^6$
5	$1.65\cdot10^6$	$1.85\cdot10^6$	$2.403\cdot10^6$	$6.48\cdot10^6$	$6.36\cdot10^6$	$3.957\cdot10^6$	$4.12\cdot10^6$	$2.523\cdot10^6$	$2.36\cdot10^6$

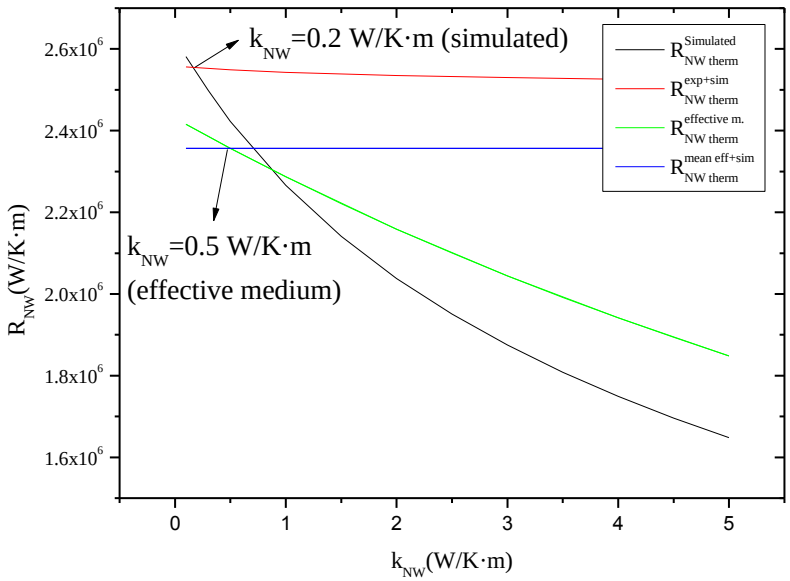

Figure 3.23. Simulation and effective medium results for 120 nm diameter NWs sample.

In Table 3.X the experimental and simulated results obtained for the thermal conductivity of the polymer nanowires with different diameters are summarized. If one compares the results obtained from the simulation with the ones expected by the effective medium theory, although there is a slight variation between them, they seem to nearly lie within the experimental errors and also follow the same tendency. On the one hand, despite the fact that a great care has been taken in the modelling, one must take into account that simulations correspond to a relatively idealistic situation. On the other hand, one must take into account that the effective medium theory is also an approximation. Under these considerations, one can conclude that the effective medium theory is working reasonably well in this case.

Table 3.X. Comparison between thermal conductivity values obtained with the effective medium theory and COMSOL Multiphysics® simulation.

NW diameter (nm)	k_{NW} (Effective medium theory) $(W \cdot K^{-1} \cdot m^{-1})$	k_{NW} (Simulation) $(W \cdot K^{-1} \cdot m^{-1})$
350	2.29±0.15	2.60
220	0.70±0.12	0.48
120	0.50±0.24	0.20

3.4. Thermal conductivity measurements of other nanostructures.

As it was widely explained in the Introduction Chapter, there is an interest in thermoelectric materials to reduce its thermal conductivity in order to enhance its figure of merit. This approach can be achieved by reducing the dimensions of the material, confining them in one or two directions, giving rise to nanowires and thin film structures. These kinds of structures were studied in Sections 3.2.1 and 3.2.2. However, in this section another nano-structure obtained through holography techniques is presented. The objective here is to study the effect of having a perfectly ordered thermoelectric structure on the phonon propagation. It is important mentioning that these results are very recent and although they look promising and seem to point out in this direction, it is still work in progress. A new set of better quality samples and more measurements are going to be performed in order to confirm the effects observed in the transport properties.

3.4.1. Holographic samples: Bi_2Te_3 nanostructure.

In this Section, the fabrication of a new type of highly ordered three dimensional (3D) structure made by holographic lithography techniques is used to study how the periodicity affects the phonon propagation, and thus the thermal conductivity, of the material grown inside. Previous Sections, 3.2.1.and 3.2.2., were focused on reducing the thermal conductivity by confining spatially a thermoelectric material in one or two directions, giving rise to nanowires and thin film structures [13, 74]. Additionally, it is also possible to fabricate nanostructured bulk materials in order to increase the phonon scattering in interfaces or defects [75].

In the Section 3.3.1.2., a reduction of the thermal conductivity of Bi_2Te_3 nanowires with their diameter were observed (Table 3.IV). These was caused by the different phonon scattering mechanisms that occure along the NW, like grain boundary scattering or surface scattering, which seemed to fit relatively well with a theoretical model (see Section 3.3.1.2.). However, while this structure is basically a well

ordered array of nanowires embedded in a two-dimensional alumina matrix, three dimensional well order interconnected structures might induce even a larger reduction in its thermal conductivity. It might be even possible to hypothesize a behavior similar to the light guidance with photonic structures, but in this case for heat transport, using "phononic structures" to guide heat. Considering this idea, this Section presents a novel approach to go a step further in controlling and reducing the thermal conductivity of the material based on the fabrication of a new type of highly ordered three dimensional (3D) photonic crystal structure made by holographic lithography techniques. Inside of this template, bismuth telluride has been grown by electrodeposition and a study of how the periodicity affects the phonon propagation and thus, the thermal conductivity, has been carried out. Moreover, these novel 3D structures show a well ordered interconnected network, which should have a great impact in the phonon scattering along the material. In addition, these structures present the advantage of giving rise to macro-sized self-standing structures, which makes their measurement and handling similar to the case of nanowires embedded in a matrix or films. It is worth mentioning that even though there are different fabrication techniques that can give rise to 3D structures, such as top-down approaches, they are usually very expensive and time consuming. Moreover, the mechanisms that provide self-organized structures at the nanoscale are not common. Directed block copolymers can be ordered in small volumes and with small thicknesses[76], and in the case of structures grown inside anodic alumina templates, a novel template with a 3D nanotubular network has been recently presented [77]. However, this structure lacks of perfect and long-range order. In order to improve these templates, the fabrication of a highly ordered 3D structure was developed by a holographic lithographic system to make the 3D matrix (based on those made for photonic crystals [78]) and then it was filled with bismuth telluride thermoelectric material by electrochemical means. The transport properties of this new nano-structure were studied and an effective decrease in the thermal conductivity, without affecting much other transport parameters, was observed in comparison to bulk, films or nanowires structures.

Sample fabrication

A glass substrate, 3 mm thick, coated with Fluorine doped Tin Oxide (FTO) on one side was chosen because of the good electrical conductivity of the FTO. Therefore, they can be used as working electrodes for the electrochemical deposition of Bi_2Te_3, and because of their transparency, to reduce reflections in the lithographic process. A drop of photoresist Shipley S1813, which is positive and broadband sensitive (from 350nm to 450nm) was dropped on top of the FTO-coated side of the substrates. Then it was spun for 60 seconds at 5000 rpm. Afterwards, a soft-bake on a hot plate at 115ºC was carried out during one min. The thickness obtained for this photoresist after this process was 2.5 µm.

Then, the template matrix was fabricated via holographic lithography. For that purpose, we required of the interference of four laser beams in a photo sensible resist, where the intensity pattern is recorded. Generally, in order to achieve this light interferogram, the most used optical set-up for this holographic lithography is the so-called "umbrella-like" configuration, which needs high stability, but that can also give rise to a wide variety of 3D structures [79]. A simplified version of this set up was reported by Wu *et al* [80], where the interference pattern was obtained from a single laser beam that was refracted in a truncated fused silica prism (Del Mar Photonics, Inc.). Following this procedure, a designed prism like the one presented in this work was fabricated in order to obtain the four refracted beams, generated at each of the prisms faces, interact in the area just below where the photoresist is (see Figure 3.24a). The light source used was a 12 mW power violet single mode laser diode (405 nm in wavelength). The laser was collimated with a coherence length larger than one meter. Firstly, the beam was expanded using a convergent lens with focal of 4 mm and numeric aperture of 0.60. A spacer filter made with a pinhole of 5 microns at the focal of the lens was used to clean high spatial frequencies. The laser was kept at 20º C using a temperature controlled mount, to keep power and wavelength stable. The typical exposure times ranged from 45 seconds to 70 seconds, with incident power at the

truncated face of the prism from 0.65 mW to 0.75 mW. The best conditions for the template fabrication were found to be an exposure of 0.75 mW for 65 s. After the exposure, the photoresist was developed using MF-319 during 60 s and then cleaned in deionized water.

Figure 3.24b shows a simulation with COMSOL Multyphysics® of the light intensity pattern obtained from the four beams interference. The angles of the prism are maintained, but it was scaled to the dimensions of the light wavelength in order to perform a simulation of the interference clearly. The maxima and minima in intensity, Figure 3.24b, are exposed in the resist and after an appropriate development, a template of interconnected channels is generated, as it can be schematically seen in Figure 3.24c.

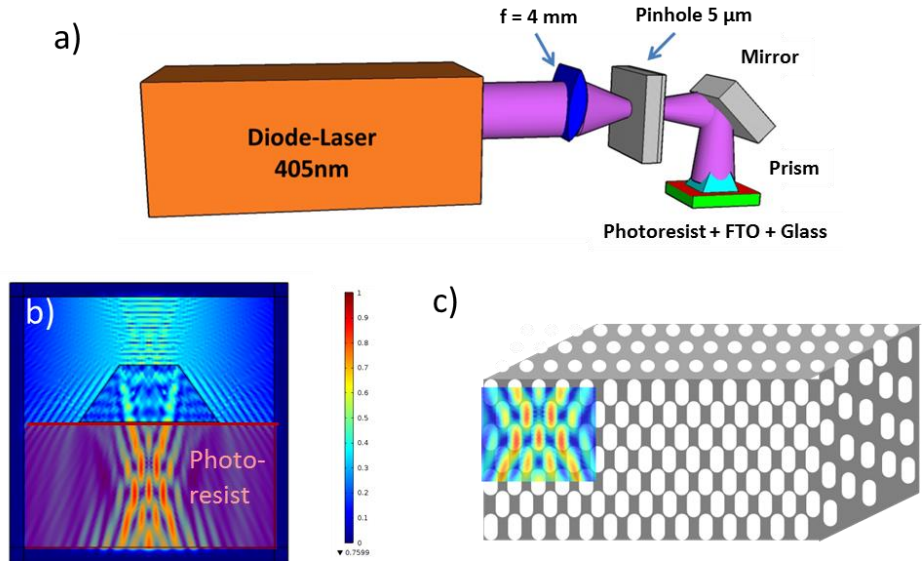

Figure 3.24. a) Experimental setup of the holographic lithography used in this work. b) Two dimensional COMSOL® simulation of the interference pattern generated by a laser beam when it is refracted by the prism (note that the prism is in 1:2000 scale). The photoresist is underneath the base of the prism. c) Schematic view of the 3D interconnected structure created in the resist. The 2D interference pattern extends over an area and also in the volume of the photoresist.

Figure 3.25a shows the central area of the interferogram that corresponds to the interference of the four beams, and therefore, where the three dimensional photonic crystal structure is generated. In this area, the obtained structure can be considered as an interconnected net, with size diameters of around 450 nm. This 3D structure is the one of interest to study. Figure 3.25b shows the areas at which the interference is due to three or two beams, which result in 2D periodic structures.

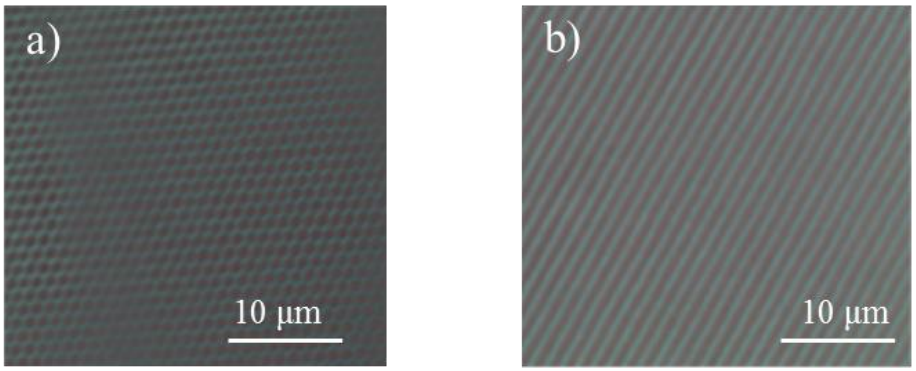

Figure 3.25. a) Optical microscope image of the central part of the template, which corresponds to four-beam interference, before the electrodeposition of Bi_2Te_3, showing the top view of a perfect photonic crystal b) Optical microscope image of the region corresponding to two beam interference, where a highly ordered 2D trenched structure can be seen.

Once the 3D holographic structure was fabricated, Bi_2Te_3 was deposited inside by template assisted pulsed electrodeposition in a conventional three-electrode cell, as explained in Chapter 2, with the 3D structure fabricated on FTO surface as working electrode. The solution used was the one described in [81]. Once the 3D structure was filled with Bi_2Te_3 its morphology was studied with SEM, its crystal orientation with X-Ray Diffraction and its composition with an EDX microscope (see Chapter 2). Also films on the same substrate, but without the photonic crystal matrix on top were grown for comparison.

The electrodeposition was optimized to achieve the best conditions to obtain the maximum filling of the template with

stoichiometric Bi_2Te_3. This process was performed by the fabrication team of the group. Figure 3.26 shows Scanning Electron Micrograph of the central part of the interferogram, that is, the 3D structure. Here, the upper part of the filled interferogram, which consists of interconnected wires (see Figure 3.24c) can be seen. The mean diameter of these wires was around 450 nm. The composition was measured by EDX and aroused a stoichiometry of $Bi_{2.1\pm0.1}Te_{2.9\pm0.2}$.

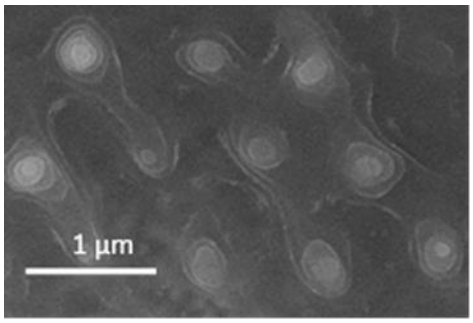

Figure 3.26. Scanning Electron Microscope (SEM) images of the central part of the pattern after the growth of Bi_2Te_3. The nanowires tips can be seen in the image have been measured showing 450 nm of diameter.

The crystallographic orientation of the 3D Bi_2Te_3 structure was measured by preserving only the area where the 3D structure is (that is, the central area where the four laser beams interfere in the holographic lithography process), while removing the rest, and then performing XRD measurement on it. Figure 3.27 shows the diffraction peaks obtained for pure resist and a Bi_2Te_3 structure. Apart from the diffraction peaks of the resist, two peaks from Bi_2Te_3 can be clearly seen, i.e. one corresponding to [0 1 5] (27.7º) and another one to [0 1 1] (41.1º). Thus, the sample can be then considered as polycrystalline, slightly oriented along [1 1 0].

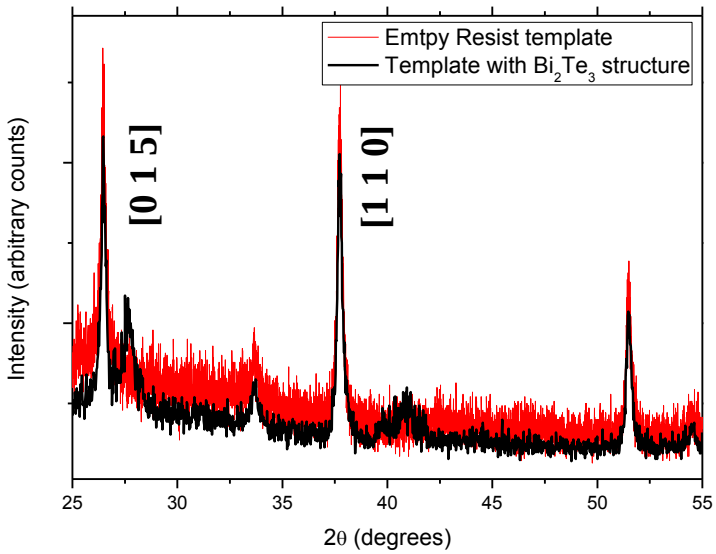

Figure 3.27. XRD spectra for the whole resist (red) and for the 3D structure Bi_2Te_3 structure of the central region (black).

Measurement of the transport properties

The thermal conductivity of the holographic sample was measured using the SThM working in DC heating mode, with the Wollaston probe 1 described in Section 3.1.1. With the AFM station, we position the probe at different locations of the center of Bi_2Te_3 structure where the four beam interferogram occurred.

Similarly as for films, the thermal resistance of the sample was determined at different locations. From the result, the thermal conductivity of the composite (Bi_2Te_3 plus photoresist) was obtained using the Equation 2.21, i.e. $R_{sample}^{th} = \frac{1}{4 \cdot k_{sample} \cdot b}$. Finally, once the value of the thermal conductivity of the composite was determined, in order to calculate the thermal conductivity of the Bi_2Te_3 nanostructures, the effective medium theory was used [28, 58]. Mathematically it is expressed as, $k_{comp} = k_{photoresis} \cdot x_{photoresist} + k_{Bi2Te3} \cdot x_{Bi2Te3}$, where k is the thermal conductivity and x is the percentage of each material.

These percentages were calculated from the SEM pictures and they were determined to be 20 ± 5% for the Bi_2Te_3 nanostructure and 80 ± 5% for the photoresist. The thermal conductivity of pure and clean photoresist (S1813) layer with 2.5 µm thickness was also measured with this technique and gave a thermal conductivity of 0.19 ± 0.01 $W \cdot K^{-1} \cdot m^{-1}$. Finally, the thermal conductivity of the Bi_2Te_3 structure was determined to be 0.30 ± 0.13 $W \cdot K^{-1} \cdot m^{-1}$.

This thermal conductivity results can be compared to those found for electrodeposited Bi_2Te_3 films and for 300 nm diameter Bi_2Te_3 nanowires measured (see Section 3.3.1.) with the 3ω-technique, that were 1.6 ± 0.2 $W \cdot K^{-1} \cdot m^{-1}$ and 1.37 ± 0.20 $W \cdot K^{-1} \cdot m^{-1}$, respectively [28]. From this comparison and despite the fact that this particular Bi_2Te_3 holographic structure is not that well oriented as the NW of Section 3.3.1., one can see that a drastic reduction in the thermal conductivity in this 3D structure seems to occur. There are theoretical works that predict a dramatic reduction of thermal conductivity in highly ordered 3D structures by means of the fabrication of phonon crystals, which could block the propagation of certain phonons and even make phonon guidance [82]. This reduction is observed even though the mean free path for phonons in Bi_2Te_3, which is around 3 nm [82], is smaller than the period of these structures. So, in principle having a periodic structure seems to affect the phonon propagation even at higher sizes than the one proposed for a phononic crystal[83]. Another simpler explanation for this reduction can be due to the fact that we have an interconnected 3D structure, with many joint points that produce more phonon scattering centers than a conventional Bi_2Te_3 film or NW. Moreover, in this 3D structure one obtains also a higher surface to volume ratio than for films, which also enhances the surface scattering of phonons. Although the result of thermal conductivity for the Bi_2Te_3 holographic structure is encouraging, we consider it as a preliminar result. In the near future, we expect to grow and measure the thermal conductivity of holographic structures highly oriented in the [1 1 0] and with perfect stoichiometry, whose thermal conductivity results can be better compared to the Bi_2Te_3 nanowires presented in Table 3.IV.

Additionally, the electrical conductivity and the Seebeck coefficient out of plane were also determined to calculate the figure of merit of this material. On the one hand, the electrical conductivity measurements were carried out in a commercial four-probe station (Keithley) with probes of 1 μm in radius. Due to the characteristics of the sample, the one dimensional model can be used to have an estimation of the electrical conductivity from the data obtained when two tips were positioned on top of the sample and the other two in the FTO substrate. On the other hand, the Seebeck coefficient was measured by a Seebeck Microprobe System (PANCO GmbH) [84], that was explained in Chapter 2.

The electrical conductivity was estimated from *I-V* curves taken at different locations of the central part of the interferogram with a four-probe station. The contribution of the photoresist can be considered as negligible, given that it is an isolating material. The current applied between the top and bottom probes ranged between $-8\cdot10^{-4}$ A to $+8\cdot10^{-4}$ A, while the other two probes were in charge of measuring the voltage across the Bi_2Te_3 3D structure. The electrical resistivity obtained for the Bi_2Te_3 nano-structure was determined to be $\rho = (1.8 \pm 0.5)\cdot10^{-5}$ Ω·m, which is around two times the electrical resistivity of bulk Bi_2Te_3 .[35] Nevertheless, one must take into account that the Bi_2Te_3 3D structure is not perfectly oriented, as shown in the XRD spectra (Figure 3.27), then the conductivity can be affected[34] .

Figure 3.28 shows the results obtained and a map of the Seebeck coefficient on a 50 μm x 50 μm area of the surface of the 3D structure. At the central area of the interferogram a Seebeck coefficient of -26 ± 4 μV/K was determined. The Seebeck coefficient of the photoresist was also measured and gave a value of around 1 μV/K, which is negligible in comparison to Bi_2Te_3. This value can be compared with the averaged Seebeck coefficient, -40 ± 5 μV/K obtained with the same technique for an electrochemically grown Bi_2Te_3 film of 3 μm thickness that it is not perfectly oriented. As it was mentioned previously, in the near future there is a plan to grow a new set of holographic structures with excellent composition, orientation in the [1 1 0] directtion and robustness , whose *S* and σ are expected to improve considerably.

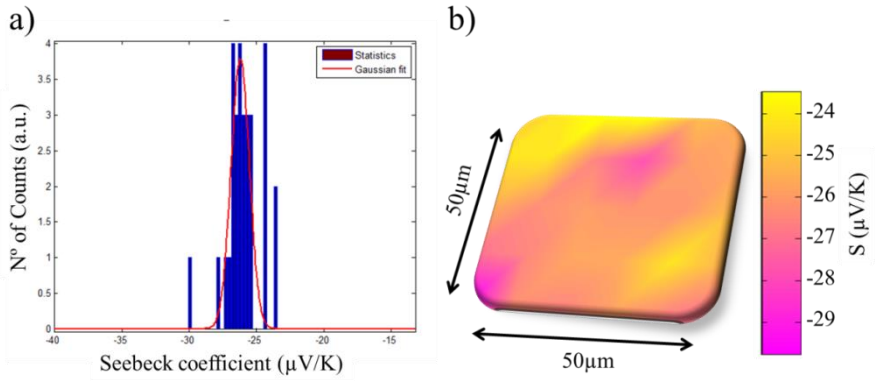

Figure 3.28. Seebeck coefficient map of the central part of the Bi_2Te_3 structure.

These values, compared to the ones found in bismuth telluride films and nanowires grown by electrochemistry, are not surprising because the 3D structure is not expected to vary much these parameters as a consequence of the size of the structure. In the case of carrier confinement effects on the thermoelectric properties, it has been shown that for bismuth telluride nanowires the effect appears for diameters lower than 30 nm [85], which is again much smaller than our 3D structure dimensions.

Once the transport properties were measured, the figure of merit of the holographic structure was calculated using the equation, $ZT = \frac{\sigma \cdot S^2}{k} T$, where σ, S and k are the electrical conductivity, Seebeck coefficient and thermal conductivity, respectively, and T is the absolute temperature. Unfortunately, the figure of merit obtained for this 3D structure is 0.04, which is quite low compared with bulk Bi_2Te_3, which is around 1. The main difference resides in the low Seebeck coefficient and electrical conductivity obtained in these non-optimized electrochemically grown Bi_2Te_3 in comparison to those of bulk. However, electrochemistry is the best way to replicate the structure formed with the photoresist, and although the intrinsic value of the Seebeck coefficient is low, there is nowadays much research to obtain improved values comparable to those of bulk (-240 μV/K [34]) [81]. Any improvement in the quality of electrodeposited Bi_2Te_3 could be applied to the holographic structure in order to improve its power factor while keeping a low thermal conductivity. Further prospects are based on the

optimization of electrodeposition of the Bi_2Te_3 inside the 3D-holographic structure, which would lead to a higher crystalline orientation and better stoichiometry of these nano-structures, having a positive impact in its Seebeck coefficient and electrical conductivity.

In summary, this initial results seem to point out in the direction that perfect order in the Bi_2Te_3 reduces the thermal conductivity. To confirm it, a new set of samples is being fabricated to perform more measurements. The holographic lithography has been used to fabricate 3D templates of interconnected channels in which Bi_2Te_3 has been grown via electrochemical deposition. The thermal conductivity measured for this structure, $k = 0.30 \pm 0.13\ \mathrm{W \cdot K^{-1} \cdot m^{-1}}$, shows a reduction of around 85% with respect to a single crystalline bulk Bi_2Te_3, $k \sim 2.2\ \mathrm{W \cdot K^{-1} \cdot m^{-1}}$ [34]. Such reduction is initially interpreted as an effect of the ordering of microstructures at microscopic scale. Although more studies need to be done in order to confirm it. As a consequence, these results involve further improvements in thermoelectricity as it is expected to enhance the figure of merit. Moreover, this method can be used not only for creating 3D structures of Bi_2Te_3, but also other thermoelectric materials can be grown inside this template via electrodeposition, expanding the possibilities of these holographic structures.

Regarding the thermoelectric efficiency of the structure, although it seems to be low, its electrical conductivity and Seebeck coefficient is very similar to other not perfectly Bi_2Te_3 electrodeposited structures, such as thin films or nanowires. Other techniques, such as sputtering, result in better power factors, but cannot be used to fill the holographic 3D templates. As a future work, the optimization of the electrodeposition of Bi_2Te_3 inside of these templates will result in better orientation and stoichiometries, involving higher figures of merit. As far as the templates themselves are concerned, further improvements could be performed using a smaller wavelength laser in order to reduce the size of the channels, which could reduce even more the thermal conductivity of these holographic structures. Moreover, these structures might be the basis for the fabrication of future phononic dispersion crystals, when reducing the size, with strongly reduced thermal conductivity for high efficient thermoelectric devices.

3.5. Conclusions.

In summary, this Chapter covers thermal measurements of organic and inorganic films and nanowires carried out by Scanning Thermal Microscopy working in DC and AC heating modes. In each Section, it was first explained carefully how the thermal resistance of the sample was measured and how its thermal conductivity was obtained. In order to determine accurately or prove the validity of some of the thermal measurements carried out experimentally. The use of COMSOL Multiphysics® simulations was required for both films and nanowires. Afterwards, a deep analysis of the thermal conductivity obtained was performed to elucidate the factors that influence the scattering of phonons in each case.

Regarding SiGe films, it was observed a clear reduction in the thermal conductivity of the films in comparison to similar ones grown by other techniques. This was correlated to an increment of phonon scattering at the boundaries caused by the clusters formation during the metal induced crystallization proccess. It was possible to understand this process through the information obtained from Raman spectra.

Regarding polymeric non-oriented preferentially PCDTBT films, the mechanisms that affect the thermal transport are different depending on if the film is undoped or doped. For an undoped PCDTBT film, the thermal conductivity is mainly dominated by the phonon conductivity of the lattice. However, when these films were doped with $FeCl_3$, the electronic term of the total thermal conductivity becomes relevant, resulting in higher values of the thermal conductivity compared to those obtain for the undoped film. Therefore, the electrons play an important role in the heat transport of doped PCDTBT. Moreover, as the doping with Fe ions increase, the lattice term of the thermal conductivity can be also become influenced. Despite the fact that the electrical conductivity of the doped PCDTBT films, the thermal conductivity remains similar, as the combination of lattice and electronic terms result in a similar total thermal conductivity. In terms of the thermoelectric performance of these films, larger power factors

can be achieved with the doping while keeping a relatively low total thermal conductivity of the polymer.

The nanowires are considered one-dimensional structures and because of this confimenent the mechanisms for phonon scattering are expected to increase, involving a large reduction of the thermal conductivity in these structures in comparison to two-dimensional ones or bulk material. These effects were analyzed in inorganic nanowires (Bi_2Te_3) and organic nanowires (P3HT).

On the one hand, the thermal conductivity of Bi_2Te_3 NWs was observed to reduce as its diameter becomes smaller. In order to explain this effect, a theoretical analysis made with the Kinetic-Collective model, that include the different mechanisms for phonon scattering (Umklapp, surface scattering, grain boundary scattering, etc.) that happen in Bi_2Te_3 NWs, is used. These results showed a good agreement between them. The fact that the thermal conductivity of the nanowire reduces with its diameter contributes positively to improve the efficiency of Bi_2Te_3 thermoelectric nanowires.

On the other hand, the heat transport in organic P3HT NWs is quite different to those observed in inorganic nanowires. It was observed that the crystalline orientation plays a major role in this structures. While for large diameter nanowires the thermal conductivity becomes high, because of the π-π stacking is perpendicular to the length of the nanowires, as the diameter of the NW is reduced, as consequence of stronger confinement of the polymer NWs the π-π stacking begins to disorder and the thermal conductivity is reduced. The conclusions of this work explain the wide variety of thermal conductivity results obtained for polymers and set the foundations for polymeric thermal transport engenieering by controlling the polymer orientation.

Finally, although arrays of nanowires embedded in 2D-alumina matrices have resulted to present low values of thermal conductivity, it is expected that complex ordered 3D-structures could involve lower thermal conductivity values. To this end, holographic structures, consisted of a network of interconnected channels were fabricated.

Although the results obtained are very recent and a new set of samples must be measured, a reduction of thermal conductivity for this structure of around 85 % was observed in comparison to bulk structure. This drastic reduction could be explained from an increment of phonon scattering caused by the 3D photonic crystal consisted in interconnected nano-channels that were formed by the holographic pattern. This nano-structure opens the door for high efficient thermoelectric devices and is a step forward in this field.

All these results show the potential of SThM to measure thermal properties of nanostructures made of different organic and inorganic thermoelectric materials. Nevertheless, more importantly is the fact that the obtained thermal conductivity results and a deeper analysis of them made possible to understand how the heat transport at the nanoscale becomes affected by different phonon scattering mechanisms, the influence of lattice and electrical terms to the total thermal conductivity, the impact of the crystal orientation or the confinement, among others.

References

1. S. Volz, *Applied Physics Letters*, 1999, **75**, 2056-2058.
2. Z. Wang and N. Mingo, *Applied Physics Letters*, 2010, **97**, 101903.
3. X. Chen, Y. Wang, Y. Ma, T. Cui and G. Zou, *The Journal of Physical Chemistry C*, 2009, **113**, 14001-14005.
4. A. J. H. McGaughey and McGaughey, *Applied Physics Letters*, 2011, **99**, 131904-131904-131903.
5. T. Borca Tasciuc, *Annual Review of Heat Transfer*, 2013, **16**, 211-258.
6. L. Shi, *Journal of Microelectromechanical Systems*, 2001, **10**, 370-378.
7. M. Hinz, *Applied Physics Letters*, 2008, **92**, 043122-043122-043123.
8. C. D. S. Brites, P. Lima, N. J. O. Silva, A. Millan, V. Amaral, F. Palacio, A. MillÃ¡n and L. Carlos, *Nanoscale*, 2012, **4**, 4799-4829.
9. Y. Zhang, *Applied Physics Letters*, 2010, **96**, 062107-062107-062103.
10. S. Lefèvre, S. Volz and P.-O. Chapuis, *International Journal of Heat and Mass Transfer*, 2006, **49**, 251-258.
11. M. M.-R. A. Wislon, B. Abad, J. A. Perez, J. Schomacker, M. Martín Gonzalez, D. Andra Borca-Tasciuc and T. Borca-Tasciuc, *Nanoscale*, 2015, **Under revision**.
12. E. Puyoo, S. Grauby, J.-M. Rampnoux, E. Rouviere and S. Dilhaire, *Review of Scientific Instruments*, 2010, **81**, 073701-073705.
13. D. M. Rowe, *CRC Thermoelectrics Handbook: Macro to Nano.*, CRC Press, Broken Sound Parkway NW, 2005.
14. Y. Shiraki and N. Usami, *Silicon-Germanium (SiGe) Nanostructures: Production, Properties and Applications in Electronics*, Elsevier Science, 2011.
15. T. Borca-Tasciuc, W. Liu, J. Liu, T. Zeng, D. W. Song, C. D. Moore, G. Chen, K. L. Wang, M. S. Goorsky, T. Radetic, R. Gronsky, T. Koga and M. S. Dresselhaus, *Superlattices and Microstructures*, 2000, **28**, 199-206.
16. W. Shin, M. Ishikawa, M. Nishibori, N. Izu, T. Itoh and I. Matsubara, *Materials Transactions*, 2009, **50**, 1596-1602.
17. C. Prakash, *Microelectronics Reliability*, 1978, **18**, 333.

18. J.A. Perez, J.J. Romero, B. Abad, M. Muñoz-Rojo, A. Mello, F. Briones, M. Martín-Gonzalez, *Scientific Reports (Submitted)*, 2015.
19. O. W. Käding, H. Skurk and K. E. Goodson, *Applied Physics Letters*, 1994, **65**, 1629-1631.
20. M. Muñoz-Rojo, J. Maiz, B. Abad, A. Wilson, A. Nogales, D. A. Borca-Tasciuc, T. Borca-Tasciuc, M. Martín-Gonzalez, *To be Submitted*, 2015.
21. C. L. Choy, *Polymer*, 1977, **18**, 984-1004.
22. O. Bubnova and X. Crispin, *Energy and Environmental Science*, 2012, **5**, 9345-9362.
23. M. Morana, P. Koers, C. Waldauf, M. Koppe, D. Muehlbacher, P. Denk, M. Scharber, D. Waller and C. Brabec, *Advanced Functional Materials*, 2007, **17**, 3274-3283.
24. A. Babel, Y. Zhu, K. F. Cheng, W. C. Chen and S. A. Jenekhe, *Advanced Functional Materials*, 2007, **17**, 2542-2549.
25. P. Magri, C. Boulanger and J. M. Lecuire, *Journal of Materials Chemistry*, 1996, **6**, 773-779.
26. M. S. Martin Gonzalez, A. L. Prieto, R. Gronsky, T. Sands and A. M. Stacy, *Journal of the Electrochemical Society*, 2002, **149**, C546-C554.
27. A. L. Prieto, M. Martin Gonzalez, R. Gronsky, T. Sands, M. S. Sander, M. S. Martin Gonzalez and A. M. Stacy, *Journal of the American Chemical Society*, 2001, **123**, 7160-7161.
28. M. Muñoz-Rojo, S. Grauby, J. M. Rampnoux, O. Caballero-Calero, M. Martin-Gonzalez and S. Dilhaire, *Journal of Applied Physics*, 2013, **113**, 054307-054308.
29. E. Puyoo, S. Grauby, J.-M. Rampnoux, E. Rouviere and S. Dilhaire, *Journal of Applied Physics*, 2011, **109**, 024302-024309.
30. D. A. Borca-Tasciuc and T. Borca, *Journal of Applied Physics*, 2005, **97**, 084303-084309.
31. D. A. Borca-Tasciuc, G. Chen, A. Prieto, M. S. Martin-Gonzalez, A. Stacy, T. Sands, M. A. Ryan and J. P. Fleurial, *Applied Physics Letters*, 2004, **85**, 6001-6003.
32. K. G. Biswas, T. D. Sands, B. A. Cola and X. Xu, *Applied Physics Letters*, 2009, **94**, 223116-223113.
33. A. I. Persson, Y. K. Koh, D. G. Cahill, L. Samuelson and H. Linke, *Nano Letters*, 2009, **9**, 4484-4488.
34. A. Jacquot, N. Farag, M. Jaegle, M. Bobeth, J. Schmidt, D. Ebling and H. Böttner, *Journal of Electronic Materials*, 2010, **39**, 1861-1868.

35. F. Xiao, C. Hangarter, B. Yoo, Y. Rheem, K.-H. Lee and N. V. Myung, *Electrochimica Acta*, 2008, **53**, 8103-8117.
36. J. P. Fleurial, L. Gailliard, R. Triboulet, H. Scherrer and S. Scherrer, *Journal of Physics and Chemistry of Solids*, 1988, **49**, 1237-1247.
37. C.-L. Chen, Y.-Y. Chen, S.-J. Lin, J. C. Ho, P.-C. Lee, C.-D. Chen and S. R. Harutyunyan, *The Journal of Physical Chemistry C*, 2010, **114**, 3385-3389.
38. A. Mavrokefalos, A. L. Moore, M. T. Pettes, L. Shi, W. Wang and X. Li, *Journal of Applied Physics*, 2009, **105**, 104318.
39. D. Li, *Applied Physics Letters*, 2003, **83**, 2934-2936.
40. A. I. Hochbaum, *Nature*, 2008, **451**, 163, 7175.
41. E. J. Menke, M. A. Brown, Q. Li, J. C. Hemminger and R. M. Penner, *Langmuir*, 2006, **22**, 10564-10574.
42. B. Qiu, L. Sun and X. Ruan, *Physical Review B*, 2011, **83**, 035312.
43. D. Li, Y. Wu, P. Kim, L. Shi, P. Yang and A. Majumdar, *Applied Physics Letters*, 2003, **83**, 2934-2936.
44. A. L. Moore, M. T. Pettes, F. Zhou and L. Shi, *Journal of Applied Physics*, 2009, **106**, 034310-034317.
45. C. de Tomas, A. Cantarero, A. F. Lopeandia and F. X. Alvarez, *Journal of Applied Physics*, 2014, **115**, 164314.
46. C. de Tomás Andrés, A. Cantarero Sáez and F. X. Àlvarez Calafell, *Doctoral Thesis On Thermal Transport by Phonons in Bulk and Nanostructured Semiconductor Materials*, 2015.
47. M. Jaegle, *COMSOL Conference 2008 Hannover*, 2008.
48. J. Martín, M. Krutyeva, M. Monkenbusch, A. Arbe, J. Allgaier, A. Radulescu, P. Falus, J. Maiz, C. Mijangos, J. Colmenero and D. Richter, *Physical Review Letters*, 2010, **104**, 197801.
49. S. Shen, A. Henry, J. Tong, R. Zheng and G. Chen, *Nature Nanotechnology*, 2010, **5**, 251-255.
50. B.-Y. Cao, Y.-W. Li, J. Kong, H. Chen, Y. Xu, K.-L. Yung and A. Cai, *Polymer*, 2011, **52**, 1711-1715.
51. J. Martin, M. Campoy-Quiles, A. Nogales, M. Garriga, M. I. Alonso, A. R. Goni and M. S. Martin-Gonzalez, *Soft Matter*, 2014.
52. C. Bounioux, P. Diaz-Chao, M. Campoy-Quiles, M. S. Martin-Gonzalez, A. R. Goni, R. Yerushalmi-Rozen and C. Muller, *Energy & Environmental Science*, 2013, **6**, 918-925.
53. X. Feng, G. Liu, S. Xu, H. Lin and X. Wang, *Polymer*, 2013, **54**, 1887-1895.

54. J. C. Duda, P. E. Hopkins, Y. Shen and M. C. Gupta, *Applied Physics Letters*, 2013, **102**, 251912.
55. J. Martín and M. Martín González, *Nanoscale*, 2012, **4**, 5608.
56. J. Martín, C. V. Manzano and M. Martín-González, *Microporous and Mesoporous Materials*, 2012, **151**, 311-316.
57. J. Martín, A. Nogales and M. Martín-González, *Macromolecules*, 2013, **46**, 1477-1483.
58. M. Muñoz-Rojo, J. Martin, S. Grauby, T. Borca-Tasciuc, S. Dilhaire and M. Martin-Gonzalez, *Nanoscale*, 2014, **6**, 7858-7865.
59. R. Prasher, *Nano Letters*, 2005, **5**, 2155-2159.
60. Y. Zhang, C. Hapenciuc, E. Castillo, T. Borca Tasciuc, R. Mehta, C. Karthik and G. Ramanath, *Applied Physics Letters*, 2010, **96**, 062107.
61. X. Feng and X. Wang, *Thin Solid Films*, 2011, **519**, 5700-5705.
62. H. W. Ro, B. Akgun, B. T. O'Connor, M. Hammond, R. J. Kline, C. R. Snyder, S. K. Satija, A. L. Ayzner, M. F. Toney, C. L. Soles and D. M. DeLongchamp, *Macromolecules*, 2012, **45**, 6587-6599.
63. Z. Wu, A. Petzold, T. Henze, T. Thurn-Albrecht, R. H. Lohwasser, M. Sommer and M. Thelakkat, *Macromolecules*, 2010, **43**, 4646-4653.
64. L. Piraux, M. Kinany-Alaoui, J. P. Issi, D. Begin and D. Billaud, *Solid State Communications*, 1989, **70**, 427-429.
65. H. G. Kilian and M. Pietralla, *Polymer*, 1978, **19**, 664-672.
66. J. Maiz, J. Martin and C. Mijangos, *Langmuir*, 2012, **28**, 12296-12303.
67. J. Martín, Aurora Nogales and Carmen Mijangos, *Macromolecules*, 2013, **46**, 7415-7422.
68. J. A. Lim, F. Liu, S. Ferdous, M. Muthukumar and A. L. Briseno, *Materials Today*, 2010, **13**, 14-24.
69. T. J. Prosa, M. J. Winokur, J. Moulton, P. Smith and A. J. Heeger, *Macromolecules*, 1992, **25**, 4364-4372.
70. P. W. Bridgman, *Proc. Am. Acad. Arts Sci.*, 1925, **60**, 306.
71. J. Martín, J. Maiz, J. Sacristan and C. Mijangos, *Polymer*, 2012, **53**, 1149-1166.
72. M. Steinhart, *Advances in Polymer Science*, 2008, **220**, 123-187.
73. M. Brinkmann, *Journal of Polymer Science Part B: Polymer Physics*, 2011, **49**, 1218-1233.

74. M. S. Dresselhaus, G. Chen, M. Y. Tang, R. G. Yang, H. Lee, D. Z. Wang, Z. F. Ren, J. P. Fleurial and P. Gogna, *Advanced Materials*, 2007, **19**, 1043-1053.
75. M. M.-González, O. C.-Calero and P. D.-Chao, *Renewable and Sustainable Energy Reviews*, 2013, **24**, 288-305.
76. D. J. C. Herr, *Journal of Materials Research*, 2011, **26**, 122-139.
77. J. Martín, O. Caballero-Calero, J. F. Fernández and M. M. Gonzalez, *Nature Communications*, 2014, **5,** 5130.
78. M. Campbell, D. N. Sharp, M. T. Harrison, R. G. Denning and A. J. Turberfield, *Nature*, 2000, **404**, 53-56.
79. Y. V. Miklyaev, D. C. Meisel, A. Blanco, G. von Freymann, K. Busch, W. Koch, C. Enkrich, M. Deubel and M. Wegener, *Applied Physics Letters*, 2003, **82**, 1284-1286.
80. L. Wu, Y. Zhong, C. T. Chan, K. S. Wong and G. P. Wang, *Applied Physics Letters*, 2005, **86**, 241102.
81. O. Caballero-Calero, P. Díaz-Chao, B. Abad, C. V. Manzano, M. D. Ynsa, J. J. Romero, M. M. Rojo and M. S. Martín-González, *Electrochimica Acta*, 2014, **123**, 117-126.
82. M. Maldovan, *Physical Review Letters*, 2013, **110**, 025902.
83. M. Maldovan, *Nature*, 2013, **503**, 209-217.
84. G. K. D. Platzek, C. Drasar, E. Müller, *Materials Science Forum*, 2005, **492-493**, 587-592.
85. I. Bejenari and V. Kantser, *Physical Review B*, 2008, **78**, 115322.

Chapter 4

Electrical Transport Measurements of Nanostructures

The electrical properties of nanostructures, like films or nanowires, are a major concern in a wide range of applications, like solar cells[1], electrical circuits[2] or thermoelectric devices,[3] among others. Regarding thermoelectric materials[3], accurate measurements of the electrical conductivity of the sample are required in order to determine the thermoelectric figure of merit of the material.

This chapter begins with an electrical based technique called Harman, which is able to determine the efficiency of a thermoelectric material with a single measurement. The conditions and limitations of using this technique to achieve proper measurements of films and nanowires are studied. Secondly, the measurement of the electrical conductivity of films and nanowires will be obteined by different approaches, and its results will be discussed from a physical point of view.

4.1. Harman Transient Technique to determine directly the Figure of Merit of thermoelectric nanostructures.

As it was explained in the Introduction Chapter, the efficiency of a thermoelectric material is related to the figure of merit: $zT = \left(\frac{S^2 \cdot \sigma}{k}\right) \cdot T$, where S, σ, and k are the Seebeck coefficient, the electrical conductivity and the thermal conductivity, respectively. Numerous studies carried out in the past two decades have shown the performance of thermoelectric materials is enhanced in nanostructures such as thin films, nanowires and quantum dots due to size and quantum effects [4, 5]. Nowadays, first thin film devices are emerging on the market[6, 7]. In order to improve the efficiency of these devices, films with a larger figure of merits are being fabricated, whose zT must be measured experimentally.

One of the bottlenecks when searching for high efficiency, low dimensional materials is the complexity to quickly assess their figure of merit. There are two different ways to determine materials' performance experimentally. The most popular consists of measuring each of the three components of zT independently, using different measurement techniques. However, this approach is time consuming and needs overcoming three different sets of challenges. In contrast, the direct measurement of zT using the Harman method requires only one experimental set-up. Hence, this method could provide a quick way to scan for best nanostructured thermoelectric materials and could be a powerful tool for material scientists. Nevertheless, its application in practice has only been shown with high accuracy in bulk material, while for the thin film case, similar results have been reported in literature but the zT measured values have not been reproduced yet.

In the original Harman method [8], DC current is applied through a thermoelectric sample subjected to one-dimensional electrical and heat conduction along its length and insulated adiabatically. The applied current generates a temperature gradient due to opposite Peltier effects (heating vs. cooling) at the junctions between the thermoelectric sample and the two electrodes at the sample's ends. While Joule

heating may occur within the sample, it does not create a temperature difference between the electrodes because of the symmetric boundary conditions to heat transfer. At steady-state, the current is turned off, which results in an instantaneous drop in voltage because the ohmic component of the voltage across the sample, V_e, vanishes. However, due to the slower characteristic response of heat transport compared to the electrical transport, a temperature difference still remains across the sample, generating a Seebeck voltage, with initial value V_S. The figure of merit is then calculated from [8, 9]:

$$zT = \frac{V_S}{V_e} \quad . \tag{4.1}$$

While this method looks simple, the measurement is non-trivial for small zT samples or for nanostructures such as thin films or nanowires because they produce either small V_s or very fast decaying Seebeck signals. This technique was modified from a transient signal to electrical resistance measurements under alternating (AC) currents in order to increase the accuracy of Seebeck voltage measurement [10]. In the modified method, two different regimes are distinguished: a low frequency (LF or DC) regime, where the applied current generates a frequency independent steady temperature because of Peltier effect, (Figure 4.1a), and a high frequency (HF) regime (Figure 4.1b), where the applied voltage varies so fast that an insignificant AC temperature gradient is established. The voltage developed in the LF regime, V_{LF}, is composed of both the Seebeck and the ohmic voltage components. The voltage measured in the HF regime, V_{HF}, contains only the ohmic voltage. Therefore, the difference between V_{LF} and V_{HF} equals the thermoelectric voltage, $V_{LF} - V_{HF} = V_s$. Consequently, when the same current is used to perform AC and DC measurements, the figure-of-merit can be calculated as [10],

$$zT = \frac{V_{LF}}{V_{HF}} - 1 \tag{4.2}$$

Regardless of the method used, the key to a successful measurement consists of determining accurately the generated Seebeck voltage. When measuring bulk, adiabatically insulated samples having low resistance electrical contacts, the Seebeck voltage of samples with

zT~1 is of magnitude similar to the ohmic voltage and has a relatively low rate of decay which can be easily captured with an oscilloscope. However, when the same methods are employed to nanostructures, a small, fast decaying Seebeck voltage is commonly generated, which require voltage measurement equipment with high sensitivity and high frequency response.

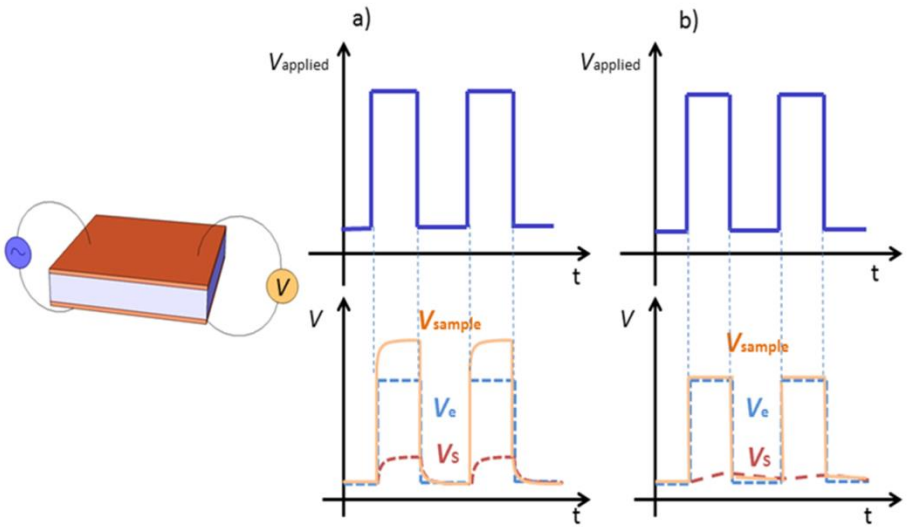

Figure 4.1. Schematic view of the signals measured by the Harman method at high and low frequencies. The left side illustrates the measurement setup: a freestanding thermoelectric thin film connected to a voltage source and a voltmeter. a) In the low frequency regime, a Seebeck voltage raise/decay is observed when the applied current is changing. b) In the high frequency regimes, temperature gradients cannot be established and thus the Seebeck voltage component is negligible. Figure taken from reference [11].

Because of these difficulties, the Harman methods, although have been widely used to measure the figure of merit of bulk samples [10, 12-14], are hardly applied to thin film samples [15-18] or nanowires. There are only very few works that measure the zT of films thinner than 6 µm

through these methods[15, 18]. An added challenge to these measurements is the complexity to assure the validity of original conditions required by the original Harman technique (free standing, adiabatically insulated sample). For instance, measurements of thin film samples are subjected to the presence of a substrate underneath the sample. Depending on the type of substrate used, as well as the quality of contact electrodes, the frequency, voltage and gradient of temperature created by the sample might be influenced considerably. Consequently, the measured, or extrinsic, zT can be very different from the real or intrinsic zT of the film. Although the parasitic thermal and electrical losses have been previously studied in other works[16] and also 3D models[19] have been carried out to study the steady state response of thermoelectric devices, very little attention has been paid in its transient response. To the best of our knowledge, an in-depth study of the frequency response during the transient Harman method for thin-film materials has not been carried out yet.

Therefore, the objective of this Section consists of determining how these non-ideal conditions influence the frequency regime by numerical simulations and to determine the suitability and limitations of this technique. This task is undertaken for the modified Harman method, which, as described above, is more suitable to use for thin-film and nanowire characterization. In a first step (Section 4.1.2.1.), the upper bound of the low frequency regime (f_{LF}) and the lower bound of the high frequency regime (f_{HF}) are determined as a function of thin film thickness or nanowire radius, thermal conductivity and power factor, as well as thermal isolation conditions (vacuum vs. natural convection) for the case of freestanding samples. In a second step (Section 4.1.2.2.), a more realistic case in which an electrical connection is attached to the top of the thin film is considered. This simplified geometry is used to analyze the effect of the electric connection properties and its dimensions on both the f_{HF} and the obtained zT. In all cases, the zT value determined from simulated data is compared with the known zT intrinsic value of the sample to demonstrate the profound effect the non-ideal boundary conditions can have on the measurements.

4.1.1. Numerical simulations.

A commercially available software package COMSOL Multiphysics® was used to implement user-defined equations describing the thermoelectric effects [19] in order to investigate the transient thermoelectric transport in nanostructured samples. The equations introduced to COMSOL® Multiphysics software were given by Antonova *et al* [19]. The thermoelectric equations of the heat flow and the continuity of electric charge are coupled to achieve the thermoelectric constitutive equations,

Constitutive equations

$$\mathbf{q} = [\Pi] \cdot \mathbf{J} - [k]\Delta \mathrm{T}$$

$$\mathbf{J} = [\sigma] \cdot (\mathbf{E} - [S] \cdot \nabla \mathrm{T})$$

$$\mathbf{D} = [\varepsilon] \cdot \mathbf{E}$$

Field equations

$$\rho \mathrm{c} \frac{\partial \mathrm{T}}{\partial \mathrm{t}} + \nabla \cdot \mathbf{q} = \dot{\mathrm{q}}$$

$$\nabla \cdot \left(\mathbf{J} + \frac{\partial \mathbf{D}}{\partial \mathrm{t}} \right) = 0$$

$$\mathbf{E} = -\nabla \mathrm{V}$$

Coupled- Field Equations

$$\rho c \frac{\partial T}{\partial t} + \nabla([\prod] \cdot \mathbf{J}) - \nabla([k] \cdot \nabla T) = \dot{q}$$

$$\nabla \left([\varepsilon] \cdot \nabla \frac{\partial V}{\partial t} \right) + \nabla([\sigma] \cdot [S] \cdot \nabla T) + \nabla \cdot \left([\sigma] \cdot \vec{\nabla} V \right) = 0$$

where

$$\rho = density, kg/m^3$$
$$c = specific\ heat\ capacity, J/(kgK)$$
$$T = absolute\ temperature, K$$
$$\dot{q} = heat\ generation\ rate\ per\ unit\ volume, W/m^3$$
$$\mathbf{q} = heat\ flux\ vector, W/m^2$$
$$\mathbf{J} = electric\ current\ density\ vector, A/m^2$$
$$\mathbf{E} = electric\ field\ intensity\ vector, V/m$$
$$\mathbf{D} = electric\ flux\ density\ vector, C/m^2$$
$$[k] = thermal\ conductivity\ matrix, W/Km$$
$$[\sigma] = electrical\ conductivity\ matrix, S/m$$
$$[S] = Seebeck\ coefficient\ matrix, V/K$$
$$[\Pi] = T[\alpha] = Peltier\ coefficient\ matrix, V$$
$$[\varepsilon] = dielectric\ permittivity\ matrix, F/m$$

These equations were re-written in order to fit with the partial differential equation module (PDE) of COMSOL®,

$$\rho c\frac{\partial T}{\partial t}-\vec{\nabla}\left((\sigma S^2T+k)\vec{\nabla}T\right)-\vec{\nabla}\left(\sigma ST\vec{\nabla}V\right)=\sigma((\vec{\nabla}V)^2+\sigma\vec{\nabla}T\vec{\nabla}V) \quad (4.3)$$

$$\vec{\nabla}\left(\sigma S\vec{\nabla}T\right)+\vec{\nabla}\left(\sigma\vec{\nabla}V\right)=-\vec{\nabla}\left([\varepsilon]\vec{\nabla}\frac{\partial V}{\partial t}\right) \quad (4.4)$$

where S, σ and k are the Seebeck-coefficient, the electric conductivity, and the thermal conductivity, respectively, $[\varepsilon]$ is the dielectric constant and $\rho \cdot c$ is the density multiplied by the thermal capacity of the sample. The variables are the temperature, *T*, the voltage, *V*, and the time, *t*.

The PDE equations in COMSOL® are defined as,

$$\begin{aligned} k\frac{\partial^2 u}{\partial t^2}+d\frac{\partial u}{\partial t}+\nabla\cdot(-k\nabla u-\alpha u+\gamma)+\beta\cdot\nabla u+au=f \qquad & \text{in } \Omega \\ n\cdot(-k\nabla u-\alpha u+\gamma)+qu=g-h^T\mu \qquad & \text{on } \partial\Omega \\ hu=r \qquad & \text{on } \partial\Omega \end{aligned} \quad (4.5)$$

where $k, d, \alpha, \gamma, \beta, a, f, g, h^T, r$ are the coefficient of the differential equation and boundary coefficients whilst *u* is the field variable. The Ω is the computational domain, $\partial\Omega$ is the domain boundary and ***n*** is the outward unit normal vector on $\partial\Omega$. The second equation is a generalization of a Neumann boundary conditions, whereas the third equation is a general constraint with a Dirichlet boundary condition as a special case.

Comparing it with equation Equation 4.3 and Equation 4.4 the PDE coefficients and field variable can be written as,

$$k=\begin{pmatrix}\lambda+\sigma\alpha^2T & \sigma\alpha T\\ \sigma\alpha & \sigma\end{pmatrix}\quad f=\begin{pmatrix}\sigma((\nabla V)^2+\sigma\nabla T\nabla V)\\ \nabla\left([\varepsilon]\nabla\frac{\partial V}{\partial t}\right)\end{pmatrix}\quad d_a=\begin{pmatrix}\rho c\\ 0\end{pmatrix} \quad (4.6)$$

$$u=\begin{pmatrix}T\\ V\end{pmatrix} \quad (4.7)$$

whilst the other coefficients of Equation 4.5 are zero.

Dirichlet boundary conditions were used to establish one electrode grounded and free evolution of temperature, while the other electrode is fixed at room temperature and a square voltage is applied to it. Running this simulation will be equivalent to vacuum conditions,

as no convective terms of the films are considered. A simple parametric sweep was used to simulate different thicknesses but in order to approach to the 2D structures it would be interesting to change the area of the film at least 100 times bigger than its thickness.

A box of air was added to simulate the effects of convection and conduction from the thermoelectric material to the air. For that purpose, we used the conjugate heat transfer module of COMSOL®. Then, we considered the heat equation in fluid for the air box, whose continuity and momentum equations are,

$$\frac{\partial \rho}{\partial t} + \nabla(\rho v) = 0$$

$$\rho \frac{\partial v}{\partial t} + \rho(v \cdot \nabla)v = \nabla\left[-p\mathbf{I} + \mu(\nabla v + (\nabla v)^T) - \frac{2}{3}\mu(\nabla \cdot v)\mathbf{I}\right] + \mathbf{F} \quad (4.8)$$

where v is the velocity field, ρ and C are the density and the heat capacity at constant pressure, p is the pressure, μ is the dynamic viscosity and $\mathbf{I}$ is the identity matrix. Finally, the body force vector, $F = -g \cdot \rho(T)$, must be considered to simulate the effects of gravity in convection. The temperature at the sides of the box of air was fixed at room temperature whilst the rest evolved freely.

Regarding the simulation of Section 4.1.2.2., a new PDE equation was set for the electrodes and wire equivalent to the previous one (Equation 4.3 and Equation 4.4). Dirichlet boundary conditions were used to fix the top part of the wire at room temperature and the film with the electrodes and the wires was embedded in a box of air of 3 x 3 mm big to simulate effects of natural convection. Parametric sweeps were used to simulate different electrical conductivity of the electrodes and different radius of the wire. In all simulations, a fine mesh for the structure was considered until no changes in the results of the simulation were observed with the increase of the number of elements.

Figure 4.1 shows the general configuration of the sample. The Dirichlet boundary condition was applied to fix the electrically energized electrode (bottom) at room temperature, while an AC square voltage waveform was applied to the other (top) electrode, letting its temperature evolve as a function of time. The mesh was selected

adequately considering a minimum number of elements that gave no variations in the results when further increasing the number of nodes.

The thermoelectric material selected for these investigations is p-type Bi_2Te_3 with copper for electrodes and wires. This thermoelectric material presents a large zT at room temperature (see Introduction Chapter) and it is being used in commercial room-temperature thermoelectric devices. Thus, there is a great interest in exploring its properties in nanostructured forms such as thin films and nanowires [20, 21]. Reference [22] was used to take the temperature dependent values of the Seebeck coefficient, thermal conductivity and electrical conductivity of the sample.

The sample of interest was modeled in air, conditions typically employed in Harman measurements on bulk samples, in order to determine the effect of convective losses on the thermoelectric response. The size of the air-filled chamber surrounding the sample was increased until the results were size-independent. Specifically, an air box size of 10 mm^3 was used in the modeling with side walls fixed at room temperature. Details of the equations used to model convective losses are given above. Simulations with the heat convection coefficient as an input parameter have been also carried out in order to study the effects over a wide range of heat transfer coefficients. As it was mentioned previously, the main parameters of interest in this work are the upper bound of the low frequency (*LF)* regime (f_{LF}) and the lower bound of the high frequency (*HF)* regime (f_{HF}). On the one hand, the former is the maximum frequency at which a steady-state temperature rise is obtained using the modified Harman technique. In practice, this frequency is of interest because it requires less time to perform the AC measurements. On the other hand, the latter is the minimum frequency at which no temperature gradient is generated in the sample. For these studies, this limit is defined as the condition when the temperature difference across the sample is 10% of the steady-state temperature difference, since smaller temperature gradients would produce negligible V_S values.

4.1.2. Thermoelectric nanostructures simulations.

This Section studies the effect of sample properties and boundary conditions on the frequency regimes and the gradient of temperature created by a free standing thermoelectric thin film. In all cases investigated here, convection from the surrounding air is taken into account, as it is usually the standard ambient for thermoelectric device operation. At the end of this Section, a comparison between the extrinsic zT extracted for the different simulation conditions is presented.

4.1.2.1. Ideal case: Free standing cross plane simulations for intrinsic Bi_2Te_3 thin films and nanowires.

Simulations of the voltage and temperature evolution with time for p-type Bi_2Te_3 films were first performed in a simplified case. In this scenario, the voltage was homogeneously applied to the top surface while the bottom surface of the film was grounded. The film presented a thickness of 60 μm and was freestanding in the air with the bottom face fixed at room temperature. Simulations for a film-on-substrate geometry indicated that this temperature boundary condition approximates well the transport for the studied film in the presence of a substrate with thermal conductivity higher than 1 $W \cdot K^{-1} \cdot m^{-1}$. The temperature and the voltage distribution along the sample thickness are shown in Figure 4.2 as a function of time for an applied pulse of 10 mV in amplitude and 0.05 seconds in length. Due to the one-dimensional nature of the transport, the temperature and voltage are constant in the horizontal direction, so only results for the vertical cross-section of the sample are shown. The first half of the pulse period is considered in the analysis, since the response for each half-period is identical, except for the polarity. The lower bound of the high frequency range (f_{HF}) is determined from the exponential fitting of the temperature rise (considering the time at which $\Delta T = 0.05 \cdot T_{max}$, where T_{max} is the maximum temperature reached by the hot side and ΔT is the difference of temperature).

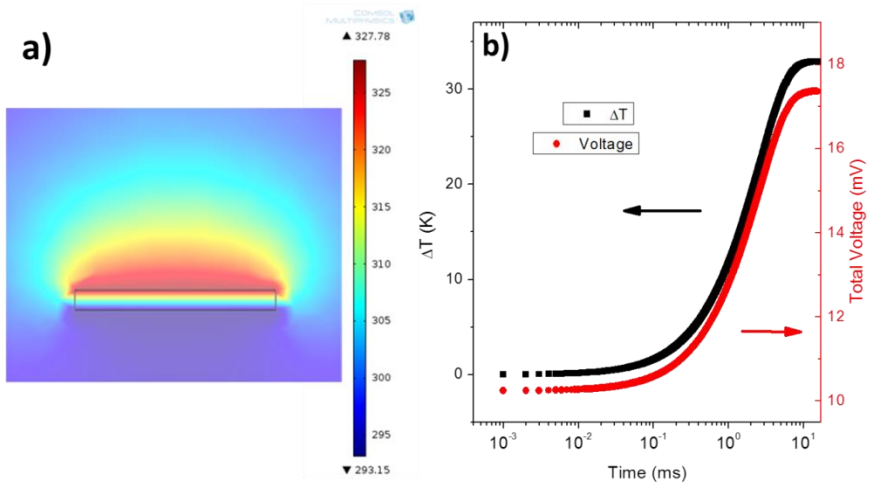

Figure 4.2. a) Steady-state temperature distribution in a 60 μm Bi_2Te_3 under a 10 mV pulse of 0.05 s length. b) Temperature and voltage as function of time for the applied voltage pulse. Only the response to the first half of the pulse is shown. Figure taken from reference [11].

In Figure 4.2a the steady-state temperature distribution within the sample is shown. The heating of the air in the vicinity of the upper side of the sample is clearly observed. The convective heat transfer inside the box is equivalent to a situation where the convective heat coefficient associated with natural convection from the film top and side surfaces is 10 $W \cdot K^{-1} \cdot m^{-2}$. It must be mentioned that results are nearly independent of this natural convection factor in a wide range of values up to about 10000 $W \cdot K^{-1} \cdot m^{-2}$. Moreover, the results are not significantly modified under vacuum conditions, which confirm the small effect of natural convection for these films. In Figure 4.2b the temperature at the upper side of the sample as a function of time is presented. The temperature increases nearly exponentially with the time to steady-state is reached. The voltage evolution as a function of time is also shown in this Figure. An immediate increase of the voltage is produced when the pulse is applied (corresponding to the applied voltage V_e). The voltage then increases slowly because of the Seebeck component, which generates a temperature difference across the sample. From Figure 4.2b, one can see that an electric pulse with

duration of less than 10 ms will not be sufficiently long for the temperature to reach steady state. As an example, when the electric pulse is less than 0.1 ms the temperature increase is lower than 1.6 K and the estimated Seebeck voltage is below 0.36 mV instead of the ~7.4 mV observed in the steady state. Two time constants are defined based on this type of analysis: the one at which the temperature reaches its maximum value (for this example, approximately around 10 ms), and the one at which the temperature increase is a tenth of the maximum temperature increase (approximately around 0.1 ms here). These values are then used to determine f_{HF} and f_{LF} that will give the frequency requirements of the applied voltage for the steady-state Seebeck voltage to be accurately measured or absent, respectively.

Following this procedure, the low and high frequency regimes were obtained for different thicknesses of the Bi_2Te_3 films, whose aspect ratio (area to thickness ratio) was approximately 100 (to maintain the two-dimensional (2D) character of the geometry). The maximum temperature gradient created in these samples was around 34 K for the 10 mV applied pulse voltage. It is important noting that increasing the pulse amplitude produces an increase in the temperature difference; however the values of the low and high frequencies remain nearly unaltered.

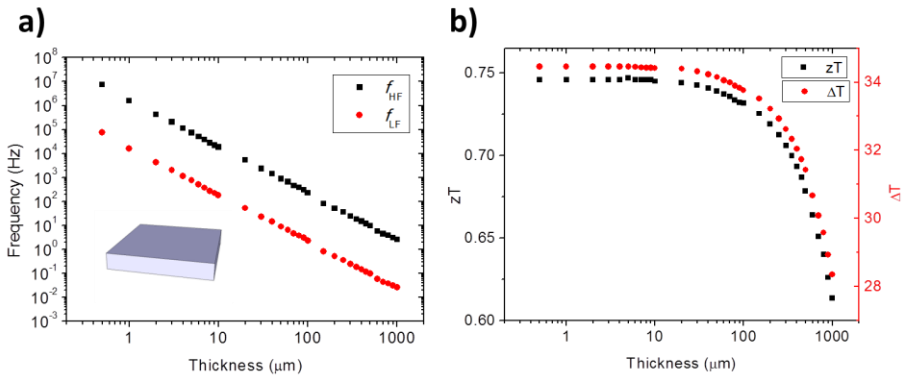

Figure 4.3.Upper bound of low frequency, f_{LF}, and lower bound of high frequency, f_{HF}, as a function of film thickness. b) zT and maximum difference of temperature (ΔT) obtained from the simulation. Figure taken from reference [11].

In Figure 4.3a and 4.3b the values of the f_{LF} and f_{HF} and the values of the extrinsic zT and difference of temperature reached as a function of film thickness are presented. The data shows a significant increase of the two bounds of frequency with the reduction in the sample thickness. This points out that the modified Harman technique becomes difficult to use for sample thicknesses under 5µm, because of the high f_{HF} required, over 10^5 Hz. Furthermore, the effective zT (from Equation 4.2) is modified slightly with the thickness of the film because the temperature difference reached across sample increases for thicker films, and S, σ and k are temperature dependent so they change. However, in all cases, the simulated zT values match with the theoretical intrinsic ones that are predicted based on properties estimated at averaged temperature. Even though there are not many reports of Harman measurements of Bi_2Te_3 films, in reference [15] the temporal evolution of voltage was reported for a Bi_2Te_3/Sb_2Te_3 thin film superlattice of 5.4 µm thickness presenting a similar lower bound of approximately 100 kHz for the high frequency regime, as predicted here.

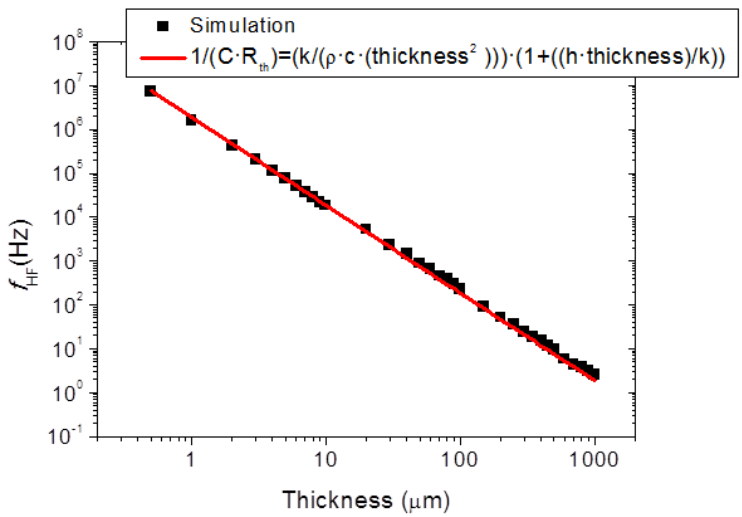

Figure 4.4. Comparison of the lower bound of the high frequency predicted by analytical model and by simulation data. The model is in good agreement with the simulated data. Figure taken from reference [11].

The lower bound of the high frequency regime can also be estimated from a lumped heat capacity model for the film while assuming that heat transfer occurs by conduction across the film thickness and convection to the ambient. This model leads to the next analytical expression,

$$f_{HF\ theory} = \frac{1}{R_{th} \cdot C} = \frac{k}{\rho \cdot c \cdot (thickness^2)} \cdot \left(1 + \frac{h \cdot (thickness)}{k}\right) \quad (4.9)$$

where R_{th} is the sample thermal resistance, C is the thermal capacity, ρ is the density, c the specific heat and h the convective coefficient. The term $\frac{h \cdot (thickness)}{k}$ in the second part of Equation 4.9 is much smaller than 1, even for h values of 10000 $W \cdot K^{-1} \cdot m^{-2}$, which reveals little influence of convection on the high frequency regime of films. Figure 4.4 shows a comparison of the high frequency values obtained from Equation 4.9 (red line) and the results of numerical simulations (black dots). A good agreement between both results is observed, as it can be seen.

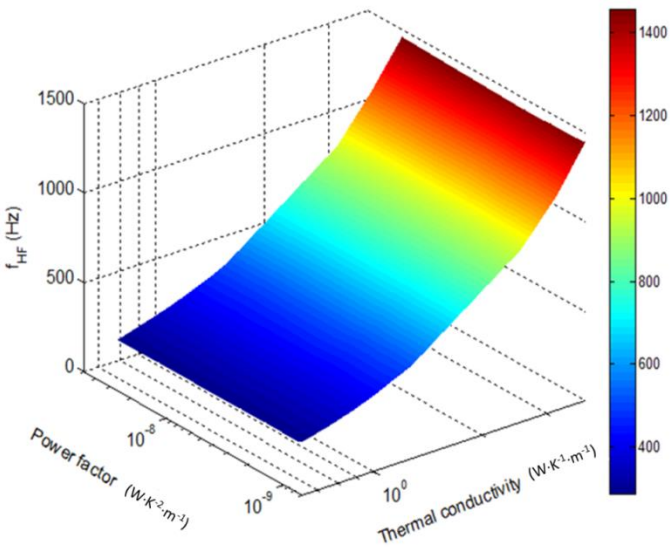

Figure 4.5. f_{HF} as function of power factor and thermal conductivity for a 60 µm p-type Bi_2Te_3 sample. The power factor was modified keeping constant the electrical conductivity and varying S, and vice-versa resulting in the same results. Figure taken from reference [11].

Next, the effect of the material properties on f_{HF} is assessed. For that purpose, the analysis of f_{HF} was carried out on a 60 µm thickness sample while the thermal conductivity and the power factor (the product between electrical conductivity and the squared Seebeck coefficient) was varied. The objective was to understand how variations of material properties modify the lower bound of the high frequency regime. Figure 4.5 shows f_{HF} as a function of the power factor and the thermal conductivity. In Figure 4.5, the power factor is varied by changing the Seebeck coefficient without varying the electrical conductivity, as well as changing electrical conductivity while the Seebeck coefficient was kept constant.

From this Figure, the f_{HF} is observed to depend strongly on the thermal conductivity, while it has not a noticeable dependence on the power factor. This fact can be understood considering the heat transfer in the sample. If the thermal conductivity of the sample is low, it takes longer to reach steady state and the frequency is low. Above a thermal conductivity of around 1 $W \cdot K^{-1} \cdot m^{-1}$, it requires a lower bound for f_{HF} at 0.5 kHz to establish a steady-state temperature rise across a 60 µm thick film. Since the heat transfer depends on both thermal properties and material thickness, similar effect is observed when the sample thickness is reduced. For example, Figure 4.6. shows the effect of the thermal conductivity on f_{HF} for samples with different thicknesses and an aspect ratio of at least 100 times. This Figure illustrates the increase in $f_{HF}$with the thermal conductivity of the sample and its inverse dependence on the material thickness, which was also observed in Figure 4.3a. In conclusion, all these results agree well with the theoretical values obtained from Equation 4.9.

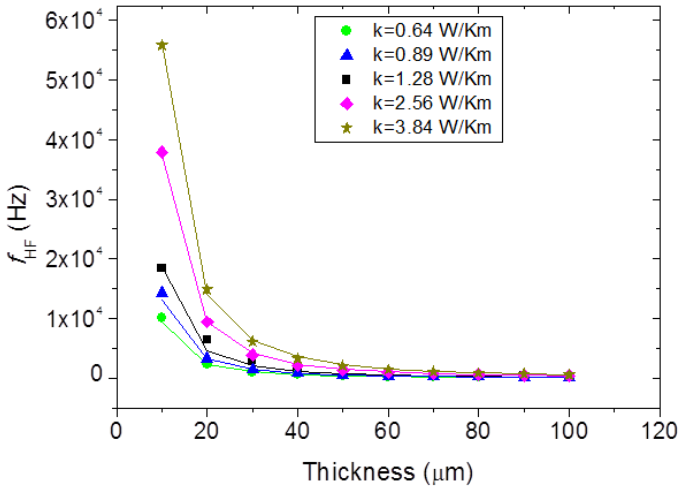

Figure 4.6. f_{HF} as a function of the thickness of materials with different thermal conductivities and same power factor. The dots represent the simulated values while the lines are calculations using Equation 4.9. Figure taken from reference [11].

A similar study was performed on p-type Bi_2Te_3 nanowires (NW) with different diameters. As before, the voltage was applied homogeneously at the top and bottom of the nanowire. The Bi_2Te_3 wire was oriented with the *c*-axis parallel to the NW and the same temperature dependent properties [22] were used to be consistent with previous analysis. No confinement effects were considered in this case since evaluating the change in thermoelectric transport properties as a function of wire diameter is outside the scope of this work (note that size effects can usually be taken into account by replacing the bulk value of thermal conductivity with an effective value). As in the thin film case, the ground electrode was set at room temperature while the hot side of the nanowire evolved freely. The wire was freestanding and set in air at room temperature, where convection effects were taken into account on all its sides. The length of the NW was 20 μm whereas the NW radius ranged from 50 nm to 250 nm. The voltage applied to the NW was 10 mV, which created temperature differences lower than one Kelvin.

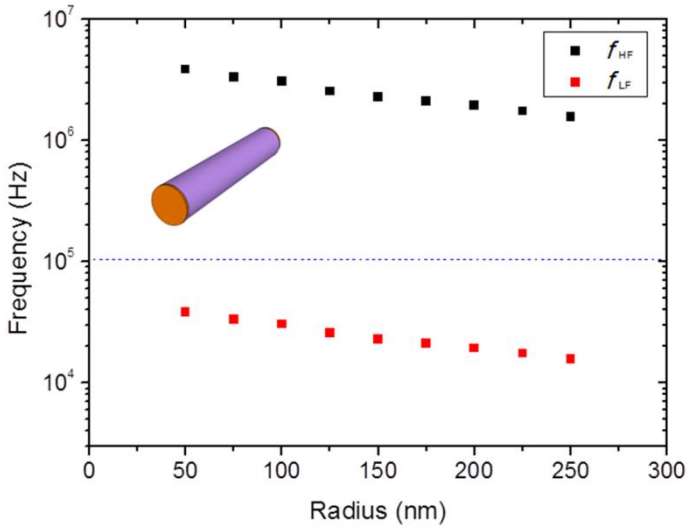

Figure 4.7. f_{HF} and f_{LF} dependence versus NW radius. The dashed line shows the typical electronic devices limitation when measuring frequency. Schematic view of the NW sample with electrodes painted in brown is shown in the inset of the graph. Figure taken from reference [11].

In Figure 4.7 the effect of the reduction in the nanowire radius on the f_{HF} and f_{LF} is shown. The frequency increases dramatically for 1D structures as compared with thin films, especially when their diameter is in the range of 100 nm or less. For a given diameter the HF and LF frequency limits are about two orders of magnitude apart. For instance, in order to avoid the thermoelectrical response of a freestanding NW of 100 nm radius, f_{HF} should be higher than 10 MHz. The high frequencies observed in this case are caused by the low time constant associated with the nanostructure, which is able to rapidly respond to a change in temperature to the applied heat. As a consequence, individual one-dimensional (1D) structures, such as nanowires, are challenging to measure with the original or modified Harman method.

4.1.2.2. The effect of electrical contacts.

Simulations of a thin film Bi_2Te_3 sample sandwiched between electrodes that have different transport properties were carried out in order to analyze how electrical and thermal contacts affect the lower bound of the high frequency regime. Moreover, a contact wire was connected to the top electrode to approach the reality. Joule, Thomson and thermoelectric effects were considered for the film, the wire and the electrodes. The external face of the bottom electrode was fixed at room temperature while the temperature of the top electrode and the wire were let to evolve freely.

These simulations were first performed on a 60 μm thick p-type Bi_2Te_3 film with an area of 600 x 600 μm^2 (width/length ten times larger than the thickness to approach to the 2D case). That is a typical film that might be produced by electrodeposition [23] although this work can be extended to other thicknesses and fabrication techniques. The electrodes have the same area as the Bi_2Te_3 film and a thickness of 20 μm, because in soldering processes the thickness of the contact metals is usually increased to this range. The contact wire was made of copper and had a diameter of 100 μm with a thermal conductivity of 400 $W \cdot K^{-1} \cdot m^{-1}$, an electrical conductivity of $6 \cdot 10^7\ S/m$ and a Seebeck coefficient of 1.7μV/K [24]. In order to simulate the effect of a contact resistance (that depends on the quality of the contact between the film and electrode) the electrical conductivity of the electrode was varied by around 5 orders of magnitude with copper as the higher limit. Meanwhile, the electrode thermal conductivity and specific heat were assumed to be similar to copper. The simulations recorded the steady-state temperature and voltage for each case. In Figure 4.8 results for an electric pulse of 10 mV and a length of 0.05 seconds are shown.

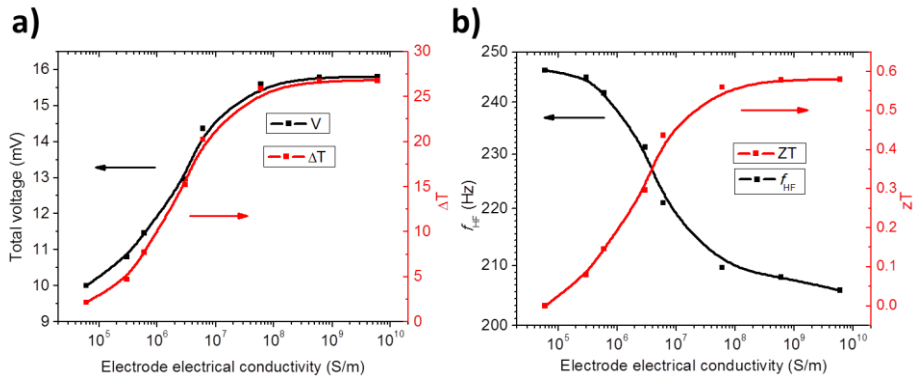

Figure 4.8. a) Temperature difference (right) and the total electrical voltage (left) generated at steady- state across a 60 µm thick p-type Bi_2Te_3 as a function of the electrode electrical conductivity and for an applied voltage of 10 mV. Trend lines are used as a guide to the eye. b) The lower bound of the high frequency regime and extrinsic *zT* as a function of the electrical conductivity of the electrodes. Figure taken from reference [11].

In Figure 4.8a it is observed that high electrical conductivity electrodes, i.e. low electrical contact resistances, do not degrade the temperature gradient established by the Peltier effects and the Seebeck voltage until it plateaus after about 10^8 S/m. This corresponds to an equivalent contact resistivity of around $5 \cdot 10^{-7}$ Ω·m, approximately an order of magnitude smaller than the thermoelectric film resistivity. The reduction of f_{HF} in Figure 4.8b in comparison to f_{HF} in Figure 4.3 is caused mainly to the heat dissipation along the external wire and heat capacity of the electrodes. While the f_{HF} in Figure 4.8b will give the limit for which steady-state is achieved in the sample, performing measurements in this frequency will not result in accurate measurements if the contact resistance is high. Figure 4.8b shows that the figure of merit (*zT*) is profoundly affected by contact resistance and becomes impossible to measure if electrode electrical conductivity is less than 10^8 S/m.

Furthermore, although a low contact resistivity improves the amplitude of the Seebeck and temperature signals, the contact wire also plays a major role. As an example, for the 60 µm thick Bi_2Te_3 sample

without the influence of any contacts the steady-state temperature was determined to be around 34 degrees and the total voltage around 17.4 mV (Figure 4.2). In contrast, even for a contact resistivity below $5 \cdot 10^{-8} \Omega/m^2$ the maximum temperature difference reached is about 26.8 degrees while the total voltage is 15.8 mV. This corresponds to an extrinsic *zT* for the film and electrode assembly of 0.58. This reduction will be discussed further in this Section.

To study the effect of the contact wire radius, the simulations were performed on a Bi_2Te_3 film of 60 μm thickness sandwiched between 20 μm copper electrodes with thermal conductivity of 400 $W \cdot K^{-1} \cdot m^{-1}$, an electrical conductivity of $6 \cdot 10^7$ S/m and a Seebeck coefficient of 1.7 μV/K. In all simulations the wire was attached to the top electrode and had a length of 1 mm. The voltage applied to the bottom electrode was fixed at room temperature. The wire was grounded at its free end, while its temperature and that of the top electrode were let evolve freely.

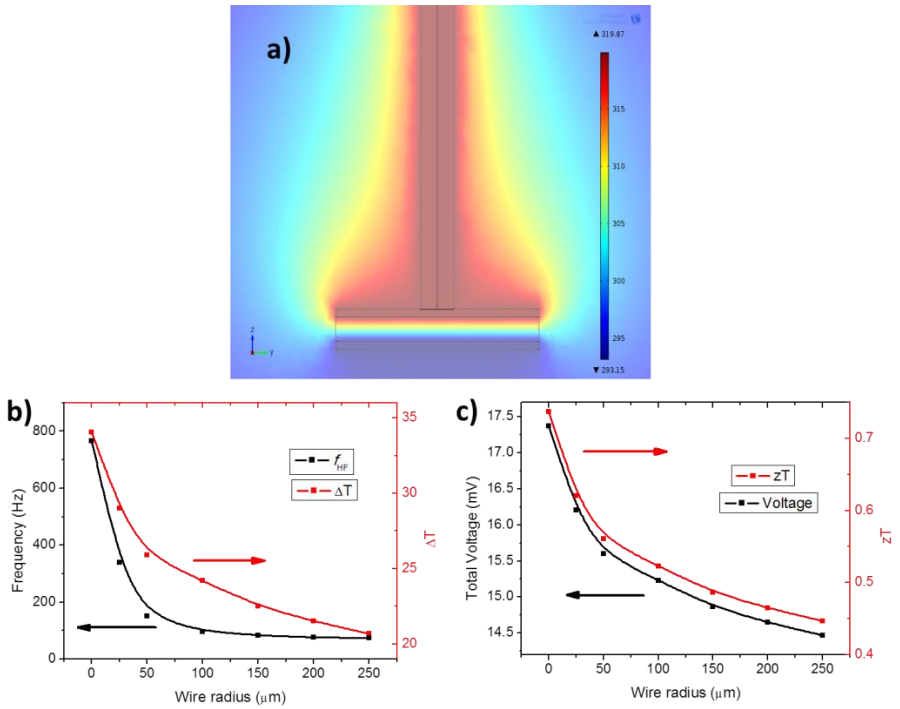

Figure 4.9. a) Temperature distribution for a system composed of a 60 μm-Bi_2Te_3 film with a copper wire connected on top. b)f_{HF} and

temperature difference (ΔT) and c) total voltage and extrinsic *zT* obtained as a function of the copper wire radius. Figure taken from reference [11].

In Figure 4.9a the temperature distribution in the sample with a wire diameter of 100 μm is shown, which illustrates the strong fin effect of the wire. Figure 4.9b and 4.9c shows f_{HF} and temperature difference (ΔT) and total voltage and *zT* obtained in the film as a function of the wire diameter, respectively. When reducing the wire diameter approaching the case with no wire, the frequency, temperature difference, total voltage and the figure of merit increase. However, at the practical dimensions (wire radius of 50 μm or larger, which can be easily attached manually) the temperature difference of around 26 K is still around 8 degrees smaller than that of the ideal case. As a result the extrinsic *zT* is around 0.56 instead of 0.74 expected. Contact wires with large diameters could result in massive heat loss and involve a reduction of the order of magnitude in the measured temperature difference, resulting in an artificially low extrinsic *zT*. These aspects are relevant not only to Harman measurement, but to thin film device design as-well. Furthermore, given these discrepancies, the analytical Equation 4.9 will not work well in the presence of the electrodes and contact wires. Therefore, a revised equation to take into account these effects shall be considered. In reference [16], the wire thermal resistance was expressed as,

$$R_{fin} = \frac{\tanh\left(\sqrt{\frac{l^2 \cdot h_{fin} \cdot p_{fin}}{k_{fin} \cdot A_{fin}}}\right)}{\sqrt{h_{fin} \cdot p_{fin} \cdot k_{fin} \cdot A_{fin}}} \tag{4.10}$$

where "fin" stands for our wire and *p*, *A*, *k*, *l* and *h* are the perimeter, cross section area, thermal conductivity, length and convection on the lateral side of the wire, respectively.

Thus, after taking this into account the additional heat capacity of wire and electrode and the thermal dissipation along the wire the

revised lumped heat capacity model yields the new frequency prediction that can be expressed as,

$$f_{HF} = \left(\frac{1}{R_{fin}} + k_{film} \cdot \frac{A_{film}}{thickness} + h \cdot \left(A_{film} - A_{fin} \right) \right) \cdot \frac{1}{C_{total}} \quad (4.11)$$

where "film" stands for the thermoelectric film and C_{total} is the total heat capacity of the system calculated as, $C_{total} = c_{fin} \cdot \rho_{fin} \cdot V_{fin} + c_{elect} \cdot \rho_{elect} \cdot V_{elect} + c_{film} \cdot \rho_{film} \cdot V_{film}$, where c is the specific heat, ρ is the density and V is volume. The electrode thermal resistance, R_{elec} is much smaller than R_{fin}, so its contribution does not need to be included in Equation 4.11.

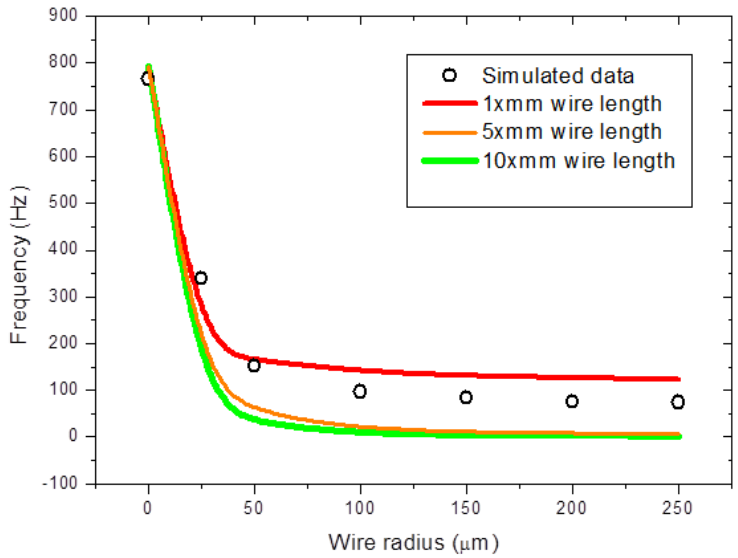

Figure 4.10. f_{HF} as a function of the length of the wire. The dots represent the simulated values while the lines are calculations using Equation 4.11. Figure taken from reference [11].

In Figure 4.10 a comparison of the f_{HF} obtained from simulated data and Equation 4.11 is shown. The wire in the simulation has a length of 1 mm, while for Equation 4.11 different wire lengths have been considered. In all cases a clear increase in the frequency is

observed in smaller wire radius, but there is a noticeable difference in the frequency values and tendency between the simulation and the values obtained from Equation 4.11 to 1 mm-length wire, while longer wires show a tendency which resembles that of the simulated data, but with lower values. This might indicate that the 1 dimensional model given by Equation 4.11 is not appropriate to reproduce with high accuracy the f_{HF} results obtained by three-dimensional simulation. Nevertheless, Equation 4.11 can be used to quickly obtain an order of magnitude estimation of these values. Finally, it was observed that for large diameter wires the f_{HF} is mainly estimated by $\frac{1}{C_{total}R_{fin}}$, while as the diameter of the wire reduces f_{HF} tends to Equation 4.9, as expected.

When considering just the effect of electrodes (no contact wires,), f_{HF} increased to around 755Hz and extrinsic zT to 0.74, equivalent to zT determined under atmospheric conditions without electrodes. The high frequency obtained for such electrode thickness without the wire is essentially the same to the one determined without electrodes. Nevertheless, the reduction of the thickness of the electrodes results in approaching of the high frequency value corresponding to the one without layer electrodes (765Hz).

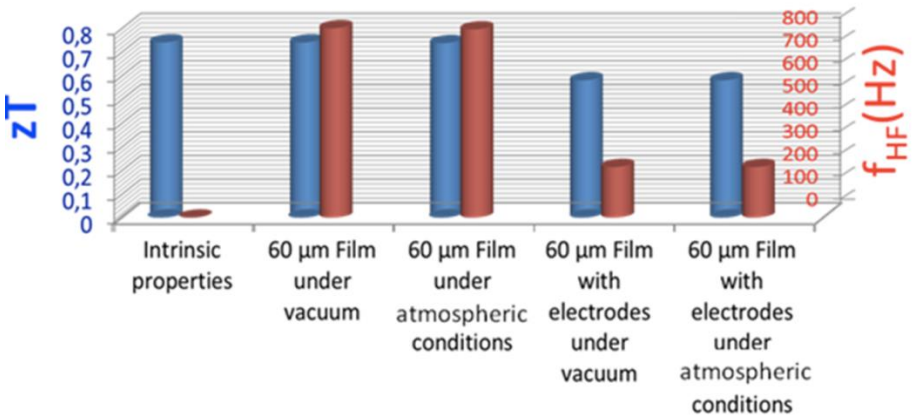

Figure 4.11. Theoretical and simulated zT values (blue columns) and high frequencies (f_{HF}, red columns) determined in different conditions. Figure taken from reference [11].

The lower bound of the high frequency regime and the simulated values of zT was compared for all cases discussed above, i.e. films with and without contact resistance and wire electrodes in vacuum or atmospheric conditions. Figure 4.11 shows these results where both f_{HF} and zT are plotted for each case. The frequency limit obtained under vacuum conditions is comparable to the ones determined under atmospheric conditions, regardless of the presence of wires and electrodes. On the other hand, when electrical connections (50 μm diameter and 1 mm length wire) were considered, a clear reduction of both f_{HF} and zT was obtained from the simulations, indicating that the thermal dissipation occurring on the wires greatly affects the Harman measurement. The zT values obtained are reduced by nearly a 30% with respect to the intrinsic value of the material, making the determination of the figure-of-merit very inaccurate.

Therefore, very small wire diameters, below 10 μm, shall be used to carry out an accurate and direct measurement of the figure of merit, as clearly seen in Figure 4.9, which involve a reduction of zT of only about 10%.

In summary, the implementation of an experimental set-up to carry out Harman measurements in nano-structures, such as films or nano-wires, become very challenging. The high frequency regimes observed, either for thin films or nanowires, in the Harman method require of special electronic devices which are able to detect very small and fast signals. Moreover, the heat loss associated with the contact wire and the contact resistance can profoundly affect zT results, involving an underestimation of it even in some of the best scenarios shown above. For all these reasons, the Harman technique is rather difficult to use in thin films and can be nearly discarded to measure nanowires. The measurement of each of the transport properties, such as the thermal or electrical conductivity, might be preferable for nano-structures.

4.2. Electrical property measurements of films.

In this Section, the electrical conductivity of thermoelectric Bi_2Te_3 films is evaluated in its out of plane direction. As it was mentioned in the Introduction Chapter, there are a wide variety of techniques that can be used to measure the electrical conductivity of materials and techniques capable to measure electrical properties along different directions are required for samples with anisotropic electric transport properties.

Bi_2Te_3 crystals are highly anisotropic along directions parallel and perpendicular to the plane of the film[25]. Measurements in the in-plane directions of films can be obtained in a simple way using the four point probe technique [26, 27] or the Van der Pauw method[28], among others (see Introduction Chapter). However, measurements in the cross-plane direction of films require of more complex analysis and in most of the cases specific set ups. In cross-plane measurements, effects such as the possible non-uniform spreading of the current across the film and within electrodes, and the influence of the contact resistances between the interfaces[29, 30] make necessary a careful analysis of the electric transport of the sample.

An important consideration in electrical measurements is the influence of the contact resistance. If the sample has low resistance, the contact resistance contributes more to the total resistance measured. Bi_2Te_3 is sometimes considered as semi-metal and so the interface contact resistance in cross-plane measurements can influence the resistance results. As a consequence, this parameter must be also accurately determined in order to obtain the electrical conductivity of the film properly.

This Section starts with a scanning probe microscopy (SPM) approach to measure the electrical contact resistance at the interface of a Bi_2Te_3 film and its gold electrode. Finally, the electrical conductivity of Bi_2Te_3 films was measured using a specific set up, the four probe technique and a three dimensional (3D) finite element model.

4.2.1. Electrical contact resistance at the interface Au- Bi_2Te_3 films.

The influence of the electrical contacts is essential to be considered when measuring the electrical transport properties of any sample. For instance, when an actual thermoelectric device is carried into effect, the behavior of the electrical contacts might have a considerable impact on its efficiency. In fact, when a current is passed through the sample, the voltage drops across the contact resistances and heat is generated because of the Joule effect. Consequently, the larger the electrical resistivity of the contacts is, the more Joule heat is generated at the interface and the higher the electrical voltage drop is, which causes a variation of the gradient of temperature in the thermoelectric sample modifiying also the value of the Seebeck coefficient. These effects are not solely important for thermoelectricity, but in every electric device. But reducing the contact resistance in thermoelectrics is one of the bottle necks for device production and improving the efficiency of the thermoelectric materials into the final device. In fact, the smaller the dimensions of the material (thin films or nanowires), the higher the influence of the electrical contacts is. Therefore, it is very helpful and necessary to use a method to characterize the characteristics of the electrical contacts. Although there are different methods that provide a way to determine or remove the influence of the resistance of the electrical contacts in thin films, such as the four probe technique [31] or the variable thickness method [15], in this Section an alternative method of measuring the electrical contact resistances directly is presented. Additionally, some works have been reported recently regarding measurements of contact resistance and electrical characterization with different techniques for nanowires or nanotubes [21, 32, 33, 34], molecules [35] and polymeric or organic thin films [26, 36, 37].

In this Section, a novel way of measuring the electrical contact resistance of a thermoelectric thin film in cross plane configuration by means of the Kelvin Probe Microscopy (KPM) technique [38] is presented. The cross plane direction is defined as the direction perpendicular to the surface of the substrate, that is, the direction in

which the thermal gradient will be established for the device to work as a thermoelectric device. It is worth mentioning that the bismuth telluride films were optimized in order to have their *c*-axis parallel to the surface of the substrate. The reason for that optimization is the better performance of the thermoelectric material in the direction perpendicular to the surface of the substrate (cross plane direction). The KPM technique offers the possibility of getting a topographic and a surface potential map of the different components of the sample, simultaneously, which consists of the film, its top and bottom electrical contacts and the substrate where it is hold [39]. The working principle of this technique is based on applying simultaneously a DC and an AC voltage through a conductive atomic force microscopy (AFM) tip. These voltages produce different electrostatic forces in the tip, and from the interaction of these forces with the surface under study, the local work function can be obtained [40] (see Chapter 2.2.1.2.).

KPM for in plane measurements, i.e. along the direction parallel to the surface of the substrate, of the potential drops at the contacts have been performed in previous works for thin film transistors with a KPM [41]. In this case the devices are designed in such a way that the potential drops at the contacts are located in the in plane direction. However, no measurements of contact resistances in cross plane configuration have been carried out with this technique beforebecause of the complexity of the set-up and the measurement in this direction. In this Section, measurements of the electrical contact resistances between two gold electrodes that sandwich a Bi_2Te_3 thin film were carried out with the KPM technique. It was also possible to observe differences in the contact resistances at the Au- Bi_2Te_3 interfaces depending on how the electrodes were attached to the film.

4.2.1.1. Film fabrication.

The bismuth telluride film (Figure 4.12a) was grown by electrodeposition in a three electrode electrochemical cell, according to reference [42] and Chapter 2. The working electrode used was a silicon

wafer (Si (110)) with 5 nm chromium and 150 nm gold layers deposited on top by electron beam evaporator. The reference electrode was made of Ag/AgCl (3M KCl), while the counter electrode was a platinum mesh. The electrochemical bath was described in reference [42]. The electrodeposition process consisted of a constant applied potential of -40 mV for 2 hours, resulting in a film of 4.5 μm thickness preferentially oriented along [1 1 0] direction (Figure 4.12b). Then, a good electrical contact between the bottom gold electrode and the bismuth telluride film is granted because of the electrodeposition process itself. After the film was grown by electrodeposition, the sample was extracted and cleaned and then it was introduced in the same electron beam evaporation system mentioned above. At that point, a second gold layer of 150 nm was evaporated at the surface of the film, creating the top electrode of the device. Given that this is a physical deposition method, the goodness of the electrical contact between this top electrode and the film depends on the conditions of the deposit, the roughness of the bismuth telluride films and other parameters [23]. This parameters make this contact different from the one obtained with the bottom electrode. Figure 4.12 shows a scanning electron microscope of the final sample.

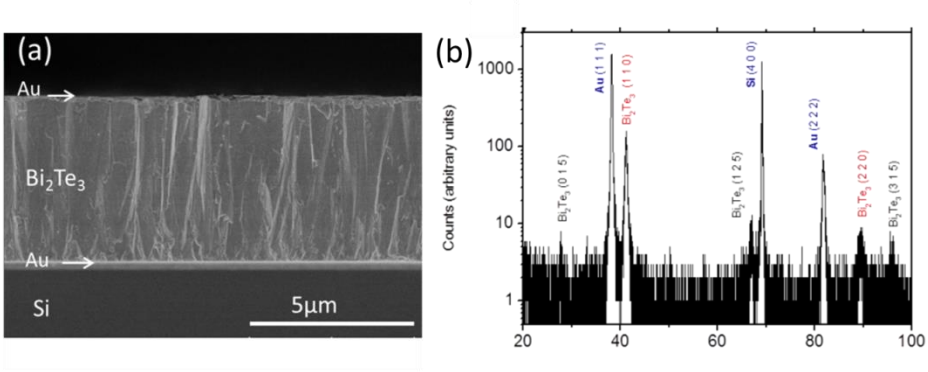

Figure 4.12. (a) Scanning electron Microscope image of the edge of a 4.5μm electrodeposited Bi_2Te_3 film. Gold electrodes can be found on the top and bottom of the sample. (b) XRD of the bismuth telluride film, where the preferential orientation along (110) can be seen. The counts are in log scale to enhance the minority orientations so all of them can be observed. Figure taken from reference [43].

After the Bi_2Te_3 thin film was sandwiched between two gold electrodes and held to the Si substrate, it was cut and its cross side was scanned with KPM at different bias voltages. From the measured surface potential map the contact resistance of the contacts was determined. To this end, a Cervantes Fullmode Atomic Force Microscopy (AFM) system developed by Nanotec Electrónica S.L.[44] and Multi75E-G BudgetSensors® probes made of Si with Cr/Pt conductive coating were used. In order to achieve accurate measurements many experimental requirements are required, such as the need of a considerably flat surface (in the order of nanometers rms), the right positioning of the tip on the electrical contacts and on the thin film and a careful adjustment of the first and second harmonic parameters of the AFM signal in order to analyze the topography and surface potential with high precision, among others. In exchange for these difficulties, one obtains the possibility to measure precisely and locally the electrical contact resistance between the electrodes and the film as well as the morphology of the sample edge.

A special experimental set up was developed in order to carry out measurements of the cross section of the sample. Conductive epoxy resist (see Chapter 2.1.2.6.) was employed to connect two 50 µm diameter gold wires on the top and bottom gold electrodes of the film. Afterwards, the whole sample with the contacts was sandwiched between two pieces of glass of 500 µm thickness in order to gain access to the cross section of the sample for its measurement with the tip of the AFM. The pieces of glass were glued with Crystalbond™ to an alumina substrate, which was also glued to the AFM holder. Finally, the two gold wires were connected to two gold pads where other electrical wires made connection to a voltage source, which was in charge of passing current through the Bi_2Te_3 film. Figure 4.13 shows schematically the experimental set up described above.

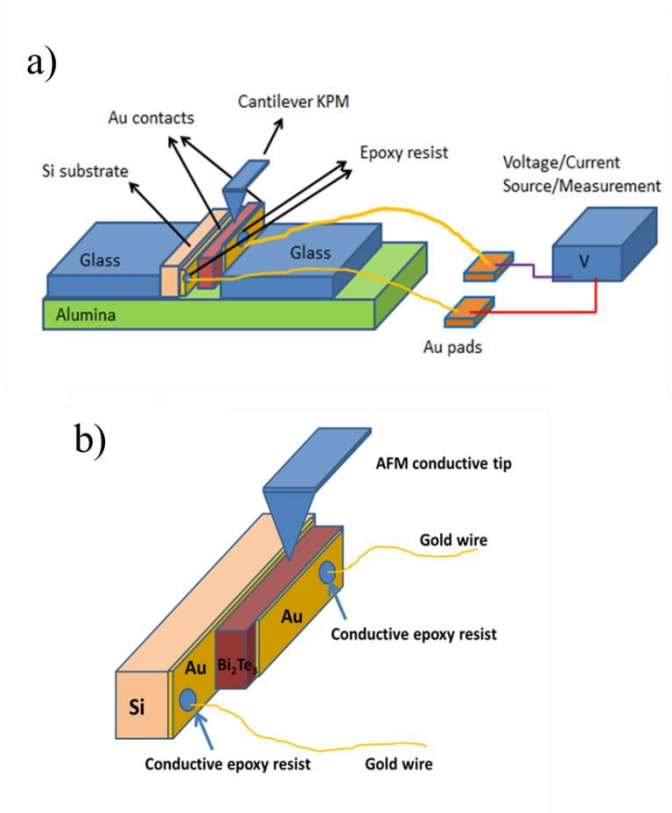

Figure 4.13. (a) Schematic set up of the experimental system and (b) the film in more detail. The sample is sandwiched between two gold electrodes, placed on a Si substrate, and it is positioned vertically thanks to two 500μm pieces of laboratory glass. This system is held on an alumina substrate which is pasted on the AFM holder. A voltage source is in charge of passing a current through the sample. The KPM tip scans the sample in the current direction, i.e. in perpendicular direction to the plane of the electrodes. Figure taken from reference [43].

It is necessary to cut along the thickness of the film in such a way that the resulting surface is smooth enough to carry out the KPFM measurements (with a roughness on the order of nanometers), so one can achieve access to its cross section. Moreover, this cut has to maintain the gold of both surfaces of the film without damaging it, i.e. as unaltered as possible. Different ways of fulfilling these requirements were tried. As a first approach, the sample was broken controlling the

cut with a previous scratching of the silicon substrate with a diamond tip. However, this resulted in a shearing effect [45]. This is caused by the difference of the Young and Poisson modulus of the whole sample, which is mainly dominated by the Si substrate (hardness number of around 7) while the Bi_2Te_3 film is quite soft (hardness number of around 2.5). Moreover, this cutting procedure gave rise not only to a non-perpendicular cut of the film, but also the interface between the bismuth telluride and the silicon substrate was not smooth enough to be measured, making not possible to detect the gold layers with the AFM.

As a second approach, an ulterior polishing of the cross section was made after the sample was broken at the "Centro de Microscopía de la Universidad Complutense (UCM)". For that purpose, in order to have the film in between two substrates of the same hardness, another silicon substrate of similar dimensions was glued on top of the thin film sample. Afterwards, the whole sandwich was embedded in a resist and it was polished with 0.1 μm and 0.05 μm diamond particles. However, during the polishing tension on the surface of the sample resulted in some of the thin film detaching from the bottom gold layer and the voltage drop along the thin film, when using the gold layers as electrodes, was larger than expected. At the same research center, an attempt to cut the film with a thin diamond blade was carried out, but the tensions suffered during this cutting process resulted in partial detachment of the film from the substrate, making it not ideal for AFM measurements.

Finally, it was decided to improve the first method by submerging the sample into liquid nitrogen before breaking. This process resulted in a flatter cross section of the sample, and it didn't required further polishing. Even though, the Au-Bi_2Te_3 interface close to the Si substrate presented in all cases a step that emerged between materials, as expected from the different mechanical properties of the sample, where the tip could hook on or scratch. Nevertheless, it is smaller than the situation where the sample was broken without immersing it into liquid nitrogen. The average surface roughness of the Bi_2Te_3 area and its areas closer to the interfaces were around 50 nanometers, which assure accuracy when measuring, but the roughness

for a full edge scan ranges in the micro-meters due to the steps found in the Au-Si and Au-air interfaces.

4.2.1.2. Kelvin Probe Microscopy measurements.

As it was explained in Chapter 2.2.1.2., the first harmonic of the force acting at the tip in KPM measurements gives information of the sample surface potential. This term can be written as,

$$F_\omega = \frac{\partial C}{\partial z} U_{ac} U_{dc} \tag{4.12}$$

where U_{dc} is the *dc* voltage that can be expressed as, $U_{dc} = U_{feedback} - \phi$, being ϕ the surface potential and the $U_{feedback}$ the *dc* voltage applied by the AFM in order to fulfill the $F_\omega = 0$ condition, which makes possible to determine the sample surface potential [40].

The sample consists of gold electrodes, the Bi_2Te_3 film and the Si substrate that have different work functions. Consequently, one must be able to detect differences in the surface potential given by the KPM image. Figure 4.14 shows a simplified profile of the expected surface potential for unbiased and biased situations.

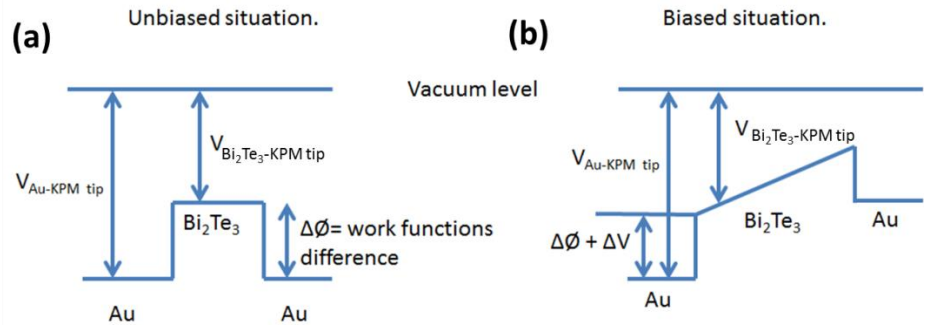

Figure 4.14. Energy bands diagram of the gold electrodes and Bi_2Te_3 film at (a) unbiased and (b) biased situation. Figure taken from reference [43].

In the unbiased situation, the KPM measures the work functions of the Bi_2Te_3 thin film and the gold electrodes. However, when a difference of voltage is applied between electrodes (biased situation), the surface potential measured by the tip does not correspond solely to the work function of the material scanned, but also the voltage of the scan area.

Firstly, it is mandatory to measure the work function difference between both materials obtained in the unbiased case. Once it is done, one can subtract it in the biased situation and measure the voltage drop in the Au-Bi_2Te_3 interface. This is essential to measure the contact resistance between the gold electrodes and the Bi_2Te_3 thin film.

Even though the least aggressive way of breaking the sample was used, its full topographic profile has a significant lean. Moreover, a full KPM scan of the sample should be avoided due to the relative large thickness of the Bi_2Te_3 thin film (4.5 µm) in comparison to the size of the electrodes (100 nm). Otherwise one would not have enough resolution to study the area of interest, which involves the interface between the electrodes and the sample that is the region that gives information about the contact resistance. With this working procedure, a more accurate detection of the KPM signals can be obtained, which involve a more accurate determination of the Au-Bi_2Te_3 interface electrical contact resistance.

Figure 4.15a shows a topographic image of the full cross-section of the Au/Bi_2Te_3/Au/SiO_2/Si (thin film sample held on Si substrate). Figure 4.15b, 4.15c and 4.15d are KPM pictures of the unbiased case focused on the Au- Bi_2Te_3 interfaces and the Bi_2Te_3 film. A profile of the surface potential profile is observed from where the work function difference between materials is obtained. Although an accurate difference between work functions should be taken under vacuum conditions, the work function difference that was determined experimentally under atmospheric conditions, around 140 mV and 180mV in the Au-Bi_2Te_3 interfaces close to air and Si respectively, is in the order of the theoretical values of the work function difference between the gold, 5.3-5.45eV [46], and Bi_2Te_3, 5.3eV [47]. Great care was taken in the KPM measurement of the interface Au- Bi_2Te_3 because of

the similitude between their work functions and the step that emerged between materials when breaking the sample, as was explained previously.

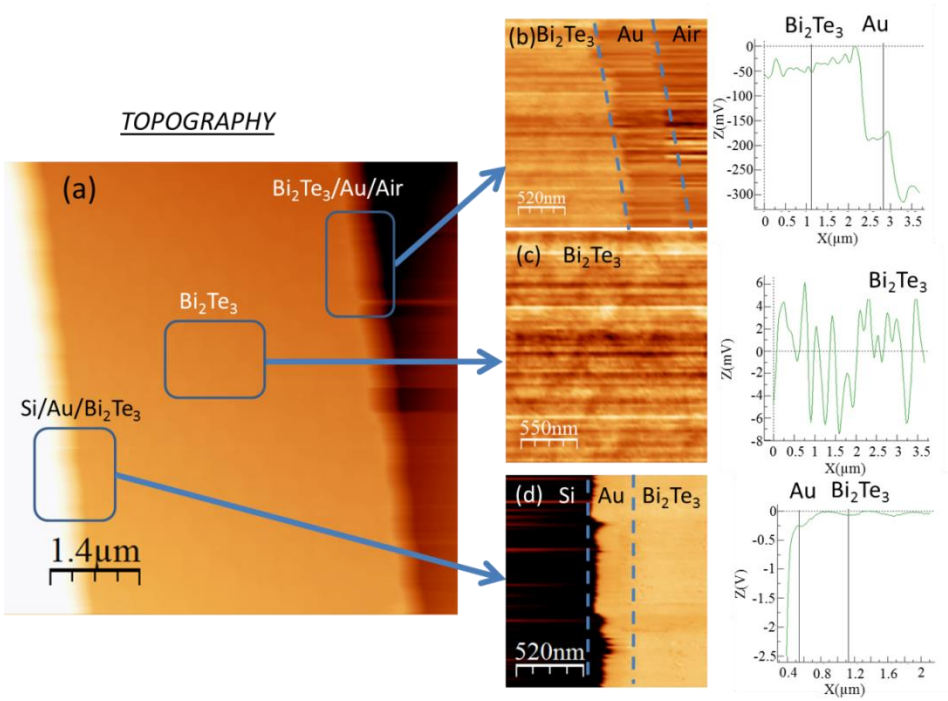

Figure 4.15. (a) Topographic picture of a 4.5µm edge of the Bi_2Te_3 thin film with gold electrodes on a SiO_2 substrate. (b) Inset picture shows a zoom of a KPM image, when the bias voltage is 0V, of the, air, gold electrode and Bi_2Te_3 thin film. The graph reveals that difference between the surface potential of the electrode and the Bi_2Te_3 thin film is of the order of difference between work functions, 140 mV. (c) Inset KPM picture is a zoom of the Si substrate, the gold electrode and the Bi_2Te_3 thin film. Again, the difference of surface potentials, at bias voltage equals 0V, is of the order of the difference between work functions as expected, 180mV. Figure taken from reference [43].

After the work function difference was measured, multiple scans at different voltages of the same interface of Au-Bi_2Te_3 were taken. The applied voltages ranged between 0.05 V and 0.3 V in steps of 0.05 V. It was proceeded to measure the difference of surface potential between the gold and the Bi_2Te_3 thin film for the biased cases. Then, the work function difference previously measured at zero volts, $\Delta\emptyset_{Au-Bi_2Te_3}(V_{applied} = 0)$, was subtracted to it, $\Delta\emptyset_{Au-Bi_2Te_3}(V_{applied} \neq 0)$, in order to obtain the voltage drop at the interface, that is,

$$\Delta V_{interface} = \Delta\emptyset_{Au-Bi_2Te_3}(V_{applied} \neq 0) - \Delta\emptyset_{Au-Bi_2Te_3}(V_{applied} = 0) \quad (4.13)$$

The passing current through the sample was recorded. Then, the contact resistance can be determined using Ohms law,

$$R_{contact} = \frac{\Delta V_{interface}}{I} \quad (4.14)$$

Figure 4.16a and 4.16b show the measuring procedure and the signal obtained when a voltage of 0.1 V was applied between electrodes. A distinction between the surface potential of the gold electrode and the Bi_2Te_3 thin film is clearly observed.

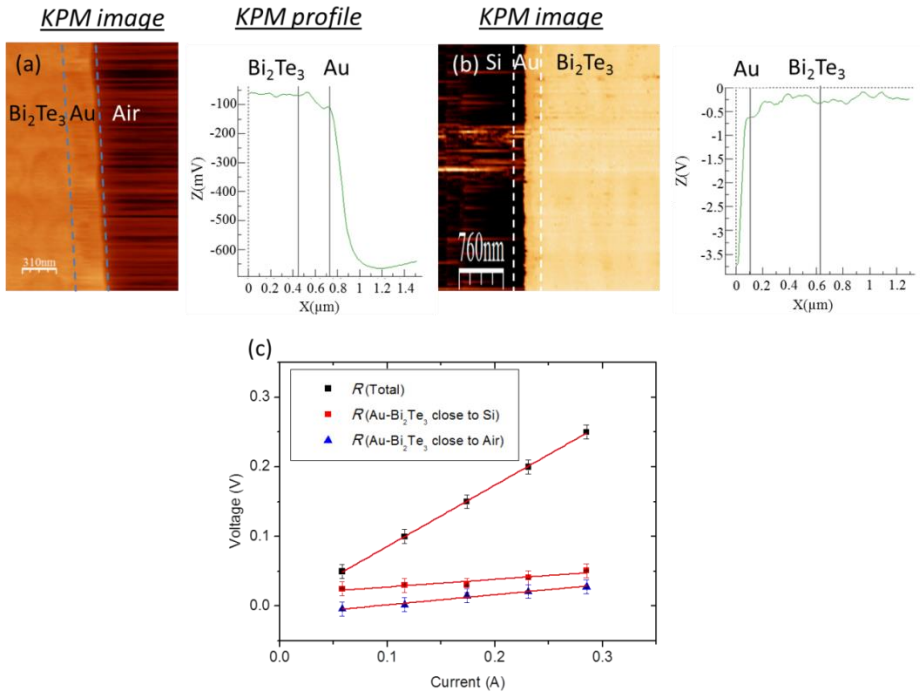

Figure 4.16. (a) KPM image and surface potential profile of the gold electrode and Bi_2Te_3 thin film close to air when is biased at 0.1 V. (b) KPM image and surface potential profile of the gold electrode and Bi_2Te_3 thin film close to Si substrate when is biased at -0.1 V. (c) Analysis of the electrical contact resistance after the analysis of the difference of voltage between the gold and Bi_2Te_3 thin film for different KPM images, that corresponds to biased voltages ranging from 0 V to 0.25 V. The contact resistance of the side close to the SiO_2 substrate, where the thermoelectric thin film started to grown via electro-deposition, is smaller in comparison to those closer to the air, which was deposited after the thin film was grown by gold evaporation. Figure taken from reference [43].

The obtained results are presented in Figure 4.16c. On the one hand, the total resistance of the system is $0.87 \pm 0.01\Omega$, measured from the *I-V* curve obtained from the voltage/current source/multimeter. One must take into account that this resistance includes the intrinsic resistances of the different materials and all contact resistances present in the experimental setup, such as the epoxy contact resistances, wires

resistances, etc. On the other hand, the KPM measures directly and locally the contact resistance at the Au-Bi_2Te_3 interfaces without being influenced by other electrical resistances of the circuit. At the measured voltages, the whole system and the contacts presented an ohmic behavior as shown in Figure 4.16c. The electrical contact resistance of the interface closer to the air was determined to be $0.15 \pm 0.01\Omega$ while the one closer to the SiO_2 substrate was found to be $0.11 \pm 0.01\Omega$. These results show that the contact between the Au-Bi_2Te_3 interface closer to Si substrate is better than the one made by evaporation on top of the sample. Even though both electrodes are made of gold, one must take into account that the lower electrical resistance interface matches with the area where the Bi_2Te_3 thin film was grown by electrodeposition. This is important, because during this growth process the atoms were able to bond and to organize in the gold in a better way than when they are directly deposited on the thin film via electron beam evaporation.

The electrical resistivity of Bi_2Te_3 thin film is around 1.5 $\mu\Omega \cdot m$ [48]. Considering a Au/Bi_2T_3/Au sample area of 0.5 mm^2 and a thickness of 4.5 µm, it results in an electrical resistance of around 15 µΩ. This resolution cannot be reached by our KPM for this sort of measurement. The resulting total electrical resistance of the whole system was determined to be $0.87 \pm 0.01\ \Omega$. If subtracting the electrical resistances of the contacts, $0.15 \pm 0.01\ \Omega$ and $0.11 \pm 0.01\ \Omega$, a resistance for the rest of the system of $0.61 \pm 0.02\ \Omega$ was obtained. This resistance becomes affected by the wire resistances, the resistances that arose from contacting the gold wires to the gold pads, the electrical wires used and the contact resistances from the epoxy resist that was used to connect gold wires to the electrodes of the thin film sample. Since the resistance of Bi_2Te_3 is negligible, it was observed that the total resistance measured with a two probe system is largely influenced by other electrical resistances. A reduction of this resistance might be achieved with different approaches, like for example by the improvement of the wire contacts to the electrodes of the sample using a ball bonder device. However, the electrical contact resistance at the interface should always be taken into account as it cannot be removed.

4.2.1.2. Analysis and Discussion.

Contact resistances are consequence of defects, impurities or variation in the crystal size and orientation, formation of oxides or secondary phases at the interface between two different materials, among others. As it is mentioned in reference [49], the growth of a semiconductor on top of a metal, or vice-versa, does not usually involve an energy gap at its interface. However, the differences on the lattice parameters of the materials generate strains between layers, causing the dislocation of atoms and the formation of defects. Moreover, there might be also variations in the stoichiometry of the thermoelectric compounds, as well as diffusion of the metal into the semiconductor. As a consequence, the transport of heat and electricity through the interface becomes affected considerably because of these surface features. Additionally, the cases in which a contact is not added in high vacuum just after the film is grown should be contemplated as it involves the formation of oxide/carboxylate/hydroxide-type phase after the film is exposed to air before adding the metal contact.

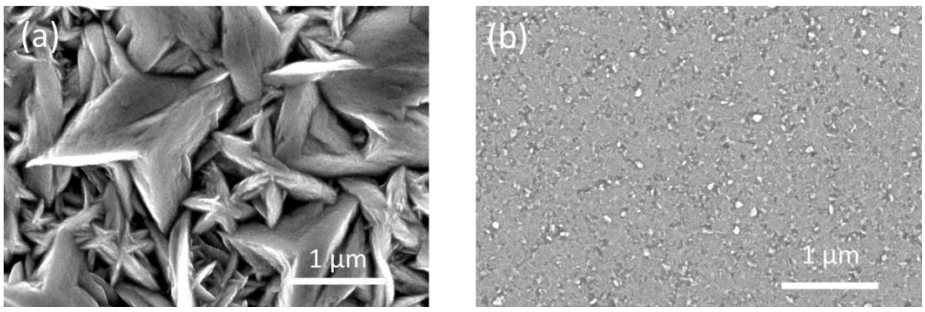

Figure 4.17. SEM micrograph of a free-standing Bi_2Te_3 electrodeposited films showing of the different morphology between (a) the top part and (b) the bottom part of the film. Figure taken from reference [43].

In macroscopic devices, the values of the electrical contact resistance between a semiconductor and a metal are usually found between 10^{-8} and 10^{-9} Ωm^2. However, in thin film samples, the resistances are expected to be smaller [50]. As an example, assuming no energy gap at Bi_2Te_3-metal interface, the electrical contact resistance was predicted in reference [49] to be around 10^{-12} $\Omega \cdot m^2$. This value can be compared to the ones that we have determined experimentally, $(2,8\pm0,1)\cdot10^{-8}$ $\Omega \cdot m^2$ and $(3,8\pm0,1)\cdot10^{-8}$ $\Omega \cdot m^2$ for the interface closer to SiO_2 substrate and the interface closer to air, respectively. These results are also comparable to the ohmic contacts desirable for applications in actual devices (around 10^{-9} $\Omega \cdot m^2$) [49 51 52 53 54] . In order to explain this, one has to consider that the growing method used for bismuth telluride films was electro-deposition, which involves a surface roughness[42] larger than the obtained for film grown with high vacuum techniques, such as Molecular Beam Epitaxy (MBE) [55] or Metal Organic Chemical Vapor Deposition (MOCVD) [56] . It is also worth noting the different morphologies of the surface and the bottom of the film. Figure 4.17 shows these differences in morphology of both surfaces of the film, when one of the films is detached from the substrate. Another possible reason could be that the samples are in contact with the atmosphere before the top gold electrode was evaporated, this could lead to an oxidation of the first layers. This might be avoided for samples that are grown in vacuum and straightaway gold coated without taking the sample to air. In order to determine if electrodeposited Bi_2Te_3 films samples oxidized under air exposure, they were studied over one year aging in air by different techniques like micro-Raman, X-ray diffraction and Rutherford backscattering spectrometry (RBS). The results showed no oxygen containing phases within the resolution limit of each technique [57]. So, oxidation seems not to make a difference, in this case.

In summary, the KPM is a powerful technique to determine the interface contact resistance of films, under the right set up. It gives very valuable information that must be taken into account when carrying out electrical measurements of films.

4.2.2. Electrical conductivity of Bi_2Te_3 films out of plane.

In this Section, the four probe method was used to determine the out of plane electrical conductivity of thermoelectric Bi_2Te_3 films grown via electro-deposition process. In bulk Bi_2Te_3 crystals the electric transport is highly anisotropic along directions parallel and perpendicular to the plane[25]. Because of that, a setup to minimize current flow along different directions was designed for the film measurements. For that purpose, film disc-shaped mesas were fabricated with diameters ranging from 120 μm up to 80 μm and with different film thicknesses sandwiched between a common bottom electrode and a disk shaped top electrode for each mesa. While the disk geometry is similar to Cox and Strack, the employment of mesa structures was chosen to minimize current spreading into the in-plane direction of the film. A three-dimensional (3D) finite element model was used to predict the distribution of the electric field in the measured structures and take into account the non-uniform spreading of the current in the electrodes in the vicinity of the probes. The modeling shows that relevant errors could arise in the measured film electrical conductivity if simpler one-dimensional models are employed, unless the electrode thickness and disc diameters are carefully selected.

4.2.2.1. Film fabrication.

The Bi_2Te_3 films were grown through electrodeposition (see Chapter 2), in similar conditions as the one published by C. V.Manzano *et al.* [23] . It resulted in films with three different thicknesses, 4.6 ± 0.3 μm, 6.4 ± 0.7 μm and 7.2 ± 0.4 μm on 150 nm Pt layer held on Si substrates. Afterwards, a lithography process was used to pattern discs with 120 μm to 80 μm diameters on top of the films in order to reduce the spreading of the electrical field across the film when passing a current across them. In this process, a photoresist (S1805) was spun at 5,000 rpm for 60 seconds, and pre-baked for one minute on a hot plate at 115ºC. Then, the photoresists was exposed to ultra-violet light under

the presence of a photomask to pattern the discs. Afterwards, the developer MF-319 was used for 60 seconds to remove the exposed photoresist. Thereafter, 150 nm of gold was deposited on top of the sample by electron beam evaporation.

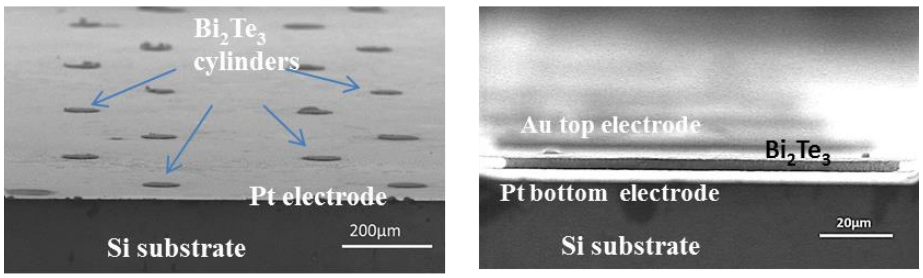

Figure 4.18. a) Overview of patterned areas of the film and electrode structures obtained after the lithography process and mesa attack. b) Lateral view of one 100 µm diameter test structure. Figure taken from reference [58].

Finally, the photoresist was removed with acetone and it was proceeded with a mesa etching with dilute nitric acid (1:3) for 5 minutes. Figure 4.18 shows Scanning Electron Microscopy (SEM) images of the discs obtained after this process.

4.2.2.2. Four probe station measurements.

A four probe station (4200-SCS Parameter Analyzer-Keithley) was used to carry out the electrical resistance measurements of films. Firstly, the electrical conductivity of the Pt and Au electrodes at the bottom and top sides of the film, respectively, were determined with the Van der Pauw (VdP) technique[28]. For that purpose, two samples were prepared that consisted of 150 nm of Pt and Au, equivalent to the electrodes size of the film-discs, which were evaporated on squared (5 mm x 5 mm) Si wafers with oxide on its surface. According to the VdP method, the probes of the station were positioned at the corners of the sample and the current-voltage curves measured as described in

reference [28]. The electrical conductivity for the Pt and Au film were determined to be $(3.1 \pm 0.2)\cdot 10^6$ S/m and $(3.6 \pm 0.1)\cdot 10^7$ S/m, respectively.

Afterwards, it was proceeded to measure the resistance of the Bi_2Te_3 discs. For that purpose, it was positioned carefully two probes on top of each disc while the other two were positioned on the bottom electrode. Figure 4.19a shows a schematic view of the experimental set up. Figure 4.19b shows an optical image of the position of the probes on a 120 μm diameter disc. Between the top and bottom current probes, a current ranging between $-1\cdot 10^{-4}$ A and $+1\cdot 10^{-4}$ A was applied across the sample while the voltage drop was recorded by the two voltage probes. For every disc, *I-V* curves were recorded and the electrical resistance determined from the slope of the curve.

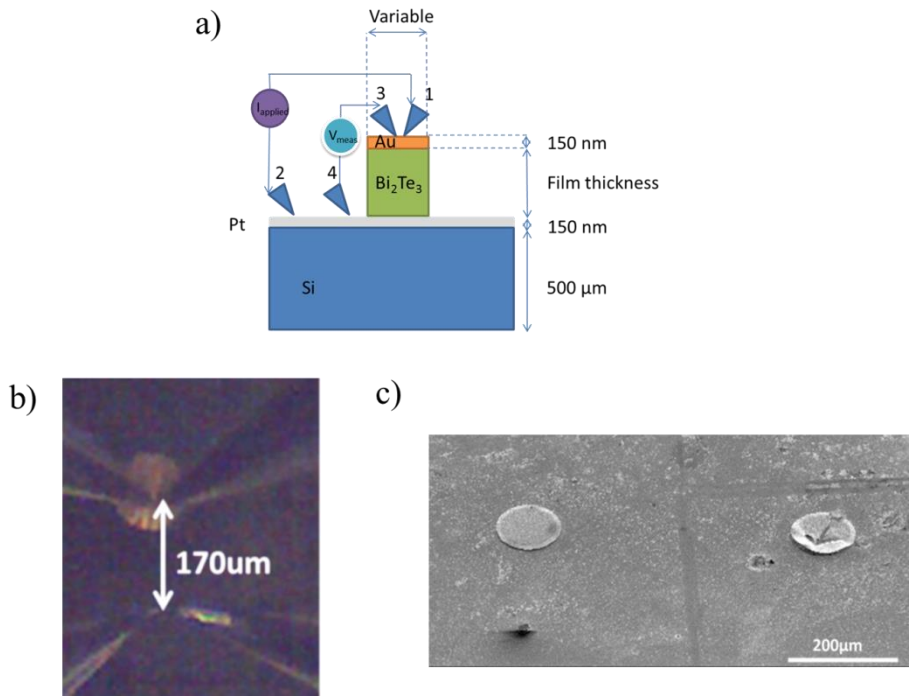

Figure 4.19. a) Schematic view of the experimental set-up with the four probe station. b) Optical microscope image of the four probes positioning on a 120 μm disc-film whose thickness was 4.6 μm. The separation between the top and bottom probes was 170 μm. c) SEM picture of two measured discs. The disc on the left side of the picture

looks in good conditions after four probe measurements while the one on the right appears scratched and broken. The data extracted from discs under these conditions are no longer considered in the subsequent analysis. Only the test structures that remained unaltered after each measurement were taken into consideration for the analysis. Figure taken from reference [58].

Optical images of the positions of the probes and the test structures were taken during the *I-V* measurements in order to determine the probes separation distance (Figure 4.19b). After the *I-V* measurements, SEM images were taken from the listed samples in order to check the status of the test structures after the probes were positioned on them. Figure 4.19c shows one of these SEM images in which one can observe that some structures were too scratched or broken to be considered.

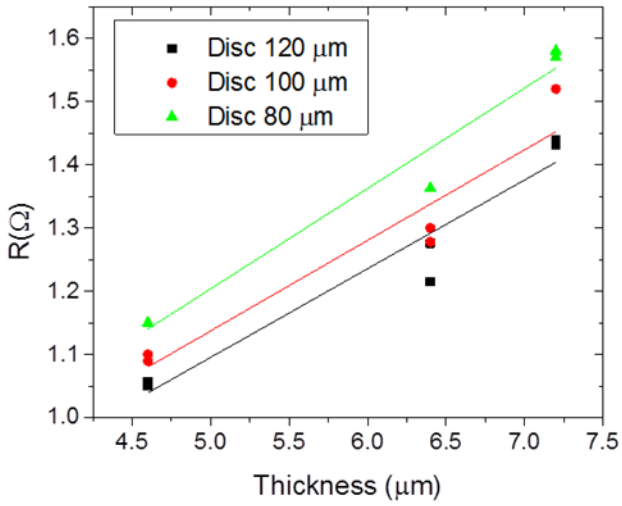

Figure 4.20. Electrical resistances of different disc diameters versus the thickness of the films. The black squares, red circles and green triangles correspond respectively to 120 µm, 100 µm and 80 µm diameter discs. For 4.6 µm, 6.4 µm and 7.2 µm thicknesses, top to bottom probes distances were around 170 µm, 219 µm and 290 µm, respectively. Straight lines correspond to the linear fit of the data. Figure taken from reference [58].

The electrical resistances (R_{exp}) obtained experimentally were plotted versus the thickness of the films. Figure 4.20 shows these resistances for three different film thickness and disc diameters measured. A linear fit was drawn through the data. A deviation from from linearity is observed in all cases, which indicates 3D spreading effects. This implies that the one dimensional model that is usually used to calculate the electrical conductivity of high conductive films is not accurate enough and another approach, such as 3D modeling, should be used. This effect should be taken into account and it is discussed later in the next Section.

4.2.2.3. Analysis and Discussion.

A three dimensional COMSOL® Multiphysics model was developed to simulate the electrical transport measurements of the test structures and to determine the electrical conductivity of the Bi_2Te_3 films.

The geometry of the model consisted of an insulating substrate representing the oxide coated Si wafer ($\sigma = 1 \cdot 10^{-12}$ S/m) with a 150nm layer of Pt on top with an electrical conductivity of $(3.1 \pm 0.2) \cdot 10^6$ S/m, which was determined from the VdP measurements as mentioned above. Then, the thermoelectric film with a thickness equivalent to each experimental sample was built on top of the Pt electrode, followed by an Au electrode of 150 nm thickness, whose electrical conductivity $(3.6 \pm 0.1) \cdot 10^7$ S/m was also determined by the VdP technique.

Afterwards, two probes with 0.5 μm radius were positioned on top of the disc, while the other probes were positioned at the bottom electrode separated by a known distance from the top probes. The separation between the top and bottom probes was obtained from the optical pictures of each discs that were taken while carrying out four probe measurements (Figure 4.19b). Figure 4.21a shows the geometry of the COMSOL® model, while Figure 4.21b and 4.21c show the voltage distribution at the top and bottom electrodes, respectively.

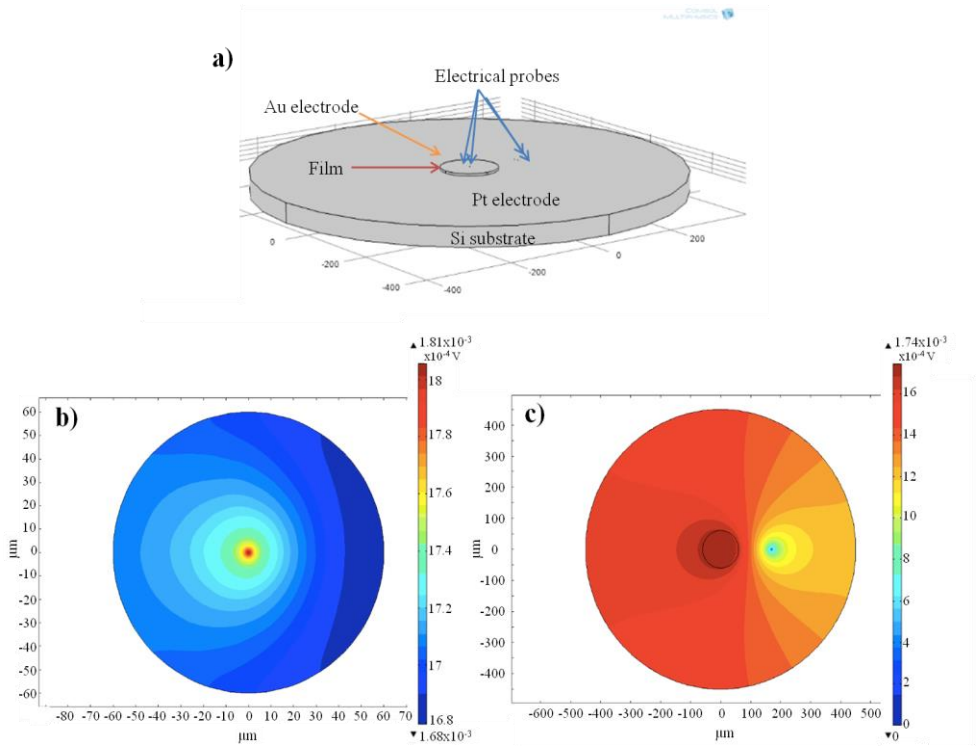

Figure 4.21. a) Model geometry of the simulation. Voltage slices of the b) top and c) bottom electrodes, on top and underneath the sample respectively. The non-uniformity of the electrical voltage is indicated by the non-uniformity in color, particularly near the current probes locations. Figure taken from reference [58].

The COMSOL® module "electrical currents" was used to define a current source at one of the top probes while a grounded probe is defined at the bottom. The voltage difference was measured with the other two probes. Moreover, the effects of the electrical contact resistance must be also taken into account. To this end, these effects were simulated using thin contact impedances at the boundaries between the film and both electrodes, where one must define the resistivity and thickness of the contact. Consequently, this theoretical model presents two unknown variables that must be fitted from experiments, i.e. the electrical conductivity of the film and the contact resistivity. For each sample, we varied each of these parameters within

a range of possible values until the simulated electrical resistance, $R_{simulated}$, matched with the one obtained experimentally, R_{exp}, with less than 5% of difference. For simplicity, for each value of contact resistivity within the search range it was fitted for the film electrical conductivity.

Figure 4.22 shows the fitted electrical conductivity of the film versus the electrical contact resistivity for the different film thicknesses and diameters of the discs.

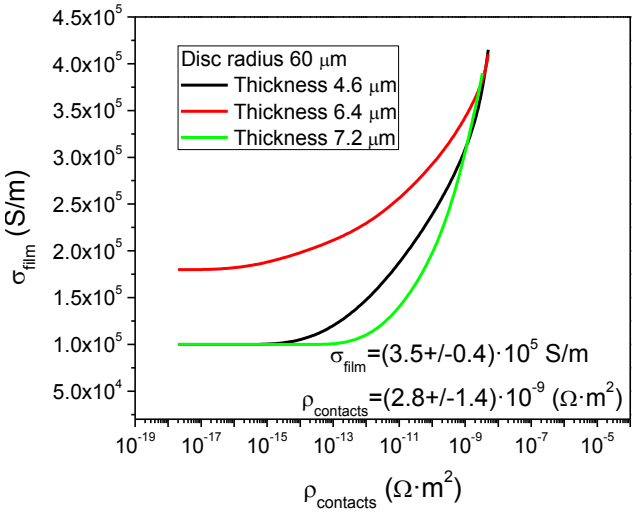

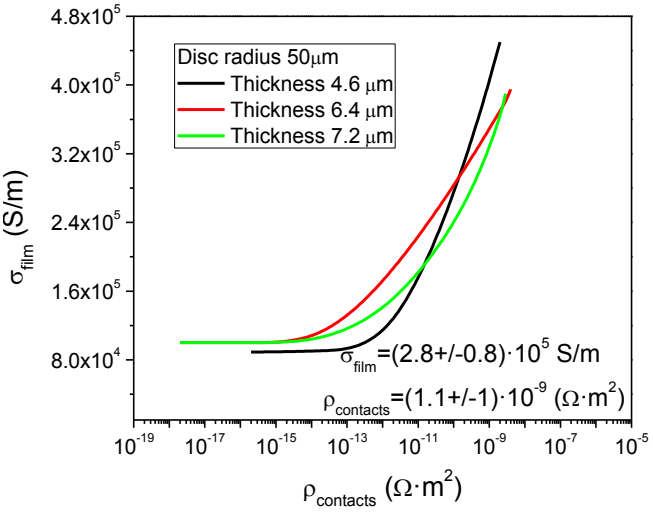

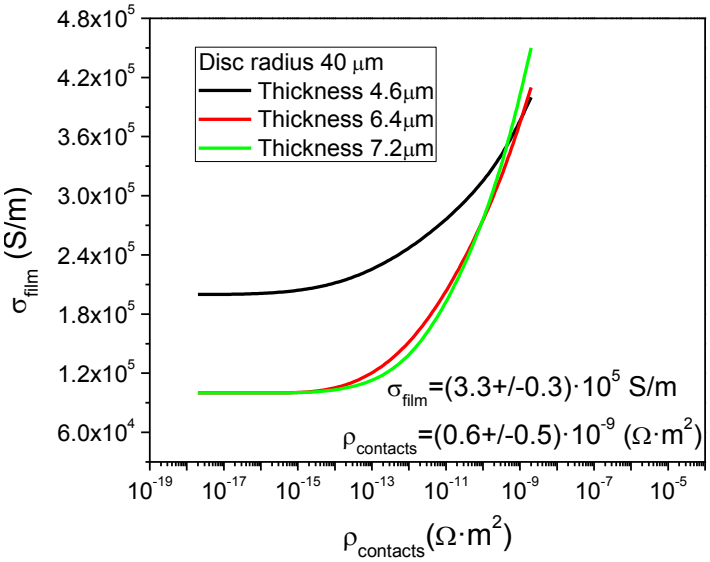

Figure 4.22. Fitted electrical conductivity of the film (σ_{film}) versus the contact resistance per unit area ($\rho_{contact}$) for 4.6 μm, 6.4 μm and 7.2 μm film thickness determined for a set of a) 60 μm, b) 50 μm and c) 40 μm disc radius samples. For each disc radius the intersection of the curves provides a fitted value for electrical conductivity of the film and the contact resistivity. Figure taken from reference [58].

While measurements performed for just one disc diameter might induce a relatively large uncertainty (see Figure 4.22), it was considered individually the electrical conductivity of the film and contact resistivity per unit area of each diameter disc measured and performed a statistical average. As a result, the averaged electrical conductivity for the electro-deposited Bi_2Te_3 was determined to be: $\langle\sigma_{Bi_2Te_3\_film}\rangle = (3.2 \pm 0.4)\cdot 10^5$ S/m, while the averaged contact resistivity was $\langle\rho_{contact\_resistance}\rangle = (2 \pm 1)\cdot 10^{-9}\ \Omega\cdot m^2$. The uncertainty of the fitted results was obtained from the difference between the intersected points. Finally, the effect of the anisotropy of the film was also considered in the COMSOL® simulation. For that purpose, it was performed simulations with an in plane electrical conductivity of $\sim 7\cdot 10^4$ S/m, which was determined experimentally, but the results showed a

variation of less than 1 % in comparison to the ones obtained without anisotropy.

In reference [25] the electrical conductivity of single crystal bulk Bi_2Te_3 for [1 1 0] and [0 0 1] directions resulted to be ~ $3 \cdot 10^4$ S/m and $1 \cdot 10^5$ S/m, respectively. It involves an anisotropy factor of ~ 4. Our film presents an electrical conductivity out of plane direction [0 0 1] of $(3.2 \pm 0.4) \cdot 10^5$ S/m, which is around 3 times higher than reported for the bulk single crystal [25], but the anisotropy factor with respect to the measurements performed in the in-plane direction is ~4.5, which is on the same order of magnitude of the anisotropy factor reported for a bulk single crystal. This can likely be explained by the high orientation of the electrodeposited Bi_2Te_3 films along the [1 1 0] direction in the in-plane of the film, as can be observed in Figure 4.23, where only the Pt/Si electrode and the (1 1 0) and (2 2 0) diffraction maxima from Bi_2Te_3 can be identified. The (1 1 0) Bi_2Te_3 maxima is narrow indicating a high crystallinity. Finally, it is also important to take into account that the electrochemical deposition technique uses an electric field during the growth. The electric field can favor the growth of Bi_2Te_3 grains oriented along the highest electrical conductivity direction.

Regarding the contact resistance, its value was found to be similar to the best resistance per unit area measurements found in literature, which are estimated to be between 10^{-8} to 10^{-9} $\Omega \cdot m^2$ [59, 43]. Moreover, this result is in the same order of magnitude of the one presented in Section 4.2.1., where the contact resistance of the Au-Bi_2Te_3 film was measured with the KPM. The one in that section is slightly larger than the one obtained here but it can be associated to the fact that the film fabricated in Section 4.2.1. is a bit rougher and less optimized than the one measure here. This difference comes from the fact that this film has been grown with pulsed electrodeposition while the other one was fabricated with continuous electrodeposition. This implies that the pulsed electrodeposited films are more smooth, more compact, more textured and with bigger crystal size.

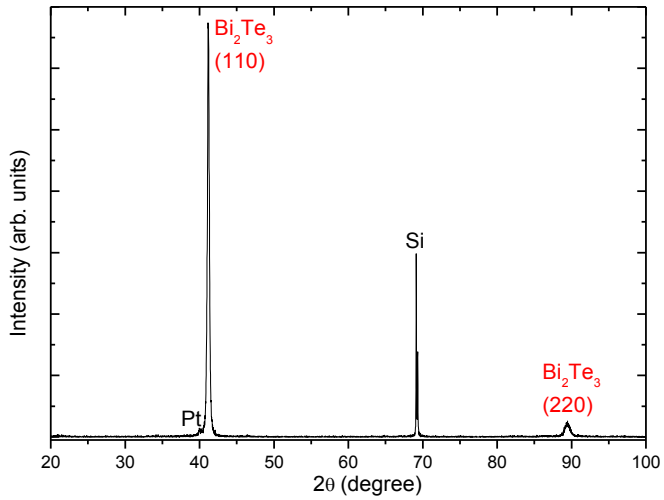

Figure 4.23. Example of X-Ray diffraction of highly oriented Bi_2Te_3 electrodeposited films used in this study. Figure taken from reference [58].

Next it was investigated under what conditions a simpler one-dimension electrical transport model could be used to fit the experimental results accurately. The one-dimensional (1D) transport is expressed mathematically as $= \rho \cdot \frac{l}{A}$, where ρ the electrical resistivity, R is the electrical resistance, and l and A the length and area of the sample, respectively. This model involves that the measured resistance should be linear with the thickness of the film, which is not the case in Figure 4.20. To find the reason for this trend the COMSOL Multiphysics® results were used in order to determine the voltage drops across the top electrode, the film, and the bottom electrode. Then the COMSOL Multiphysics® voltages were used to calculate the electrical resistance contributions due to each layer and these results were compared with predictions of the 1D model. The electrical resistance of the film expressed with the 1D-theory yields,

$$R_{total} = \rho_{top\ elc} \cdot \frac{l_{elec}}{A_{elec}} + \rho_{film} \cdot \frac{l_{film}}{A_{film}} + \rho_{bot\ elc} \cdot \frac{l_{elec}}{A_{elec}} \qquad (4.15)$$

where R_{total} is the total resistance across film and electrodes, $\rho_{top\ elc}$, $\rho_{bot\ elc}$ and ρ_{film} the electrical resistivity of top and bottom electrodes and film, respectively, and l_{elc} , l_{film} and A_{elc}, A_{film} are the length and the area (perpendicular to the current direction) of the electrodes and the film, respectively.

Figure 4.21b shows that at the top electrode, the current probe with 0.5µm radius causes a necking effect that prevents a full uniform voltage distribution of the surface. The thicker the electrode is, the more uniform the voltage on the surface is. On the one hand, Figure 4.24a shows the voltage drop across the film and the electrodes in its cross plane direction. On the other hand, Figure 4.24b displays the voltage obtained along the radius of the film at its top and bottom faces for a 4.6µm thickness film. From these figures, a discrepancy between the three-dimensional COMSOL Multiphysics® simulation and the 1D theory of around 1% was detected for the Au (first term in Equation 4.15) and Pt (third term in Equation 4.15) electrodes with 150nm thickness, while a discrepancy of around 11% was found for the thermoelectric film contribution (second term in Equation 4.15). Even though there seem to be so far a good agreement between theory and simulation, these elements contribute less than 5% to the total resistance obtained between probes. That is because the larger contribution to the total resistance comes from the Pt electrode resistance along its in-plane surface, between the center of the disc and the bottom probes. In Figure 4.21c the voltage drop at the bottom electrode from the center of the film to the grounded probe positioned at 170 µm is shown. This contribution is not contemplated in the 1D-analysis (Equation 4.15) and has a considerable impact in the results. In order to consider the effect of the field spreading and the resistance influence at the bottom electrode, one must solve the analytical expression coming from Laplace's equation for constriction resistance obtained for non-quantum contacts [60]. Whilst this analytical study might be complicated, the 3D COMSOL Multiphysics ® simulation takes this effect already into account simplifying the analysis.

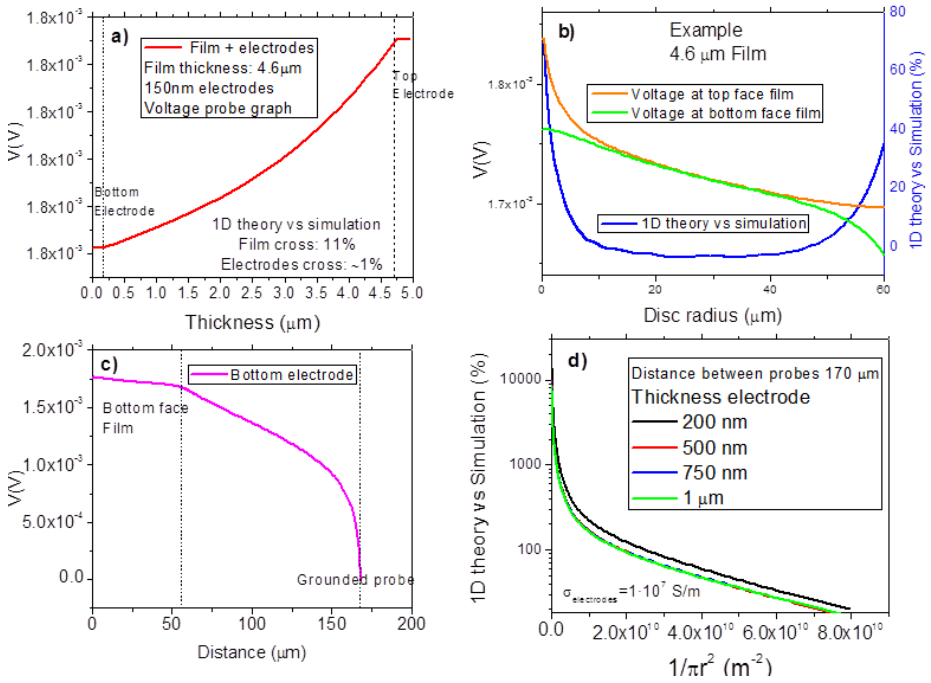

Figure 4.24. a) Voltage drop just across the electrodes and the film from the top voltage probe, separated 3μm from the top current probe, to the bottom of the sample. A discrepancy of 11 % and 1 % respect to the 1D theory is observed for the film and electrodes, respectively. b) Voltage along the film radius at its top and bottom faces. The discrepancy between the 1D theory and the simulation varies along this distance. c) Voltage drop along the bottom electrode from the center of the film disc to the grounded probe. d) The discrepancy between the simulation and 1D-theory results for the electrical resistance of a 4.6 μm thickness sample with an electrical conductivity of $1{\cdot}10^5$ S/m and both electrodes with the same variable thickness but same electrical conductivity, $1{\cdot}10^7$ S/m. The distance between top to bottom probes is 175 μm. Figure taken from reference [58].

In order to find out if the discrepancy between the 1D model and COMSOL can be alleviated by using electrodes with larger thicknesses, Figure 4.24d shows the difference between the simulation and the 1D theory calculated for a 5 μm film with an electrical conductivity of $1{\cdot}10^5$ S/m and electrodes with identical thicknesses and electrical conductivity of $1{\cdot}10^7$ S/m and distance (kept constant for all

simulations in Figure 4.24d) between top and bottom probes of 170 μm. The percentage of discrepancy between theory and simulation has been calculated according to the expression,

$$1D\ Theory\ vs\ Comsol\ Simulation(\%) = \left(\frac{R_{theory} - R_{simulation}}{R_{theory}}\right) \cdot 100 \quad (4.16)$$

where $R_{theory} = \rho_{film} \cdot \frac{l_{film}}{A_{film}}$ is the resistance of the film calculated from the 1D theory while $R_{simulation}$ is the resistance obtained from the simulation.

In Figure 4.24d it is shown that the discrepancy reduces monotonically in all cases when the diameter of the film becomes smaller as well as when the thickness of the electrode increases, as it approaches to the 1D case. As an example, a 2 μm radius film involves a discrepancy between the simulation and the 1D theory of around 14 % and 25 % for the 1 μm and 200 nm thickness electrodes, respectively. Therefore, for a proper estimation of the electrical conductivity of the film with the 1D theory, radiuses below 2 μm and electrodes as thick as possible are desired. Consequently, the effect of the field spreading in the electrodes becomes extremely important, especially at the bottom electrode one, and has an important influence in the total resistance as the radius of the film becomes bigger than 2 μm.

In summary, in this Section is presented a way of measuring the electrical conductivity of films with high accuracy and with the help of a COMSOL Multiphysics® model. The finite element model shows that significant errors could arise in the measured film electrical conductivity if simpler one-dimensional models are employed, as they do not account for the non-uniform distribution of the electric field, among other effects. Furthermore, for high electrical conductivite films, the contact resistances at the interfaces play an important role and must be carefully evaluated. Consequently, either complex analytical expressions or modelling combined with experimental resistance measurements must be used to determine properly the electrical conductivity of the film. Regarding the obtained results, the high electrical conductivity of the measured Bi_2Te_3 films is good news in

thermoelectricity as it enhances the power factor ($\sigma \cdot S^2$) and so contributes to increase the figure of merit (zT) of the material. This improvement has been associated with the high quality of the electrodeposited films, especially in terms of crystalline orientation in the [1 1 0] out of plane direction, which is the one that is considered to contribute with the best transport properties of the Bi_2Te_3 thermoelectric material.

4.3. Electrical property measurements of nanowires.

In this Section, we study the electrical conductivity of Bi_2Te_3 nanowires in- and out- an alumina template. For that purpose, we used different techniques, two probe measurements with a conductive Atomic Force Microscopy (AFM) and measurements on a microchip with the Kelvin Probe Microscopy (KPM). Finally, we observed with KPM oscillations on the surface potential of isolated Bi_2Te_3 that can be related to the topological insulator nature of the material.

4.3.1. *I-V* curves and current maps of Bi_2Te_3 nanowires array.

In this Section, the electrical conductivity of nanowires embedded in a matrix is measured with an AFM in contact mode, which is used to take *I-V* curves of the nanowires and current maps of the samples.

4.3.1.1. Nanowires fabrication.

Bi_2Te_3 nanowires with different diameters were fabricated via pulsed-electrodeposition in similar conditions to reference [23] into porous alumina template (see Chapter 2.1.1.1.). For that purpose, it was first necessary to fabricate alumina templates with different pores diameters, ranging from 45 nm to 250 nm. It was achieved by a two-step anodization process [61] [62] by our group at the Instituto de Microelectrónica de Madrid (IMM-CISC). Then, the nanowires were grown inside of these templates through electrodeposition, which was carried out in a conventional three electrode electrochemical cell using a bi-potentiostat (see Chapter 2.1.1.1.). The porous alumina template is placed on the working electrode, the counter-electrode is a platinum wire and the reference electrode is Ag/AgCl. The solution used to obtain Bi_2Te_3 nanowires is described in reference [42]. Figure 4.25a and 4.25b show SEM images of the top and lateral view of the nanowires embedded in alumina matrix. The nanowires presented a crystalline orientation in the [1 1 0] direction and a homogeneous composition along the length of the nanowire (Bi_2Te_3).

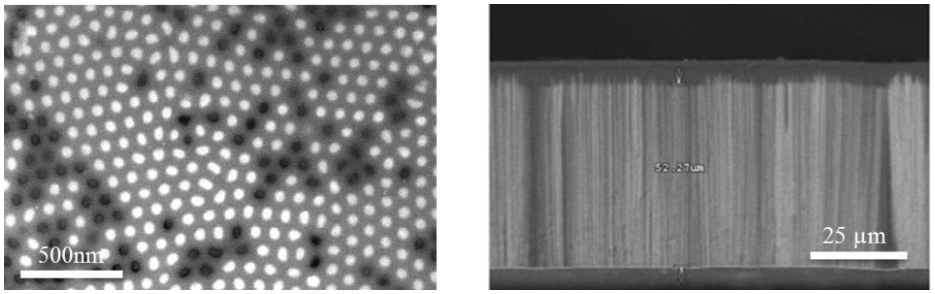

Figure 4.25. a) SEM image of the top view and b) lateral view of 55 nm diameter nanowires. The tips of the nanowires are seen in white in the left picture, after the sample was polished. The lateral view shows the length of the nanowire, which needs to be polished around 10 µm for all the nanowires to reach the alumina surface.

4.3.1.2. Conductive AFM measurements.

In order to measure the electrical resistance of the nanowires, we used an AFM from Veeco® (Lawrence Berkeley National Laboratory) which can apply a difference of voltage between the probe and the holder at which the nanowire array is located. The sensitivity of this device reaches up to femto-ampers (fA). The probe was a pure solid Pt probes (Rocky Mountain Probes®), while the Silicon probes coated with Pt/Ir were discarded as they peeled during the scan, which would involve a worse contact between tip and NW. Figure 4.26 shows the experimental set up used.

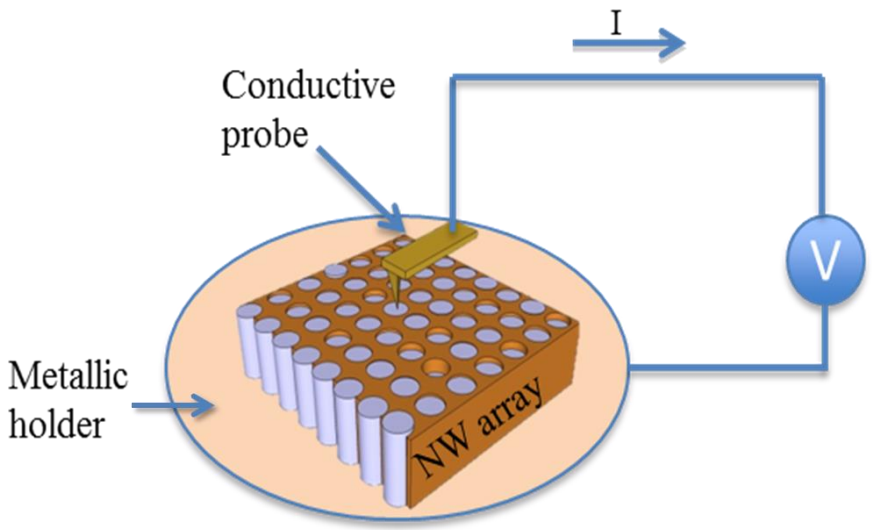

Figure 4.26. Experimental set up where a voltage bias is applied between the probe and the bottom of the sample, while the current across the nanowire is recorded. This experimental set up could be considered as a two probe technique.

With this set up and under the application of a voltage bias, one can scan the surface of the sample and get simultaneously a topographic image and a current map of the surface of the sample. Figure 4.27a and 16 b shows the topography and current map of 250nm diameter nanowires embedded in alumina matrix. Figure 4.27b shows that the alumina does not conduct electricity while the nanowires do.

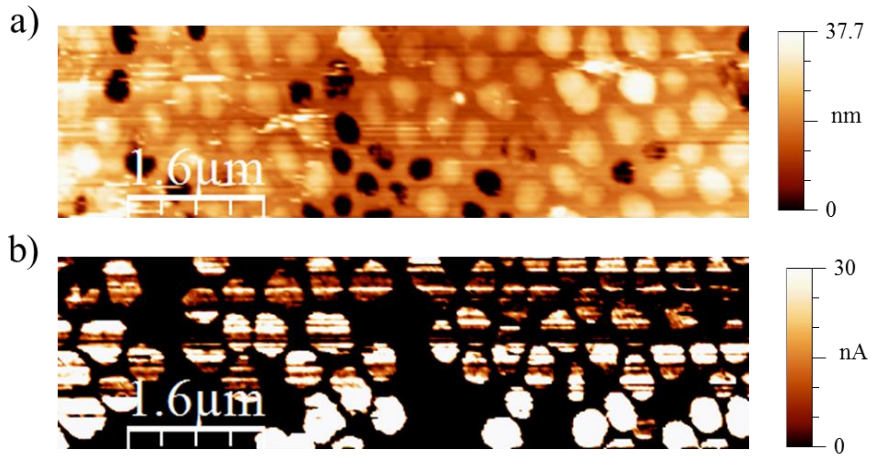

Figure 4.27. a) Topographic and b) current map of 250 nm diameter nanowires (white spots). The black part corresponds to the alumina and empty pores, which is non-conductive.

Once the nanowires were located, the tip was positioned on top of the nanowires whose good conduction was proved by the current map (Figure 4.27b). Then, *I-V* curves can be taken for several NWs. However, before measuring, one must first consider the most adequate set point in order to achieve an ohmic contact and reproducible *I-V* curves. For that purpose, the set point or force applied between the probe and the nanowire was varied from 0.5 V to 3 V. It was observed that for a set point below 2 V, a non-linear contact or Schottky contact happened. From these kinds of curves, the resistance of the nanowire cannot be determined. However, above or equals to a set point of 2 V an ohmic contact occurs and linear *I-V* curves are obtained. Figure 4.28 shows an example of the type of curves obtained for a set point below and above 2 V. From a force curve prior to the measurement, it was obtained a calibration for the probe of 4.347 V/µm with a spring constant of 0.3 N/m. Therefore, a set point of 2 V corresponds to force applied of ~138 nN.

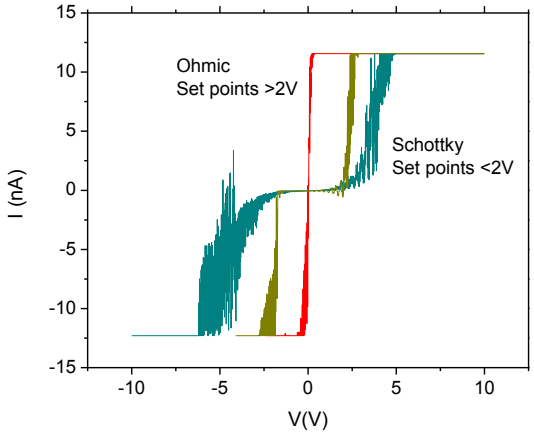

Figure 4.28. *I-V* curves obtained for different set points on top of 250 nm diameter nanowires. An ohmic (linear) behavior is observed for set points above 2 V (red curve), while a Schottky contact usually happens for lower set points, i.e. 1 V and 1.5 V that corresponds to blue-green and olive colored curves, respectively.

From the linear slope of the *I-V* curve in ohmic regime, the total resistance can be determined. This total resistance can be expressed as:

$$R_{NW\,total} = R_{contc} + R_{NW} \tag{4.17}$$

where R_{contc} is the contact resistance between probe and nanowire, and R_{NW} is the nanowire resistance. At each nanowire four *I-V* curves were taken at a set point 2 V. The first *I-V* curve was dismissed as the probe in the first indentation might be in charge of breaking the 2 - 3 nm oxide layer that is formed on top of the wire. The other *I-V* curves taken in each nanowire were considered and a good agreement was observed between them. Figure 4.29 shows an example of the forward and backward *I-V* curve obtained for 250 nm diameter nanowires. From the inverse of the slope, the resistance of the nanowire can be determined. The slopes with linear fit factors (R) between 1 and 0.9 were selected for a better estimation of the resistance.

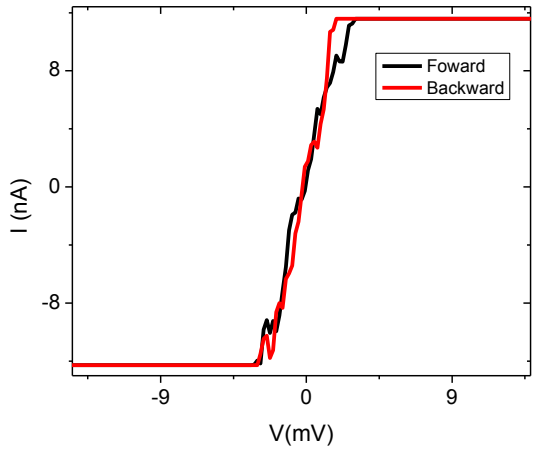

Figure 4.29. Forward and backward *I-V* curves for 250 nm nanowires.

We took more than twenty *I-V* curves with ohmic behavior for each diameter nanowire sample and determined the averaged total resistance for each of those, i.e. nanowire resistance plus contact resistance (Equation 4.17). Then, the averaged total resistance, $< R_{NW} >$, obtained for each nanowire diameter was plotted versus the L_{NW}/A_{NW} , where L_{NW} is the length and A_{NW} the area of the nanowire (Figure 4.30). Assuming that for the range of NW diameters studied the electrical conductivity remains equals, because of the mean free path of electrons in Bi_2Te_3 NWs is below its diameter (~40 nm[63]) , the slope of this graph should give the electrical resistivity of the nanowires while the contact resistance can be obtained from the interception of the linear fit with the *y*-axis.

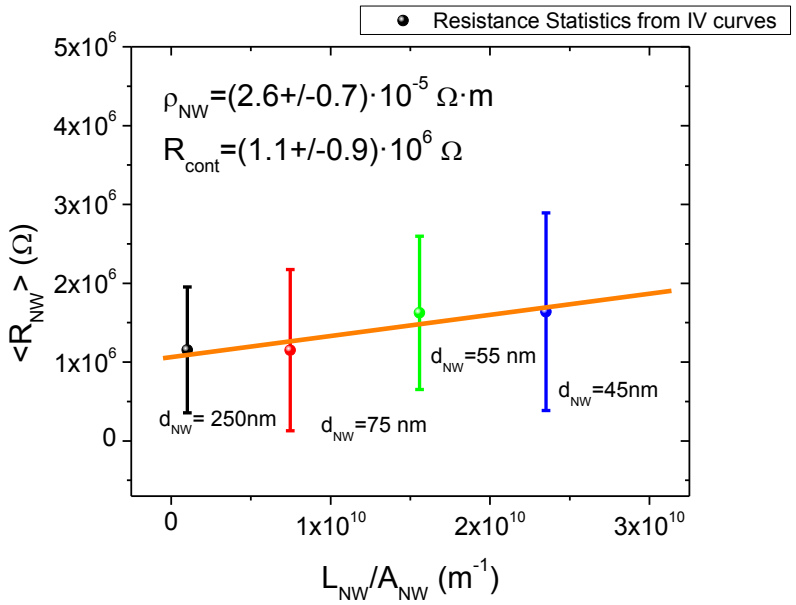

Figure 4.30. Averaged total resistance versus L_{NW}/A_{NW} for the different nanowires diameters. The linear slope gives us the electrical resistivity of the film while the intercept between the slope and the *y*-axis gives us the contact resistance.

Figure 4.30 shows the total resistance versus L_{NW}/A_{NW} for the different Bi_2Te_3 nanowire diameters. From the fitting, the electrical resistivity of the NWs was determined to be $\rho_{NW} = (2.6 \pm 0.7) \cdot 10^{-5}\ \Omega \cdot m$, i.e. an electrical conductivity of $\sigma_{NW} = (3.8 \pm 1.1) \cdot 10^{4}\ \Omega \cdot m$, while the contact resistance was found to be $R_{contc} = (1.1 \pm 0.9) \cdot 10^{6}\ \Omega$: Although the error of the averaged resistances of the cores of the NWs embedded in matrix data is large, it seems to follow a linear trend, which indicate that there is no apparent quantum confinenent effects for these diameters that might vary the result of the electrical conductivity of the nanowire within these diameter sizes.

4.3.1.3. Analysis and Discussion.

This technique involves huge resistance dispersion, and a large experimental error of the electrical conductivity of the NWs, due to the fact that the nanowire-tip contact can vary strongly in each *I-V* curve, because of changes in the shape of the probe or damage of the probe after several *I-V* curves, among others. In order to try to reduce the dispersion of the data, slopes with linear fit factors (R) between 1 and 0.9 were selected and a new Pt probe was also used every time a new sample of nanowires was measured. Even though these precautions were taken, Figure 4.30 still shows that the dispersion of the resistance for each nanowire diameter is quite big. Therefore, one can conclude that the accuracy that can be achieved with this technique is not sufficient despite of the precautions taken and that a proper linear fit was obtained for the *I-V* curves measured. Although the data dispersion was wide, the result obtained for the electrical conductivity of the measured nanowires is in the order of magnitude of those observed in literature. In reference [64], the electrical conductivity of only 300 nm diameter nanowires embedded in alumina was measured using the same technique. A metal on top of the nanowires was deposited in this case in order to improve the tip to nanowire contact resistance. An electrical conductivity between $5 \cdot 10^4$ S·m and $10 \cdot 10^4$ S·m was found for these nanowire sizes, which is in the order of magnitude of the ones that have been measured in this Section. These results are nearly an order of magnitude lower than those found for Bi_2Te_3 bulk or the films measured in Section 4.2.2. The electrodeposition of these nanowires is expected to be improved in the future in order to achieve higher crystalline nanowires so that the electrical conductivity can be increased, involving larger power factor and better thermoelectric performances.

In summary, the two probe AFM-contact technique must be carefully consider before carrying out electrical conductivity measurements of nanowires, taking into account the important influence of the contact resistance. In this Section, *I-V* measurements on several nanowires were taken and the averaged total resistance obtained. Under the assumption that electrical conductivity of the

nanowires is not expected to change for these range of diameters (between 250 nm and 45 nm), the linear fit obtained from the plot $< R_{NW} >$ *versus* L_{NW}/A_{NW} resulted in the electrical conductivity of the NWs. Despite the large data dispersion induced by this measuring technique, the electrical conductivity of the nanowires was successfully compared with other values in literature, but in order to achieve higher accuracy other techniques are desired. In the following section, another approach is presented in which the alumina template is dissolved and the NW was placed onto a microchip to be measured with Kelvin Probe Microscopy.

4.3.2. Topological Insulators and Surface conduction of Bi_2Te_3 nanowires.

4.3.2.1. Topological Insulators.

Topological Insulators (TI) are new states of quantum matter that presents surface conducting states which are protected by time-reversal symmetry [65]. TI are that interesting because of the exotic metallic states that they present on their surfaces, making the electrons insensitive to scattering by impurities[66 65 67 68]. Nanostructured topological insulators are an emerging class of materials with both novel quantum effects and potential applications in low-power electronics, thermoelectrics and spintronics devices [67 68]. Nanostructured TIs, with their inherently large surface-to-volume ratio, are especially suitable for exploring device applications utilizing surface state (SS) transport [69 70]. However, the various surface structural and chemical heterogeneities that usually exist in nanomaterials might significantly alter the potential landscape of SS and affect surface transport. Moreover, bulk carriers are often present in significant amounts due to unintentional doping and thermal excitations [69 71]. Therefore, the carrier transport mechanism in nanostructured TIs are not well-understood yet, and the realization of SS dominated transport remains a challenge, especially at room temperature.

Bismuth Telluride (Bi_2Te_3) is a TI [65, 72, 73] appart of a thermoelectric material with a bulk band gap (~0.16-0.18 eV) much higher than the thermal energy at room temperature [74]. Moreover, as it was explained previously, it is a highly efficient thermoelectric material [75, 76]. The rate of surface to volume increases as the dimensionality of the material is reduced and surface effects should become even more evident in those structures than in bulk. The existence of TI effects at the surface of Bi_2Te_3 has been proved in all dimensional structures with techniques such as Scanning Tunneling Microscopy (STM) [77], magnetoresistance measurements [70] or angle-resolved photoemission spectroscopy (ARPES) [72, 70, 78]. The determination of the Dirac cone in bulk[72] or nanowires [70] made of Bi_2Te_3 reveals its TI nature. Regarding the

particular case of Bi_2Te_3 nanowires, they have the potential to decouple electrical and thermal transport, enabling high electrical conductivity (dominated by surface) and low thermal conductivity (dominated by bulk), enhancing the thermoelectric figure of merit[74]. Nevertheless, the influence of the TI states on the thermoelectrics properties is a subject to study more in dept in the coming years.

In order to carry out measurements of the electrical properties of single nanowires, two terminal devices were fabricated. They consisted of a two electrodes microchip separated by ~1 μm gap with a nanowire bridging between both of them (Figure 4.31a). Electrical contacts to the NWs were fabricated by removing the surface oxide and depositing tungsten via focused ion beam. Tungsten serves as the contact[79] to the NW while the Au pads (connecting the tungsten) are connected to external circuits for biasing the NW. Then, a lab-built KPM from the Lawrence Berkeley National Laboratory (LBNL) was used to map simultaneously the topology and surface potential (chemical potential) distribution of individual Bi_2Te_3 NWs with diameters of 45 nm, 75 nm and 250 nm. In this KPM setup, higher surface potential corresponds to lower work function, and the absolute value of the surface potential is calibrated by setting that of the grounded Au electrode to zero. As shown in Figure 4.31b, the NW has two conduction channels: metallic surface states and semiconducting bulk states. The actual conduction pathways depends critically on the chemical potential and is still under debate in the community [80]. The home-built KPM setup has a spatial and potential resolution of ~20 nm and ~10 mV, respectively [81] [82], allowing us to decipher the microscopic conduction mechanism.

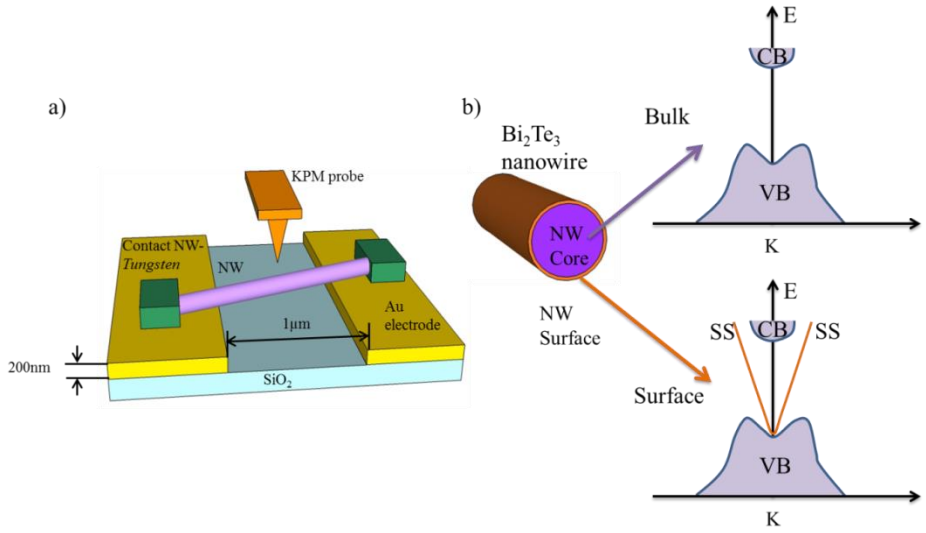

Figure 4.31. a) Schematic diagram of the measurement set-up. b) Energy band structure at the core of the nanowire (bulk) and at its surface. Figure taken from reference [83].

Figure 4.31a and 4.31b shows schematically the set up and the energy band structure at the core of the nanowire (bulk) and at its surface. While at the bulk there is a band gap, at the surface of the nanowire there is a conduction state which should improve the electrical conduction of the material.

4.3.2.1. Nanowires and microchip fabrication.

Nanowires made of Bi_2Te_3 with diameters ranging from 250 nm to 45 nm were grown via electrodeposition process inside of a porous alumina matrix, as it was explained in Chapter 2 and Section 4.3.1.1. In order to have dispersed nanowires in solution, the alumina matrix was selectively dissolved in a phosphoric acid (7 wt. %) and chromic oxide (1.8 wt.%) solution at 45 ˚C for one day. This solution was filtered with ethanol under vacuum conditions to pick up the nanowires in a similar way to reference [84]. Finally, the filter was submerged in a little flask with ethanol in order to have nanowires dispersed in solution. Figures

4.32a-d show transmission electron images of a 45 nm Bi_2Te_3 nanowire as well as its diffraction pattern (inset Figure 4.32b). All the nanowires are n-type bismuth telluride with 250 nm, 75 nm and 45 nm diameters. Their composition was studied by energy dispersive X-ray (EDX) and showed a ratio Bi-to-Te of 42% to 58%, with a variation of composition less than 5% between different diameters, which is between the experimental error of the technique. The axis of the nanowire is oriented in the [1 1 0] crystallographic direction and present a lattice constant of 3.68 Å. These results were obtained from Transmission Electron Microscopy (TEM) analysis and the Bi_2Te_3 structure is shown schematically in Figure 4.32e.

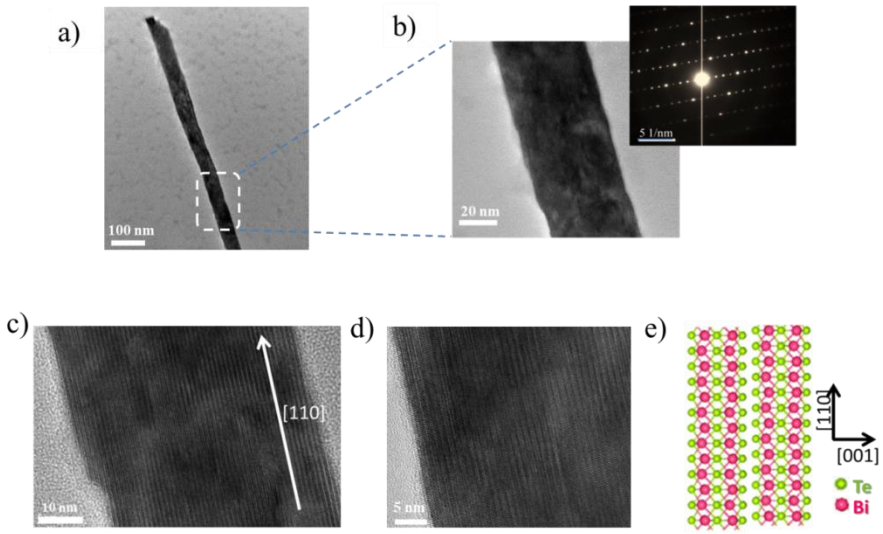

Figure 4.32. a) Transmission electron microscopy image of a 45 nm nanowire with its diffraction pattern. b) Zoom in of the nanowire that is oriented in the [110] direction. c) Schematic view of the crystalline structure of the Bi_2Te_3 atoms along the axis of the nanowire. Figure taken from reference [83].

In order to study the electrical properties of nanowires, microchips consisted of two electrodes separated by ~1 μm gap were fabricated. For that purpose, a Si wafer onto which 300 nm of SiO_x was deposited by plasma-enhanced chemical vapor deposition (PECVD) was used to obtain an isolating substrate. Afterwards, 5 nm of chromium (Cr) and 200 nm of gold (Au) were deposited on top. The

focused ion beam (FIB) was in charge of drawing a 1µm gap coil/line that divides the deposited gold in two electrodes. This attack was carried out with gallium ions at an aperture of 60 µm, an intensity of 120 pA and a dose of 25.5 mC/cm^2. Figure 4.33a shows an optical image of the coil drawn by FIB. Then, by drop cast, a drop of nanowires solution was poured on top of the microchip until a single nanowire bridges the gap. In order to assure good electrical contact between the nanowire and the gold electrodes, the end of the nanowires was cut and a local metal deposition (wolframium) was done through ion beam assisted deposition (GIS). This deposition was performed at $3 \cdot 10^{-6}$ mbar, a reservoir temperature for the wolframium of 60 ºC, an aperture of 30 µm, current of 18 pA, a refreshing time of 0.015 ms and a dose of 400 mC/cm^2. Figure 4.33b shows a scanning electron microscopy (SEM) image of a connected nanowire.

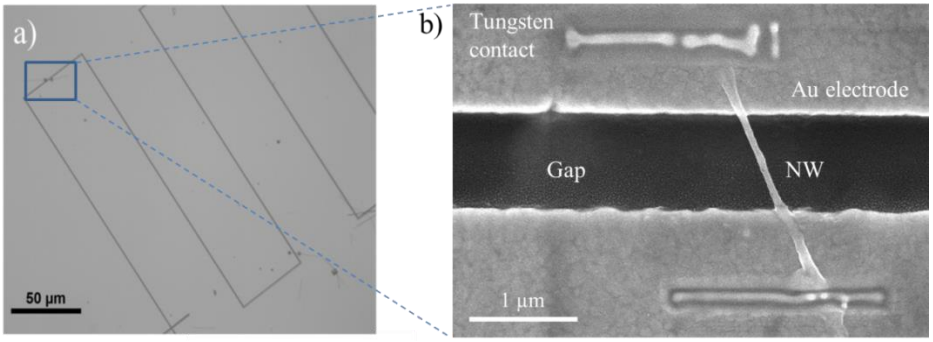

Figure 4.33. a) Optical image of the coil. b) SEM image of a 75nm diameter nanowire bridging the gold electrodes with metal contacts. Figure taken from reference [83].

4.3.2.2. Surface conduction of the nanowires.

The electrical conductivity measurements of the nanowire surface were carried out with the Kelvin Probe Microscopy (KPM). When we passed a current across the nanowire, the KPM was in charge of

measuring the surface voltage drop along it. Therefore, using the 1D theory of conduction, one can determine its electrical conductivity.

To this end, it was first proceed to map out the potential distribution of the NWs when a voltage bias is applied, with the results of a 45 nm NW shown in Figure 4.34. It can be seen in the SEM and AFM images (Figure 4.34a and 4.34b) that the NWs have a clean and smooth structure across the ~3 µm lengths between the tungsten contacts. The electrode on the right is grounded, while a bias of ±0.35 V is applied to the left electrode. It can be seen that the potential changes roughly linearly along the NW (Figure 4.34c-f). From right to left, there is an increase of ~160 mV and a decrease of ~148 mV with the 0.35 V and -0.35 V applied bias, respectively. The mismatch between the applied bias and the actual potential drop along the NW reveals the existence of contact resistance. Note that the potential changes both on the freestanding part of NW and the part of the NW on Au electrode, likely due to the insulating surface oxide layer, which is removed only at the tungsten contacts.

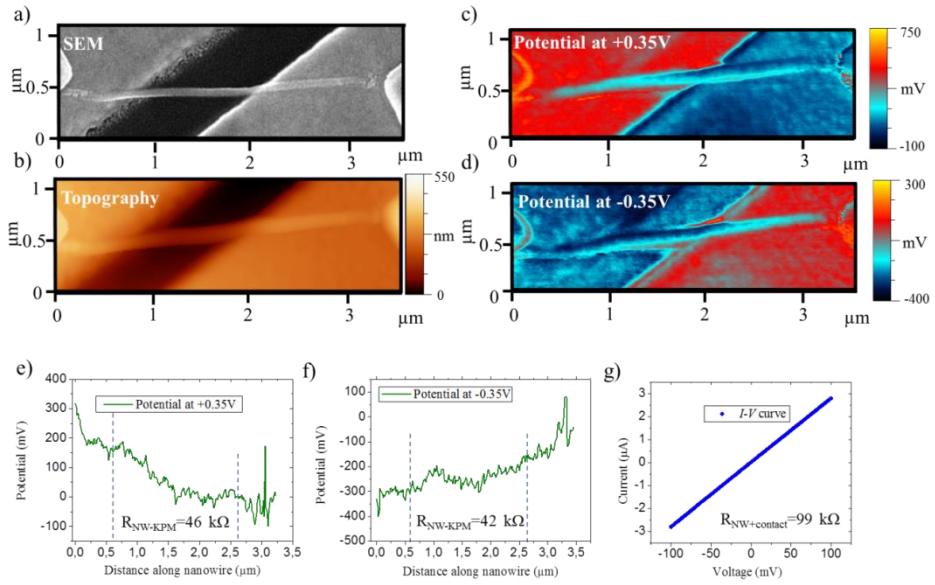

Figure 4.34. Accurate determination of electrical conductivity via surface potential mapping. a) and b) show a SEM and topographic image of 45 nm diameter nanowire. c) and d) show the 2D-surface

potential map of the nanowire while applying a bias of 0.35 V and -0.35 V to the left electrode, respectively. e) and f) shows the surface potential profile along the nanowire for the two different bias applied. The dashed blue line corresponds to the analyzed voltage drop along the nanowire. From the slope of the potential drop and the current that is flowing, the electrical resistance can be determined. g) Shows the I-V curve obtained from two-probe measurements, also performed. Figure taken from reference [83].

I-V measurements of this NW shows a total resistance of 99 $k\Omega$ (Figure 4.34g). Combined with the measured potential profiles along the NW, we obtain an average contact resistance of 56 $k\Omega$ and the resistance of the NWs to be 46 $k\Omega$ and 42 $k\Omega$, at 0.35 V and -0.35 V bias, respectively. Taking into account the diameter and length of the NW and take the average of the measured resistances at $\pm$0.35 V bias, we obtain a conductivity of $(2.93\pm0.17)\times10^4$ S/m. Using this method, we also measured the 75 nm and 250 nm NWs, and obtained contact resistance of 18 $k\Omega$ and 30 $k\Omega$, respectively.

The analysis of the linear voltage drop at the suspended part of the nanowire within the information of the current that is passing through the nanowire, which was obtained from an *I-V* curve, makes possible the determination of the electrical conductivity using the equation,

$$\sigma_{NW} = \frac{I}{\Delta V_{NW}} \cdot \frac{L_{NW}}{A_{NW}} \tag{4.18}$$

where I and ΔV_{NW} are the current and voltage along the nanowire, while L_{NW} and A_{NW} are the length and section of the nanowire analyzed.

Figure 4.35 shows the electrical conductivity of the NWs *versus* its diameter. In comparison, Figure 4.35 also shows the conductivity directly obtained from the *I-V* curves (assuming no contact resistance). The dramatic difference of the NW conductivity obtained from these two methods highlights the importance of KPM in obtaining the accurate conductivity.

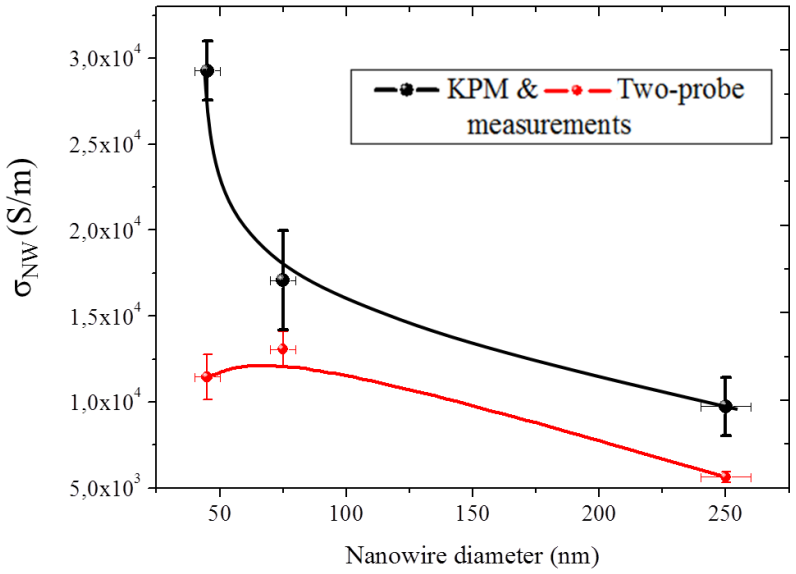

Figure 4.35. Electrical Conductivity of nanowires with different diameter. Figure taken from reference [83].

Note that four point probe measurements also could not provide accurate results due to the fact that little fractures, grain boundaries or defects on the nanowire sometimes are not detected with a SEM image of the nanowire and one might lead to an underestimation of the electrical conductivity of the nanowire. As an example, Figure 4.36 shows a nanowire that seems to be in good conditions, according to SEM, for electrical measurements, but the KPM reveals that, when a voltage bias is applied across it, a drastic drop occurs in the middle of the nanowire which might be associated with an invisible grain boundary that is not appreciated in the SEM or topographic AFM image. Techniques based on two or four probe measurements would not be able to detect it, which would involve an underestimation of the electrical conductivity of these nanowires. This implies that these types of nanowires are difficult to detect, but they will show different electrical behavior from other nanowires and should be something to take into account when measuring isolated nanowires.

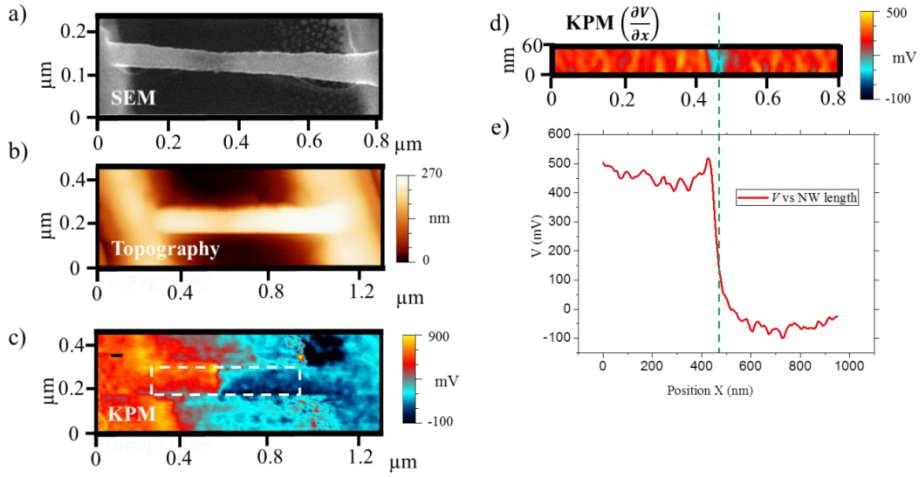

Figure 4.36.a) Topographic and b) SEM images of 75 nm diameter nanowire. c) KPM map and d) derivative of the potential and e) the surface potential profile along the nanowire length when a voltage bias across it is applied. Figure taken from reference [83].

Another aspect that might influence the measurements of the electrical conductivity of the nanowires in two or four probes is the diffusion of the metal of the contact to the surroundings, which can be observed with Kelvin Probe Microscopy. Figure 4.37a shows the topographic image of the tungsten contact in the nanowire, which has a size of around ~600 nm^2. However, Figure 4.37b shows the diffusion of the metal along the nanowire and electrode, which is not detected with a SEM or topographic image. Diffusion is found in an area twice the one found topographically. Consequently, one should consider this effect carefully when taking *I-V* curves with two or four probes under the presence of contacts made in a similar way, otherwise the electrical conductivity of the nanowire would be overestimated. Figure 4.37c shows a simulation of the implantation of gallium ions at 30keV, according to the experimental conditions, in a NW during the tungsten deposition. The attacked area of the gallium ions in the NWs was calculated to be around 12 nm. Nevertheless, this simulation do not take into account the effects of the heating during the deposition process which might alter the crystalline structure of the Bi_2Te_3 material in the proximity of the contact.

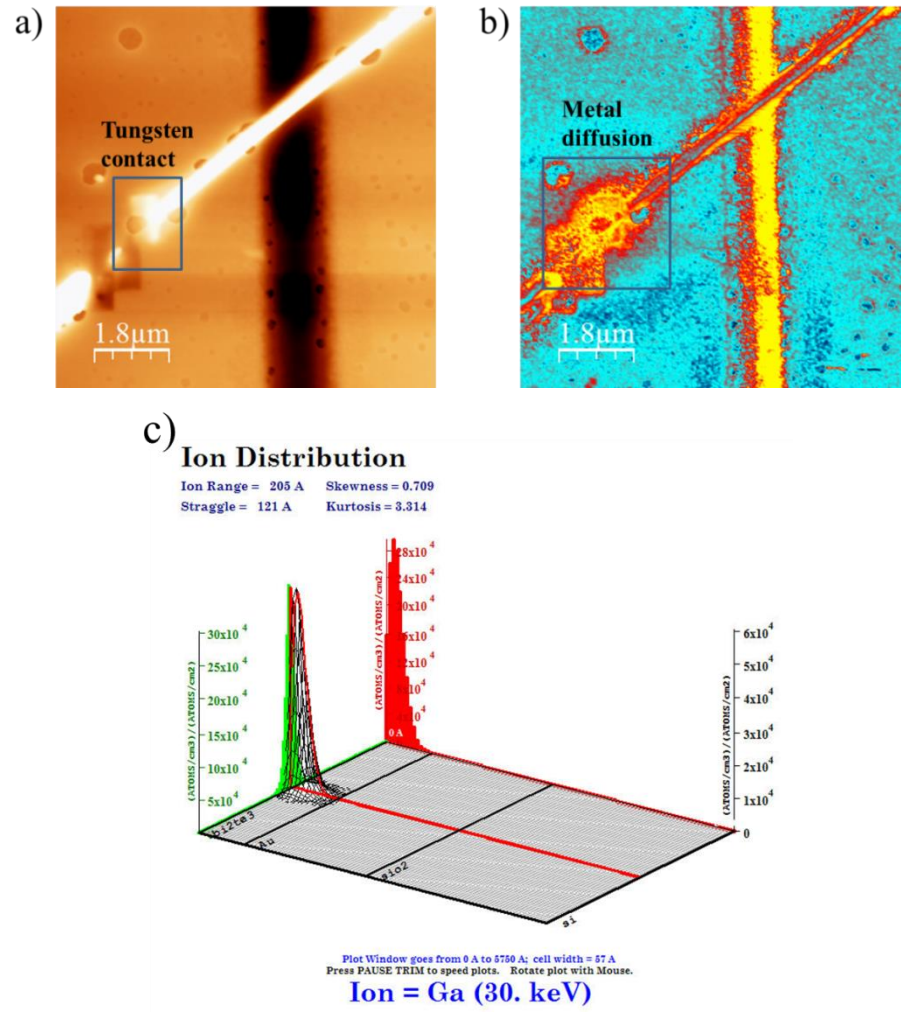

Figure 4.37. a) Topographic image of the tungsten contact on a 250nm diameter nanowire. b) Potential image of the contact at 0 bias where clearly is observed the diffusion of the metal along the nanowire. c) Simulation of the implantation of gallium ions in a 75 nm diameter nanowire during tungsten deposition at an energy of 30 keV. The grey base of the 3D graph show the different materials presented along the cross section of the sample, i.e. Bi_2Te_3 NW, Au electrode and SiO_2 substrate. The green peak corresponds to the lateral distribution (later straggling) and the red is the penetration depth of the ions, while the black distribution is a combination of them.

From Figure 4.35 it is possible to see that the actual conductivity of the NW increases dramatically with the decrease of the NW diameter. The bulk conductivity is expected to be the same for different NW sizes, but the surface conductivity will increase with the decrease of NW diameter because of the increased surface-to-volume ratio. Therefore, surface conduction is likely the dominant conduction pathway in the 45 nm diameter NW. It is expected that in smaller NWs the surface-dominated conductivity will increase further, while the bulk conductivity may start to decrease when the diameter is below the electron mean free path (61 nm)[63]. Therefore, these narrow Bi_2Te_3 nanowires are a promising system to implement room temperature surface transport in topological insulators.

In order to estimate the power factor of these nanowires, Seebeck coefficient measurements of the arrays of nanowires embedded in alumina matrix were carried out with a Seebeck Microprobe system (Chapter 2.2.3), which resulted in an average value of $-50 \pm 7\ \mu V \cdot K^{-1}$. This result has been cross-check with an independent home-made Seebeck coefficient system, whose measurements were carried out at the National Insitute of Materials of Japan (NIMS) in collaboration with another members of the thermoelectric group. Then, the power factor can be estimated to vary between $28 \pm 9\ \mu W \cdot K^{-2} \cdot m^{-1}$ and $73 \pm 21\ \mu W \cdot K^{-2} \cdot m^{-1}$ for the 300 nm and 45 nm diameter NW, respectively. As the thermal conductivity of these nanowires was also measured in Chapter 3.3.1.2. (Table 3.IV), the zT of these nanowires were observed to increase from 0.01 to 0.02 at room temperature, as the diameter of the NW reduces from 300 nm to 45 nm size. As the diameter of those nanowires becomes even smaller than 45 nm size the surface conduction is expected to increase (Figure 4.36), while the thermal conductivity (Chapter 3) shall be very low. Therefore, NWs with smaller diameters migh be very promising for future thermoelectric and topological insulator applications.

4.3.2.3. Potential ripples on the nanowires surface.

The NWs are clean, [1 1 0] oriented, and have smooth surfaces, as revealed by the scanning electron microscopy (SEM) images and KPM topography images (Figure 4.38a-d). For both the 45 nm and the 250 nm NW imaged, no apparent structural defects were observed. In the surface potential images (Figure 4.38e and 4.38f) the NWs, however, showed periodic oscillations. These ripple structures are more visible in the three dimensional (3D) plot of the potential maps (Figure 4.38g and 4.38h). These maps are independent of the scanning direction of the KPM and are reproducible with different AFM tips. Consequently, it excludes the possibility of experimental artefacts in inducing the ripple structures.

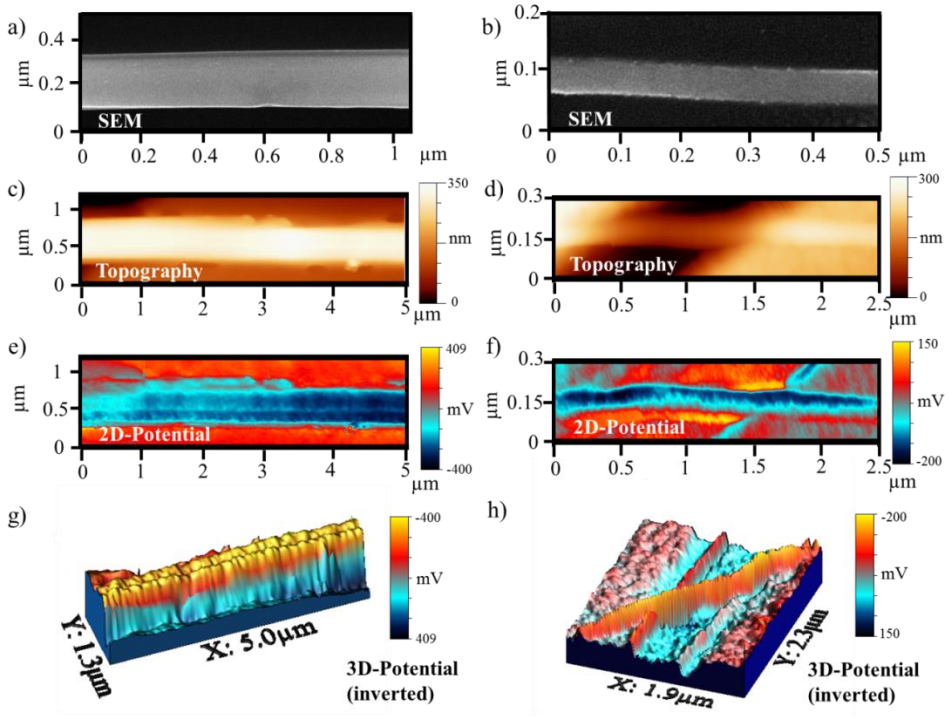

Figure 4.38. SEM, a) and b), and topographic, c) and d), images of 250 nm and 45 nm diameter Bi_2Te_3 nanowires. two-dimensional (2D), e) and f), and three-dimensional (3D), h) and i), maps of the surface potential of these nanowires. Surface potential ripples are observed at the surface of the NW. Figure taken from reference [83].

The amplitude and periodicity of these potential ripples were further analyzed for the NWs with different diameter, as shown in Figure 4.39. The periodicity (distance between neighbouring ripples) increases with NW diameter, from ~90 nm to ~210 nm. Their peak-to-peak amplitude ranges from ~10 mV to ~80 mV, with no obvious dependence on NW diameter. The average angle of the potential spiral lines relative to the NW axis is ~80°, independent of the NW diameter. It is worth noting that the surface potential images correspond to the projections of the curved NW surfaces onto the substrate plane. Thus the observed angles also correspond to the line projections of the three dimensional surface potential ripples on the substrate. It is expected that the actual spiral structures to be periodic rings on the NW surface.

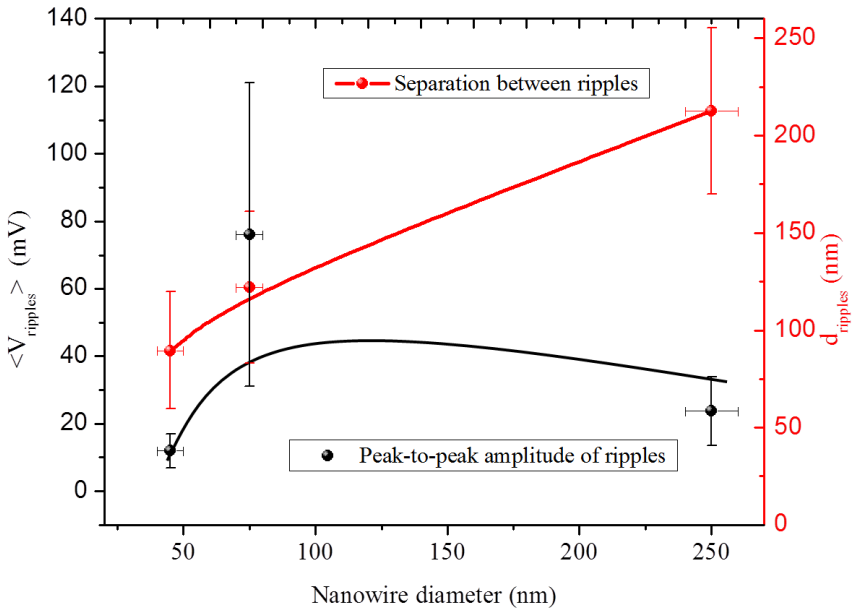

Figure 4.39. Amplitude and separation of the spirals versus different diameters nanowires diameters. Lines are drawn to guide the eye. Figure taken from reference [83].

The periodicity, amplitude and angle of these potential ripples show no observable difference for the parts of the NW on top of Au

electrodes and the parts that are free-standing. It indicates that these ripples are intrinsic to the NWs independent of the substrate. This might be attributed to the oxide layer (~2-5 nm) on the NW surface that isolates the NW from the gold substrate. Previous works have shown similar structures on single crystal Bi_2Te_3 surfaces using scanning tunneling microscopy (SThM) [85], where the periodicity was observed to be ~100 nm, in the same scale as the results presented here. These ripples were suspected to result from strain, although no direct evidence was provided. It is expected that similar mechanisms may play a role in these NW systems which are more prone to strain due to the reduced dimension. Since the Dirac surface states have a small density of states, the local chemical potential is very sensitive to structural perturbations. Therefore, periodic surface lattice strain might induce the observed potential ripples. To examine this effect, transmission electron microscopy (TEM) measurements were performed of the NWs. It can be seen that the NWs have a single crystalline structure in the bulk with no observable strain effects, while the surface have vacancy defects and the lattice constants also fluctuate at different surface locations. However, these lattice constant variations give the impression to be random rather than periodic. In addition, the presence of the surface oxide layer makes it hard to identify the position of the outmost Bi_2Te_3 layer that determines the surface potential. Moreover, it is expected that the surface strain may change when the NWs are deposited on the Au substrate (with a ~1μm gap). These factors complicate the analysis of the mechanism of potential ripples, and make difficult the correlation of the observed potential ripples with the structure of the NWs.

In summary, the surface conduction of Bi_2Te_3 nanowires with different diameters was studied by means of the Kelvin Probe Microsocopy (KPM). An increment of the electrical conductivity at the surface of the nanowire was observed as the diameter was reduced, indicating that surface conduction become dominant. Moreover, potential ripples at the surface of the nanowires were observed, which might involve new potential applications and that could be controlled by structural disorder or defects on the surface of the nanowires. Therefore, it is postulated that as the diameter of the nanowire becomes smaller, the electrical transport mechanism becomes dominated by

surface states and that by tuning the structural and/or chemical disorder, it might be possible to both manipulate the conduction pathways of nanostructured TIs and modulate their local potential energy landscapes. It will pave the way for practical TI devices for thermoelectrics, spintronics or quantum computing, among others.

4.4. Conclusions.

In this Chapter, the Harman method was first studied with COMSOL Multiphysics ® modeling as an alternative to measure the all three parameters (Seebeck coefficient, electrical conductivity and thermal conductivity). Afterwards, this Chapter covers electrical measurements of films and nanowires of inorganic materials carried out mostly by Scanning Probe Microscopy techniques, like Kelvin Probe Microscopy or conductive Atomic Force Microscopy, but also with other techniques, such as two probes and four probes method. In each Section, it is first explained how the electrical measurements were performed. Then, a physical explanation for the results obtained is given in each case.

The measurement of figure of merit (zT) of thermoelectric nanostructures with the Harman technique seems to be very challenging from what observed from simulations carried out with COMSOL Multiphysics ® (Section 4.1.). The high frequency working regimes observed in the Harman method for both films and nanowires require of special electronic measurement systems, which are able to detect very small and fast signals. Moreover, the heat loss associated with the contact wire and the contact resistance can profoundly affect zT results, involving an underestimation of it. For all these reasons, it is possible to conclude that the Harman technique is rather difficult to measure accurate zT values in thin films and can be nearly discarded to measure nanowires. The measurement of each of the transport properties, such as the thermal or electrical conductivity, might be preferable for nanostructures.

Regarding electrical conductivity measurements of films (Section 4.2.2.), a proper evaluation of the contact resistance and the field spreading in the sample and electrodes must be carried out to measure accurately. The electrical conductivity determined for the Bi_2Te_3 electrodeposited film resulted to be three times larger than single crytal bulk for a Bi_2Te_3, but seem to be in agreement with the anisotropy factor (in-plane versus out of plane electrical conductivity values) found for this material in single crystal. This high value of the

electrical conductivity was associated with the high crystallinity orientation in the [1 1 0] direction of the film. As in the electrochemical deposition technique an electric field is applied during the growth, this may favors the growth of Bi_2Te_3 grains oriented along the highest electrical conductivity direction. For these reasons, the mobility of the electrons might be increased given rise to this high electrical conductivity value. This is a step forward to obtain films via electrodeposition with larger power factors. On the other hand, the contact resistance at the interface between electrodes an film was evaluated with a novel approach, using the Kelvin Probe Microscopy (Section 4.2.1.), but also from the fitting of the experimental data with a COMSOL Multiphysic simulation (Section 4.2.2.), obtaining good agreement between them. Moreover, another relevant conclusion is the fact that the one dimensional theory do not determine accurately the electrical conductivity of low resistive and large area films, mainly because of the field spreading effect, and instead, the use of 3D simulations is required.

The electrical conductivity of Bi_2Te_3 one-dimensional nano-structures was measured with two different approaches: i) Bi_2Te_3 nanowires embedded in a matrix whose core electrical conductivity was measured with a conductive AFM; ii) suspended Bi_2Te_3 nanowires on a micro-chip, whose surface electrical conductivity was measured with Kelvin Probe Microscopy. It was observed that although from the first approach the core electrical conductivity of the nanowires seems to not be varied with the diameter, the conductivity at the surface of the nanowire seems to be enhanced as the diameter of the NW becomes smaller. This is explained due to the topological insulator (TI) nature of the Bi_2Te_3 that have exotic metallic surface states (SS) that are protected by time-reversal symmetry and are thus immune to inelastic scattering by trace amounts of defects and nonmagnetic impurities. Therefore, Bi_2Te_3 might present conducting states at the surface, but insulating behavior at the core of the wires. Consequently, in the particular case of Bi_2Te_3 nanowires, they have the potential to decouple electrical and thermal transport, enabling high electrical conductivity (dominated by surface) and low thermal conductivity (dominated by bulk), enhancing the thermoelectric figure of merit. Moreover, exotic

surface potential ripples were found on the surface of the nanowire, whose amplitude and separation was studied for each diameter nanowire. It might be possible to both manipulate the conduction pathways of these nanostructured TIs and modulate their local potential energy landscapes (ripples) by tuning the structural and/or chemical disorder. Consequently, the observed effects will pave the way for practical TI devices to be used for thermoelectrics, spintronics or quantum computing, among others.

References

1. Y. Zhang, T. Mori, J. Ye and M. Antonietti, *Journal of the American Chemical Society*, 2010, **132**, 6294-6295.
2. L. Huang, Y. Huang, J. Liang, X. Wan and Y. Chen, *Nano Res.*, 2011, **4**, 675-684.
3. H. J. Goldsmid, in *Introduction to Thermoelectricity*, Springer Berlin Heidelberg2010, **121**, 9, 139-166.
4. M. S. Dresselhaus, G. Chen, M. Y. Tang, R. G. Yang, H. Lee, D. Z. Wang, Z. F. Ren, J. P. Fleurial and P. Gogna, *Advanced Materials*, 2007, **19**, 1043-1053.
5. L. D. Hicks and M. S. Dresselhaus, *Physical Review B*, 1993, **47**, 12727-12731.
6. H. Bottner, J. Nurnus, A. Gavrikov, G. Kuhner, M. Jagle, C. Kunzel, D. Eberhard, G. Plescher, A. Schubert and K. H. Schlereth, *Microelectromechanical Systems, Journal of*, 2004, **13**, 414-420.
7. G. Span, M. Wagner, T. Grasser and L. Holmgren, *physica status solidi (RRL) – Rapid Research Letters*, 2007, **1**, 241-243.
8. T. C. Harman and Harman, *Journal of Applied Physics*, 1958, **29**, 1373-1374.
9. T. C. Harman and Harman, *Journal of Applied Physics*, 1958, **29**, 1471-1473.
10. H. Iwasaki and H. Hori, *24th International Conference on Thermoelectrics*, 2005, 501-504.
11. M. Muñoz Rojo, J. J. Romero, D. Ramos, D.-A. Borca-Tasciuc, T. Borca-Tasciuc and M. Martín Gonzalez, *International Journal of Thermal Sciences*, 2015, **89**, 193-202.
12. H. Iwasaki, M. Koyano and H. Hori, *Japanese Journal of Applied Physics*, 2002, **41**, 6606-6609.
13. H. Iwasaki, S. Y. Yokoyama, T. Tsukui, M. Koyano and H. Hori, *Japanese Journal of Applied Physics*, 2003, **42**, 3707-3708.
14. S. Fujimoto, H. Kaibe, S. Sano and T. Kajitani, *Japanese Journal of Applied Physics*, 2006, **45**, 8805-8809.
15. R. Venkatasubramanian, E. Siivola, T. Colpitts and B. O'Quinn, *Nature*, 2001, **413**, 597-602.
16. E. Castillo, C. Hapenciuc and T. Borca Tasciuc, *Review of Scientific Instruments*, 2010, **81**, 044902.
17. R. Singh, Z. Bian, A. Shakouri, G. Zeng and J.-H. Bahk, *Applied Physics Letters*, 2009, **94**, 212508.

18. R. Singh, Z. Bian, G. Zeng, J. Zide and J. Christofferson, *Materials Research Society Symposium Proceedings*, 2006, **886**, 123-128.
19. E. E. Antonova and D. C. Looman, *24th International Conference on Thermoelectrics*, 2005, 215-203.
20. M. M.-González, O. C.-Calero and P. D.-Chao, *Renewable and Sustainable Energy Reviews*, 2013, **24**, 288-305.
21. M. M. Rojo, O. C. Calero, A. F. Lopeandia, J. R. Viejo and M. M. Gonzalez, *Nanoscale*, 2013, **6**, 7858-7865.
22. W. Seifert, M. Ueltzen and E. Muller, *Physica Status Solidi. A, Applied Research*, 2002, **194**, 277-290.
23. C. V. Manzano, A. Rojas, M. Decepida, B. Abad, Y. Feliz, O. Caballero-Calero, D. A. Borca-Tasciuc and M. Martin-Gonzalez, *J Solid State Electrochem*, 2013, **17**, 2071-2078.
24. S. Kasap, *Thermoelectric Effects in Metals: Thermocouples*, McGraw-Hill, 2006.
25. A. Jacquot, N. Farag, M. Jaegle, M. Bobeth, J. Schmidt, D. Ebling and H. Böttner, *Journal of Electronic Materials*, 2010, **39**, 1861-1868.
26. P. V. Pesavento, R. J. Chesterfield, C. R. Newman and C. D. Frisbie, *Journal of Applied Physics*, 2004, **96**, 7312-7324.
27. A. Mavrokefalos, M. T. Pettes, F. Zhou and L. Shi, *Review of Scientific Instruments*, 2007, **78**, -.
28. A. A. Ramadan, R. D. Gould and A. Ashour, *Thin Solid Films*, 1994, **239**, 272-275.
29. Luciana W. da Silva and M. Kaviany, *International Journal of Heat and Mass Transfer*, 2004, **47**, 2417-2435.
30. Y.-H. C. Shien-Ping Feng, Jian Yang, Bed Poudel, Bo Yu,b Zhifeng Ren, Gang Chen,, *Physical Chemistry Chemical Physics*, 2013, **15**, 6757-6762.
31. A. Mavrokefalos, M. T. Pettes, F. Zhou and L. Shi, *Review of Scientific Instruments*, 2007, **78**, 034901.
32. S. E. Mohney, Y. Wang, M. A. Cabassi, K. K. Lew, S. Dey, J. M. Redwing and T. S. Mayer, *Solid-State Electronics*, 2005, **49**, 227-232.
33. M. Shiraishi, K. Takebe, K. Matsuoka, K. Saito, N. Toda and H. Kataura, *Journal of Applied Physics*, 2007, **101**, 014311.
34. Y. Otsuka, Y. Naitoh, T. Matsumoto and T. Kawai, *Applied Physics Letters*, 2003, **82**, 1944-1946.
35. J. M. Beebe, V. B. Engelkes, L. L. Miller and C. D. Frisbie, *Journal of the American Chemical Society*, 2002, **124**, 11268-11269.

36. R. J. Chesterfield, J. C. McKeen, C. R. Newman, C. D. Frisbie, P. C. Ewbank, K. R. Mann and L. L. Miller, *Journal of Applied Physics*, 2004, **95**, 6396-6405.
37. V. Palermo, A. Liscio, M. Palma, M. Surin, R. Lazzaroni and P. Samori, *Chemical Communications*, 2007, 3326-3337.
38. S. Sadewasser and T. Glatzel, *Kelvin Probe Force Microscopy*, Springer, Springer-Verlag Berlin Heidelberg, 2012.
39. O. Vatel and M. Tanimoto, *Journal of Applied Physics*, 1995, **77**, 2358-2362.
40. J. Colchero, A. Gil and A. M. Baró, *Physical Review B*, 2001, **64**, 245403.
41. K. P. Puntambekar, P. V. Pesavento and C. D. Frisbie, *Applied physics letters*, 2003, **83**, 5539-5541.
42. M. S. Martin Gonzalez, A. L. Prieto, R. Gronsky, T. Sands and A. M. Stacy, *Journal of the Electrochemical Society*, 2002, **149**, C546-C554.
43. Miguel Muñoz-Rojo, Olga Caballero-Calero and Marisol Martín-González, *Applied Physics Letters*, 2013, **103**, 183905.
44. I. Horcas, R. Fernandez, J. M. Gomez-Rodriguez, J. Colchero, J. Gomez-Herrero and A. M. Baro, *Review of Scientific Instruments*, 2007, **78**, 013705.
45. A. K. Kaw, *Mechanics of composite materials*, CRC Press, Boca Raton, FL, United States, 2006.
46. W. M. H. Sachtler, G. J. H. Dorgelo and A. A. Holscher, *Surface Science*, 1966, **5**, 221-229.
47. D. Haneman, *Journal of Physics and Chemistry of Solids*, 1959, **11**, 205-214.
48. F. Xiao, C. Hangarter, B. Yoo, Y. Rheem, K.-H. Lee and N. Myung, *Electrochimica Acta*, 2008, **53**, 8103-8117.
49. L. W. da Silva and M. Kaviany, *International Journal of Heat and Mass Transfer*, 2004, **47**, 2417-2435.
50. F. Li, X. Huang, W. Jiang and L. Chen, *AIP Conference Proceedings*, 2012, **1449**, 458-462.
51. S.-P. Feng, Y.-H. Feng, J. Chang, B. Yang, B. Poudel, Z. Yu, G. Ren and Chen, *Physical Chemistry Chemical Physics*, 2013, **15**, 6757.
52. A. M. Pettes, R. Melamud, S. Higuchi and K. E. Goodson, *Impact of contact resistances on the low-dimensional scaling of thermoelectric energy conversion devices*, 2007.
53. D. E. Wesolowski, R. S. Goeke, A. M. Morales, S. H. Goods, P. A. Sharma, M. P. Saavedra, K. R. Reyes Gil and C. A. Apblett, *Journal of Materials Research*, 2012, **27**, 1149-1156.

54. E. Preisler, J. Bayersdorfer, M. Brunner, J. Bock and S. Elschner, *Superconductor Science & Technology*, 1994, **7**, 389-396.
55. D.-H. Kim, E. Byon, G.-H. Lee and S. Cho, *Thin Solid Films*, 2006, **510**, 148-153.
56. A. Giani, A. Boulouz, F. Pascal-Delannoy, A. Foucaran, E. Charles and A. Boyer, *Materials Science and Engineering: B*, 1999, **64**, 19-24.
57. O. Caballero-Calero, P. D.-Chao, B. Abad, C. V. Manzano, M. D. Ynsa, J. J. Romero, M. M. Rojo and M. M. González, *Electrochimica Acta*, 2013, **123**, 117-126.
58. M. M. Muñoz Rojo, C. V. Manzano, D. Granados, M.R. Osorio, T. Borca-Tasciuc and M. Martín-Gonzalez, *Submitted to Journal of Applied Physics* 2015.
59. R. M. A.M. Pettes, and S. Higuchi, *26th International Conference on Thermoelectrics (ICT)*, 2007.
60. F. G. S. A. Mikrajuddin, H.K. Kim, Kikuo Okuyama, *Materials Science in Semiconductor Processing*, 1999, **2**, 321-327.
61. A. L. Prieto, M. Martin Gonzalez, R. Gronsky, T. Sands, M. S. Sander, M. S. Martin Gonzalez and A. M. Stacy, *Journal of the American Chemical Society*, 2001, **123**, 7160-7161.
62. J. Martín, C. V. Manzano and M. Martín-González, *Microporous and Mesoporous Materials*, 2012, **151**, 311-316.
63. A. Mavrokefalos, *Journal of applied physics*, 2009, **105**, 104318-104318.
64. Y. Kim, L. Cagnon, U. Goesele and J. Lee, *Physica status solidi. Rapid research letters*, 2010, **4**, 43-45.
65. H. Zhang, C.-X. Liu, X.-L. Qi, X. Dai, Z. Fang and S.-C. Zhang, *Nat Phys*, 2009, **5**, 438-442.
66. Y. Ando, *Journal of the Physical Society of Japan*, 2013, **82**, 102001.
67. J. E. Moore, *Nature*, 2010, **464**, 194-198.
68. M. Z. Hasan and C. L. Kane, *Reviews of Modern Physics*, 2010, **82**, 3045-3067.
69. H. Peng, K. Lai, D. Kong, S. Meister, Y. Chen, X.-L. Qi, S.-C. Zhang, Z.-X. Shen and Y. Cui, *Nat Mater*, 2010, **9**, 225-229.
70. S. S. Hong, Y. Zhang, J. J. Cha, X.-L. Qi and Y. Cui, *Nano Letters*, 2014, **14**, 2815-2821.
71. L. Fu and C. L. Kane, *Physical Review B*, 2007, **76**, 045302.
72. Y. L. Chen, J. G. Analytis, J.-H. Chu, Z. K. Liu, S.-K. Mo, X. L. Qi, H. J. Zhang, D. H. Lu, X. Dai, Z. Fang, S. C. Zhang, I. R.

Fisher, Z. Hussain and Z.-X. Shen, *Science*, 2009, **325**, 178-181.
73. J. Gooth, B. Hamdou, A. Dorn, R. Zierold and K. Nielsch, *Applied Physics Letters*, 2014, **104**, 243115.
74. D. M. Rowe, *CRC Thermoelectrics Handbook: Macro to Nano.*, CRC Press, Broken Sound Parkway NW, 2005.
75. M. D. Rowe, G. Min and K. S. Williams, *An up-date on the thermoelectric recovery of low temperature waste heat*, World renewable energy congress (GBR), Pergamon, Amsterdam, PAYS-BAS, 2000.
76. H. B. Radousky and H. Liang, *Nanotechnology*, 2012, **23**, 502001.
77. Z. Alpichshev, J. G. Analytis, J. H. Chu, I. R. Fisher, Y. L. Chen, Z. X. Shen, A. Fang and A. Kapitulnik, *Physical Review Letters*, 2010, **104**, 016401.
78. G. Wang, X.-G. Zhu, Y.-Y. Sun, Y.-Y. Li, T. Zhang, J. Wen, X. Chen, K. He, L.-L. Wang, X.-C. Ma, J.-F. Jia, S. B. Zhang and Q.-K. Xue, *Advanced Materials*, 2011, **23**, 2929-2932.
79. A. J. DeMarco and J. Melngailis, *Journal of Vacuum Science & Technology B*, 2001, **19**, 2543-2546.
80. Y. Wang, F. Xiu, L. Cheng, L. He, M. Lang, J. Tang, X. Kou, X. Yu, X. Jiang, Z. Chen, J. Zou and K. L. Wang, *Nano Letters*, 2012, **12**, 1170-1175.
81. Y. Zhang, D. Ziegler and M. Salmeron, *ACS Nano*, 2013, **7**, 8258-8265.
82. Y. Zhang, O. Pluchery, L. Caillard, A.-F. Lamic-Humblot, S. Casale, Y. J. Chabal and M. Salmeron, *Nano Letters*, 2015, **15**, 51-55.
83. M. Muñoz Rojo, Y. Zhang, C. Manzano, R. Alvaro, M. Salmeron and M. Martín-Gonzalez, *Submitted to Nature Communications*, 2015.
84. V. Vega, T. Bohnert, S. Martens, M. Waleczek, J. Montero-Moreno, D. Gorlitz, V. Prida and K. Nielsch, *Nanotechnology*, 2012, **23**, 465709.
85. Y. Okada, W. Zhou, D. Walkup, C. Dhital, S. D. Wilson and V. Madhavan, *Nat Commun*, 2012, **3**, 1158.

Chapter 5

Conclusions

The general conclusions that can be extracted from this thesis work are summarized in the following parts:

1. **Thermal transport property measurements:** The SThM working either in DC or AC mode is shown to be a powerful technique to carry out local thermal measurements of nano-structures, either organic or inorganic. The following points summarizes the most important results achieved for:

   1.1 Thermal transport in films:

   a) Inorganic films: Silicon Germanium.

   The thermal conductivity of Silicon Germanium (SiGe) films grown through metal induced crystallization under two different thermal treatments (*in-situ* and *ex-situ*) were studied with SThM. The results showed a significant thermal reduction, $1.42 \pm 0.12\ W \cdot K^{-1} \cdot m^{-1}$ (*in-situ*) and $1.53 \pm 0.08\ W \cdot K^{-1} \cdot m^{-1}$ (*ex-situ*), in comparison to similar SiGe films ($4 - 5\ W \cdot K^{-1} \cdot m^{-1}$). This reduction of thermal conductivity was related to an increment of phonon scattering at the nano-crystalls and clusters formed during the growing process. This result has given rise to new

advances to obtain SiGe films with reduced thermal conductivity.

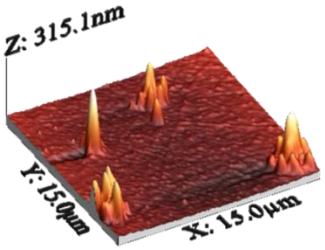

b) Organic films: undoped and doped PCDTBT polymer.

The thermal conductivity of PCDTBT polymer films grown through drop cast with and without doping them with different levels of iron atoms were studied with SThM. While the thermal conductivity of the undoped film was determined to be 0.19 ± 0.02 $W \cdot K^{-1} \cdot m^{-1}$, the thermal conductivity of the doped films remained around 1 $W \cdot K^{-1} \cdot m^{-1}$, without a variation less than 25% observed for the different doping levels considered. The total thermal conductivity of the doped films is influenced by the electronic term of the thermal conductivity, but also, the presence of the doping ions contribute to the lattice term, especially when the doping level is increased. The combination of the lattice and electrical terms results in a total thermal conductivity with similar values for the different doping concentrations of the PCDTBT films studied.

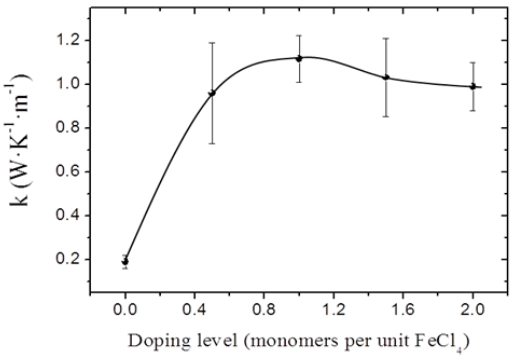

1.2 Thermal transport in nanowires:

a) Inorganic nanowires: Bi_2Te_3 nanowires embedded in alumina matrix.

The thermal conductivity of Bi_2Te_3 nanowires with different diameters, ranging from 300 nm to 45 nm, was studied with SThM. A reduction of the thermal conductivity, from 1.88 ± 0.40 $W \cdot K^{-1} \cdot m^{-1}$ to 0.51 ± 0.40 $W \cdot K^{-1} \cdot m^{-1}$, was observed as the diameter of the NW becomes smaller. In order to explain it, the Kinetic-Collective model developed by the physics group of the University of Barcelona was used. The theoretical model includes many different types of scattering for phonons in the nanowires and its results are in the order of magnitude as those obtained experimentally within the error. These results show for the first time, to the best of our knowledge, how the thermal conductivity of Bi_2Te_3 nanowires embedded in a matrix varies with its diameter, whose behavior can be explained by a theoretical model. COMSOL Multiphysics® simulations of these thermoelectric nanowires were performed in order to observe the high potential efficiencies that could be achieve with this one-dimensional structures, using the thermal conductivity values obtained.

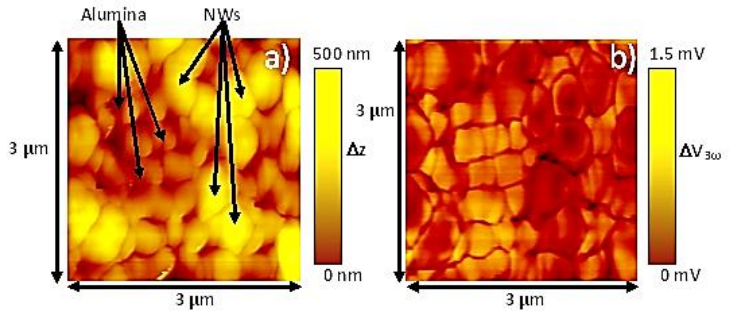

b) Organic nanowires: P3HT polymer embedded in alumina matrix.

The thermal conductivity of P3HT, a commodity polymer, NWs with different diameters, ranging from 350 nm to 120 nm, was determined with SThM. A drastic reduction of the thermal conductivity was observed as the diameter of the nanowire reduced, from $2.29 \pm 0.15\, W \cdot K^{-1} \cdot m^{-1}$ to $0.50 \pm 0.24\ W \cdot K^{-1} \cdot m^{-1}$. This reduction was related to the different orientation of the polymer chains at the different NW diameters. The COMSOL Multiphysics® was used to validate the effective medium theory used to calculate the thermal conductivities of the NWs. This work establishes the foundations to control the thermal conductivity of polymers (thermal transport engineering of polymers).

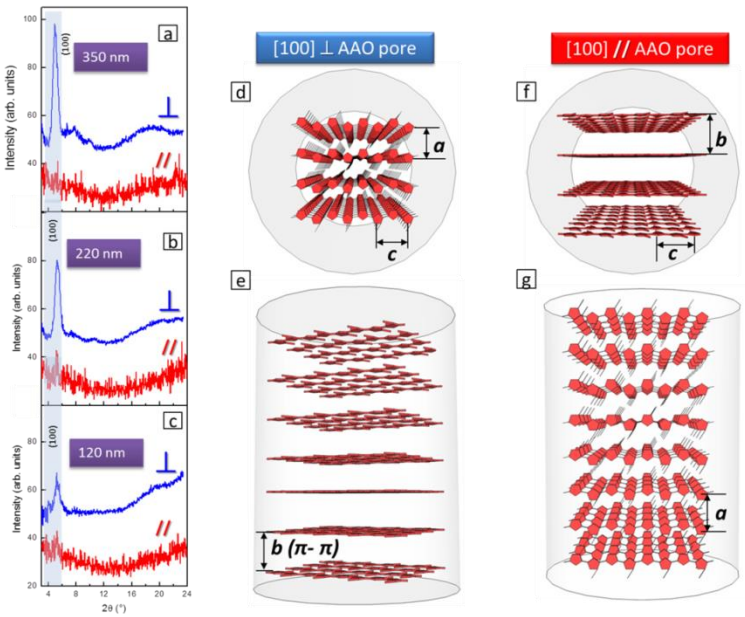

1.3. Thermal transport in other nanostructures:

a) Holographic structures: Bi_2Te_3 nano-structure.

Apart from nanowires and films, a especial structure was fabricated from the interference of four laser beams on a photoresist inside which Bi_2Te_3 was grown via electrodeposition. The thermal conductivity of this holographic structure was measured with SThM, resulting in a value of $0.30 \pm 0.13\ W \cdot K^{-1} \cdot m^{-1}$, which involves a reduction of around 85% respect to single crystalline bulk Bi_2Te_3. This is explained from the increment of phonon scattering caused by the 3D holographic structure of interconnected Bi_2Te_3 nano-channels that were obtained from the interference pattern. These structures might be the basis for the fabrication of future phononic dispersion devices with strongly reduced thermal conductivity for high efficient thermoelectric devices. Furthermore, the holographic structures have a huge potential as smaller wavelength lasers could be used to reduce the size of the channels, which might reduce even more the thermal conductivity, or deposit other kinds of materials.

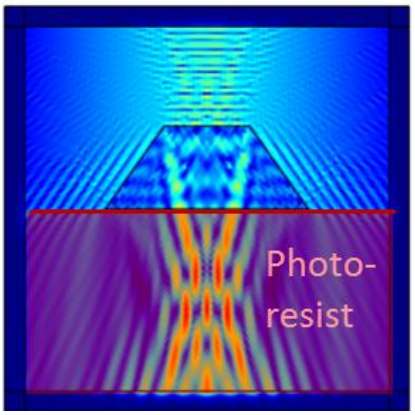

2. **Electrical transport property measurements:** Scanning Probe Microscopy was proved to be a powerful tool to carry out local measurements of the electrical properties of nano-structures. Moreover, other techniques, like Four Probe method or Harman technique, were considered to obtain electrical properties of nano-structures within the help of COMSOL Multiphysics ® modeling.

2.1. Harman Method: Films & Nanowires:

a) Direct determination of zT for films and nanowires: Modelling of Harman method.

The Harman method allows the determination of the *zT* of a thermoelectric material from a single measurement. While it has been extensively applied to bulk materials, its implementation to nano-structures, like films or nanowires, is challenging. A deep theoretical study of the working regimes for the modified transient Harman method applied to thin films and nanowires under ideal and non-ideal conditions, i.e. under the presence of electrical contacts and wires, was performed with COMSOL Multiphysics ® simulations. The low and high frequencies regimes required to measure 2D and 1D structures and the influence that the presence of electrical contacts and wire have in the determination of the figure of merit of films with the modified Harman technique were. These results are very useful for experimentalists that want to use the modified Harman method to measure nanostructures in order to choose the appropriate experimental equipment and to know the challenges that one must face.

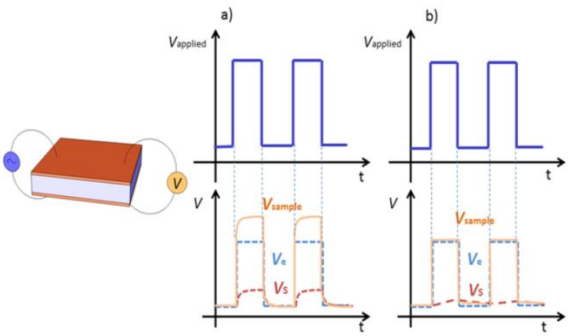

2.2. Electrical transport in films:

a) Interface Au-Bi_2Te_3 (electrode-film) contact resistance.

The electrical contact resistance at the interface of electrodes and film might have an important influence in the measured resistance. Therefore, its analysis must be carried out carefully. The Kelvin Probe Microscopy was used to scan the edge of a Bi_2Te_3 film sandwiched between gold electrodes. By measuring the voltage drop at the interface and knowing the current applied across it, the contact resistance at the interface was determined. The accuracy of this method is really good to the point that it was possible to distinguish between two different types of interfaces: i) one at which the top gold electrode was deposited by electronic beam evaporator on top of the Bi_2Te_3 film and ii) the one that correspond to the first electrodeposited layers of Bi_2Te_3 film on the bottom gold electrode, which resulted in lower contact resistance because the atoms adhesion and roughness is better in this case. This is a different approach to measure the electrical resistance of films.

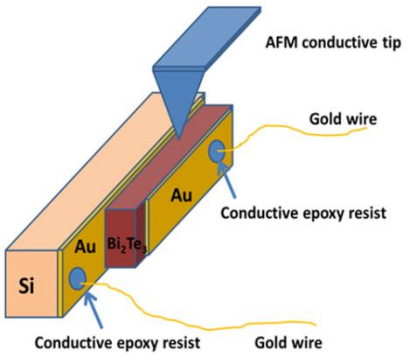

b) Electrical conductivity of Bi_2Te_3 films.

The electrical conductivity of highly oriented Bi_2Te_3 films in the [1 1 0] direction was carried out using a four probe station. Due to the anisotropic nature of the Bi_2Te_3 material, the *in plane* electrical properties are different to those found *out of plane*. While *in plane* measurements can be carried in a relatively easy way, the *out of plane* ones become more complicated. These measurements are not trivial and require a careful analysis of the spreading of the electric field and the influence of the contact resistances, among others. For that purpose, a special set up was performed consisting in the fabrication of films in shape of discs with different diameters and thicknesses. To this end, lithography processes and mesa attacks were needed. The resistance of the discs was measured with the four probe station and COMSOL Multiphysics® simulations were used to analyze and determine the electrical conductivity of the films and deeply understand the physics behind. An electrical conductivity for the film of $(3.2 \pm 0.4)\cdot 10^5$ S/m was found, which is three times larger than the one expected for bulk single crystal Bi_2Te_3. This large value is mainly related with the high orientation of the film and the fact that this electrochemical deposition technique uses an electric field during the growth, which favors the growth of Bi_2Te_3 grains oriented along the highest electrical conductivity direction. This is a step forward to obtain films via electrodeposition with larger power factors to higher efficient thermoelectric materials.

Another important conclusion is the fact that the finite element model shows that significant errors could arise in measurements of the electrical conductivity of low resistive films if simpler one-dimensional models are employed, as

they do not account for the non-uniform distribution of the electric field, among other effects.

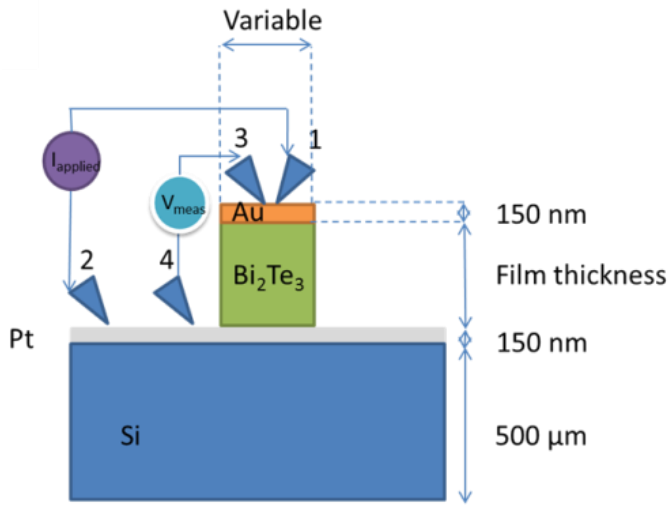

2.3. Electrical transport in nanowires:

a) Electrical conductivity of Bi_2Te_3 nanowires embedded in alumina matrix.

The electrical conductivity of nanowires embedded in alumina matrix with different diameters ranging from 250 nm to 45 nm was measured with conductive atomic force microscopy. For that purpose, a conductive AFM probe positioned on top of the nanowire and took *I-V* curves. These two-probe measurements carry a large error cause mainly because of the contact resistance between the probe and the nanowire. However, considering certain measuring conditions an average resistance was obtained from an statistical study for each nanowire diameter. Assuming that there is no variation in the electrical conductivity of the nanowires for the range of diameters considered, the linear fit obtained from the plot of the averaged electrical resistance versus L_{NW}/A_{NW} gave information of the electrical

conductivity of the nanowires. It was determined to be $(3.8 \pm 1.1) \cdot 10^4 \Omega \cdot m$, which was successfully compared with literature values.

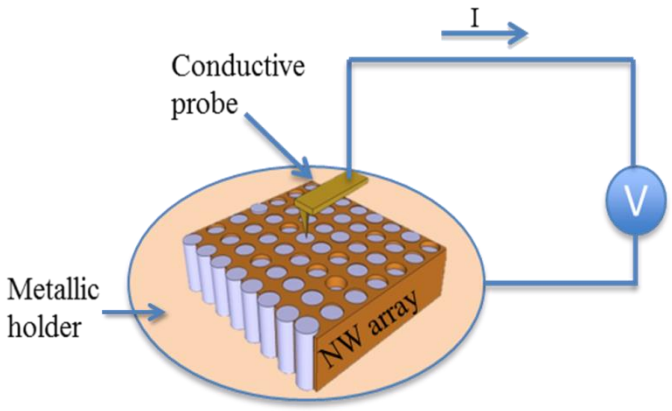

b) Surface conduction and topological insulators effects.

Bi_2Te_3 is also known as a topological insulator material. TI have exotic metallic surface states (SS) that are protected by time-reversal symmetry and are thus immune to inelastic scattering by trace amount of defects and nonmagnetic impurities. Therefore, Bi_2Te_3 might present conducting states at the surface, but insulating behavior for bulk. When this material becomes nanostructured, the inherently large surface-to-volume ratio is especially suitable for exploring device applications utilizing SS transport. In order to observe these effects, the surface conduction of Bi_2Te_3 nanowires with different diameters was studied using Kelvin Probe Microscopy (KPM). For that purpose, the nanowire was placed on a microchip, bridging electrodes separated by ~ 1 μm gap. Then, while passing a current across it, the voltage drop along the NW was studied locally with the KPM. From these measurements, the surface conduction of the NW was determined. It was observed that the conductivity increases from ~$1 \cdot 10^4$ S/m to

~$3 \cdot 10^4$ S/m as the diameter becomes smaller, which was correlated to the surface states found for these materials. Moreover, exotic surface potential ripples were found on the surface of the nanowire, whose amplitude and separation was studied for each diameter wire. It might be possible to both manipulate the conduction pathways of these nanostructured TIs and modulate their local potential energy landscapes by tuning the structural and/or chemical disorder. Consequently, the observed effects will pave the way for practical TI devices for thermoelectrics, spintronics or quantum computing, among others.

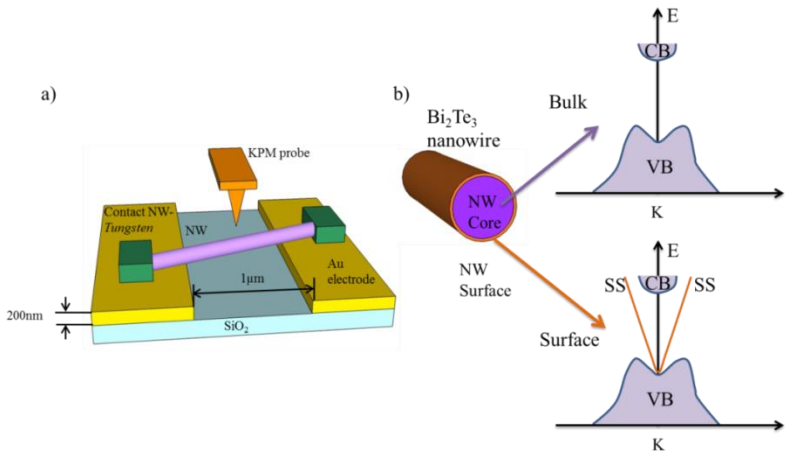

In summary, transport property measurements of nanostructures made of different materials are presented in this work. The results bring new insights and limitations in measuring, analyzing and understanding these nanostructures. In terms of thermoelectricity, thermal and electrical measurements are mandatory to determine the efficiency of these materials. Measurements of these transport properties in thermoelectric nanostructures is challenging, but in this work, the candidate has been able to use an Atomic Force Microscopy (AFM) under the proper working modes and measuring conditions, within the help of simulations and other codes for the analysis, to determine the thermal and electrical conductivity of thin films and nanowires.

Conclusiones

Las conclusiones generales que se pueden extraer de este trabajo de tesis doctoral se resumen en las siguientes partes:

1. **Medidas de las propiedades de transporte térmicas:** El microscopio de barrido térmico (SThM) trabajando tanto en modo DC como AC ha mostrado ser una potente técnica para llevar a cabo medidas térmicas locales de nano-estructuras, tanto orgánicas como inorgánicas. Los siguientes puntos resumen los resultados más relevantes que se han obtenido:

1.1 Transporte térmico en películas:

c) Películas Inorgánicas: Silicio Germanio.

La conductividad térmica de películas de silicio germanio (SiGe) crecidas mediante cristalización inducida por metal bajo dos tratamientos térmicos (*in-situ* y *ex-situ*) fueron estudiadas por SThM. Los resultados mostraron una reducción térmica significativa, $1.42 \pm 0.12\ \mathrm{W \cdot K^{-1} \cdot m^{-1}}$ (*in-situ*) and $1.53 \pm 0.08\ \mathrm{W \cdot K^{-1} \cdot m^{-1}}$ (*ex-situ*), en comparación con películas de SiGe obtenidas por técnicas similares ($4 - 5\ \mathrm{W \cdot K^{-1} \cdot m^{-1}}$). Esta reducción en la conductividad térmica se relacionó con un incremento de la dispersión de fonones en las intercaras entre nano-cristales y cúmulos formados durante el proceso de crecimiento. Este resultado ha dado lugar a nuevos avances para obtener películas de SiGe con conductividad térmica reducida.

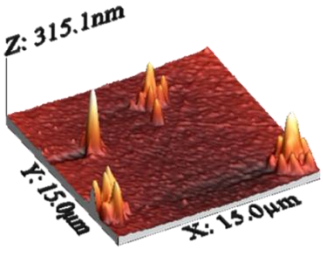

d) Películas Orgánicas: polímero PCDTBT dopado y sin dopar.

La conductividad térmica de películas poliméricas de PCDTBT, crecidas por método de goteo, dopadas y sin dopar con átomos de hierro fueron estudiadas mediante SThM. Mientas la conductividad térmica de las películas dopadas es de $0.19 \pm 0.02\ W \cdot K^{-1} \cdot m^{-1}$, la conductividad térmica de las películas dopadas se encuentra alrededor de $1\ W \cdot K^{-1} \cdot m^{-1}$, con una variación entre ellas menor que un 25%. La conductividad térmica total de las películas dopadas es influenciada por el término electrónico, pero también, por la presencia de iones que contribuyen al término de conductividad fonónica, especialmente cuando el nivel de dopado aumenta. La combinación de los términos fonónicos y electronicos produce un valor similar en la conductividad térmica total para las diferentes concentraciones de dopado estudiados para las películas de PCDTBT.

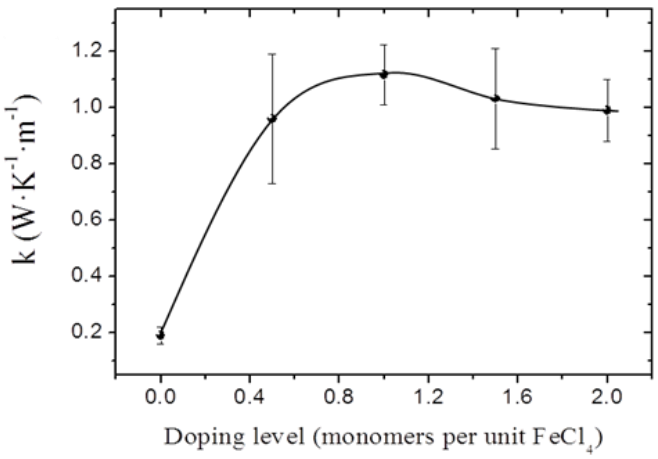

1.2 Transporte térmico en nanohilos:

c) Nanohilos inorgánicos: Nanohilos de Bi_2Te_3 embebidos en matriz de alúmina.

La conductividad térmica de nanohilos de Bi_2Te_3 con diferentes diámetros, entre 300 nm y 45 nm, fue estudiada con SThM. Una reducción de la conductividad térmica, de $1.88 \pm 0.40\ W \cdot K^{-1} \cdot m^{-1}$ a $0.51 \pm 0.40\ W \cdot K^{-1} \cdot m^{-1}$, fue observada conforme el diámetro del nanohilo se reduce. Para explicar esto, el modelo Cinético-Colectivo desarrollado por el departamento de física de la Universidad de Barcelona fue utilizado. El modelo teórico incluye diferentes tipos de dispersión fononica para los nanohilos y sus resultados se encuentran en el mismo orden de magnitud que los obtenidos experimentalmente con su error. Estos resultados muestran por primera vez, respecto a lo que se conoce hasta el momento, como la conductividad térmica de nanohilos de Bi_2Te_3 varía con el diámetro, cuyo comportamiento puede ser explicado mediante modelos teóricos. Simulaciones de esos nanohilos termoeléctricos se han llevado a cabo con COMSOL Multiphysics® para observar las buenas eficiencias termoeléctricas que podrían obtenerse con este tipo de estructuras unidimensionales, usando los valores de conductividad térmica obtenidos.

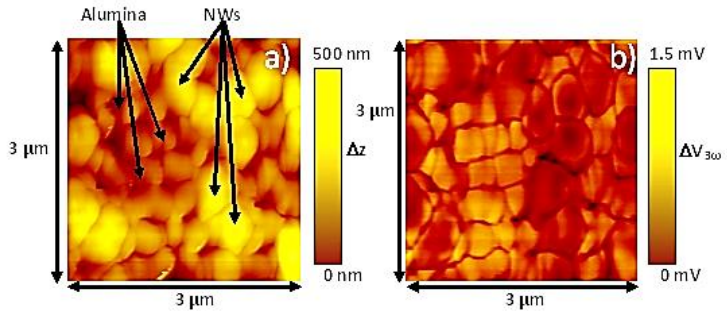

d) Nanohilos orgánicos: polímero P3HT embebido en matriz alúmina.

La conductividad térmica de nanohilos de P3HT, un polímero modelo, con diferentes diámetros, entre 350 nm y 120 nm, fue determinada mediante SThM. Una drástica reducción de la conductividad térmica fue observada conforme el diámetro del nanohilo se reducía, de $2.29 \pm 0.15\ \mathrm{W \cdot K^{-1} \cdot m^{-1}}$ a $0.50 \pm 0.24\ \mathrm{W \cdot K^{-1} \cdot m^{-1}}$. Esta reducción se relacionó con las diferentes orientaciones de las cadenas poliméricas en los diferentes diámetros de nanohilos. Simulaciones con COMSOL Multiphysics® fueron utilizadas para validar la teoría media efectiva utilizada para calcular las conductividades térmicas de dichos nanohilos. Este trabajo establece los pilares para controlar la conductividad térmica de polímeros (Ingeniería de transporte térmico de polímeros).

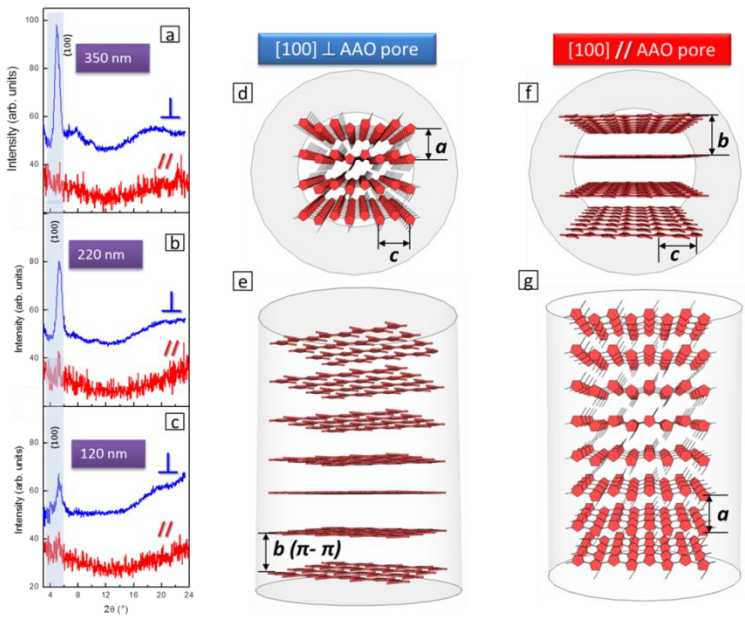

1.3. Transporte térmico en otras nano-estructuras:

a) Estructuras holográficas: Nano-estructuras de Bi_2Te_3.

Además de nanohilos y películas, una estructura especial fue fabricada a partir de la interferencia de cuatro rayos láseres sobre una fotoresisna dentro de la cual Bi_2Te_3 fue crecido mediante electrodeposición. La conductividad térmica de esta estructura holográfica fue medida mediante SThM, dando un valor de $0.30 \pm 0.13\ W \cdot K^{-1} \cdot m^{-1}$, lo que involucra una reducción de un 85% respecto el Bi_2Te_3.monocristallino en volumen. Esto es explicado por un aumento de la dispersión fonónica causado por la estructura holográfica tridimensional de nano-canales interconectados Bi_2Te_3 que se obtuvieron del patrón de interferencia. Estas estructuras podrían ser la base para la fabricación de futuros dispositivos de dispersión fonónica con conductividades térmicas altamente reducidas. Además, las estructuras holográficas tienen un alto potencial puesto que láseres con menor longitud de onda pueden ser utilizados para reducir el tamaño de los canales, lo que podría reducir aún más la conductividad térmica, o bien se podrían depositar otros tipos de materiales.

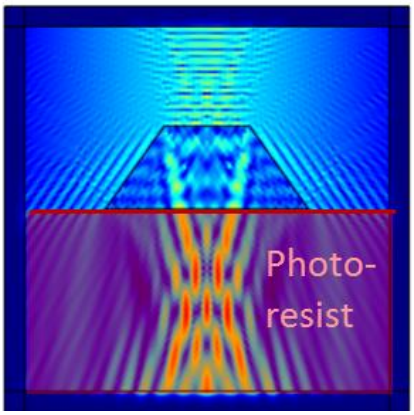

2. **Medidas de propiedades de transporte electrónico:** Las técnicas de sonda local probaron ser una herramienta muy potente para llevar a cabo medidas locales de las propiedades eléctricas de nano-estructuras. Además, otras técnicas, como la estación de cuatro puntas o el método de Harman, fueron consideradas para obtener las propiedades eléctricas de nano-estructuras junto con la ayuda de simulaciones con COMSOL Multiphysics ®.

2.1. Método Harman: Películas & Nanohilos:

a) Determinación directa de la zT de películas y nanohilos: Simulaciones del método Harman.

El método Harman posibilita la determinación de la *zT* de materiales termoeléctricos mediante una única medida experimental. A pesar de que este método ha sido ampliamente utilizado para materiales en volumen, su implementación en nano-estructuras, como películas o nanohilos, es todavía un reto. Un análisis teórico de los regímenes de trabajo que deben usarse en películas delgadas y nanohilos bajo condiciones ideales y no ideales, es decir en presencia de contactos y cables eléctricos, es llevado a cabo usando simulaciones con COMSOL Multiphysics ®. Los regímenes de bajas y altas frecuencias requeridos para medir estructuras bidimensionales and unidimensionales y la influencia que los contactos y cables eléctricos tienen en la medida de la figura de mérito de películas termoeléctricas con el método de Harman son presentadas en esta sección. Estos resultados son extremadamente útiles para los científicos experimentales que deseen usar el método

Harman para medir sus nano-estructuras así como para conocer los retos a los que se enfrentan.

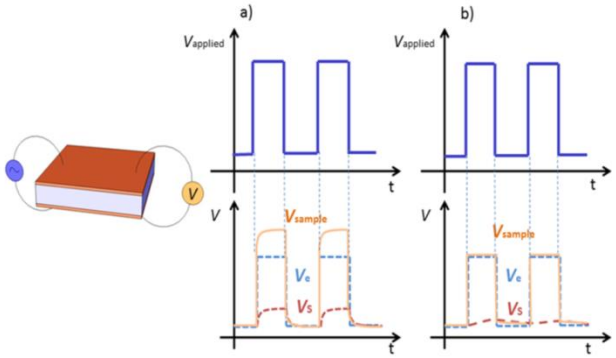

2.2.Transporte electrónico en películas:

c) Resistencia de contacto en la intercara Au-Bi_2Te_3 (electrodo-película).

La resistencia de contacto en la intercara entre electrodos y películas delgadas puede tener una importante influencia en la medida de la resistencia. Por tanto, su análisis debe llevarse a cabo de forma cuidadosa. La microscopía por sonda Kelvin fue utilizada para escanear el borde de una película de Bi_2Te_3 entre dos electrodos de oro. Midiendo la caída de voltaje en la intercara y conociendo la corriente aplicada a través de esta, la resistencia de contacto en la intercara fue determinada. La precisión de este método es realmente buena hasta el punto de que es posible distinguir entre las dos intercaras medidas: i) una en la cual el electrodo de oro se depositó encima de la película mediante evaporación por haz de electrones y ii) el otro que corresponde a las primeras capas de Bi_2Te_3 electrodepositadas en el electrodo de oro de abajo, lo que da lugar a menor resistencia de contacto puesto que la adherencia y rugosidad es mejor en este caso. Este método

supone una aproximación diferente a la hora de medir la resistencia de contacto en películas.

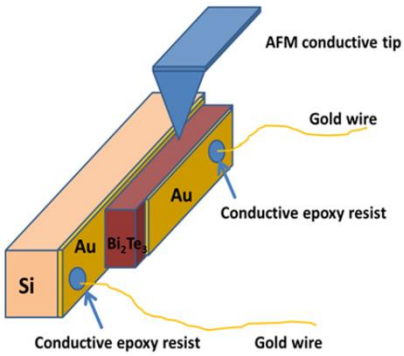

d) Conductividad eléctrica de películas de Bi_2Te_3.

La conductividad eléctrica de películas de Bi_2Te_3 altamente orientadas en la dirección [1 1 0] fue medida usando una estación de cuatro puntas. Dada la naturaleza anisotrópica del material de Bi_2Te_3, las propiedades eléctricas en el plano son diferentes a aquellas fuera del plano. Mientras que las medidas eléctricas en el plano pueden llevarse a cabo de una forma relativamente sencilla, las medidas fuera del plano son más complicadas. Dichas medidas no son triviales y requieren de un análisis cuidadoso de la dispersión del campo eléctrico y la influencia de las resistencias de contacto, entre otros. Para lograr este fin, un montaje especial fue llevado a cabo, consistente en la fabricación de películas en forma de discos con diferentes diámetros y espesores. Procesos de litografía y de ataques químicos fueron utilizados para lograr tal fin. La resistencia fue medida con la estación de puntas y simulaciones con COMSOL Multiphysics® fueron utilizadas para analizar y determinar la conductividad eléctrica de las películas y entender de forma precisa los procesos físicos. Una conductividad eléctrica de $(3.2 \pm 0.4)\cdot 10^5$ S/m fue encontrada para la película, siendo esta tres veces mayor que la esperada para el Bi_2Te_3 monocristalino

en volumen. Este valor tan alto está relacionado principalmente con la alta orientación de la película en la dirección [1 1 0] y el hecho de que la técnica de deposición por electroquímica usa un campo eléctrico que favorece el crecimiento de los granos de Bi_2Te_3 orientados a lo largo de la dirección con mayor conductividad eléctrica. Por estos motivos, la movilidad de los electrones puede ser aumentada dando lugar a altos valores de conductividad eléctrica. Esto es un paso adelante para obtener películas con altos factores de potencia mediante electrodeposición y provocar así un aumento de la eficiencia termoeléctrica de dichos materiales.

Otra conclusión importante es el hecho de que el modelo por elementos finitos muestra que errores importantes pueden surgir en la medida de la conductividad eléctrica de películas altamente conductoras si se utilizan modelos unidimensionales, puesto que no se tiene en cuenta la distribución no uniforme del campo eléctrico, así como otros efectos.

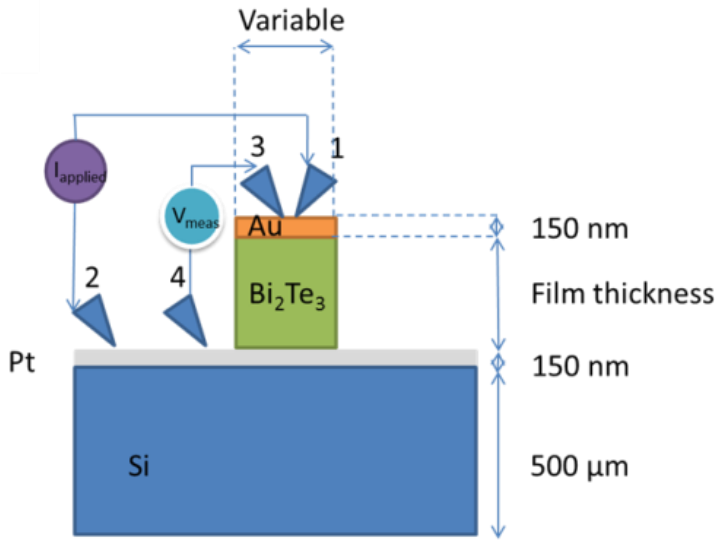

2.3. Transporte electrónico en nanohilos:

a) Conductividad eléctrica de nanohilos de Bi_2Te_3 embebidos en matriz alúmina.

La conductividad eléctrica de nanohilos embebidos en matriz alúmina con diámetros entre 250 nm y 45 nm fue medida por microscopía de fuerzas atómica conductiva. Para lograr este fin, una punta de AFM conductora se posicionó encima de los nanohilos y se tomaron curvas *I-Vs*. Estas medidas a dos puntas usualmente llevan mucho error experimental, especialmente causado debido a la resistencia de contacto entre la punta y el nanohilo. Sin embargo, bajo ciertas condiciones de medida, la resistencia promedio de los nanohilos puede ser obtenida a partir de un estudio estadístico para cada diámetro de nanohilo. Asumiendo que no hay variación en la conductividad eléctrica de los nanohilos para el rango de diámetros considerado, el ajuste lineal obtenido de la gráfica de la resistencia eléctrica promedio frente a L_{NW}/A_{NW} da información de la conductividad eléctrica de los nanohilos. Este valor es $(3.8 \pm 1.1) \cdot 10^4 \Omega \cdot m$, el cual ha sido comparado exitosamente con valores de la literatura.

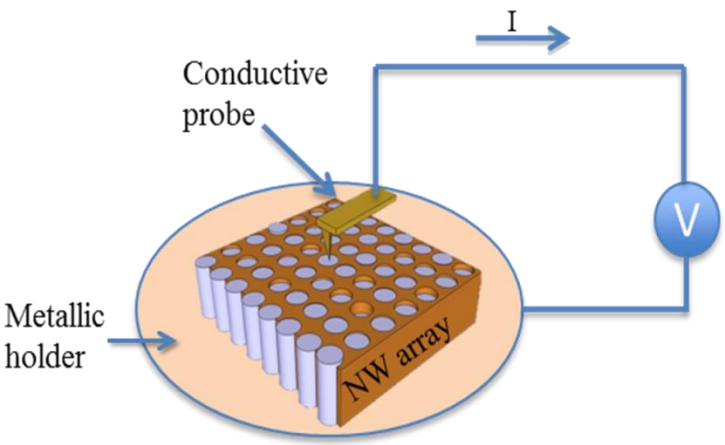

b) Conducción superficial y efectos de aislantes topológicos.

El Bi_2Te_3 es también conocido como aislante topológico. Los aislantes topológicos tienen estados superficiales (SS) exóticos que son protegidos por simetría de inversión temporal y que por tanto son inmunes a la dispersión inelástica debida a defectos o impurezas no magnéticas. Por tanto, el Bi_2Te_3 podría presentar estados conductores en su superficie pero un comportamiento aislante en volumen. Cuando este material se nano-estructura, el gran ratio inherente de superficie frente a volumen es especialmente interesante para explorar aplicaciones basadas en transporte superficial. Para observar dichos efectos, la conducción superficial de nanohilos de Bi_2Te_3 de diferentes diámetros fue estudiado usando Microscopía de sonda Kelvin (KPM). Con tal fin, el nanohilo se posicionó en un microchip, puenteando dos electrodos separados por ~ 1 µm gap. Mientras se aplica una corriente al nanohilo, la caída de voltaje a lo largo de este se estudia con el KPM A partir de estas medidas, la conducción superficial del nanohilo se pudo determinar. Se observó que conforme el diámetro del nanohilo se reduce, la conductividad eléctrica aumentaba de $\sim 1 \cdot 10^4$ S/m a $\sim 3 \cdot 10^4$ S/m, lo que fue relacionado con los estados superficiales encontrados para estos materiales. Adicionalmente, ondulaciones del potencial superficial fueron encontrados en la superficie del nanohilo, cuya amplitud y separación fue estudiada para cada diámetro. Podría ser posible tanto la manipulación de los caminos de conducción de dichos aislantes topológicos nano-estructurados como la modulación de sus paisajes de potencial superficial locales mediante el ajuste del desorden estructural y/o químico. Consecuentemente, los efectos observados darán lugar a un

nuevo camino para dispositivos termoeléctricos, de espintronica o de computación cuántica, entre otros, basados en aislantes topológicos.

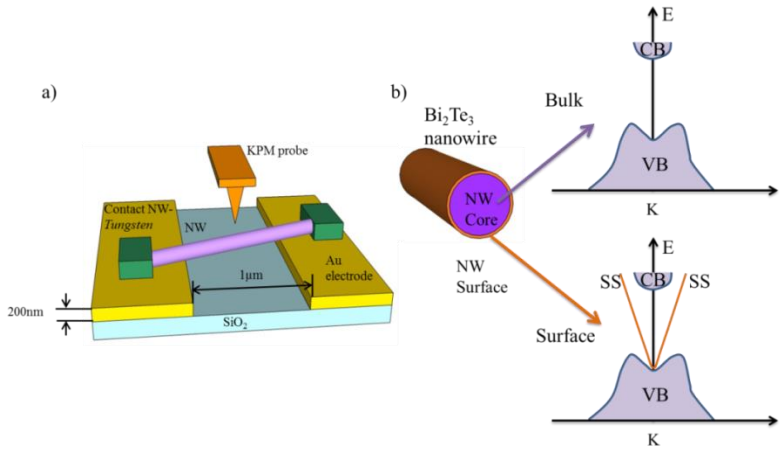

En resumen, las propiedades de transporte de nanoestructuras fabricadas con diferentes materiales son presentadas en este trabajo. Los resultados muestran nuevos conocimientos y limitaciones en la medida, el análisis y la compresión de dichas nanoestructuras. En términos de termoelectricidad, las medidas térmicas y eléctricas son fundamentales para determinar la eficiencia de dichos materiales. Las medidas de las propiedades de transporte en nanoestructuras son un desafío pero en este trabajo, el candidato ha sido capaz de usar un Microscopio de Fuerzas Atómicas bajo el modo de trabajo y las condiciones de medida adecuadas, junto con la ayuda de simulaciones y otros códigos de análisis, para determinar la conductividad térmica y eléctrica de películas y nanohilos.

List of publications

During this doctoral thesis, the PhD student has participated in 15 publications. The number of citations of each article has been taken from Google Scholar the 30th of May of 2015:

Publications as first author:

1. **"Electrical contact resistances of thermoelectric thin films measured by Kelvin Probe Microscopy". Authors: M. Muñoz Rojo**, O. Caballero-Calero and M. Martín-González**. Applied Physics Letters, 103,** (18), 183905-183905-5 (2013). Cited by: 1.

2. **"Fabrication of Bi_2Te_3 nanowire arrays and thermal conductivity measurements by 3ω-scanning thermal microscopy". Authors: M. Muñoz Rojo**, S. Grauby, J.-M. Rampnoux, O. Caballero-Calero, M. Martín-González and Stefan Dilhaire. **Journal of Applied Physics**, 113, 054308 (2013). Cited by: 13.

3. **"Review on measurement techniques of transport properties of nanowires". Authors: M. Muñoz Rojo**, O. Caballero-Calero, A.F. Lopeandia, Javier Rodriguez-Viejo, M. Martín-González**. Nanoscale, 5**, 11526-11544 (2013). Cited by: 12.

4. **"Decrease in Thermal Conductivity in Polymeric P3HT Nanowires by Size-Reduction induced by Crystal Orientation: New Approaches towards Organic Thermal Transport Engineering". Authors: M. Muñoz Rojo**, J. Martin, S. Grauby, T. Borca-Tasciuc, S. Dilhaire and M. Martín-González. **Nanoscale,** 6, 7858-7865 (2014). Cited by: 2.

5. **"Modeling of transient thermoelectric transport in Harman method for films and nanowires". Authors: M. Muñoz Rojo**, J. J. Romero, D. Ramos, D. Borca-Tasciuc, T. Borca-Tasciuc and M. Martín-González. **Journal of Thermal Science, Elsevier ,** 89, 193-202 (2015).

6. **"High Electrical Conductivity in out of plane direction of electrodeposited Bi_2Te_3 films". Authors: M. Muñoz Rojo**, C.V. Manzano, D. Granados, M. R. Osorio, T. Borca-Tasciuc and M. Martín-González. ***Submitted to Journal of Applied Physics (Under reviewer's revision).***

7. **"Strong Reduction in Thermal Conductivity by Electrodeposition of Bismuth Telluride into a 3D photonic template". Authors: M. Muñoz Rojo*,** O. Caballero-Calero***,** Jerónimo Buencuerpo and M. Martín-González**.** ***(To be submitted).*** ***** Authors contributed equally to this work appearing both as first authors.

8. **"AC Seebeck Coefficient and Thermal Conductivity Measurements of High and Low Thermal Conductivity Films using Scanning Wollaston Hot Probe in the 3ω Mode". Authors:** Adam A. Wilson***, M. Muñoz Rojo***, B. Abad, J. Andrés Perez, Jason Schomacker, M. Martín González, D. Andra Borca-Tasciuc and T. Borca-Tasciuc. ***Submitted to Nanoscale (Under second reviewer's revision).*** ***** Authors contributed equally to this work appearing both as first authors.

9. **"Potential ripples and surface conduction of topological insulator nanowires of Bi_2Te_3". Authors: M. Muñoz Rojo*,** Yingjie Zhang*****, C.V. Manzano, R. Álvaro, Miquel Salmeron and M. Martín González. ***Submitted to Nature Communications.*** ***** Authors contributed equally to this work appearing both as first authors.

Publications as co-author related to the work presented in this thesis:

1. **"Improvement of Bismuth Telluride electrodeposited films by the addition of Sodium Lignosulfonate". Authors:** O. Caballero-Calero, P. Díaz Chao, B. Abad, C.V. Manzano, M.D. Ynsa, J.J. Romero, **M. Muñoz Rojo** and M. Martín González. **Electrochimica Acta,** 123, 117-126 (2014). Cited by: 5.

2. **"Low thermal conductivity of nanocrystalline Silicon Germanium films by Sputtering". Authors:** J. A. Perez, J. J. Romero, B. Abad, **M. Muñoz Rojo**, A. Mello, F. Briones and M. Martin-Gonzalez. **S*ubmitted to Scientific Reports*.**

3. **"Enhancement of thermoelectric efficiency of PCDTBT polymer films". Authors:** J. Maiz, **M. Muñoz Rojo**, B. Abad, A. Wilson, A. Nogales, T. Borca-Tasciuc and M. Martín-González. **(*To be Submitted)***

4. **"Effect of anisotropy on the thermoelectric properties of highly oriented electrodeposited Bi_2Te_3 films". Authors:** C.V. Manzano, B. Abad, **M. Muñoz Rojo**, Y.R. Koh, S. Hodson, X. Xu, A. Shakouri, T. Sands, T. Borca-Tasciuc and M. Martín-González. **(*To be Submitted*)**

Other publications as co-author not shown in this thesis:

1. **"Quantitative nanoscale surface voltage measurement on organic semiconductor blends". Authors**: Alexandre Cuenat, Andrés Muñiz-Piniella, **M. Muñoz-Rojo**, Wing C Tsoi and Craig E Murphy. **Nanotechnology** 23 (2012) 045703 (7pp). Cited by: 7.

2. **"Fabrication and Mechanical Characterization of Semi-Free-Standing (Conjugated) Polymer Thin Films". Authors:** J. Martín, **M. Muñoz Rojo**, M. Encinar, M. Calleja, M. Martín-González. **Langmuir, 30(18), 5217-5223 (2013)**. Cited by: 3. **(Langimur Cover: May 13, 2014 Volume 30, Number 18.)**

APPENDIX

List of Figures

List of Tables

List of variables

α = Thermal Coefficient

ε = Electric Field

ϵ = Emissivity

λ = Wavelength

μ = Electrochemical Potential or Fermi Level

Π = Peltier coefficient

ρ = Electrical Resistivity

σ = Electrical Conductivity

ω = Pulsation or Angular Frequency

A = Area

b = Thermal Exchange Radius Probe

C = Heat Capacity

c = Specific Heat Capacity

d = diameter

E = Energy

F = Force

f = Frequency

G = Conductance Coefficient

h = Convective Heat Transfer Coefficient

$\hbar$ = Dirac Constant or Reduced Planck Constant

I = Current

J = Current Density

K = Boltzman Constant

k = Thermal Conductivity

L = Length

m_{fp} = Mean free path

P = Power

p = Perimeter

Q = Heat Transfer Rate

q = Charge

R = Resistance

S = Seebeck Coefficient

T = Temperature

t = Thickness

TCR = Temperature Coefficient of Resistance

U = Electric Potential

V = Voltage

v = Velocity

w = Width

z = Figure of Merit